NATIONAL INSTITUTE FOR FUSION SCIENCE

平成 10 年度核融合科学研究所共同研究 研究会
「プラズマ閉じ込めに関連する数値計算手法の研究」
Proceeding of 1998-Workshop on MHD Computations
"Study on Numerical Methods Related to Plasma Confinement"

研究代表者　加古　孝（電気通信大学）
所内世話人　渡辺　二太
Ed. by T. Kako and T. Watanabe

(Received - Mar. 11, 1999)

RESEARCH REPORT
NIFS-PROC Series

NAGOYA, JAPAN

Proceeding of 1998-Workshop on MHD Computations

"Study on Numerical Methods related to Plasma Confinement"

Edited by T. Kako and T. Watanabe

November 25 – 27, 1998
National Institute for Fusion Science
Toki, Japan

Abstract

This is the proceeding of " Study on Numerical Methods related to Plasma Confinement " held in National Institute for Fusion Science. In this workshop, theoretical and numerical analyses of possible plasma equilibria with their stability properties are presented. There are also various talks on mathematical as well as numerical analyses related to the computational methods for fluid dynamics and plasma physics.

Preface

This volume contains 21 papers contributed at the 1998-Workshop on MHD Computations held in Toki, November 25-27, 1998. This workshop was held as one of the collaboration research projects of the National Institute of Fusion Sciences (NIFS). On the other hand, for more than seventeen years, we have been continuing the workshop on the numerical computations related to the thermonuclear fusion research, organizing the domestic researchers in plasma physics and applied mathematics.

The purpose of this workshop is to study various possible plasma behaviors and its controllability in the fusion research. The main basic mathematical model treated in the workshop has been Magneto-Hydro-dynamics (MHD).

This year, there were more than 30 participants in the workshop, and we had 24 contributed talks under the following themes: 1) Study of plasma equilibria and their stability analysis applied to plasma control; 2) Proposal of new numerical methods and simulation techniques related to fluid dynamics and electromagnetism; 3) Study of related mathematical as well as numerical analyses.

We hope that this volume will contribute to the further development of the research in this field.

Organizers

IMAI, Hitoshi (Tokushima University, Tokushima, Tokushima 770)

USHIJIMA, Teruo (Univ. Electro-Communications, Chofu, Tokyo 182-8585)

KAKO, Takashi (University of Electro-Communications, Chofu, Tokyo 182-8585)

TANABE, Kunio (Institute of Statistical Mathematics, Minato-ku, Tokyo 106)

TODOROKI, Jiro (National Institute for Fusion Science, Toki, Gifu 509-5292)

HAMADA, Shigeo (Nihon University, Chiyoda-ku, Tokyo 101)

WAKATANI, Masahiro (Kyoto University, Uji, Kyoto 611)

WATANABE, Tsuguhiro (National Inst. for Fusion Science, Toki, Gifu 509-5292)

Contents

List of Participants

Aiso, Hideaki	National Aerospace Laboratory
Chiba, Fumihiro	The University of Electro-Communications
Fukuyama, Atsushi	Kyoto University
Furukawa, Masaru	Kyoto University
Hamada, Shigeo	Nihon University
Hataue, Itaru	Kumamoto University
Ida, Akihiro	Nagoya University
Idomura, Yasuhiro	Kyoto University
Igarashi, Hajime	Hokkaido University
Ikuno, Soichiro	Tsukuba University
Imai, Hitoshi	Tokushima University
Kako, Takashi	The University of Electro-Communications
Kamitani, Atsushi	Yamagata University
Kawaguchi, Hideki	Hokkaido University
Kondoh, Shigeo	The University of Tokyo
Kurata, Michinari	Nagoya University
Liaqat, Ali	The University of Electro-Communications
Ma, Xiao-Feng	The University of Electro-Communications
Nakamura, Yuji	Kyoto University
Sanuki, Heiji	National Institute for Fusion Science

iv

Suzuki, Takashi   Osaka University

Takaku, Yuichi   Nihon University

Takase, Haruhiko   Japan Atomic Energy Research Institute

Takeda, Tatsuoki   The University of Electro-Communications

Tatsuno, Tomoya   Kyoto University

Todoroki, Jiro   National Institute for Fusion Science

Tohnai, Tomoya   Okayama University

Ushijima, Teruo   The University of Electro-Communications

Wakatani, Masahiro   Kyoto University

Watanabe, Tsuguhiro   National Institute for Fusion Science

Evolution of Field Reversed Configuration[1]

S. Hamada and Y. Takaku
College of Science and Technology Nihon university
25th November 1998

Abstract

The model is studied systematically. An integral theorem and relations among several decay rates of relevant quantities are obtained. The quasi-steady solution of this model is also studied to make clear under which circumstance it is maintained to be a stationary solution of the time dependent model equation. A formal criterion for a quasi-steady solution to be an attractor is deduced.

1 Introduction

The 1 1/4 D time dependent model of Field Reversed Configuration (FRC) was proposed by Steinhauer, Milroy and Slough in 1985 for the first time and numerically solved to examine validity of their 1 1/4 D quasisteady model[1]. Although there are more realistic models of FRC[2][3] other than this one, it may be worth studying systematically because it is the simplest model with perfect inner consistency. Our study has not yet finished but our schedule is as follows. First, we formulate again this model so as to fit our purpose. Second, quasi stationary solutions are shown to be maintained under a certain circumstance. Third, it is studied under which circumstance it could be an attractor. Finally, it will be studied what would happen if the foregoing circumstances are violated. Here, we report results up to the second problem and, as for the third problem, only a formal criterion for the quasisteady solution to be an attractor. Assumptions for the model are as follows.

1. **long racetrack shape of separatrix** Length $L(t)$ of the uniform part of separatrix is sufficiently longer than the radius $r_s(t)$

$$\frac{L}{r_s} \gg 1 \qquad (1.1)$$

   L and r_s are treated as slowly dependent on time t and length of all the magnetic surfaces are taken to be equal to $L(t)$.

2. **axial symmetry** We set cylindrical coordinates (r, θ, z) with z axis aligned on the axis of symmetry and $z = 0$ on the equatorial plane of the separatrix. As we concentrate mainly on structure of the uniform part of separatrix, almost all field quantities are taken to be independent of z, that is, the z component of magnetic field B_z, the θ component of electric field E_θ, the r component of plasma velocity v_r, the plasma pressure p, the plasma density ρ and the electric resistivity η are taken to be functions of r, t only. One exception is the z component of plasma velocity v_z, which is taken to be a function of r, z, t. Another exception is a parameter Θ of plasma temperatures, which is taken to be spacially uniform. (See next item.)

---

3. **Uniformity of temperatures** We assume that the ratio of the plasma pressure to the density is spacially uniform and dependent only on time t.

$$\frac{p}{\rho} = \frac{kT_i}{m_i} + \frac{ZkT_e}{m_i} = \Theta(t) \tag{1.2}$$

where m_i and m_e are the ion and electron mass, T_i and T_e the ion and electron temperatures, Z the charge number of ion and k the Boltzmann's constant.

4. **uniformity of main coil** The main coil has a uniform inner radius r_w and sufficiently longer than the separatrix length $L(t)$. As a result, we have the well known axial force balance relation[6]

$$\langle \beta \rangle = 1 - \frac{r_n^2}{r_w^2} \tag{1.3}$$

where $\langle \beta \rangle$ is the β ratio averaged inside the separatrix and r_n is the radius of the neutral surface. (Notice the well known relation that $2r_n^2 = r_s^2$.)

5. **functional form of v_z** We assume that

$$v_z(r,z,t) = \frac{2z}{L}v_z(r,\frac{L}{2},t) \quad (1.4) \qquad v_z(r,\frac{L}{2},t) = \frac{1}{2}\frac{dL}{dt} + \nu(r,t) \tag{1.5}$$

where ν is the z component of relative velocity of plasma to the separatrix end. The function ν is determined later. See eq. (3.2).

6. **basic laws used for the model** In addition to the foregoing assumptions. the model is based upon the following laws.

pre-Maxwell equations:

$$\frac{\partial \vec{B}}{\partial t} = -\nabla \times \vec{E} \quad (1.6) \qquad \nabla \cdot \vec{B} = 0 \quad (1.7) \qquad \mu \vec{j} = \nabla \times \vec{B} \tag{1.8}$$

generalized Ohm's law

$$\eta \vec{j} = \vec{E} + \vec{v} \times \vec{B} \tag{1.9}$$

equilibrium equation

$$\nabla p = \vec{j} \times \vec{B} \tag{1.10}$$

mass continuity equation for particle transport

$$\frac{\partial \rho}{\partial t} + \nabla \cdot (\rho \vec{v}) = 0 \tag{1.11}$$

where μ is the permiability of vacuum, $\vec{j}$ the electric current density and η the electric resistivity of the plasma.

2   Dimensionless Flux ψ, Coordinate u and Time Variable τ

We define a dimensionless flux ψ as

$$\psi(r,t) = \frac{1}{\pi r_s^2 B_e} \int_0^r 2\pi r B_z(r,t) dr \tag{2.1}$$

so that ψ is related to the magnetic flux Φ as

$$\Phi(r,t) = \pi r_s^2(t) B_e(t) \psi(r,t) \tag{2.2}$$

Here, $B_e(t)$ is the value of B_z at the inner wall $r = r_w$ of the main coil. It will be called "external field" hereafter. From this definition of ψ, we have

$$B_z = \frac{B_e r_s^2}{2r} \frac{\partial \psi}{\partial r} = 2B_e \frac{\partial \psi}{\partial u} \tag{2.3} \quad where \quad u = \frac{2r^2}{r_s^2(t)} - 1 \tag{2.4}$$

The coordinate u was introduced by Tuszewski and Linford[4]. As it is well known, this coordinate has many advantages. The axis of the system, the neutral surface and the separatrix always correspond to the values $-1, 0, 1$ of u, respectively. Inside the separatrix, every magnetic surface $\psi = const.$ has two radii $r_+(\psi) > r_-(\psi) > 0$ and , correspondingly, two coordinates $u_+(\psi) > u_-(\psi)$. The remarkable relation $u_- = -u_+$ always holds. Therefore, we have $\psi(u) = \psi(-u)$ so that $\psi(u)$ is an even function of u in the domain $[-1, 1]$ of u. p and ρ are also even functions of u but B_z is an odd function of u on account of (2.3). Furthermore, the function ν in eq. (1.5) is easily seen to be an odd function of u. Since the neutral surface corresponds to $u = 0$ because $u_+ = u_-$, we always have $r_n^2 = r_s^2/2$ on account of (2.4). These facts suggest that we had better to use the coordinate u rather than r.

In order to make resulting equation dimensionless, we introduce a dimensionless time variable τ and, correspondingly, decay rate $1/\tau_f$ of an arbitrary quantity f, which are defined as

$$\tau(t) = \int_0^t \frac{\eta(0,t)}{\mu r_n^2(t)} dt \tag{2.5} \quad \frac{1}{\tau_f} = -\frac{1}{f}\frac{df}{d\tau} = -\frac{\mu r_n^2}{\eta(0,t)f}\frac{df}{dt} \tag{2.6}$$

where $\eta(0,t)$ is the electric resistivity on the neutral surface.

Now, almost all relevant quantities except ν in (1.5) can be expressed in terms of $\psi(u,\tau)$ in the following way.

$$p = \frac{B_e^2}{2\mu}(1 - 4\psi'^2) \tag{2.7} \quad \rho = \frac{B_e^2}{2\mu\Theta}(1 - 4\psi'^2) \tag{2.8} \quad \mu j_\theta = -4B_e\frac{\sqrt{u+1}}{r_n}\psi'' \tag{2.9}$$

$$E_\theta = -\frac{\eta(0,\tau)}{\mu r_n(\tau)}\frac{B_e}{\sqrt{u+1}}\{\frac{\partial \psi}{\partial \tau} - (\frac{1}{\tau_{B_e}} + \frac{1}{\tau_{r_s^2}})\psi + \frac{u+1}{\tau_{r_s^2}}\psi'\} \tag{2.10}$$

$$rv_r = \frac{\eta(0,\tau)}{\mu}\frac{1}{2\psi'}\{-\frac{\partial \psi}{\partial \tau} + (\frac{1}{\tau_{B_e}} + \frac{1}{\tau_{r_s^2}})\psi - \frac{u+1}{\tau_{r_s^2}}\psi' + \frac{4\eta(u,\tau)}{\eta(0,\tau)}(u+1)\psi''\} \tag{2.11}$$

where $'$ means the partial derivative with respect to u.

3 Equation of Mass Continuity

The equation of mass continuity (1.11) is expressed in the cyrindrical coordinates as

$$(\frac{\partial \rho}{\partial t})_r + \frac{1}{r}\frac{\partial \rho r v_r}{\partial r} + \rho\frac{\partial v_z}{\partial z} = 0$$

Changing independent variables (r, t) to (u, τ), using (1.4, 5) for v_z, (2.8) for ρ and (2.11) for $r v_r$, we obtain an equation for $\psi(u, \tau)$. In the domain $[-1, 1]$ of u, the even and odd parts of this equation should hold separately. Thus, we obtain from the even part.

$$(\frac{1}{\psi'}\frac{\partial \psi}{\partial \tau})' = \frac{1}{1 + 4\psi'^2}[\{\frac{1 - 4\psi'^2}{\psi'}(\frac{\psi}{\tau_{B_e}r_s^2} + 4g(u, \tau)\psi'')\}'$$

$$-(\frac{1}{\tau_{B_e^2/\Theta}} + \frac{1}{\tau_{r_s^2}} + \frac{1}{\tau_L})(1 - 4\psi'^2)] \tag{3.1}$$

where g is a function defined as $g(u, \tau) = (\bar{\eta} + \tilde{\eta}u)/\eta(0, \tau)$ with the even part $\bar{\eta}$ and the odd part $\tilde{\eta}$ of $\eta(u, \tau)$. The equation (3.1) is used to determine $\psi(u, \tau)$. On the other hand, from the odd part of the mass continuity equation we obtain

$$\nu = \frac{\eta(0, \tau)}{\mu r_n^2}\frac{L}{2(1 - 4\psi'^2)}\left[\frac{8\psi'\psi''}{\tau_{r_s^2}} + [\frac{1 - 4\psi'^2}{\psi'}\{\frac{\psi'}{\tau_{r_s^2}} - \frac{4(\tilde{\eta}u + \bar{\eta})}{\eta(0, \tau)}\psi''\}]'\right] \tag{3.2}$$

This equation is used to determine $\nu(u, \tau)$ after the equation (3.1) is solved.

4 Flux Loss Time τ_Φ and Particle Loss Time τ_N

From (2.2), we have a relation

$$\frac{1}{\tau_\Phi} = \frac{1}{\tau_{B_e}} + \frac{1}{\tau_{r_s^2}} + \frac{1}{\tau_\psi} \quad where \quad \frac{1}{\tau_\Phi} = -\frac{\partial \Phi(0, \tau)}{\Phi(0, \tau)\partial\tau}, \quad \frac{1}{\tau_\psi} = -\frac{\partial\psi(0, \tau)}{\psi(0, \tau)\partial\tau} \tag{4.1}$$

From physical point of view, $r v_r$ should be continuous everywhere. This means that the even and odd parts of the right hand side of (2.11) should be continuous, separately. In particular, the odd part should vanish and continuous at $u = 0$. Then, we obtain the following two equations

$$\frac{1}{\tau_\Phi} = -\frac{4\psi''(0, \tau)}{\psi(0, \tau)} \quad (4.2) \qquad \lim_{u \to 0}\frac{1}{\psi'}(\frac{\psi}{\tau_\Phi} + 4g\psi'') = 0 \tag{4.3}$$

For the total ion number N inside the separatrix, we have $N = (L/m_i\Theta)\pi r_s^2(B_e^2/2\mu)\langle\beta\rangle$. Then, we have a relation

$$\frac{1}{\tau_N} = \frac{1}{\tau_L} - \frac{1}{\tau_\Theta} + \frac{1}{\tau_{r_s^2}} + \frac{1}{\tau_{B_e^2}} + \frac{1}{\tau_{\langle\beta\rangle}} \quad (4.4) \quad where \quad \frac{1}{\tau_{r_s^2}} = -\frac{\langle\beta\rangle}{1 - \langle\beta\rangle}\frac{1}{\tau_{\langle\beta\rangle}} \tag{4.5}$$

where (4.5) is obtained from (1.3). The particle loss rate can also be obtained by calculating ion number per unit time passing through the separatrix.

$$\frac{1}{\tau_N} = \frac{2\pi r_s L\rho_s}{m_i N}\{\frac{\mu r_n^2 v_{rs}}{\eta(0, \tau)} - \frac{dr_s}{d\tau}\} = \frac{\beta_s}{\langle\beta\rangle}\{\frac{\mu r_s v_{rs}}{\eta(0, \tau)} + \frac{1}{\tau_{r_s^2}}\} = \frac{4g_s(1 - 4\psi_s'^2)\psi_s''}{(1 - 4\psi'^2)\psi_s'} \tag{4.6}$$

Here, the suffix s means the value on the separatrix $u = 1$ and the final expression is obtained with use of (2.11). This expression for particle loss rate is the same as those obtained for quasisteady models[4][5].

5 Basic Equation for the Model

Since $\psi'(0, \tau) = 0$ on the neutral surface (see eq. (2.3)), the equation (3.1) has singularity on both sides at $u = 0$. Noticing an identity

$$(\frac{\psi}{\psi'})' = \frac{1}{1 + 4\psi'^2}\{(\frac{1 - 4\psi'^2}{\psi'}\psi)' + 8\psi'^2)\} \tag{5.1}$$

multiplying $1/\tau_\psi$ on both the sides, adding them to both sides of (3.1) and using (4.1) and (4.4) we get

$$\frac{\partial \psi(u, \tau)}{\partial \tau} = \psi'(u, \tau) \int_0^u \frac{du}{1 + 4\psi'^2} \left[\{\frac{1 - 4\psi'^2}{\psi'}(\frac{\psi}{\tau_\Phi} + 4g(u, \tau)\psi'')\}' \right.$$
$$\left. -(\frac{1}{\tau_N} - \frac{1}{\tau_{\langle\beta\rangle}})(1 - 4\psi'^2) + \frac{8\psi'^2}{\tau_\psi} \right] - \frac{\psi(u, \tau)}{\tau_\psi} \tag{5.2}$$

where the singurarities have been removed as seen from (4.3). This is our basic equation. In order to determine the time variation of ψ at a time τ, it needs to know, together with $\psi(u, \tau)$, several decay rates $1/\tau_\Phi, 1/\tau_N, 1/\tau_\psi$ and $1/\tau_{r_s^2}$ or $1/\tau_{\langle\beta\rangle}$ at the same time τ. The former three decay rates, however, can be determined by (4.2), (4.6) and (4.1) if $\psi(u, \tau)$ and $1/\tau_{r_s^2}$ are given. Differentiating both sides of (5.2) with respect to u, and trying directly to calculate $1/\tau_{\langle\beta\rangle}$, we obtain an integral theorem instead of $1/\tau_{\langle\beta\rangle}$ itself. That is

$$\int_0^1 \frac{du}{1 + 4\psi'^2} \left[\{\frac{1 - 4\psi'^2}{\psi'}(\frac{\psi}{\tau_\Phi} + 4g(u, \tau)\psi'')\}' - (\frac{1}{\tau_N} - \frac{1}{\tau_{\langle\beta\rangle}})(1 - 4\psi'^2) + \frac{8\psi'^2}{\tau_\psi} \right] = 0 \tag{5.3}$$

This theorem is clearly necessary for the basic equation to be compatible with the requirement

$$\psi(1, \tau) = 0 \quad and \quad \frac{\partial \psi(1, \tau)}{\partial \tau} = 0 \tag{5.4}$$

The decay rate $1/\tau_{r_s^2}$ or $1/\tau_{\langle\beta\rangle}$ is determined so that this theorem holds. That is

$$\frac{1}{\tau_{r_s^2}} = \frac{\langle\frac{2g\beta\beta'^2}{(2-\beta)^2(1-\beta)}\rangle + \frac{1}{\tau_N}(1 + \frac{\langle\beta\rangle}{2-\beta_s} - \langle\frac{1}{1-\beta/2}\rangle) - \frac{1}{\tau_{B_e}}(2 - \langle\frac{1}{1-\beta/2}\rangle)}{1 + (2 - \frac{1}{\langle\beta\rangle})(1 - \langle\frac{1}{1-\beta/2}\rangle)} \tag{5.5}$$

Notice that the decay rate of the external field $1/\tau_{B_e}$ is a known variable. The angle bracket means integration from $u = 0$ to 1: average of an even function inside the separatrix. By the way, we obtain from (5.5) and (4.4)

$$\frac{1}{\tau_L} - \frac{1}{\tau_\Theta} = -\frac{2 - \frac{1}{\langle\beta\rangle}}{1 + (2 - \frac{1}{\langle\beta\rangle})(1 - \langle\frac{1}{1-\beta/2}\rangle)}\{\langle\frac{2g\beta\beta'^2}{(2-\beta)^2(1-\beta)}\rangle$$
$$+ (\frac{\langle\beta\rangle}{2 - \beta_s} - \frac{1}{2 - \frac{1}{\langle\beta\rangle}})\frac{1}{\tau_N} + (\frac{2}{2 - \frac{1}{\langle\beta\rangle}} - \langle\frac{1}{1-\beta/2}\rangle)\frac{1}{\tau_{B_e}}\} \tag{5.6}$$

6　Quasisteady State

We call ψ satisfying (5.2) but independent of time τ "quasisteady solution" and denote it as $\psi_0(u)$ with suffix 0. All quantities relevant to ψ_0 will also be shown by the same suffix 0. In order for the equation (5.2) to have a quasisteady solution, $g, \tau_\Phi, \tau_N, \tau_\psi$ and $\tau_{r_s^2}$ or $\tau_{\langle\beta\rangle}$ have to be independent of time τ. Furthermore, we have $1/\tau_\psi = 0$, $1/\tau_{\langle\beta\rangle} = 1/\tau_{r_s^2} = 0$ for the quasisteady state. Thus, the basic equation (5.2) becomes the following ordinary differential equation for the quasisteady state

$$\{\frac{1 - 4\psi_0'^2}{\psi_0'}(\frac{\psi_0}{\tau_{\Phi 0}} + 4g\psi_0'')\}' - \frac{1}{\tau_{N0}}(1 - 4\psi_0'^2) = 0 \tag{6.1}$$

Boundary conditions for this equation are as follows.

$$\psi_0'(0) = 0 \qquad (6.2) \qquad \lim_{u \to 0} \frac{1}{\psi_0'}(\frac{\psi_0}{\tau_{\Phi 0}} + 4\psi_0'') = 0 \quad . \tag{6.3}$$

$$\psi_0(1) = 0 \qquad (6.4) \qquad \psi'(1) = \frac{1}{2}\sqrt{1 - \beta_{0s}} \tag{6.5}$$

The problem (6.1 ~ 5) was investigated by one of the authors[5] in case of $g = 1$. That is, for a pair of parameters $0 < \alpha < \infty$, $0 < \beta_{0s} < 1$, there is a unique solution $\psi_0, \tau_{\Phi 0}, \tau_{N0}$ with a single neutral surface and negative flux inside the separatrix. The flux loss time $\tau_{\Phi 0}$ is a function of α and β_s, and the particle loss time τ_{N0} is given by $\tau_{N0} = \tau_{\Phi 0}/\alpha$. This results do not change for non-uniform g. Thus, there may be a two dimensional domain D such that, if $(\tau_{\Phi 0}, \tau_{N0}) \in D$, there is at least a solution which satisfies (6.1 ~ 4) except (6.5).

Now, let us consider conditions under which, if the initial value of ψ is equal to $\psi_0(u)$, the quasisteady state $\psi_0(u)$ is maintained as a stationary solution of the equation (5.2). First, g should be independent of time. Second, $\tau_N = \tau_{N0}$ should be maintained by somehow controlling the edge layer. Third, $1/\tau_{\langle\beta\rangle} = 1/\tau_{r_s^2} = 0$ should be maintained by controlling the external field B_e so that (see (5.5))

$$\frac{1}{\tau_{B_e 0}} = \frac{1}{2 - \langle\frac{1}{1-\beta_0/2}\rangle}\{\langle\frac{2g\beta_0\beta_0'^2}{(2 - \beta_0)^2(1 - \beta_0)}\rangle + \frac{1}{\tau_{N0}}(1 + \frac{\langle\beta_0\rangle}{2 - \beta_{0s}} - \langle\frac{1}{1 - \beta_0/2}\rangle)\} \tag{6.6}$$

Under these three conditions, $\psi_0(u)$ continues to be a solution of (5.2). In fact, if at a time τ the three conditions are satisfied and $\psi(u, \tau) = \psi_0(u)$, then, the basic equation (5.2) and the integral theorem (5.3) become

$$\frac{\partial\psi}{\partial\tau} = \psi_0' \int_0^u \frac{8\psi_0'^2/\tau_\psi}{1 + 4\psi_0'^2}du - \frac{\psi_0}{\tau_\psi} \qquad and \qquad \int_0^1 \frac{du}{1 + 4\psi_0'^2}\frac{8\psi_0'^2}{\tau_\psi} = 0$$

respectively. We, therefore, have $1/\tau_\psi = 0$ from the integral theorem and the right hand side of the basic equation vanishes. Thus, $\psi_0(u)$ continues to be a solution of the time dependent equation.

7 Small Deviation $\delta\psi$ from a Quasisteady State

We put $\psi(u,\tau) = \psi_0(u) + \delta\psi(u,\tau)$ and consider behavior of $\delta\psi$ within a range of linear theory. We assume that g is not only independent of τ but also uniform: $g = 1$, for simplicity. Since the particle loss rate is always given by (4.6), we assume that the deviation of particle loss rate $\delta(1/\tau_N)$ due to the perturbation $\delta\psi$ is given by

$$\frac{1 - 4\psi_{0s}'^2}{\psi_{0s}'}\delta\psi_s'' - \left(\frac{1}{\psi_{0s}'^2} + 4\right)\psi_{0s}''\delta\psi_s' = \frac{\delta\langle\beta\rangle}{4\tau_{N0}} + \frac{\langle\beta_0\rangle}{4}\delta\left(\frac{1}{\tau_N}\right) \tag{7.1}$$

An assumption included here is that the value of τ_{N0} on the right hand side is fixed by somehow controlling the edge layer. We fix the decay rate of the external field at the value of $1/\tau_{B_e0}$ given by (6.6). Then, if $\delta\psi = 0$, we have $1/\tau_{\langle\beta\rangle} = 0$. But if $\delta\psi \neq 0$, as it can be seen from (5.5) and (4.5) we have a deviation given by

$$\delta\left(\frac{1}{\tau_{\langle\beta\rangle}}\right) = \frac{1 - \frac{1}{\langle\beta_0\rangle}}{1 + (2 - \frac{1}{\langle\beta_0\rangle})(1 - \langle\frac{1}{1-\beta_0/2}\rangle)}[\delta\langle\frac{2\beta\beta'^2}{(2-\beta)^2(1-\beta)}\rangle$$

$$+ \frac{1}{\tau_{N0}}\left(\delta\frac{\langle\beta\rangle}{2 - \beta_s} - \delta\langle\frac{1}{1 - \beta/2}\rangle\right) + \frac{1}{\tau_{B_e0}}\delta\langle\frac{1}{1 - \beta/2}\rangle$$

$$+ \delta\left(\frac{1}{\tau_N}\right)\left(1 + \frac{\langle\beta_0\rangle}{2 - \beta_{0s}} - \langle\frac{1}{1 - \beta_0/2}\rangle\right)] \tag{7.2}$$

The deviations $\delta(1/\tau_\Phi)$ and $\delta(1/\tau_\psi)$ due to $\delta\psi$ can also be calculated from (4.2) and (4.1). Now, linearizing the basic equation (5.2), we get

$$\frac{\partial}{\partial\tau}\left(\frac{\delta\psi}{\psi_0'}\right)' = \frac{1}{1 + 4\psi_0'^2}\left[\left\{-\frac{1 + 4\psi_0'^2}{\psi_0'^2}\left(\frac{\psi_0}{\tau_{\Phi0}} + 4\psi_0''\right)\delta\psi' + \frac{1 - 4\psi_0'^2}{\psi_0'}\left(\frac{\delta\psi}{\tau_{\Phi0}} + 4\delta\psi''\right)\right\}'\right.$$

$$+ \frac{8\psi_0'}{\tau_{N0}}\delta\psi' + \delta\left(\frac{1}{\tau_{\langle\beta\rangle}}\right)\left\{(1 - 4\psi_0'^2) - \frac{\langle\beta_0\rangle}{1 - \langle\beta_0\rangle}\left(\frac{1 - 4\psi_0'^2}{\psi_0'}\psi_0\right)'\right\}$$

$$\left. -\delta\left(\frac{1}{\tau_N}\right)(1 - 4\psi_0'^2)\right] \tag{7.3}$$

Notice that $\delta(1/\tau_\Phi)$ and $\delta(1/\tau_\psi)$ disappear by cancelling each other. Denoting [   ] on the right hand side as $L(\delta\psi)$, the equation is written in a short form:

$$\frac{\partial}{\partial\tau}\left(\frac{\delta\psi}{\psi_0'}\right)' = \frac{L(\delta\psi)}{1 + 4\psi_0'^2} \tag{7.3'}$$

8 a Criterion for ψ_0 to be an Attractor

Multiplying $(1 + 4\psi_0'^2)\psi_0'^4(\delta\psi/\psi_0')'$ on both sides of (7.3') and integrating from $u = 0$ to 1, we get

$$\frac{1}{2}\frac{\partial}{\partial\tau}\langle(1 + 4\psi_0'^2)\psi_0'^4\left(\frac{\delta\psi}{\psi_0'}\right)'^2\rangle = \langle\left(\frac{\delta\psi}{\psi_0'}\right)'\psi_0'^4 L(\delta\psi)\rangle \tag{8.1}$$

If the right hand side of this equation is always negative for any permissible $\delta\psi$, the quasisteady state ψ_0 is an attractor. In fact, if the condition holds, we have

$$\langle(1+4\psi_0'^2)\psi_0'^4(\frac{\delta\psi}{\psi_0'})'^2\rangle \to 0$$

Then, we have at each point of u

$$\delta\psi'\psi_0' - \delta\psi\psi_0'' \to 0$$

On the other hand, the differential equation of $\delta\psi$

$$\delta\psi'\psi_0' - \delta\psi\psi_0'' = 0$$

has the general solution $\delta\psi = const.\psi_0'$ and only one solution satisfying the boundary condition $\delta\psi(u=1) = 0$ is $\delta\psi = 0$. Therefore, if the right hand side of (8.1) is always negative, $\delta\psi$ indefinitely tends to zero and the quasisteady state is an attractor. The right hand side of (8.1) can be rewritten by integration by parts as

$$\langle(\frac{\delta\psi}{\psi_0'})'\psi_0'^4 L(\delta\psi)\rangle = -\langle\frac{\delta\psi}{\psi_0'}\{\psi_0'^4 L(\delta\psi)\}'\rangle$$

So, if we define a linear operator $\mathcal{L}$ as

$$\mathcal{L}(\delta\psi) = \frac{1}{\psi_0'}\{\psi_0'^4 L(\delta\psi)\}' \tag{8.2}$$

the criterion for ψ_0 to be an attractor is that the inequality

$$\langle\delta\psi\mathcal{L}(\delta\psi)\rangle > 0 \tag{8.3}$$

is always satisfied.

9 Conclusion

The 1 1/4D time dependent model of field reversed configuration has been formulated in somewhat different way from the original work[1], and in its process, an integral theorem has been obtained together with relations among decay rates of several relevant quantities. Conditions that the quasisteady state is maintained as a stationary solution of the time dependent equation have been listed up. A formal criterion has been proposed for a quasisteady state to be an attractor.

references

[1] L.C. Steinhauer, R.D. Milroy and J.T. Slough, Phys. Fluids 28 p888 1985
[2] L.C. Steinhauer, Phys. Fluids B2(11) p2679 1990
[3] D.E. Schumaker, J.K. Boyd, S.P. Auerbach and B. McNamara, J. of Computational Phys. 45 p266 1982
[4] M. Tuszewski and R.K.Linford Phys. Fluids 25 p765 1982
[5] S. Hamada, Nuclear Fusion, 26 p729 1986
[6] W.T. Armstrong, R.K. Linford, J. Lipson, D.A. Platts and E.G.Shertwood, Phys.Fluids 24 p2068 1981

The Construction of Generalized Magnetic Coordinates

Michinari Kurata

Dept. of Energy Engineering and Science,

Graduate School of Engineering, Nagoya University

and

Jiro Todoroki

National Institute for Fusion Science

Abstract

Generalized Magnetic Coordinates (GMC) are curvilinear coordinates (ξ, η, ζ) in which the magnetic field is expressed in the form

$$B = \nabla\Psi(\xi,\eta,\zeta) \times \nabla\zeta + H^{\varsigma}(\xi,\eta)\nabla\xi \times \nabla\eta$$

The GMC construction algorithm is applied to the simple periodic model magnetic field. The coordinates are expanded in the Fourier series in three dimensions. It is obtained after about $10 \sim 35$ times iterations. The coordinates are well constructed by the comparatively small number of Fourier modes.

Keywords:

generalized magnetic coordinates, GMC, magnetic flux coordinates, magnetic surface,

magnetic islands, ABC magnetic field, Fourier series, B-spline function

§ 1. Introduction

Magnetic flux coordinates[1,2] are widely used in the study of the MHD equilibrium and stability in the toroidal plasma when the nested magnetic surfaces exist. Unfortunately, the nested magnetic surfaces exist only in the limited region of torus; and even inside the outermost magnetic surface there might exist complicated magnetic islands structure. In such cases, the use of the conventional magnetic flux coordinates is not expected.

· The Generalized Magnetic Coordinates (GMC)[3] are the new one to supplement the magnetic coordinates system adequate to treat the general magnetic configurations. The GMC can be constructed in the region without nested magnetic surface and the region of chaotic or ergodic magnetic lines of force. So the GMC can treat the magnetic field involving magnetic islands and outside the outermost magnetic surface.

In the GMC (ξ, η, ζ) the magnetic field is expressed in the form

$$B = \nabla\Psi(\xi,\eta,\zeta) \times \nabla\zeta + H^{\varsigma}(\xi,\eta)\nabla\xi \times \nabla\eta, \tag{1}$$

here $H^\zeta \equiv \sqrt{g}B^\zeta$ does not depend on ζ, where $\sqrt{g}$ is Jacobian. The function Ψ is the covariant ζ component of vector potential. When the good magnetic surface exists, Ψ becomes independent of ζ and $\Psi(\xi,\eta)$=Const. is the magnetic surface. The ζ-dependent part of Ψ corresponds to the destruction of the magnetic surface. The GMC are to be constructed so that the ζ component of vector potential becomes dependent of ζ as little as possible.

In order to check the GMC construction algorithm, the general numerical method to construct a GMC is applied to the simple periodic model magnetic field[4,5]. In this paper the GMC are applied to the model magnetic field involving clearly magnetic islands.

§2. Construction of GMC

The algorithm to construct GMC is the new one to construct magnetic surfaces without tracing magnetic lines of force. It is based on the transformation rule of the vector potential accompanied with the change of coordinates[3].

We shall consider a curvilinear coordinate system $(\xi,\ \eta,\ \zeta)$, ζ being the angle variable corresponding to the toroidal direction. We introduce a time-like parameter τ and consider the continuous path from an initial state of coordinates to the GMC. Then coordinates are expressed as follows,

$$r=r(\xi,\eta,\zeta;\tau). \tag{2}$$

The coordinates approach to GMC when $\tau\to\infty$. The parameter τ corresponds to the iteration time in numerical calculation by computer.

The magnetic induction densities $\sqrt{g}\mathbf{B}=(H^\xi,H^\eta,H^\zeta)$ can be expressed in terms of the vector potential $\mathbf{A}\equiv(A_\xi,A_\eta,A_\zeta)$ as

$$H^\xi=\frac{\partial A_\zeta}{\partial\eta}-\frac{\partial A_\eta}{\partial\zeta},\quad H^\eta=\frac{\partial A_\xi}{\partial\zeta}-\frac{\partial A_\zeta}{\partial\xi},\quad H^\zeta=\frac{\partial A_\eta}{\partial\xi}-\frac{\partial A_\xi}{\partial\eta}. \tag{3}$$

If we introduce the notations

$$\overline{A}\equiv\oint Ad\zeta/\oint d\zeta,\quad \tilde{A}\equiv A-\overline{A}, \tag{4}$$

the principles to construct The GMC can be expressed by the following conditions;

1) H^ζ does not depend on ζ,

2) $\tilde{A}_\zeta$ is minimized,

which are represented as

$$\oint\left|\tilde{H}^\zeta\right|^2 d\zeta=0,\quad \delta\oint\left|\tilde{A}_\zeta\right|^2 d\zeta=0. \tag{5}$$

§3. Modeling and Results

We employ the ABC(Arnol'd-Beltrami Childress) magnetic field in the Cartesian coordinates added constant magnetic field in the direction of z as the model magnetic field,

$$B_x = b\cos(2\pi y) + c\sin(2\pi z),$$ (6)

$$B_y = c\cos(2\pi z) + a\sin(2\pi x),$$

$$B_z = a\cos(2\pi x) + b\sin(2\pi y) + B_0$$

with $(a=0.2, b=0.1, c=0.6)$. This magnetic field is periodic in the directions of (x,y,z). The constant magnetic field B_0 is added so that $B_z > 0$.

The (x,y,z) coordinates are expanded into Fourier series in terms of the GMC (ξ, η, ζ),

$$x = \xi + \sum_{l=-L}^{L} \sum_{m=-L}^{L} \sum_{n=1}^{L} X_{l,m,n} \exp(2\pi i[l\xi+m\eta+n\zeta]),$$ (7)

$$y = \eta + \sum_{l=-L}^{L} \sum_{m=-L}^{L} \sum_{n=1}^{L} Y_{l,m,n} \exp(2\pi i[l\xi+m\eta+n\zeta]),$$

$$z = \zeta.$$

The space is divided into $20 \sim 40$ meshes of (ξ, η, ζ). The scalar function v is also expanded by Fourier series. The GMC are obtained after about $10 \sim 35$ times iterations so far.

In the previous paper[5], we reported two magnetic field cases of $B_0=0.5, 1.0$ without involving clearly magnetic islands using the number of Fourier mode from L=1 to L=7. Fig.1 shows the Poincaré maps of magnetic surfaces of $B_0=1.0$ on the $\zeta=0$ plane in the GMC. Fig.2 shows the shape and contour of $\overline{A}_\zeta(\xi,\eta)$. When the nested magnetic surfaces exist, they are equal to $\overline{A}_\zeta=$Const..

Next, the constant B_0 is lowered to $B_0=0.45$, so that the magnetic field involves clearly magnetic islands. The variation of the magnetic field in the ζ direction is larger than the case of $B_0 = 0.5$. Fig.3 shows the GMC mesh of $\xi,\eta=Const.$ at equal intervals constructed in the number of Fourier mode L=9 on the z=0, 0.25, 0.5, 0.75 planes in the Cartesian coordinates. The Poincaré maps of magnetic surfaces of $B_0=0.45$ is also overlapped in Fig.3. The only central toroidal field of interest is drawn in the Poincaré map and the outside of it is omitted to draw. Fig.4 shows the Poincaré maps of magnetic surfaces on the $\zeta=0, 0.25, 0.5, 0.75$ planes in the GMC. The magnetic islands of poloidal mode number M=5,7 and 9 are clearly shown. The magnetic islands rotate as ζ changes. Fig.5 shows the shape and contour of averaged magnetic surface $\overline{A}_\zeta(\xi,\eta)$. The averaged magnetic surface is $\overline{A}_\zeta=$Const. when the breaking of nested magnetic surfaces exist. Fig.6 shows the Poincaré map on the $\zeta=0.75$ plane overlapped to Fig.5. The magnetic islands of M=5 rotate along the averaged magnetic surface; and the width of magnetic islands of M=5,9 could be measured by the averaged magnetic surface.

In order to evaluate the magnitude of the ζ dependent part of H^ζ, we calculate the integral,

$$I_\zeta = \int_0^1 \int_0^1 \int_0^1 \left|\tilde{H}^\zeta\right|^2 d\xi d\eta d\zeta.$$ (8)

The integral I_ζ is plotted against the number of Fourier mode L in Fig.7. It decreases exponentially as L increases. Since the GMC are constructed so that $\tilde{H}^\zeta$ becomes zero, I_ζ must converge to zero. So the error of I_ζ is caused by the finite truncation error for the most part.

In order to estimate the influence from the breaking of magnetic surfaces, we evaluate the magnitude of the ζ

dependent part of H^ξ and H^η by the integral,

$$I_\xi = \int_0^1\int_0^1\int_0^1\left|\tilde{H}^\xi\right|^2 d\xi d\eta d\zeta, \quad I_\eta = \int_0^1\int_0^1\int_0^1\left|\tilde{H}^\eta\right|^2 d\xi d\eta d\zeta \tag{9}$$

The integral I_ξ and I_η are plotted in Fig.7. Since $\tilde{A}_\zeta$ is minimized in the GMC, $\tilde{H}^\xi$ and $\tilde{H}^\eta$ are also minimized. Since $\tilde{H}^\xi$ and $\tilde{H}^\eta$ naturally contain the contribution from magnetic islands where the nested magnetic surface does not exist, only its contribution should be contained in I_ξ and I_η if the GMC are precisely made up. Since both I_ξ and I_η are not saturated and they are not very different from I_ζ, they are mostly reflected by the smallness of number of Fourier mode more than the breaking of magnetic surfaces.

In order to estimate $\tilde{A}_\zeta$ that relates with the breaking of magnetic surfaces, we calculate the integral,

$$E_{\xi\eta}(\xi,\eta) = \int_0^1\left(\left|\tilde{H}^\xi\right|^2 + \left|\tilde{H}^\eta\right|^2\right)d\zeta. \tag{10}$$

The shape and contour of $E_{\xi\eta}$ are shown in Fig.8. The shape of $E_{\xi\eta}$ seems like a crater of volcano. The shapes are roughly unchanged for the number of Fourier mode from L=1 to L=9, but the shapes become a deeper crater as L increases. Although the magnetic islands of poloidal mode number M=5 locate in the middle of the magnetic axis and the outermost magnetic surface, $E_{\xi\eta}$ is not especially large there. The largest region of $E_{\xi\eta}$ is annular and located around the outside of the outermost magnetic surface. The region of nested magnetic surfaces around the magnetic axis corresponds to the region of smaller $E_{\xi\eta}$. The similar result for $E_{\xi\eta}$ is obtained for the magnetic field of $B_0=0.5$.

At last, in order to examine the distribution of $\tilde{H}^\zeta$, we calculate the integral

$$E_\zeta(\xi,\eta)=\int_0^1\left|\tilde{H}^\zeta\right|^2 d\zeta. \tag{11}$$

The shape and contour of E_ζ are shown in Fig.9. Since the shape of E_ζ is similar to $E_{\xi\eta}$, the region of the outside of outermost magnetic surface influences on the convergence of E_ζ alike. Although E_ζ must converge to zero like I_ζ, the shape of E_ζ approaches to that of $E_{\xi\eta}$ if L becomes large to L=9. The meaning of this is not clear at the present.

§4. Summary

It is shown that the averaged magnetic surface $\overline{A}_\zeta$=Const. is equal to the magnetic surface when the nested magnetic surfaces exist. The GMC can be constructed for the magnetic field involving clearly magnetic islands by the general algorithm to construct GMC. In this model field H^ξ, H^η and H^ζ decreases exponentially as the number of Fourier mode increases. The distribution of $\tilde{A}_\zeta$ that relates with the breaking of magnetic surfaces is estimated. The largest region of $\tilde{A}_\zeta$ is located around the outside of the outermost magnetic surface. The relationship between $\tilde{A}_\zeta$ and the region where magnetic surface does not exist should be examined in further detail.

In the general magnetic configuration of interest the periodic condition in three dimension cannot be used. In order to drop the periodic conditions of magnetic field in ξ and η directions, the B-spline function should be used as the basis of expansion. The B-spline function that has local support is adequate to treat the general magnetic field involving further breaking of magnetic surfaces.

Reference

[1] S.Hamada: Nucl. Fusion **2**, 23 (1962).

[2] A.Boozer: Phys. of Fluids **24**, 1999 (1981).

[3] J.Todoroki: 核融合研究における数値解析手法と最適化 （統計数理研究所共同研究レポート 105), 1997, pp.1-10.

[4] M.Kurata and J.Todoroki: J. Plasma Fusion Res. SERIES, Vol. 1 (1998) 491-494.

[5] J.Todoroki and M.Kurata: 核融合研究における数値解析手法と最適化 （統計数理研究所共同研究レポート 110), 1998, pp.1-10.

(a) Shape
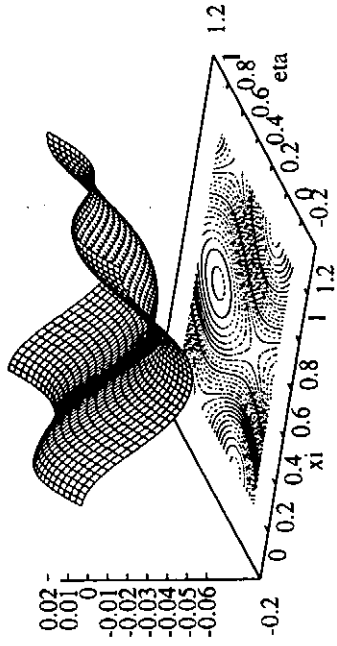
(b) Contour
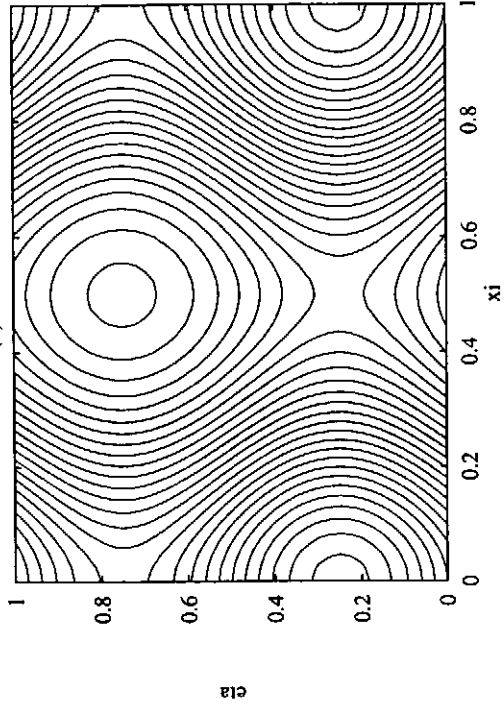
Fig.2. The shape and contour of $\overline{A}_\zeta(\xi,\eta)$ in GMC (ξ,η,ζ)
(a)Shape, (b)Contour (B$_0$=1.0, L=7).

Fig.1. The Poincaré map at ζ=0 in GMC (ξ,η,ζ)
(B$_0$=1.0, L=7).
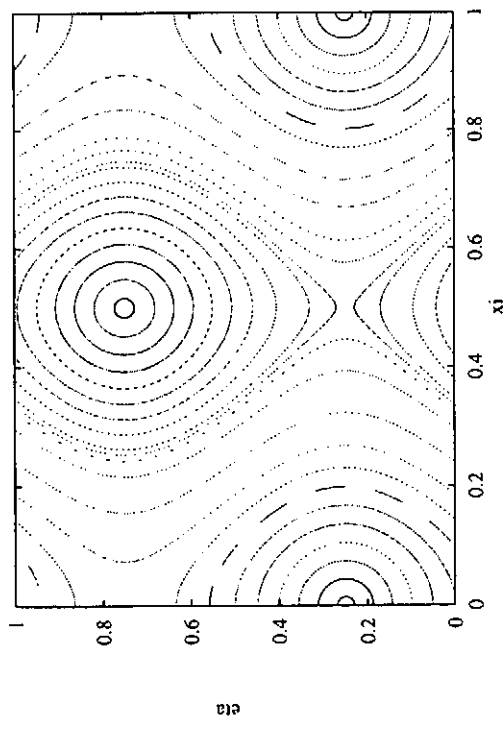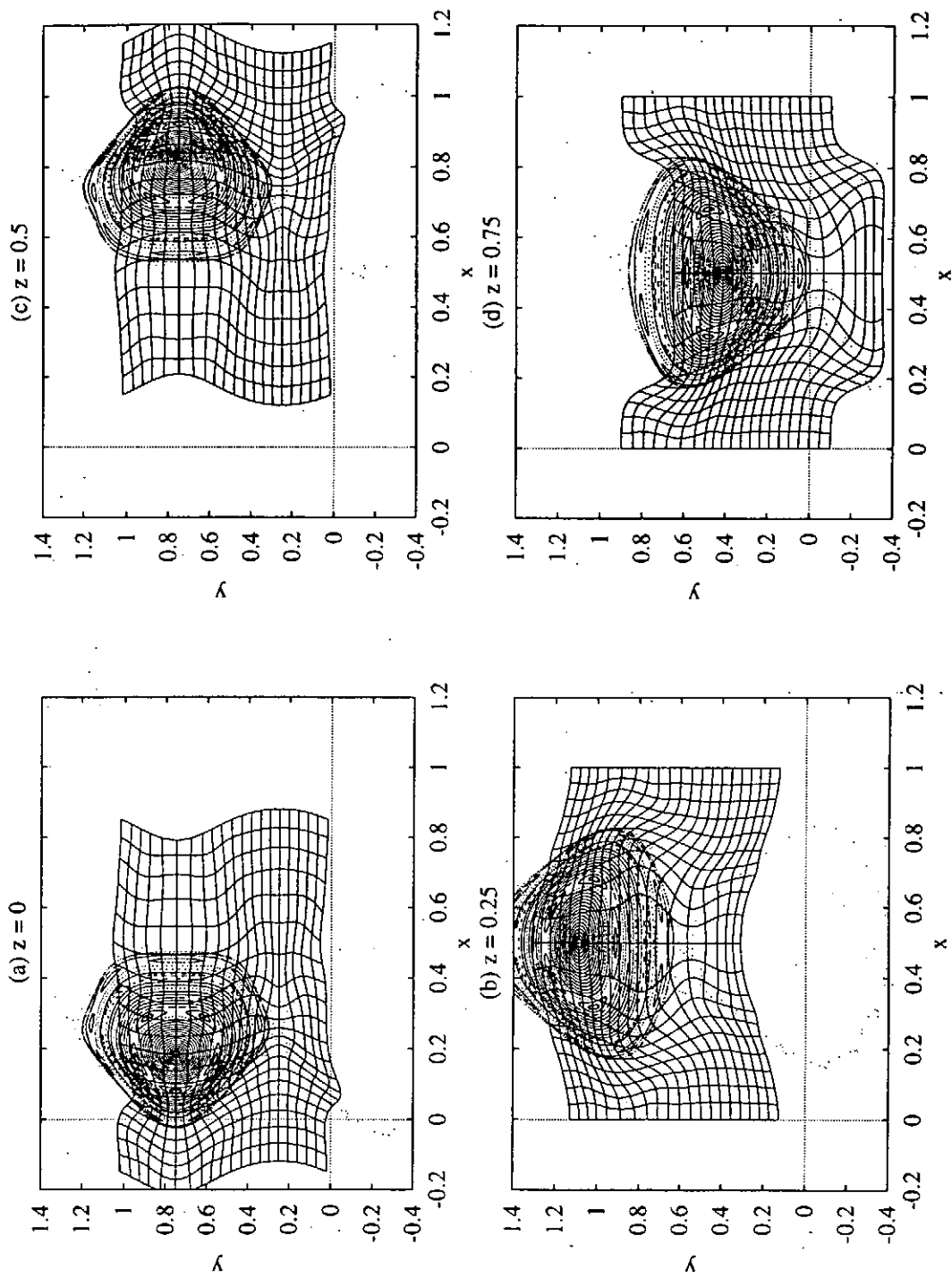
Fig.3. The GMC meshes and Poincaré map in (x,y,z) ($B_0=0.45$, $L=9$)
(a)$z=0$, (b)$z=0.25$, (c)$z=0.5$, (d)$z=0.75$.

(a) zeta = 0

(b) zeta = 0.25

(c) zeta = 0.5

(d) zeta = 0.75
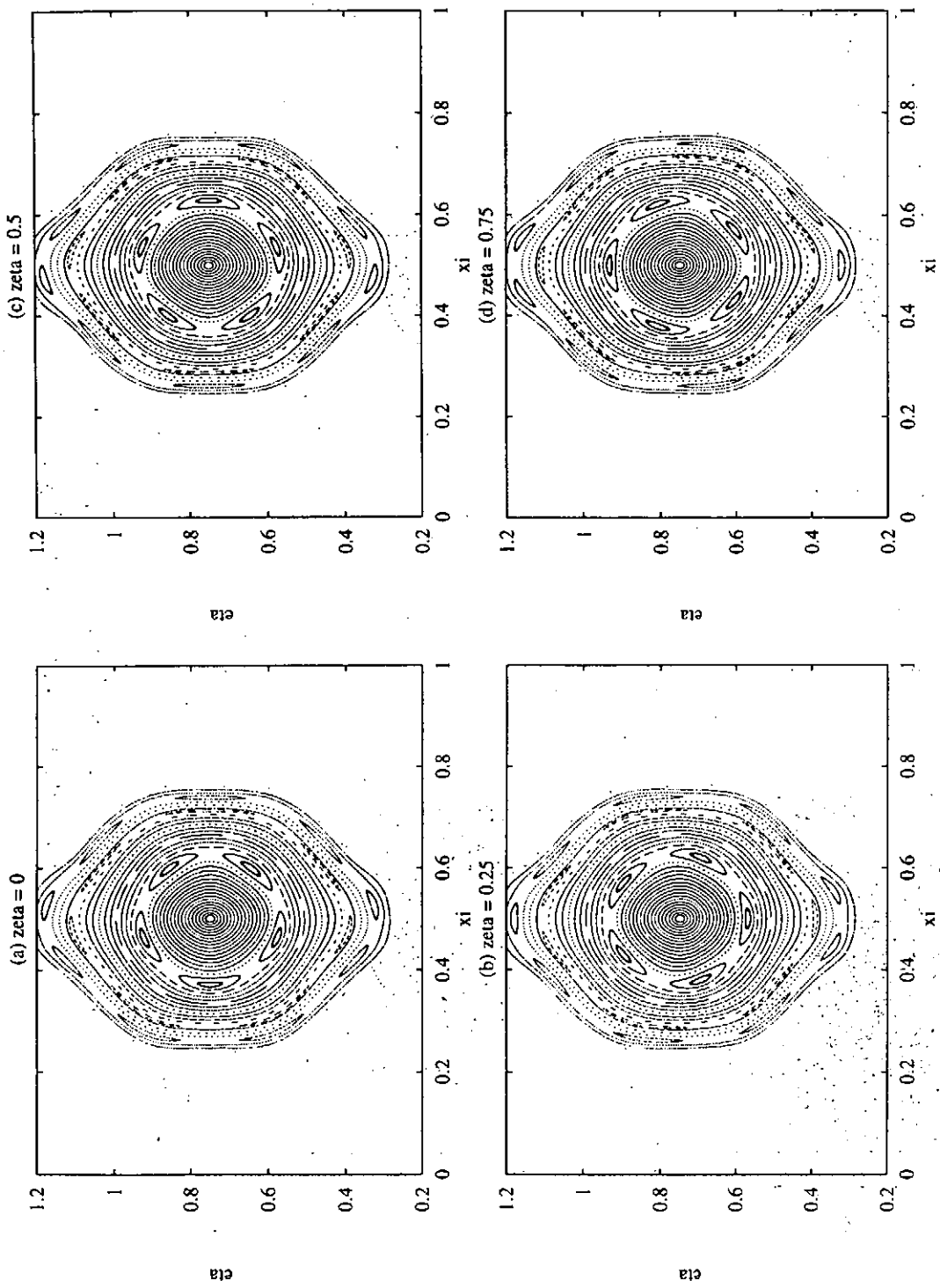
Fig. 4. The Poincaré map in GMC (ξ, η, ζ) (B_0=0.45, L=9).
(a)ζ=0, (b)ζ=0.25, (c)ζ=0.5, (d)ζ=0.75.

Fig.6. $\overline{A}_\zeta$ contour and Poincaré map at z=0.75 in GMC (ξ,η,ζ) $(B_0=0.45, L=9)$.
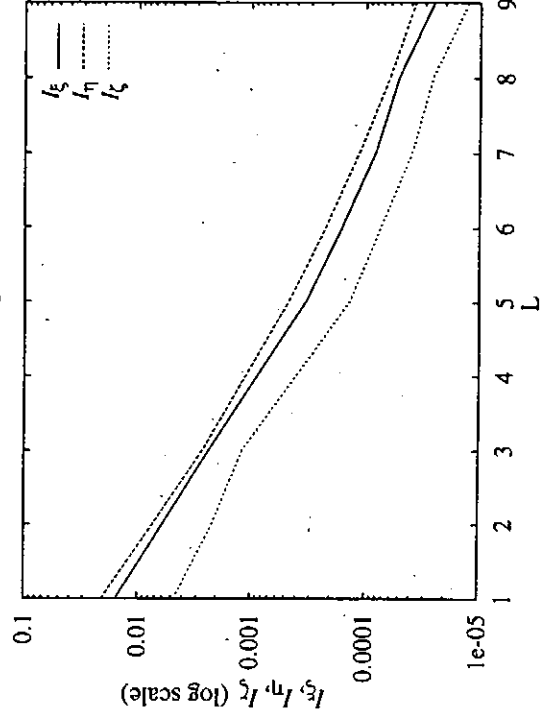
Fig.7. I_ξ, I_η and I_ζ vs. The number of Fourier mode L $(B_0=0.45)$.

(a) Shape

(b) Contour
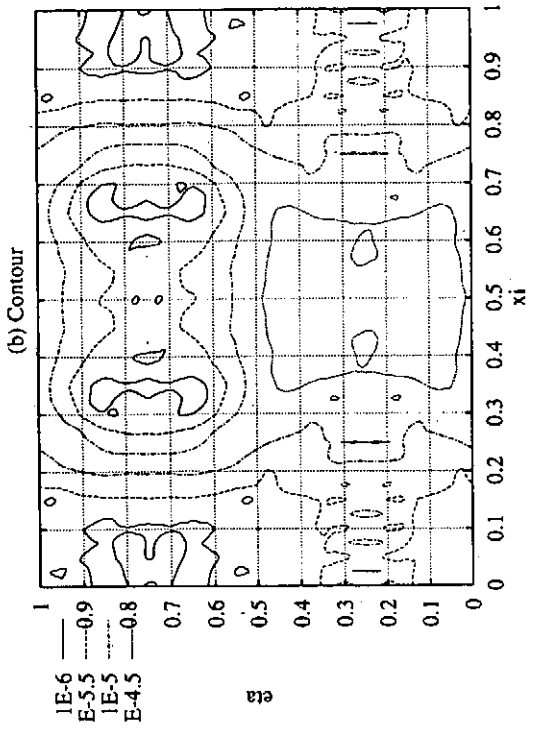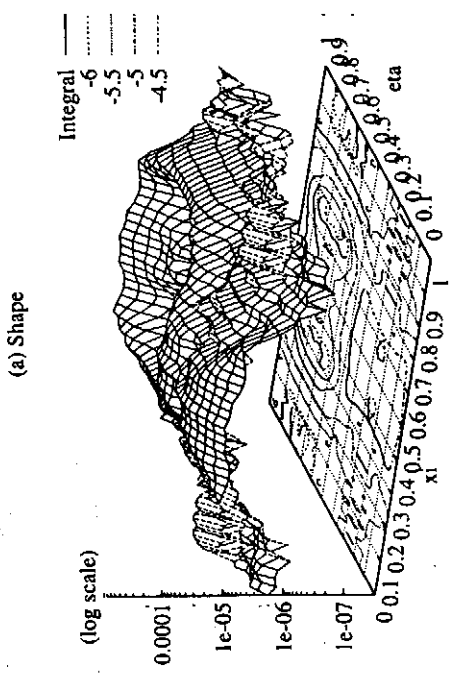
Fig.5. The shape and contour of $\overline{A}_\zeta(\xi,\eta)$ in GMC (ξ,η,ζ) (a)Shape, (b)Contour $(B_0=0.45, L=9)$.

(a) Shape

(b) Contour

Fig.8. The shape and contour of $E_{\xi\eta}$ ($B_0=0.45$, $L=9$)
(a)Shape, (b)Contour.

(a) Shape

(b) Contour

Fig.9. The shape and contour of E_ζ ($B_0=0.45$, $L=9$)
(a)Shape, (b)Contour.

Applications of Neural Network to Numerical Analyses

Tatsuoki TAKEDA, Makoto FUKUHARA,
Xiao Feng MA, Ali LIAQAT

Department of Information Mathematics and Computer Science
The University of Electro-Communications
1-5-1 Chofu-ga-Oka, Chofu, Tokyo, Japan 182-8585

Abstract

Applications of a multi-layer neural network to numerical analyses are described. We are mainly concerned with the computed tomography and the solution of differential equations. In both cases as the objective functions for the training process of the neural network we employed residuals of the integral equation or the differential equations. This is different from the conventional neural network training where sum of the squared errors of the output values is adopted as the objective function. For model problems both the methods gave satisfactory results and the methods are considered promising for some kind of problems.

Keywords: neural network, computed tomography, differential equation, collocation method, data assimilation, Lorentz equation

1. Introduction

Though the studies on an artificial neural network were originally started to construct a system which simulates a biological neural network, at present the studies are not restricted to the biological ones but the network has a variety of application fields, especially, for data processing methods. Because of the original motivation of studies of the neural network there are a lot of studies on applications of the neural network to classification and pattern recognition but there are few examples of applications of the neural network to numerical computations which need high accuracy as well as high speed. There is, of course, a limitation to the application of neural network to the numerical computation concerning the accuracy and the speed as long as we use conventional computers. However, if we make use of unique features of the neural network satisfactorily and devise a peculiar numerical procedure, it is possible to use the neural network to the

numerical computation effectively in spite of such limitations.

2. Structure and Training of Neural Network

A neural network is constructed from a lot of comparatively simple processors (units) connected each other in order to realize a certain function as a whole. For realization of the function of the system the state of connections represented by a weight assigned to each connection is the important factor and the training (learning) of the neural network is the process to determine values of the weights.

In this article we consider a multi-layer feedforward neural network as shown in Fig.1. We employ the logistic equation of a sigmoid function-type as a nonlinear transforming function (an activation function of a unit). The training algorithm we mainly consider is the error back-propagation method, i.e., the most commonly used method for this kind of the network.
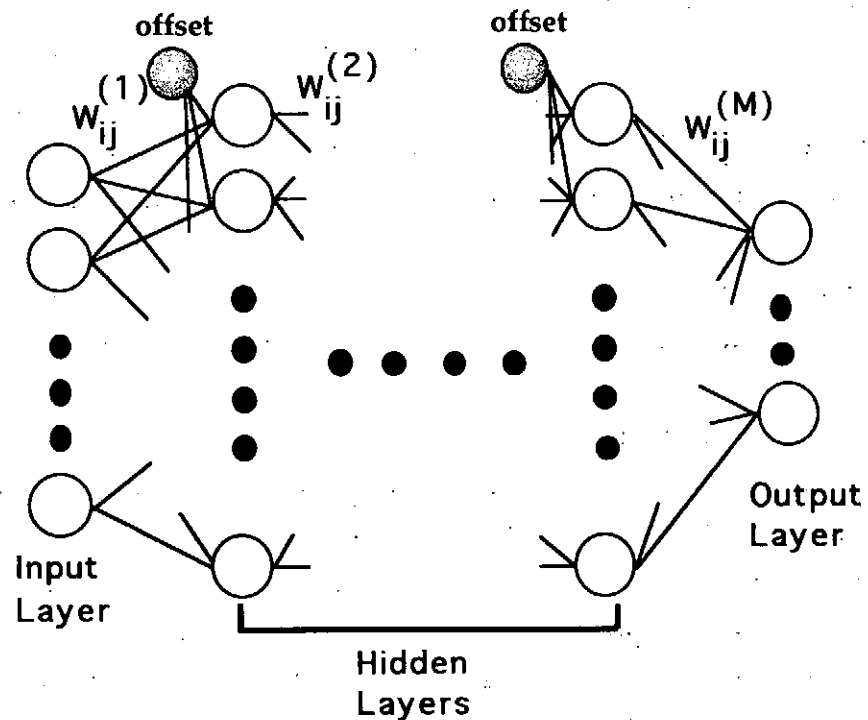
Fig.1   A multi-layer feedforward neural network

In Fig.1 $w_{ij}^{(p)}$ is the weight assigned to the connection between the i-th unit in the p-th layer and the j-th unit in the p+1-th layer. If we represent the input value to a unit from the i-th unit in the preceding layer as x_i and the corresponding weight as w_i, the output value y from this unit is obtained by nonlinearly transforming the weighted sum of the input data by the sigmoid

function $\sigma(X)$ as

$$y = \sigma(X) = \frac{1}{1 + \exp(-X)}$$

$$X = \sum_{i=1}^{n} w_i x_i$$

During the error back-propagation process the weights are updated iteratively according to the following equation.

$$\Delta w_i = -\gamma \frac{\partial E}{\partial w_i} = -\gamma C \frac{d\sigma}{dX} \frac{\partial X}{\partial w_i}$$

where E is the error function as the objective function of the optimization process of the neural network, γ is the learning rate, and C is the value transferred from the succeeding layer.

3. Numerical Analysis and Features of Neural Network

The neural network is considered as a device which has various features represented by the following items.
(1) a statistical model of the real world.
(2) a classification device.
(3) a continuous mapping device.
(4) a static or time dependent function.
(5) a smoothing operator.
(6) an interpolation device.

Though some of these features are advantageously used for numerical computations there are only a few application of the neural network for this field up to now. Because the training process of the neural network is essentially a nonlinear optimization which inevitably requires a lot of computational cost, it seems sometimes ridiculous to use the neural network for numerical computations. But some of the above features are very attractive and may make practicable the numerical computation method based on the neural network technology by setting the advantages off against the disadvantages.

4. Application of Neural Network to Computed Tomography

The simplest ideas to use the neural network for numerical computations are found in the field of inverse problems. Among them the CT (computed tomography) image reconstruction technique is one of the interesting applications. In this section we describe the technique usable for

the diagnostics for the experiments of fusion plasma experiments.

4.1 Parametric Computed Tomography

In this subsection we consider a process to obtain a density distribution n(x,y) in a cross-section of a cylindrical or a toroidal plasma by a multi-channel microwave interferometer. Analysis of the density distribution from the set of the measured phase shift data (Fig.2) is a problem to solve the first kind Fredholm integral equation. The phase shift of microwave passing through a plasma is described as

$$\phi_j = k \int_{y_L(x_j)}^{y_U(x_j)} n(x,y)dy$$

where $y_U(x_j)$ and $y_L(x_j)$ are the upper and lower limit of integration for the j-th path of micro-wave. Because in this kind of measurements the number of the microwave paths does not exceed several tens at most, usual CT techniques cannot be applied to this problem. Therefore, some assumptions such that the contours of the density distribution are only slightly deformed from concentric circles are introduced and the parameters defining the shapes and positions of the contours are analyzed. A typical example of this kind of methods is to represent the density distribution by a linear combination of a limited number of appropriate functions. For this purpose we employed the Fourier-Bessel series as

$$n(x,y) = n(r,\theta) = \sum_{m=0}^{M} \sum_{n=1}^{N} a_{mn} J_m(\lambda_{mn} r) \cos m\theta$$

$$r = \sqrt{x^2 + y^2} \text{, and } \theta = \tan^{-1}(y/x)$$

By entering the measured values corresponding to the line integrals (the phase shift data of the microwave interferometry) of the paths to the input unit of the neural network, values of the above parameters (coefficients of the Fourier-Bessel series) are obtained from the output units. In this problem the training of the neural network is carried out by preparing parameters for various model distributions and corresponding phase shift data as the supervisor data. The error function E of the neural network is represented by the sum of the squared values of differences between the nnetwork output and the supervisor data as

$$E = \sum_k (f_i - f_i^{teacher})^2$$

where f represents the coefficients a_{mn}.
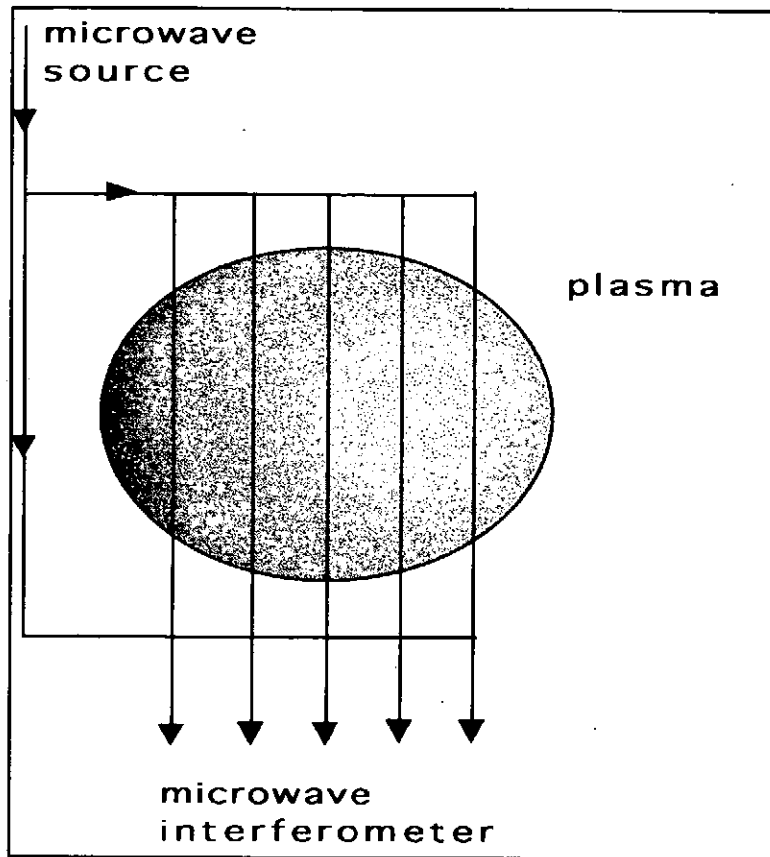
Fig.2   Schematic diagram of the plasma density measurement
by microwave interferometry.

This is a very simple application of the neural network to the inverse problems and we obtained satisfactory results for model distribution of the plasma density.   Bishop el al.[1] applied a similar method to the analysis of the JET plasma by taking into account some additional information on MHD equilibria of the measured plasma.

By this method once the network training is carried out only the forward calculation along the network is necessary for the analysis which consumes only a small amount of computation time.   However, as the density distribution is represented by only a small number of parameters the expressive power of the system is relatively low, and if one wish to carry

out more detailed analysis the size of the network increases drastically.

4.2 Non-Parametric Computed Tomography (1)

In order to cope with the above problem we devised a new CT image reconstruction method by using the neural network[2]. The most distinctive feature of this method in comparison with the previously described method is in the choice of the error function. In this method the value of the density f is obtained from the output unit for the position (x,y) given to the input units as,

$$f_i = f(x_i, y_i; W)$$

Therefore, the network structure is 2 - (hidden layer) - 1, and the size of the network is always kept rather small. The error function is given by using the residual of the integral equation as

$$E = \sum_k \left(g(r_k, \theta_k) - g_k^{measured} \right)^2$$

$$g(r_k, \theta_k) = \int_{(k)} f(x, y) ds \approx \sum_i \alpha_i^{(k)} f(x_i, y_i)$$

where r_k and θ_k are the parameters defining the path of the line integral (r_k: the distance from the origin to the k-th line, θ_k: the angle of the direction to the path). Correspondingly, the updating equation of the weights is given as follows.

$$\Delta w_{mn}^{(l)} = -\gamma \frac{\partial E}{\partial w_{mn}^{(l)}} = -2\gamma \sum_{k=1}^{K} \sum_{i=1}^{I} \left(g(r_k, \theta_k) - g_k^{measured} \right) \frac{\partial g(r_k, \theta_k)}{\partial f_i} \frac{\partial f_i}{\partial w_{mn}^{(l)}}$$

$$\approx -2\gamma \sum_{k=1}^{K} \sum_{i=1}^{I} \left(g(r_k, \theta_k) - g_k^{measured} \right) \alpha_i^{(k)} \frac{\partial f_i}{\partial w_{mn}^{(l)}}$$

We applied this method to some model distributions and obtained satisfactory results. The detailed description of the method is found in ref [2]. Because of the features (5) and (6) described in Section 3 this method may be promising for the case where sufficient number of data points are not available.

4.3 Non-Parametric Computed Tomography (2)

Though the new CT image reconstruction technique is promising there are some problems to be solved. One of them is the error amplification due to the numerical differentiation during the training process. We devised a new algorithm which does not include the

numerical differentiation. The procedure is described as follows.

(1) Continuous mapping between the parameters (r,θ) defining the integration path and the value of line integral b is constructed by using a neural network as

$$b_p = b(r_p, \theta_p) = \int_p f(x,y)d\ell$$

(2) Derivatives of b with respect to r and/or θ are calculated analytically.

$$\frac{\partial b}{\partial r} = \int_p \frac{\partial f}{\partial r}d\ell = \int_p \left(\frac{\partial f}{\partial x}\frac{\partial x}{\partial r} + \frac{\partial f}{\partial y}\frac{\partial y}{\partial r}\right)d\ell = \int_p \left(\frac{\partial f}{\partial x}\cos\theta_p + \frac{\partial f}{\partial y}\sin\theta_p\right)d\ell$$

$$\frac{\partial b}{\partial \theta} = \int_p \frac{\partial f}{\partial \theta}d\ell = \int_p \left(\frac{\partial f}{\partial x}\frac{\partial x}{\partial \theta} + \frac{\partial f}{\partial y}\frac{\partial y}{\partial \theta}\right)d\ell$$

$$= \int_p \left(\frac{\partial f}{\partial x}(-r_p\sin\theta_p + \ell\cos\theta_p) + \frac{\partial f}{\partial y}(r_p\cos\theta_p + \ell\sin\theta_p)\right)d\ell$$

(3) The second neural network which gives $\partial f/\partial x$ and/or $\partial f/\partial y$ as the output value by giving x and y as input values is constructed.

(4) Integration of $\partial f/\partial x$ along the x direction or $\partial f/\partial y$ along the y direction give the value of f.

The above procedure does not include the numerical differentiation and it is expected that the CT image reconstruction with the high accuracy is realizable. Details of this method will be described elsewhere.

5. Application of Neural Network for Solving Differential Equations

Methods to solve differential equationsby the neural network collocation methodwere proposed and tested by B.Ph. Milligen, et al.[3] and I.E. Lagaris, et al.[4]. Difference between above two methods is in the treatment of the boundary/initial conditions. In the Milligen's method the boundary/initial conditions are imposed as penalty terms added to the error function of the neural network. In the Lagaris's method, on the other hand, the solution of the differential equation is composed of the neural network output and appropriate shaping functions so that the resultant solution satisfies the boundary/initial conditions exactly. In this way, there is a possibility that the Lagaris's method gives a higher accuracy but it is rather difficult to prepare appropriate shaping functions. We tried to prepare necessary shaping functions by connecting partly defined shaping functions smoothly (the divided shaping function method).

5.1 Solution Method

The Lagaris's method is explained briefly in the following. We consider to solve the following differential equation defined in a domain Ω.

$$D u(\bar{x}) = g(\bar{x}) \quad on \quad \Omega$$

In the domain we prepare the domain composed of a set of collocation points.

$$D u(\bar{x}) = g(\bar{x}) \quad on \quad \hat{\Omega} \quad \hat{\Omega} \subset \Omega \quad |\hat{\Omega}| < \infty$$

The original continuous differential equation is solved by minimizing the following residual.

$$E = \sum_{\bar{x} \in \hat{\Omega}} (D u(\bar{x}) - g(\bar{x}))^2$$

The corresponding equation for the collocation method is as follows.

$$E = \sum_{\bar{x} \in \hat{\Omega}} (D u_t(\bar{x}, \bar{p}) - g(\bar{x}))^2$$

where the solution is constructed by using the neural network output and the appropriate shaping functions.

$$u_t(\bar{x}, \bar{p}) = A(\bar{x}) + F(\bar{x}, f_N(\bar{x}, \bar{p}))$$

The function F is exactly 0 at the Dirichlet boundary and the value of A at the same point is exactly the boundary value.

5.2 Examples of Problems

W at first we tried the divided shaping function method worked well. For this purpose we solved the poisson equation in a square domain and a T-shaped domain. For the square domain a single shaping function was used (Fig.3), and for the T-shaped domain 7subdomain were prepared and the 7. shaping functions connected smmothly and the whole shaping function was constructed (Fig.4). In both cases accuracy of the computations was not necessarily satisfactory but the divided shaping function works rather well and promising.

0.035 ---
0.021 ····
0.007 ···
-0.007 --
-0.021 ··
-0.035 ---

4.94e-05
4.12e-03 ····
3.29e-03 ··
2.47e-05 ---
1.65e-05 ···
8.23e-06 ····

(a)   (b)
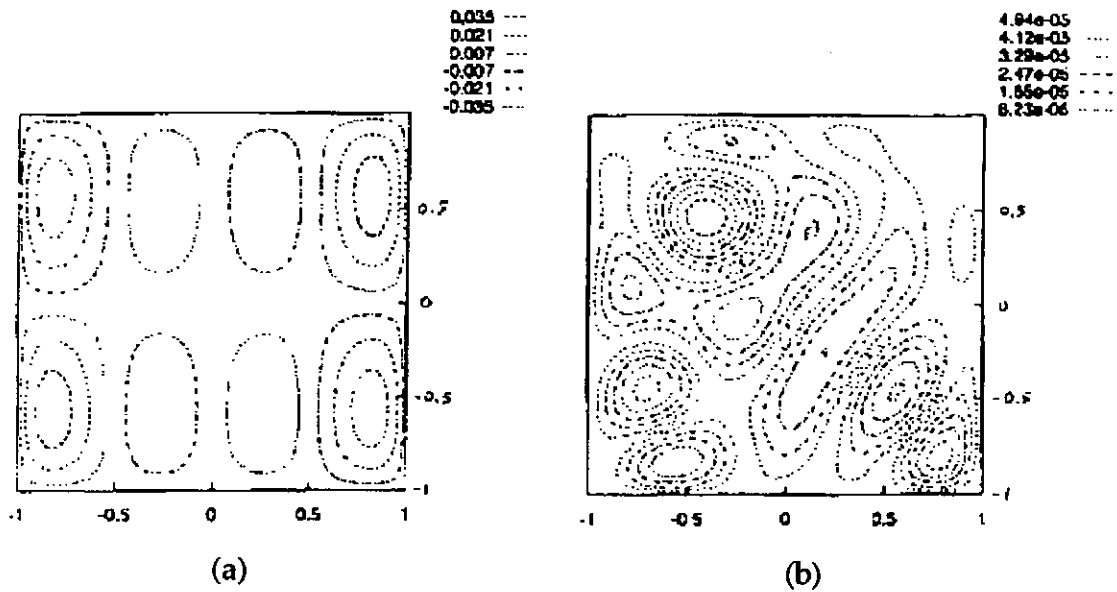
Fig.3   Solution of the Poisson equation in the square domain.
         (a) Contour plot of the solution, (b) Contour plot of the eror.

0.035 ····
0.021 ·····
0.007 ---
-0.007 ---
-0.021 ····
-0.035 ····

0.00179 ----
0.00149 ·····
0.00119 ····
0.000883 ---
0.000595 ····
0.000299 ····
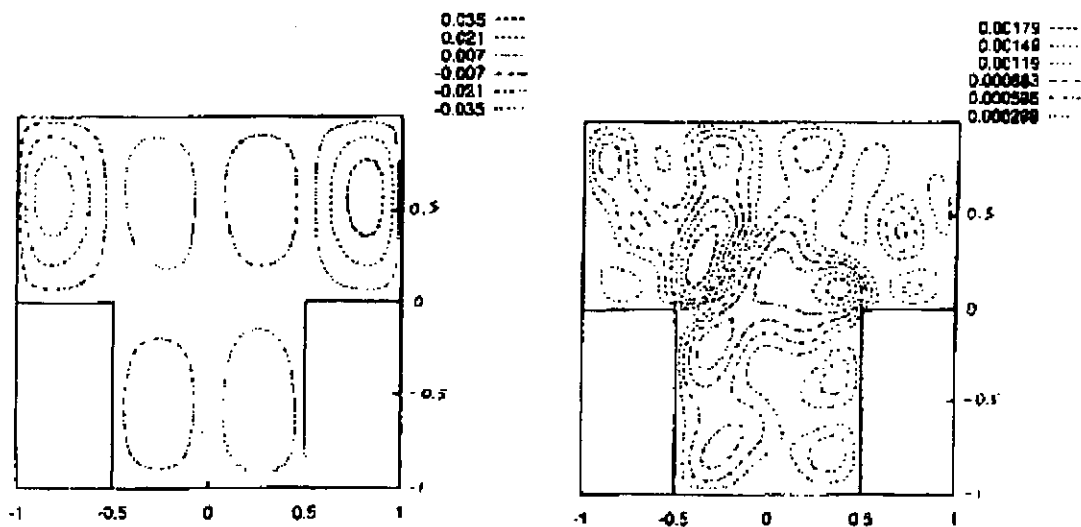
Fig.4   Solution of the Poisson equation in the T-shape domain.
         (a) Contour plot of the solution, (b) Contour plot of the eror.

Next we studied the problems concerning the data assimilation technique. For this purpose we tried to solve the Lorentz equation by assigning the initial condition of different variables at different temporal points. The results were satisfactory and the method worked well even if the initial conditions are not imposed at the different temporal points for different variables. From this experiment it is conjectured that the neural

network collocation method might be usable for the data assimilation problem where the temporal or the spatial positions for the initial/boundary conditions are prepared irregularly.

6. Improvement of Neural Network Training

For the problems treated in this article the important and urgent studies are improvement of the training characteristics. Among them the realization of the fast training is very important. Among them to increase the value of the derivative for large argument is very effective improvement. For this purpose we consider the parametrized weight method [5] and the modified sigmoid function.

6.1 Parametrized Weight Method for Fast Training

By the parametrized weight method each weight is expressed by some third order equations, by which the derivative of E with respective to the weight becomes large even for a large vlue of the argument of the sigmoid function. By this fact the increment of the weight at each iteration step becomes large and the convergence is accelerated.

$$X = \sum_{i=1}^{n} W_i x_i$$

$$W_i^{(m)} = f_i(p_1^{(m)}, \ldots p_i^{(m)}, \ldots p_n^{(m)})$$

$$p_i^{(m+1)} = p_i^{(m)} + \Delta p_i^{(m)}$$

$$\Delta p_i^{(m)} = -\gamma C \frac{d\sigma}{dX} \sum_{j=1}^{n} \frac{\partial X}{\partial W_j^{(m)}} \frac{\partial f_j}{\partial p_i^{(m)}} = -\gamma C \frac{d\sigma}{dX} \sum_{j=1}^{n} x_j \frac{\partial f_j}{\partial p_i^{(m)}}$$

$$W_i^{(m+1)} = f_i(p_1^{(m+1)}, \ldots p_i^{(m+1)}, \ldots p_n^{(m+1)})$$

$$\Delta W_i^{(m)} \equiv W_i^{(m+1)} - W_i^{(m)} = \sum_{k=1}^{n} \frac{\partial f_i}{\partial p_k^{(m)}} \Delta p_k^{(m)} + O\left((\Delta p^{(m)})^2\right)$$

$$\sum_{k=1}^{n} \frac{\partial f_i}{\partial p_k^{(m)}} \Delta p_k^{(m)} = -\gamma C \frac{d\sigma}{dX} \sum_{j=1}^{n} x_j \sum_{k=1}^{n} \frac{\partial f_i}{\partial p_k^{(m)}} \frac{\partial f_j}{\partial p_k^{(m)}}$$

$$f_i(p_1, \ldots p_i, \ldots p_n) = g(p_i)$$

$$\Delta W_i^{(m)} \approx -\gamma C \frac{d\sigma}{dX} x_i \left(\frac{dg}{dp_i}\right)^2$$

This method is especially effective for some kind of model problems but for some model problems this method does not work as expected. The deetailed description of this method will be presented elsewhere.

6.2   Modified Sigmoid Function for Fast Training

According to the same guidline as the previous subsection we replaced the argument X of the sigmoid function by a higher order equation of X, which gives a large value of derivative of the sigmoid function and makes the step length of the training large.

$$y = \sigma(X)$$

$$\frac{dy}{dX} = \frac{d\sigma}{dX}$$

$$y = \sigma(X + aX^3)$$

$$\frac{dy}{dX} = \frac{d\sigma}{dX}(1 + 3aX^2)$$

This method does not improve the convergence dramatically as the method described in the previous subsection but improves the convergence on the average.

7.   Summary

We have developed a new application methods of the neural network. This is based on the principle that the sum of squared residuals of the integral equation or the differential equation should be minimized. The concrete examples of the model problems are the CT image reconstruction and the solutions of the Poisson equation, the Lorentz equation and so on. We obtained a satisfactory results and the method may be promising for various kind of unique problems.

Reference

1.   C.M. Bishop, Rev. Sci. Instr. 65, 1803 (1994).

2.   X.F. Ma, T. Takeda, Application of neural network to CT, in this report.

3.   B.Ph. Milligen, et al., Phys. Rev. Letters 75, 3594 (1995).

4.   I.E. Lagaris, et al., Artificial neural network for solving ordinary and partial differential equations, Preprint 15-96, Dept. of Computer Science, Univ. of Ionia (1996).

5   T. Kin, T. Takeda,

ニューラルネットワークの CT への応用

馬笑峰*　　竹田辰興†

*電気通信大学 情報工学専攻　　†電気通信大学 情報工学科

Application of Neural Network to CT

Xiao Feng MA　　Tatsuoki TAKEDA

DEPARTMENT OF COMPUTER SCIENCE AND INFORMATION MATHEMETICS,
THE UNIVERSITY OF ELECTRO-COMMUNICATIONS

Abstract

This paper presents a new method for two-dimensional image reconstruction by using a multilayer neural network. Consider the general tomography problem illustrated in Fig.1. The goal is to determine the local spatial quantity $f(x,y)$ from a number of line integral measurements

$$g(r_k, \theta_k) = \int_{(k)} f(x,y)ds$$

made along various lines of sight k though a given region of space.

Multilayer neural networks are extensively investigated and practically applied to solution of various problems such as inverse problems or time series prediction problems. From learning an input-output mapping from a set of examples, neural networks can be regarded as synthesizing an approximation of multidimensional function (that is, solving the problem of hypersurface reconstruction, including smoothing and interpolation). From this viewpoint, neural networks are well suited to the solution of CT image reconstruction.

Though a conventionally used object function of a neural network is composed of a sum of squared errors of the output data, we can define an object function composed of a sum of residue of an integral equation.

$$E = \sum_k \left(g_k^{NN} - g_k^{meas} \right)^2$$

where g_k^{NN} is line integration calculated from neural network output, g_k^{meas} is the observed projection data and k is the number of integral lines. By employing an appropriate line integral for this integral equation, we can construct a neural network that can be used for CT. We applied this method to some model problems and obtained satisfactory results.

As it is not necessary to discretize the integral equation using this reconstruction method, therefore it is application to the problem of complicated geometrical shapes is also feasible. Moreover, in neural networks, interpolation is performed quite smoothly, as a result, inverse mapping can be achieved smoothly even in case of including experimental and numerical errors. However, use of conventional back propagation technique for optimization leads to an expensive computation cost. To overcome this drawback, 2nd order optimization methods or parallel computing will be applied in future.

Keywords: computerized tomography, multilayer neural networks, error back propagation

1 はじめに

コンピュータトモグラフィ(Computerized Tomography, CT)は物体の外部で得られた信号から内部の物理量分布を非破壊的に計測する方法として精力的に研究され，色々な分野で実用的に使われている。CTの技術は対象によっては高い完成度を達成しているが，今後解決すべき課題も多い。その一つが比較的少数の観測データからなるべく簡便にCT再生像を得る方法の確立である。我々はこのような目的を満足する方法としてニューラルネットワークを使った新しいCT画像再構成法を提案し，モデル実験でその有効性を確認した。

CTの実行に当っては，まず物体を横切るいくつかの径路に沿う物理量の線積分値が観測データ(投影像)として与えられる。この投影像から逆変換により対象とする物体の内部の物理量の2次元あるいは3次元分布を再構成する。解を求めるには，例えば，対象をする空間をメッシュ分割し，未知物理量を離散化して，径路に沿った線積分として表現することで連立一次方程式を得て，これを解けばよい。しかし，この問題は典型的な悪条件問題であるので，上のような方法を単純に適用するのみでは，一般に解を得ることはできない。正しい解を得るためには対象や測定系の特性などに応じた種々の解析方法が用いられる。

ところで，多層ニューラルネットワークはn次元入力データ空間からm次元出力データ空間への連続写像である。多層ニューラルネットワークを用いて，CT解析を行うには，入力データとして対象とする物体内の座標$(n=2)$，出力データとしてその位置での物理量の大きさ(像強度，$m=1$)，誤差評価関数として上記像強度の径路に沿う線積分値と観測データ(投影像強度)の差の二乗をとって学習すればよい。

比較的少数データからCT像再構成を行う具体例として円柱状あるいは軸対称トーラス状の核融合プラズマの内部の物理量の分布をCTにより解析することを考える[1]。

2 ニューラルネットワークを用いたCT像再構成法

2.1 問題の定式化

物理量の強度分布(原像)zが2次元領域Ω内において位置座標(x,y)の関数として次式のように表されるものとする(Fig.1)。

$$z = f(x,y) \tag{1}$$

この領域Ωを横切る径路$k(k=1,...,K)$はパラメータ(r_k, θ_k)で表わすことができる。この時径路kに沿った$f(x,y)$の積分が投影像$g(r_k, \theta_k)$である。即ち，

$$g(r_k, \theta_k) = \int_{(k)} f(x,y)ds \tag{2}$$

測定された投影像g_k^{meas}はこれにノイズ$n(r_k, \theta_k)$が加わったもので次式で表わされる。

$$g_k^{meas} \equiv g^{meas}(r_k, \theta_k) = g(r_k, \theta_k) + n(r_k, \theta_k) \tag{3}$$

ここで，kについてのnの平均値は0であるとする。この積分方程式の逆変換を行ない，強度分布$f(x,y)$を再現する。ニューラルネットワークを用いて再現された強度分布を$f^{NN}(x,y)$とする。
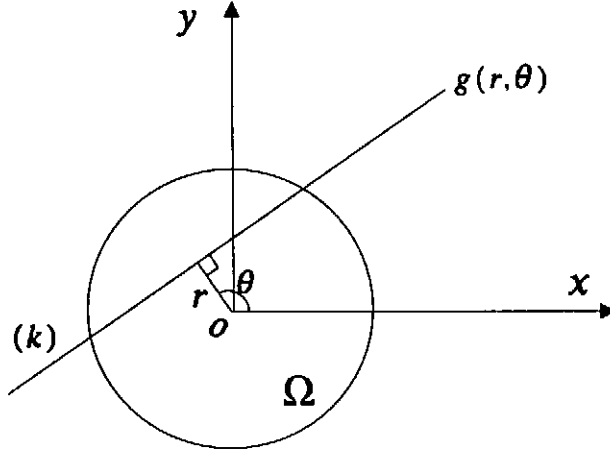
Fig.1: The computational domain for two-dimensional image reconstruction

2.2 CTのための誤差評価関数と学習

ニューラルネットワークによる写像を次式で表わす。

$$\vec{y} = \vec{y}(\vec{x}, \vec{w}) \tag{4}$$

ここで，$\vec{x}$及び$\vec{y}$は，それぞれニューラルネットワークの入力データと出力データを表す。また，ニューラルネットワークの内部のパラメータ(ウエイト及びオフセット)を$\vec{w}$で表す。多層ニューラルネットワークでは，通常，学習の際，入力データ$\vec{x}$に対する出力データが教師信号$\vec{t}$として与えられる(教師あり学習)。この場合，誤差評価関数として，全ての標本点に対する誤差のの二乗和が採用される。

$$E = \sum_{n=1}^{N} E^n, \quad E^n = \frac{1}{2} \sum_{k=1}^{K} \{y_k(\vec{x}^n; \vec{w}) - t_k^n\}^2 \tag{5}$$

ここで，Nは標本点数，Kは出力層のニューロン数である。誤差逆伝播法では次式に従ってウエイトの更新が行われる。

$$\Delta w_{mn}^{(\tau)} = w_{mn}^{(\tau)} - w_{mn}^{(\tau-1)} = -\eta \frac{\partial E}{\partial w_{mn}}\bigg|_{w^{(\tau-1)}} \tag{6}$$

ここで，τは更新ステップで，ηは学習率である。

本研究で述べる方法では，通常の教師あり学習の場合と違って，構成されたネットワークでは既知の出力(教師データ)は存在しないので，ニューラルネットワークからの出力 $f^{NN}(x,y)$ そのものを教師データと比較するのではなく，積分径路に沿った積分値を観測された投影データ g_k^{meas} と比較する。即ち，誤差評価関数は次のように定義される。

$$E = \sum_k \left(g^{NN}(r_k, \theta_k) - g_k^{meas}\right)^2 \tag{7}$$

ここで，$g^{NN}(r_k, \theta_k)$はニューラルネットワークの出力 $f^{NN}(x,y)$ から計算された線積分値であり，線積分の値は数値積分によって求める。

$$g^{NN}(r_k, \theta_k) = \int_{(k)} f^{NN}(x,y)ds \approx \sum_i \alpha_i^{(k)} f^{NN}(x_i, y_i) \tag{8}$$

ここで，$\alpha_i^{(k)}$は数値積分のウエイトである。この誤差評価関数に対して誤差逆伝播法 (EBP 法) によって，ニューラルネットワークのウエイト更新量は，次式で与えられる。

$$\Delta w_{mn}^{(\tau)} = -\eta \frac{\partial E}{\partial w_{mn}}\bigg|_{w^{(\tau-1)}}$$

$$= -2\eta \sum_{k=1}^{K} \sum_{i=1}^{I} \left(g^{NN}(r_k, \theta_k) - g_k^{meas}\right) \frac{\partial g^{NN}(r_k, \theta_k)}{\partial f_i^{NN}} \frac{\partial f_i^{NN}}{\partial w_{mn}}\bigg|_{w^{(\tau-1)}}$$

$$\approx -2\eta \sum_{k=1}^{K} \sum_{i=1}^{I} \left(g^{NN}(r_k, \theta_k) - g_k^{meas}\right) \alpha_i^{(k)} \frac{\partial f_i^{NN}}{\partial w_{mn}}\bigg|_{w^{(\tau-1)}} \tag{9}$$

ここで，$f_i^{NN} \equiv f^{NN}(x_i, y_i)$ である。ネットワークに十分学習させれば，再現領域内任意の点の座標を入力すると，その点における像の強度が出力される。

3 モデル分布再現の数値実験

3.1 モデル分布

ここでは，提案した方法によって CT 像再構成が精度よく実行できることを確認するためにモデル分布再現の数値実験を行う。再現すべきモデル分布を解析的に与え，この分布について線積分を行い投影データを計算して模擬的な観測データを用意する。モデル分布としては以下に示すような井戸型分布 [4] とガウス型二重ピーク分布 [5] を採用する。

(1) 井戸型分布

$$f_1(x,y) = \frac{1}{2} \sum_{x_0=1}^{2} \sum_{y_0=1}^{3} exp(-(10x - 10x_0 + 15)^2/2.5 - (10y - 3y_0 + 6)^2/7)$$

$$+ \frac{1}{2} \sum_{x_0=1}^{3} \sum_{y_0=1}^{2} exp(-(10x - 3x_0 + 6)^2/7 - (10y - 10y_0 + 15)^2/2.5) \tag{10}$$

(2) ガウス型二重ピーク分布

$$f_2(x,y) = exp(-(12.5x - 6)^2/7 - (12.5y - 0.5)^2/22)$$

$$+0.35exp(-(12.5x + 0.5)^2/12 - (12.5y - 0.5)^2/22) \tag{11}$$

再現領域は，$x \in [-1,1], y \in [-1,1]$ とする。これらのモデル分布の鳥瞰図と等高線図をそれぞれ Fig.2、Fig.3に示す。
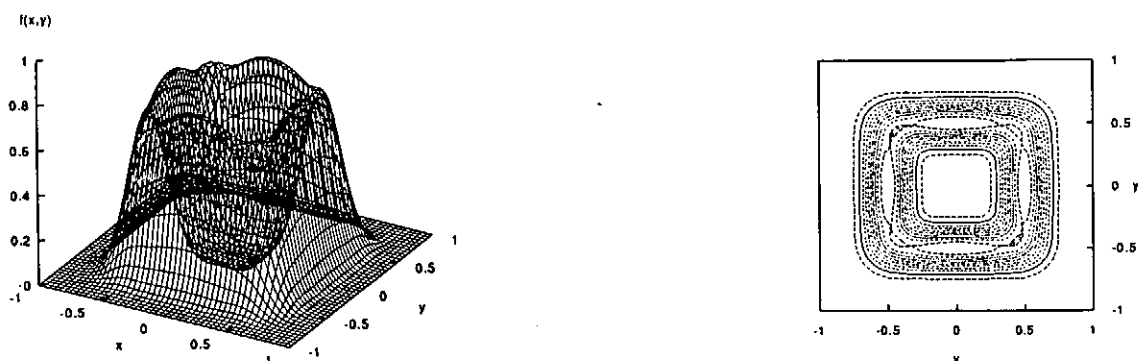
Fig.2: A bird-eye view and a contour diagram of the model distribution f_1
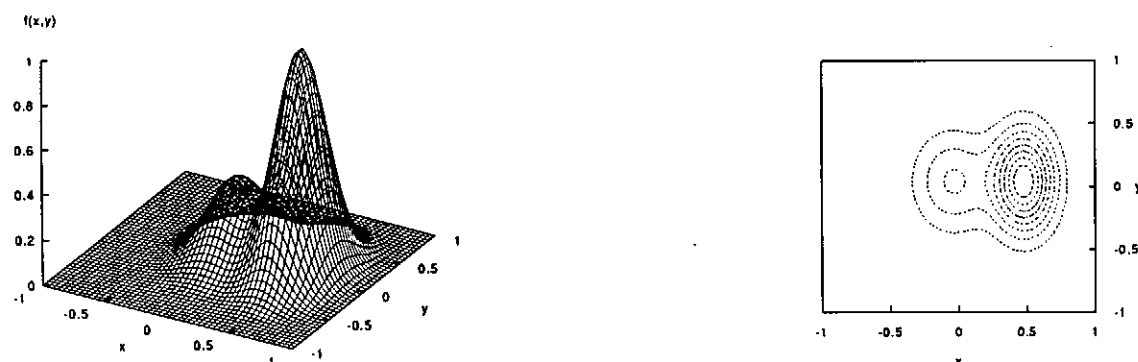
Fig.3: A bird-eye view and a contour diagram of the model distribution f_2

3.2 投影測定の配位

投影データは以下に述べるように, Fig.4に示す積分径路に沿った積分を実行して求める。投影データの測定装置は半径 $r = 2$ の円周 R_m 上に設けるものとする。なお, 投影データ計算のための積分範囲は半径 $r = \sqrt{2}$ の円 R_o の中に限られるものとする。即ち, 円 R_o の内部 (円周を含む) は式 (11) 及び式 (10) で表した強度分布で, 外部は 0 とする。Fig.4に示すように円 R_m を 6 等分した点から円 R_o を見込む角度 ($\frac{\pi}{2}$) を 51 等分して合計 300 本の積分径路を構成し, $K = 300$ 個の投影データを得る。ここで, 各径路についての線積分は 20 点の台形則によって数値的に求める。

3.3 誤差の評価

再現された強度分布が真のモデル分布にどれほど近いかを定量的に表す指標として投影データ誤差 E_p 及び平均関数値誤差 E_s を次のように定義する。

$$E_p = \sqrt{\frac{\sum_{k=1}^{K} \left[g^{NN}(r_k, \theta_k) - g_k^{meas} \right]^2}{K}} \tag{12}$$

$$E_s = \frac{\sum_{n=1}^{N} \left| f(x_n, y_n) - f^{NN}(x_n, y_n) \right|}{N} \tag{13}$$
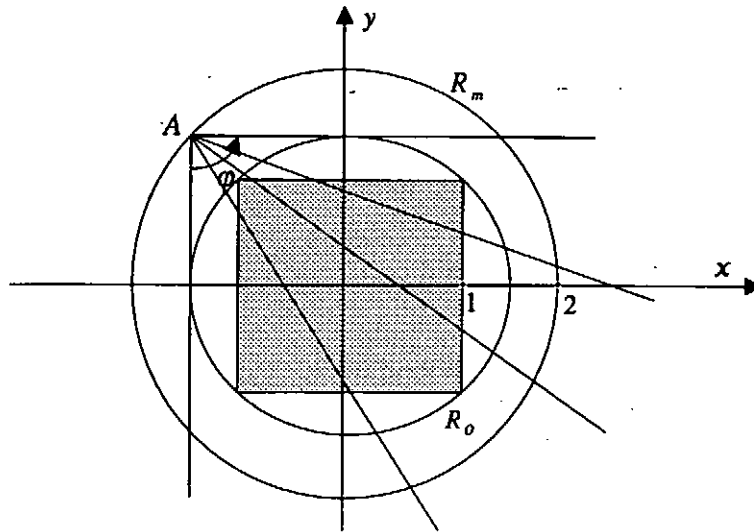
Fig.4: Paths of line integrals of the projection data

ここで，Nは学習終了後にモデル分布再現計算を行う点(一般に未学習点)の数で，本実験では，$N = 51^2 = 2601$ を用いた。

3.4　モデル分布再現実験の結果

4層のネットワーク $(2 \to 12 \to 12 \to 1)$ を用いて投影データにノイズ $n(r_k, \theta_k)$ が含まれていない場合について井戸型分布の再現実験を行った。再現された分布の鳥瞰図及び等高線図を Fig.5に，また真のモデル分布とニューラルネットワークの出力データの相関図を Fig.6に示す。この逆変換では，誤差として $E_p = 0.0042$，$E_s = 0.0135$ が得られた。
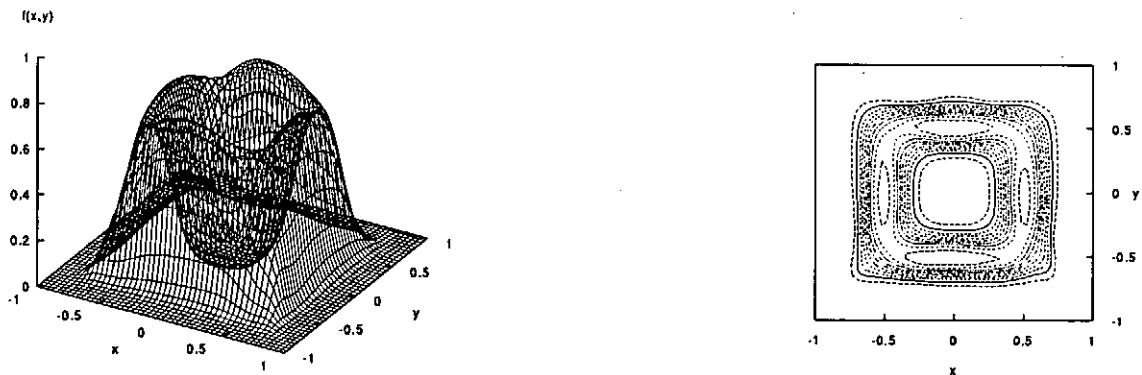
Fig.5: A bird-eye view and a contour diagram of the reconstructed distribution of f_1

次に，投影データに有限のノイズ $n(r_k, \theta_k)$ が含まれる場合を想定してガウス型2重ピーク分布の再現実験を行った。投影データは，測定ノイズを模擬するために式(3)のように各 g_k^{meas} に平均値零の正規乱数ををを加えて作成する。乱数の大きさは平均投影強度 $K^{-1} \sum g_k^{meas}$ の5%(標準偏差) となるようにする。再現された分布の鳥瞰図及び等高線図を Fig.5に，また真のモデル分布とニューラル・ネットワークの出力データの相関図を Fig.6に示す。この逆変換では，誤差として $E_p = 0.007$，$E_s = 0.022$ が得られた。
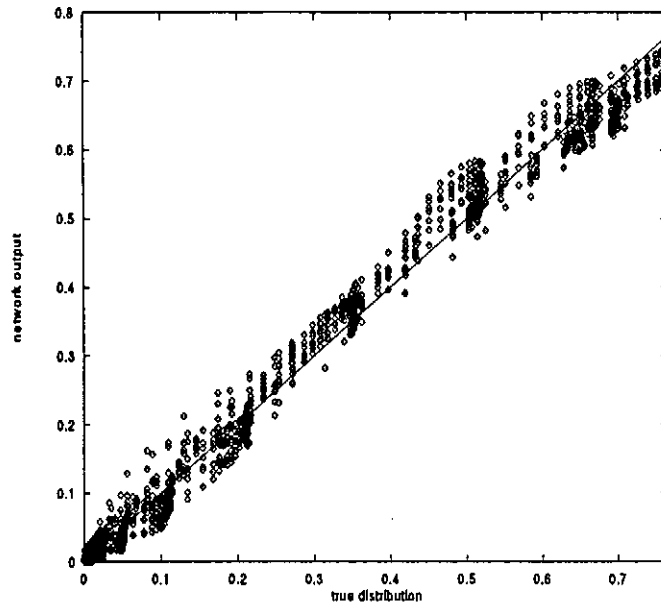
Fig.6: The correlation diagram between network output and true distribution
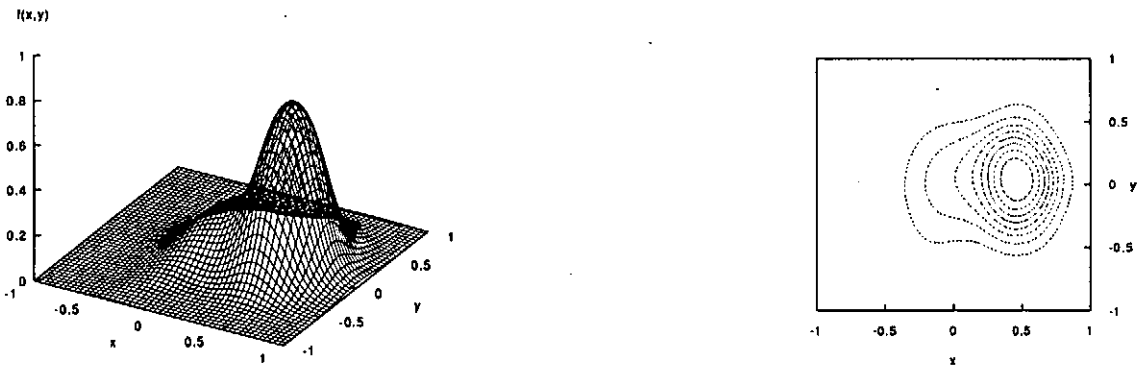
Fig.7: A bird-eye view and a contour diagram of the reconstructed distribution of f_2
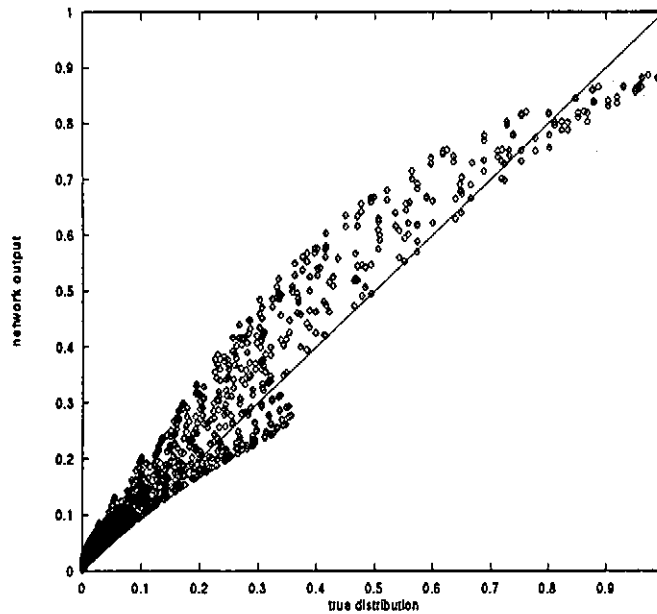
Fig.8: The correlation diagram between nework output and true distribution

4 まとめと討論

　本研究では，積分方程式の残差の二乗和を誤差評価関数とするニューラルネットワークをCT解析に応用する方法を提案した。投影データにノイズを含む場合と含まない場合についてモデル分布の再現実験を行い，満足すべき結果を得て，この方法が有効であることを確認した。

　再現アルゴリズムとしては積分方程式を離散化する必要がないので，複雑な幾何形状の問題に対しても適用が容易である。また，ニューラルネットワークによって写像を構成する時には平滑化及び内挿が同時に行われているので，実験誤差や数値計算誤差を含む場合にも正則化について特別注意を払わなくとも滑らかな逆変換が簡単に得られる。得られた解は至る所連続で微分可能であるという特徴を持つ。

　測定データが自由にかつ大量に得られる医療用CT等については高速で高精度で解析法が既に実用化されているが，物理実験や自然界の観測では測定装置の設定位置を自由に選べない等幾何学的拘束からデータ数が少ないことが多い。このような少数データのCT解析には本方法は有効である。

　学習アルゴリズムとして通常の誤差逆伝播法を使う限り計算コストは高くなるのはやむを得ない。二次の最適化方法を用いる等採用する学習アルゴリズムの改善や並列化を行うことによって計算コストの削減するという課題が残されている。

　線積分の代わりに面積分，体積分を考えれば，本方法は境界条件からポアソン方程式の源を求める逆問題の有力な手法として期待できる。

謝辞

参考文献

[1] 岩間尚文，プラズマ計測のための計算機トモグラフィ; 少数データからの像再構成，核融合研究 **68**(1992) 586.

[2] 長山好夫，プラズマ診断におけるCT(計算機トモグラフィー)の応用，核融合研究 **62**(1989) 427.

[3] C.Bishop, Neural networks and their diagnostic applications, Rev.Sci.Instr. **63**(1992)4772.

[4] 沈 雲，高村秀一，岩間尚文，黒田 勉，奥田孝美，可視光計算機トモグラフィによるプラズマ像の再生，核融合研究 **59**(1988) 30.

[5] 高見 均，岩間尚文，高村秀一，築島隆繁，スプライン関数によるトーラス接線方向投影からプラズマ像再生，核融合研究 **56**(1986) 278.

Application of the Infinite-Precision Numerical Simulation to an Inverse Problem[*]

Hitoshi IMAI[1] and Toshiki TAKEUCHI[1]

[1]*Faculty of Engineering, The University of Tokushima,*
Tokushima, 770-8506, Japan

Abstract

In the paper an inverse problem on the heat equation is solved by direct simulation using infinite-precision numerical simulation. It consists of spectral(collocation) methods and the multiple-precision arithmetic. Numerical results are relatively satisfactory. Moreover, we show another interesting approach which may increase validity of infinite-precision numerical simulation to inverse problems.

Key Words :   inverse problem, infinite, spectral method, multiple precision

1   Introduction

Inverse problems often arise in engineering, and they are very important from the practical view point. However, it is very difficult to solve them because they are ill-posed[3]. Errors grows exponentially.

Inverse problems are usually transformed into minimization(regularized) problems, then solved. A lot of theoretical regularization techniques have been developed[3, 12], however they are not always applicable to practical problems due to unpredictable errors. This is because minimization problems are not ill-posed but ill-conditioned. So, additional techniques are necessary for suppression of oscillation phenomena.

In practical(complicated) problems AI(Artificial Intelligence) approaches are valid. In such systems the fuzzy theory is often adopted, because it is easy to reflect the experience of experts to the control system. We applied the fuzzy control to a little complicated inverse problem which is concerned with the vessel design in the plasma confinement[2, 4]. The

problem is an initial value problem on the Laplace operator and it is defined in the domain with a complicated shape. We transformed the problem into a direct problem with a free boundary, and optimized iteratively by using the fuzzy control. Unfortunately, numerical results were not so satisfactory[12]. In such complicated direct problems unpredictable errors spoil sophisticated numerical methods. In our problem, the complicated solver of the direct free bounday problem may cause unpredictable errors.

We consider the direct simulation to inverse problems along the strategy. It is based on the fact that numetical simulation is practical. Inverse problems are very important from the practical view point, so numerical simulation is inevitable. It is more important than theoretical analysis. However, numerical simulation can not give global solutions to inverse problems. Therefore, if numerical methods give good local solutions, then we should satisfy. This approach may be realized by infinite-precision numerical simulation to PDE systems. The simulation to one-dimensional boundary value problems enabled incredible accuracy(errors $< 10^{-1000}$)[11, 7].

2 Our Method and Model Problem

2.1 Infinite-Precision Numerical Simulation

Errors in numerical simulation to PDE systems originate from truncation errors in the discretization and round-off errors. Realization of arbitrary precision simulations needs arbitrary reduction of both errors.

When partial differential equations have smooth solutions, truncation errors can be reduced by raising the order of approximation. We adopt the spectral method as a discretization method. Particularly, the spectral collocation method is used here. This is because it is very useful to nonlinear problems and its application is very easy like FDM. In the spectral collocation method, the order of approximation can be controlled by the number of collocation points. For example, in the spectral collocation method with Chebyshev-Gauss-Lobatto points, the N-th order approximation can be realized only by using $(N + 1)$ collocation points[1].

In addition, the multiple-precision arithmetic[9] is used for reduction of round-off errors. A lot of FORTRAN subroutines about the multiple-precision arithmetic are already known. We used the library of FORTRAN subroutines on the net (http://www.lmu.edu/acad /personal/faculty/dmsmith/FMLIB.html)[10].

Our numerical method consists of these two methods, i.e. the multiple-precision arithmetic and the spectral (collocation) method. In our method, truncation errors and round-off errors are controlled easily. This is very important in numerical simulation in applied mathematics. Of course, both errors can be reduced arbitrarily. This means theoretically we can perform numerical simulation with errors which are less than the given tolerance. From this point of view, our simulation can be called that in infinite precision[11, 7].

2.2 Model Problem

To evaluate our method we consider the following model problem. This problem is a typical inverse problem on the heat equation.

Model Problem 1

$$(1) \qquad \frac{\partial u}{\partial t} = -\frac{\partial^2 u}{\partial x^2}, \qquad 0 < t, \qquad -1 < x < 1,$$

$$(2) \qquad u(x, 0) = \cos\frac{\pi x}{2}, \qquad -1 < x < 1,$$

$$(3) \qquad u(-1, t) = 0, \qquad 0 \leq t,$$

$$(4) \qquad u(1, t) = 0, \qquad 0 \leq t.$$

The exact solution for Model Problem 1 is given as follows:

$$(5) \qquad u(x, t) = \exp\frac{\pi^2 t}{4}\cos\frac{\pi x}{2}, \qquad 0 \leq t, \qquad , -1 \leq x \leq 1.$$

The exact solution grows exponentially as t increases.

2.3 Spectral Collocation Method in Time

We use the spectral collocation method in space and time. Generally, we need an iterative method to apply the spectral collocation method in time. To do so, the time axis is divided into intervals. In each interval the initial and boundary value problem is solved. This procedure is executed iteratively[5].

For the application of the spectral collocation method to the interval $[t_s, t_e]$ we consider the following variable transform:

$$(6) \qquad t(\tau) = \frac{\Delta t}{2}\tau + \frac{1}{2}(t_s + t_e), \quad -1 \leq \tau \leq 1, \quad \Delta t = t_e - t_s$$

$$(7) \qquad \tau(t) = \frac{2}{\Delta t}(t - \frac{1}{2}(t_s + t_e)).$$

Then,

$$(8) \qquad \frac{\partial}{\partial t} = \frac{d\tau}{dt}\frac{\partial}{\partial \tau} = \frac{2}{\Delta t}\frac{\partial}{\partial \tau}.$$

Thus Model Problem 1 is transformed into the following problems.

Model Problem 1' − 1

For the interval $[0, t_e]$ (i.e. $t_s \equiv 0$),

(9)
$$\frac{2}{\Delta t} \frac{\partial u}{\partial \tau} = -\frac{\partial^2 u}{\partial x^2}, \qquad -1 < \tau \le 1, \qquad -1 < x < 1,$$

(10)
$$u(x, -1) = \cos \frac{\pi x}{2}, \qquad -1 < x < 1,$$

(11)
$$u(-1, \tau) = 0, \qquad -1 \le \tau \le 1,$$

(12)
$$u(1, \tau) = 0, \qquad -1 \le \tau \le 1$$

Model Problem 1' − 2

For the interval $[t_s, t_e]$ after the interval $[\tilde{t}_s, \tilde{t}_e]$ (i.e. $t_s \equiv \tilde{t}_e$),

(13)
$$\frac{2}{\Delta t} \frac{\partial u}{\partial \tau} = -\frac{\partial^2 u}{\partial x^2}, \qquad -1 < \tau \le 1, \qquad -1 < x < 1,$$

(14)
$$u(x, -1) = u(x, t = \tilde{t}_e), \qquad -1 < x < 1,$$

(15)
$$u(-1, \tau) = 0, \qquad -1 \le \tau \le 1,$$

(16)
$$u(1, \tau) = 0, \qquad -1 \le \tau \le 1$$

3   Numerical Results

For Model Problems 1', SCM(Spectral Collocation Method) in space and time with Chebyshev-Gauss-Lobatto points is used. We use same order approximation in t and x directions for the simplicity. N represents the order of SCM. The number of total collocation points is $(N + 1)^2$. Numerical results are estimated by maximum among absolute values of relative errors at collocation points.

First, numerical calculation is executed in double precision. A constant $\varepsilon_0 = 0.1$. Table 1 shows the time t_c when the error exceeds $\varepsilon_0 = 0.1$. In Table 1, "−" shows the case where the error exceeds 0.1 at the first interval. t_c with symbol "*" shows the last time when numerical calculation is stopped by overflow until the error exceeds ε_0. The boldface represents the largest t_c for fixed N. There is a proper value of Δt for fixed N.

Next, numerical calculation is executed in quadruple precision. Table 2 shows t_c for $\varepsilon_0 = 0.1$. In many cases, results in quadruple precision are better than those in double precision.

Table 1. t_c by SCM in double precision($\varepsilon_0 = 0.1$)

	$N=4$	$N=5$	$N=6$	$N=7$	$N=8$	$N=9$	$N=10$
$\Delta t = 0.1$	0.2	0.1	0.2	0.2	0.2	0.2	0.2
$\Delta t = 0.2$	0.2	0.2	0.4	0.6	0.4	0.6	0.4
$\Delta t = 0.3$	0.9	0.9	0.6	0.3	0.6	0.6	0.9
$\Delta t = 0.4$	7.6	4.0	1.2	1.2	0.8	0.4	0.8
$\Delta t = 0.5$	**8.0**	2.5	2.5	2.5	2.0	1.0	1.5
$\Delta t = 0.6$	7.2	7.2	5.4	3.6	3.0	1.8	1.8
$\Delta t = 0.7$	5.6	15.4	7.0	3.5	4.2	3.5	3.5
$\Delta t = 0.8$	4.0	40.8	11.2	5.6	4.8	3.2	4.0
$\Delta t = 0.9$	2.7	**71.1**	21.6	9.0	6.3	3.6	3.6
$\Delta t = 1.0$	1.0	29.0	60.0	17.0	8.0	5.0	5.0
$\Delta t = 1.1$	1.1	13.2	**172.7**	29.7	12.1	8.8	5.5
$\Delta t = 1.2$	–	7.2	85.2	75.6	18.0	9.6	6.0
$\Delta t = 1.3$	–	3.9	44.2	**284.7***	33.8	14.3	9.1
$\Delta t = 1.4$	–	1.4	23.8	218.4	81.2	21.0	11.2
$\Delta t = 1.5$	–	–	12.0	115.5	**283.5***	36.0	16.5
$\Delta t = 1.6$	–	–	6.4	62.4	**283.2***	97.6	24.0
$\Delta t = 1.7$	–	–	3.4	34.0	**283.9***	**283.9***	42.5
$\Delta t = 1.8$	–	–	1.8	19.8	198.0	**284.4***	91.8
$\Delta t = 1.9$	–	–	–	11.4	108.3	**283.1***	**283.1***
$\Delta t = 2.0$	–	–	–	6.0	60.0	**284.0***	**284.0***
$\Delta t = 2.1$	–	–	–	2.1	35.7	270.9	**283.5***

Table 2. t_c by SCM in quadruple precision($\varepsilon_0 = 0.1$)

	$N=4$	$N=5$	$N=6$	$N=7$	$N=8$	$N=9$	$N=10$
$\Delta t = 0.1$	0.2	0.1	0.2	0.2	0.2	0.2	0.2
$\Delta t = 0.2$	0.2	0.2	0.4	0.6	0.4	0.6	0.4
$\Delta t = 0.3$	0.9	0.9	0.6	0.3	0.6	0.6	0.9
$\Delta t = 0.4$	**8.8**	10.0	1.2	1.2	0.8	0.4	0.8
$\Delta t = 0.5$	8.0	6.5	2.5	2.5	2.0	1.0	1.5
$\Delta t = 0.6$	7.2	17.4	12.0	6.0	3.0	1.8	1.8
$\Delta t = 0.7$	5.6	35.7	17.5	8.4	7.0	3.5	3.5
$\Delta t = 0.8$	4.0	**98.4**	28.0	15.2	11.2	6.4	5.6
$\Delta t = 0.9$	2.7	71.1	52.2	23.4	14.4	9.0	9.0
$\Delta t = 1.0$	1.0	29.0	151.0	37.0	20.0	13.0	11.0
$\Delta t = 1.1$	1.1	13.2	**172.7**	66.0	28.6	17.6	13.2
$\Delta t = 1.2$	–	7.2	85.2	180.0	44.4	25.2	16.8
$\Delta t = 1.3$	–	3.9	44.2	**462.4**	79.3	35.1	22.1
$\Delta t = 1.4$	–	1.4	23.8	218.4	200.2	53.2	30.8
$\Delta t = 1.5$	–	–	12.0	115.5	**1365.5**	91.5	40.5
$\Delta t = 1.6$	–	–	6.4	62.4	696.0	225.6	60.8
$\Delta t = 1.7$	–	–	3.4	34.0	365.5	**3393.2**	102.0
$\Delta t = 1.8$	–	–	1.8	19.8	198.0	1737.0	241.2
$\Delta t = 1.9$	–	–	–	11.4	108.3	913.9	**4598.0***
$\Delta t = 2.0$	–	–	–	6.0	60.0	492.0	**4598.0***
$\Delta t = 2.1$	–	–	–	2.1	35.7	270.9	2725.8

Tables 3 and 4 show the largest t_c for fixed N. The calculation in quadruple precision is stabler compared with that in double precision.

Table 3.   Largest t_c by SCM in double precision($\varepsilon_0 = 0.1$)

	$N_x, N_t = 4$	$N_x, N_t = 5$	$N_x, N_t = 6$
Δt	0.5	0.9	1.1
# iteration	16	17	157
t_c	8.0	71.1	172.7
Max. of exact sol.	3.74×10^8	2.20×10^{16}	1.15×10^{185}
Max. of numer. sol.	3.38×10^8	2.24×10^{16}	1.04×10^{185}
error	0.0948	0.0204	0.0999

Table 4.   Largest t_c by SCM in quadruple precision($\varepsilon_0 = 0.1$)

	$N = 4$	$N = 5$	$N = 6$	$N = 7$	$N = 8$	$N = 9$
Δt	0.4	0.8	1.1	1.3	1.5	1.7
# iteration	22	123	157	328	909	1996
t_c	8.8	98.4	172.7	426.4	1363.5	3393.2
Max. of exact sol.	2.69×10^9	2.45×10^{105}	1.15×10^{185}	7.84×10^{456}	1.25×10^{1461}	1.16×10^{3636}
Max. of numer. sol.	2.42×10^9	2.65×10^{105}	1.04×10^{185}	8.62×10^{456}	1.23×10^{1461}	1.28×10^{3636}
error	0.0994	0.0775	0.0999	0.0999	0.0999	0.1000

Next, numerical results by the FDM(Finite Difference Method) are shown for comparison. The quadruple precision arithmetic is used. The second-order centered difference method about x is used in FDM. Crank-Nicorson method is used for time integration. n represents the number of grids in x direction. The calculation by FDM is unstabler compared with that by SCM.

Table 5. t_c by FDM in quadruple precision($\varepsilon_0 = 0.1$)

	$n = 11$	$n = 101$	$n = 1001$
$\Delta t = 0.10$	1.90	2.80	2.50
$\Delta t = 0.11$	3.30	3.96	3.74
$\Delta t = 0.12$	4.80	5.04	4.92
$\Delta t = 0.13$	6.11	4.42	4.42
$\Delta t = 0.14$	7.84	3.78	3.78
$\Delta t = 0.15$	7.80	3.30	3.30
$\Delta t = 0.16$	7.36	2.88	2.88
$\Delta t = 0.17$	5.95	2.55	2.55
$\Delta t = 0.18$	4.50	2.16	2.16
$\Delta t = 0.19$	3.61	1.90	1.90
$\Delta t = 0.20$	3.00	1.80	1.80

Table 6. Largest t_c by FDM in quadruple precision($\varepsilon_0 = 0.1$)

	$n = 11$	$n = 101$	$n = 1001$
Δt	0.14	0.12	0.12
# iteration	56	42	41
t_c	7.84	5.04	4.92
Max. of exact sol.	2.52×10^8	2.52×10^5	1.63×10^5
Max. of numer. sol.	2.75×10^8	2.75×10^5	1.78×10^5
error	0.092	0.095	0.094

Next, numerical results under the more strict condition are shown. Here $\varepsilon_0 = 0.0001$. The numerical calculation have been executed by SCM in quadruple precision.

Table 7. t_c by SCM in quadruple precision($\varepsilon_0 = 0.0001$)

	$N = 10$	$N = 11$	$N = 12$	$N = 13$
$\Delta t = 1.0$	10.0	6.0	6.0	4.0
$\Delta t = 1.1$	12.1	8.8	8.8	5.5
$\Delta t = 1.2$	15.6	10.8	9.6	7.2
$\Delta t = 1.3$	20.8	14.3	11.7	9.1
$\Delta t = 1.4$	28.0	18.2	14.0	11.2
$\Delta t = 1.5$	36.0	24.0	16.5	13.5
$\Delta t = 1.6$	**54.4**	32.0	20.8	16.0
$\Delta t = 1.7$	39.1	42.5	27.2	20.4
$\Delta t = 1.8$	18.0	63.0	36.0	23.4
$\Delta t = 1.9$	9.5	**96.9**	47.5	30.4
$\Delta t = 2.0$	4.0	50.0	72.0	42.0
$\Delta t = 2.1$	2.1	25.2	111.3	54.6
$\Delta t = 2.2$	–	11.0	**129.8**	74.8
$\Delta t = 2.3$	–	4.6	64.4	121.9
$\Delta t = 2.4$	–	2.4	33.6	**252.0**
$\Delta t = 2.5$	–	–	17.5	170.0

Table 8. Largest t_c by SCM in quadruple precision($\varepsilon_0 = 0.0001$)

	$N_x, N_t = 10$	$N_x, N_t = 11$	$N_x, N_t = 12$	$N_x, N_t = 13$
Δt	1.6	1.9	2.2	2.4
# iteration	34	51	59	105
t_c	54.4	96.9	129.8	252.0
Max. of exact sol.	1.7401×10^{58}	6.6839×10^{103}	1.2329×10^{139}	1.0715×10^{270}
Max. of numer. sol.	1.7400×10^{58}	6.6846×10^{103}	1.2327×10^{139}	1.0716×10^{270}
error	8.07×10^{-5}	9.83×10^{-5}	9.90×10^{-5}	7.99×10^{-5}

Lastly, we show the numerical result by SCM in multiple precision. The number of collocation points $N = 10$. We can not use larger N from restriction of computing resources. $\varepsilon_0 = 0.0001$. Numerical calculation is executed in various digit numbers. Here, 16 and 34 digits correspond double and quadruple precisions, respectively. The calculation in multiple precision is the better compared with that in double or quadruple precisions.

Table 9: t_c by SCM in multiple precision($\varepsilon_0 = 0.0001$)

# digits	16	34	50	100	150	200	250	300	500	1000
$\Delta t = 1.0$	3.0	10.0	12.0	12.0	12.0	12.0	12.0	12.0	12.0	12.0
$\Delta t = 1.1$	3.3	12.1	22.0	45.1	50.6	50.6	50.6	50.6	50.6	50.6
$\Delta t = 1.2$	4.8	15.6	28.8	56.4	85.2	114.0	146.4	174.0	288.0	578.4
$\Delta t = 1.3$	6.5	20.8	37.7	75.4	113.1	148.2	191.1	227.5	375.7	**755.3**
$\Delta t = 1.4$	8.4	28.0	50.4	99.4	149.8	**200.2**	**254.8**	**303.8**	**429.8**	429.8
$\Delta t = 1.5$	12.0	36.0	69.0	**138.0**	**184.5**	184.5	184.5	184.5	184.5	184.5
$\Delta t = 1.6$	17.6	**54.4**	**83.2**	83.2	83.2	83.2	83.2	83.2	83.2	83.2
$\Delta t = 1.7$	**30.6**	39.1	39.1	39.1	39.1	39.1	39.1	39.1	39.1	39.1
$\Delta t = 1.8$	18.0	18.0	18.0	18.0	18.0	18.0	18.0	18.0	18.0	18.0
$\Delta t = 1.9$	9.5	9.5	9.5	9.5	9.5	9.5	9.5	9.5	9.5	9.5
$\Delta t = 2.0$	4.0	4.0	4.0	4.0	4.0	4.0	4.0	4.0	4.0	4.0

4 Another Approach Using Some Informations

Inverse problems can not be solved efficiently without any informations. Application of SCM without any informations spoils its advantage on accuracy. Then we consider an another approach using growth rate of the solution. Such approach is possible after simple simulation(e.g. low-order approximation).

The solution of Model Problem 1 is transformed by introducing a parameter λ as follows:

(17) $$\tilde{u}(x,t) = \exp(-\lambda t)\, u(x,t), \qquad \lambda > 0$$

Model Problem 1 is transformed to Model Problem $1''$:

Model Problem $1''$

(18) $$\frac{\partial \tilde{u}}{\partial t} = -\frac{\partial^2 \tilde{u}}{\partial x^2} - \lambda \tilde{u}, \qquad 0 < t, \qquad -1 < x < 1,$$

(19) $$\tilde{u}(x,0) = \cos\frac{\pi x}{2}, \qquad -1 < x < 1,$$

(20) $$\tilde{u}(-1,t) = 0, \qquad 0 \le t,$$

(21) $$\tilde{u}(1,t) = 0, \qquad 0 \le t.$$

The exact solution for Model Problem $1''$ is given as follows:

$$(22) \qquad \tilde{u}(x,t) = \exp\left(\left(\frac{\pi^2}{4} - \lambda\right)t\right)\cos\frac{\pi x}{2}, \qquad 0 \leq t, \qquad , -1 \leq x \leq 1.$$

We solve Model Problem $1''$ by SCM in quadruple precision. Numerical calculation is executed only for the first interval $[0, \Delta t]$. Numerical results are shown in Table 10. $\lambda = 0.0$ means no information on the solution. In case of $\lambda = 3.0$, error is small for various Δt. This approach is similar to elimination of singurality[4].

Table 10.   Error by SCM in quadruple precision

	$\lambda = 0.0$	$\lambda = 1.0$	$\lambda = 3.0$	$\lambda = 5.0$	$\lambda = 10.0$
$\Delta t = 0.01$	2.14×10^{-7}	2.14×10^{-7}	2.14×10^{-7}	2.14×10^{-7}	2.14×10^{-7}
$\Delta t = 0.02$	8.14×10^{-6}	8.35×10^{-6}	8.80×10^{-6}	9.26×10^{-6}	1.05×10^{-5}
$\Delta t = 0.05$	1.23×10^{-7}	1.23×10^{-7}	6.03×10^{-8}	6.03×10^{-8}	6.03×10^{-8}
$\Delta t = 0.1$	7.68×10^{-7}	9.01×10^{-7}	2.54×10^{-6}	3.50×10^{-6}	7.31×10^{-6}
$\Delta t = 0.2$	1.58×10^{-7}	2.15×10^{-7}	4.05×10^{-7}	7.63×10^{-7}	3.44×10^{-6}
$\Delta t = 0.5$	7.78×10^{-8}	1.70×10^{-7}	6.34×10^{-7}	3.40×10^{-7}	1.51×10^{-6}
$\Delta t = 1$	4.02×10^{-9}	1.75×10^{-9}	1.74×10^{-8}	1.63×10^{-7}	1.15×10^{-5}
$\Delta t = 2$	4.07×10^{-5}	3.87×10^{-8}	6.93×10^{-10}	4.49×10^{-7}	1.20×10^{-3}
$\Delta t = 5$	9.92×10^{-1}	1.45×10^{-6}	1.61×10^{-9}	4.27×10^{-4}	6.99×10^{-2}
$\Delta t = 10$	1.00	1.00	2.07×10^{-7}	1.56×10^{-2}	5.48×10^{-1}

5   Conclusion

We considered direct simulation to inverse problems along the strategy. It is based on the fact that for inverse problems if numerical methods give good local solutions then we should satisfy. To realize the strategy we used infinite-precision numerical simulation. It was applied to an inverse problem on the heat equation. Numerical results are relatively satisfactory. Moreover, numerical results using some informations on the solution were very satisfactory; however they were not obtained in multiple-precision. We confirmed necessity of such informations to inverse problems.

We have a plan to investigate more detailed simulation to this problem. We also have a plan to apply our approach to other inverse problems[6] and free boundary problem[5, 8].

References

[1] C. Canuto, et al., *Spectral Methods in Fluid Dynamics*, Springer-Verlag, 1988.

[2] A.S. Demidov, The form of a steady plasma subject to the skin effect in a tokamak with non-circular cross-section, *Nucl. Fusion*, 15, pp. 765-768(1975)

[3] G. Hammerlin, et al., *Improperly Posed Problems and Their Numerical Treatment*, Birkhäuser, 1983.

[4] H. Imai and H. Kawarada, One-Component Asymmetric Plasmas in a Symmetric Vessel, *Japan J. Appl. Math.*, 5(2), pp.173-186(1988)

[5] H. Imai, Y. Shinohara and T. Miyakoda, Application of Spectral Collocation Methods in Space and Time to Free Boundary Problems, *Hellenic European Research on Mathematics and Informatics '94(Ed. E.A. Lipitakis)*, Hellenic Mathematical Society, 2, pp.781-786(1994)

[6] H. Imai, Application of the Fuzzy Theory and Spectral Collocation Methods to an Ill-Posed Shape Design Problem With a Free Boundary, *Inverse Problems in Mechanics(Eds. S. Saigal and L.G. Olson)*, The American Society of Mechanical Engineers, 186, pp.103-107(1994).

[7] H. Imai, T. Takeuchi, H. Sakaguchi, Y. Shinohara and Tarmizi, On Numerical Simulation of Partial Differential Equations in Arbitrary Precision, *RIMS Kokyuroku*, Kyoto Univ., *1040*, pp.92-99(1998), in Japanese

[8] H. Imai, Y. Shinohara, T. Konno, M. Natori, W. Zhou, I. Ohnishi and Y. Nishiura, Numerical Computations of Free Boundary Problems in Quadruple Precision Arithmetic Using an Explicit Method, *Gakuto International Series*, 11, pp.193-207(1998).

[9] D. E. Knuth, *The Art of Computer Programming*, Addison-Wesley, 1981.

[10] D. M. Smith, A FORTRAN Package For Floating-Point Multiple-Precision Arithmetic, *Transactions on Mathematical Software*, 17, pp.273-283(1991).

[11] T. Takeuchi, H. Imai, Tarmizi, Y. Shinohara, H. Sakaguchi and T. Miyakoda, On Numerical Simulation of Partial Differential Equations in Arbitrary Precision, *Science International(Lahore)* 10(4), (1998), to appear

[12] A. N. Tikhonov and V. Y. Arsenin, *Solution of Ill-Posed Problems*, John Wiley & Sons, 1977.

On Multiple Precision Calculation of Eigenvalues and Eigenvectors of Matrices*

Masahiro KUSHIDA[1]   Hitoshi IMAI[2]   Toshiki TAKEUCHI[2]

[1]*Department of General Education, Anan College of Technology*
Tokushima, 774-0017, Japan

[2]*Faculty of Engineering, The University of Tokushima*
Tokushima, 770-8506, Japan

Abstract

In the paper, we performed multiple precision calculation of eigenvalues and eigenvectors of matrices by means of FORTRAN. The method is very traditional and it consists of the double-step QR algorithm and the inverse iteration. However, it is performed in multiple precision arithmetic by using the newest and free library on the net. Numerical results are satisfactory.

Key Words: eigenvalue, eigenvector, multiple precision

1   Introduction

Recently, progress in computing technology enables various numerical simulations. At the same time, we can easily use powerful computers. From such a background, we have already proposed numerical simulations of partial differential equations in infinite precision[1, 2], and showed its validity for some simple problems. However, we have to develop various libraries for its application to various problems.

In the paper, we developed FORTRAN subroutines for calculation of eigenvalues and eigenvectors in multiple precision. Numerical methods which are used here are traditional.

However, the newest and free libraries which are written in FORTRAN are used for multiple precision arithmetic. So, our subroutines realize facility of numerical calculation of eigenvalues and eigenvectors in multiple precision. They are easily improved to be faster by using the parallel computing environment.

2 Numerical Method

We used the double-step QR algorithm for computing eigenvalues to avoid complex calculation and we also used the inverse iteration method for computing eigenvectors. For multiple precision arithmetic we used the newest and free FORTRAN libraries on the net.

2.1 Double-step QR algorithm

The QR algorithm is widely used for computing the complete set of eigenvalues[3]. The basic QR algorithm to the matrix A starts with $A_0 = A$ and generates a sequence of matrices $\{ A_m \}$ by the following iteration:

$$A_{m-1} = Q_m R_m, \quad A_m = R_m Q_m.$$

That is, A_{m-1} is decomposed into factors Q_m and R_m, where Q_m is unitary and R_m is upper triangular.

It is easy to show that

$$A_m = Q_m^H A_{m-1} Q_m.$$

Thus all matrices in the sequence $\{A_m\}$ are unitarily similar and therefore have the same eigenvalues. The sequence $\{A_m\}$ converges to the upper-triangular form:

$$\begin{pmatrix} \lambda_1 & & & * \\ & \lambda_2 & & \\ & & \ddots & \\ 0 & & & \lambda_n \end{pmatrix}$$

where the eigenvalues appear on the main diagonal.

The shifted matrix $A - \sigma I$ has eigenvalues $\lambda_1 - \sigma, \lambda_2 - \sigma, \ldots, \lambda_n - \sigma$. The QR algorithm to $A - \sigma I$ can be described as

$$A_{m-1} - \sigma I = Q_m R_m, \quad A_m = R_m Q_m + \sigma I.$$

When we chose σ very close to λ_n, $|(\lambda_n - \sigma)/(\lambda_i - \sigma)|$ $(i \neq n)$ becomes close to zero. So, $a_{n1}^{(m)}, a_{n2}^{(m)}, \ldots, a_{nn-1}^{(m)}$, which are components of the n-th row of A_m:

$$A_m = \left(\begin{array}{ccc|c} & & & * \\ & \hat{A}_m & & \vdots \\ & & & * \\ \hline a_{n1}^{(m)} & \cdots & a_{nn-1}^{(m)} & a_{nn}^{(m)} \end{array} \right)$$

converge to zero very rapidly. When they are small enough, $a_{nn}^{(m)}$ can be considered to be an eigenvalue of A. The remaining eigenvalues of A are obtained from eigenvalues of $\hat{A}_m$. After repeating this procedure iteratively, we can obtain the complete set of eigenvalues of A.

For a non-symmetric matrix which has complex eigenvalues, we need a complex shift σ. Then a complex matrix appears in the procedure. This is not preferable.

We can avoid complex numbers by using the double-step QR algorithm. Consider a arbitrary pair of shifts σ_1 and σ_2 in the QR-decomposition

$$A_{m-1} - \sigma_1 I = Q_m R_m, \qquad A_m = R_m Q_m + \sigma_1 I,$$
$$A_m - \sigma_2 I = Q_{m+1} R_{m+1}, \quad A_{m+1} = R_{m+1} Q_{m+1} + \sigma_2 I.$$

Let

$$\hat{Q}_m = Q_m Q_{m+1}, \qquad \hat{R}_m = R_{m+1} R_m.$$

Then

$$\begin{aligned}
A_m &= R_m Q_m + \sigma_1 I \\
&= Q_m^H (A_{m-1} - \sigma_1 I) Q_m + \sigma_1 I \\
&= Q_m^H A_{m-1} Q_m,
\end{aligned}$$

$$\begin{aligned}
A_{m+1} &= Q_{m+1}^H A_m Q_{m+1} \\
&= Q_{m+1}^H Q_m^H A_{m-1} Q_m Q_{m+1} \\
&= \hat{Q}_m^H A_{m-1} \hat{Q}_m,
\end{aligned}$$

$$\begin{aligned}
(A_{m-1} - \sigma_2 I)(A_{m-1} - \sigma_1 I) &= (Q_m Q_m^H)(A_{m-1} - \sigma_2 I) Q_m R_m \\
&= Q_m (A_m - \sigma_2 I) R_m \\
&= Q_m Q_{m+1} R_{m+1} R_m \\
&= \hat{Q}_m \hat{R}_m.
\end{aligned}$$

The above calculation is reduced into the following two steps (Double-step QR algorithm):

$$\begin{cases} (A_{m-1} - \sigma_2 I)(A_{m-1} - \sigma_1 I) = \hat{Q}_m \hat{R}_m, \\ A_{m+1} = \hat{Q}_m^H A_{m-1} \hat{Q}_m. \end{cases}$$

Suppose σ_1 and σ_2 are eigenvalues of

$$\begin{pmatrix} a_{n-1\,n-1}^{(m-1)} & a_{n-1\,n}^{(m-1)} \\ a_{n\,n-1}^{(m-1)} & a_{n\,n}^{(m-1)} \end{pmatrix}.$$

As $\sigma_2 = \bar{\sigma}_1$, both $\sigma_1 + \sigma_2$ and $\sigma_1 \sigma_2$ are real. So, the right-hand side of the following equation:

$$(A_{m-1} - \sigma_2 I)(A_{m-1} - \sigma_1 I) = A_{m-1}^2 - (\sigma_1 + \sigma_2) + \sigma_1 \sigma_2 I$$

is real. Therefore, $\hat{Q}_m$ and $\hat{R}_m$ are real. Then A_{m+1} must be real.

Thus, in the double-step QR algorithm we can avoid complex calculation. The matrix A_m converges to the following form:

$$\left(\begin{array}{c|cc} \hat{A}_m & & * \\ \hline & & \\ 0 & a_{n-1\ n-1}^{(m-1)} & a_{n-1\ n}^{(m-1)} \\ & a_{n\ n-1}^{(m-1)} & a_{n\ n}^{(m-1)} \end{array}\right) .$$

The eigenvalues of the lower right block satisfy

$$\lambda^2 - (a_{n-1\ n-1}^{(m-1)} + a_{n\ n}^{(m-1)})\lambda + a_{n-1\ n-1}^{(m-1)}a_{n\ n}^{(m-1)} - a_{n-1\ n}^{(m-1)}a_{n\ n-1}^{(m-1)} = 0.$$

The remaining eigenvalues of A are obtained from eigenvalues of $\hat{A}_m$. After repeating this procedure iteratively, we can obtain the complete set of eigenvalues of A.

Before starting the double-step QR algorithm, balancing of a matrix and transformation into the upper Hessenberg form by similarity transformation are necessary.

2.2   Inverse Iteration

We can get eigenvectors by use of the power method.

Let $\lambda_1, \lambda_2, \ldots, \lambda_n$ ($|\lambda_1| > |\lambda_2| > \cdots > |\lambda_n|$) be eigenvalues of a matrix A associated with eigenvectors $z_1, z_2, \ldots, z_n$. Start with an arbitrary vector x_0 and generate the sequence $\{x_m | x_m = A^m x_0\}$.

From the assumption $\lambda_i \neq \lambda_j$ ($i \neq j$), $z_1, z_2, \ldots, z_n$ are bases of C^n. So,

$$x_0 = c_1 z_1 + c_2 z_2 + \cdots + c_n z_n.$$

Then

$$\begin{aligned} A^m x_0 &= c_1 \lambda_1^m z_1 + c_2 \lambda_2^m z_2 + \cdots + c_n \lambda_n^m z_n \\ &= \lambda_1^m \left(c_1 z_1 + c_2 \left(\frac{\lambda_2}{\lambda_1}\right)^m z_2 + \cdots + c_n \left(\frac{\lambda_n}{\lambda_1}\right)^m z_n \right) . \end{aligned}$$

From the fact that $|\lambda_1| > |\lambda_i|$ ($i = 2, 3, \ldots, n$), it follows that $\left(\frac{\lambda_i}{\lambda_1}\right)^m \to 0$ as $m \to \infty$. Then x_m converges to the vector parallel to the eigenvector z_1. The rate of convergence is $\frac{\lambda_2}{\lambda_1}$.

When the matrix A has eigenvalues $\lambda_1, \lambda_2, \ldots, \lambda_n$ ($|\lambda_1| > |\lambda_2| > \cdots > |\lambda_n|$), and eigenvectors $z_1, z_2, \ldots, z_n$, A^{-1} has eigenvalues $\frac{1}{\lambda_1}, \frac{1}{\lambda_2}, \ldots, \frac{1}{\lambda_n}$ ($\frac{1}{|\lambda_n|} > \cdots > \frac{1}{|\lambda_2|} > \frac{1}{|\lambda_1|}$) associated with eigenvectors $z_1, z_2, \ldots, z_n$. So, the power method applied to A^{-1} obtains the eigenvector z_n. The rate of convergence is $\frac{1}{\lambda_{n-1}} / \frac{1}{\lambda_n} = \frac{\lambda_n}{\lambda_{n-1}}$. This method is called the inverse iteration.

The shifted matrix $A - \sigma I$ has eigenvalues $\{\lambda_i - \sigma\}$ associated with eigenvectors $\{z_i\}$. The inverse iteration applied to $A - \sigma I$ finds the eigenvector z_k associated with λ_k which is

the nearest eigenvalue to σ. The rate of convergence is $\dfrac{\lambda_k - \sigma}{\lambda_l - \sigma}$, where $\lambda_l - \sigma$ is the second smallest eigenvalue of $A - \sigma I$.

When σ is a good approximation of λ_k, $\lambda_k - \sigma$ is very close to zero. So, the shifted inverse iteration converge very quickly. We can adopt σ from the eigenvalues by the double-step QR algorithm. In practical calculation , we solve the linear system

$$Ax_m = x_{m-1}$$

instead of

$$x_m = A^{-1} x_{m-1}.$$

2.3   Multiple precision subroutine

A lot of FORTRAN subroutines about multiple precision arithmetic [4] are already known. We used the library FMLIB by Daivd M. Smith which is distributed on the net[5].

FMLIB is a package of FORTRAN subroutines for floating-point multiple precision arithmetic and it involves elementary functions. We can perform multiple precision arithmetic as follows.

1. Replace operators in the original FORTRAN program with FM subroutines.
2. Declare common blocks /FMUSER/, /FM/, /FMBUFF/, and /FMSAVE/.
3. Initialize several variables by calling a subroutine FMSET with demanding precision.

3   Model Problems

To evaluate our subroutines we consider the following two model problems. These problems are well-known to be difficult.

3.1   Hilbert Matrix

At first, the following Hilbert Matrix is considered:

$$\begin{pmatrix} 1 & 1/2 & 1/3 & \cdots & 1/n \\ 1/2 & 1/3 & 1/4 & \cdots & 1/(n+1) \\ 1/3 & 1/4 & 1/5 & \cdots & 1/(n+2) \\ \vdots & \vdots & \vdots & \ddots & \vdots \\ 1/n & 1/(n+1) & 1/(n+2) & \cdots & 1/(2n-1) \end{pmatrix}.$$

As the Hilbert matrix is symmetric, its eigenvalues are all real. However, it is known that the matrix has a large condition number $\mathbf{cond}A = ||A|| \cdot ||A^{-1}|| = \dfrac{|\lambda_1|}{|\lambda_n|}$. So, numerical computation is difficult.

3.2 Perturbation

Suppose A and B are following $n \times n$ matrices:

$$A = \begin{pmatrix} 0 & 1 & & & \\ & \ddots & \ddots & & \text{\Large 0} \\ & & & \ddots & 1 \\ \text{\Large 0} & & & & 0 \end{pmatrix}, \qquad B = \begin{pmatrix} 0 & 1 & & & \\ \vdots & \ddots & \ddots & & \text{\Large 0} \\ 0 & & & \ddots & 1 \\ \varepsilon & 0 & \cdots & & 0 \end{pmatrix}.$$

A has a n-tuple eigenvalue $\lambda_{A0} = 0$, and B has eigenvalues $\lambda_{Bk} = \sqrt[n]{\varepsilon}(\cos \dfrac{2k\pi}{n} + i\sin \dfrac{2k\pi}{n})$ $(k = 0, 1, \ldots, n-1)$. When $\|B - A\| = \varepsilon$ is small and n is large, difference $|\lambda_{Bk} - \lambda_{A0}| = \sqrt[n]{\varepsilon}$ is relatively large. In this case, it is difficult to compute eigenvalues.

In general, when $\|B - A\|$ is small, $\lambda_B - \lambda_A \sim \dfrac{{}^t y (B - A) x}{{}^t y x}$. Here, λ_A and λ_B are eigenvalues of A and B, respectively. x and y are right and left unit eigenvectors of A related with λ_A, respectively. It follows $|\lambda_B - \lambda_A| \leq \dfrac{\|B - A\|}{|{}^t y x|}$. If ${}^t y x = \cos \theta$ (θ is the angle between x and y) is small, $|\lambda_B - \lambda_A|$ may be large.

In the above case, the right eigenvector x and the left eigenvector y associated with $\lambda_{B0} = \sqrt[n]{\varepsilon}$ are following:

$$x = \frac{1-\varepsilon}{1 - \sqrt[n]{\varepsilon}}(1, \lambda, \lambda^2, \cdots, \lambda^{n-1})^T, \qquad y = \frac{1-\varepsilon^{-1}}{1 - \sqrt[n]{\varepsilon^{-1}}}\left(1, \frac{1}{\lambda}, \frac{1}{\lambda^2}, \cdots, \frac{1}{\lambda^{n-1}}\right)^T.$$

The values of $\cos \theta$ for several n and ε are shown in Table.1. These small values of $\cos \theta$ are not preferable.

Table. 1: $\cos \theta$ for n and ε

n	ε	$\cos \theta$	n	ε	$\cos \theta$
10	1E-01	6.75E-02	100	1E-01	6.55E-03
10	1E-10	8.10E-09	100	1E-10	5.33E-10
10	1E-20	9.80E-18	100	1E-20	2.16E-19

4 Numerical results

4.1 Hilbert matrix

We compute the eigenvalues of the 100×100 Hilbert matrix in double precision and multiple precision with 300 significant digits.

The result computed in double precision is shown in Table.2. As the Hilbert matrix is symmetric, all the eigenvalues must be real. However, 64 eigenvalues are complex. In addition, $\lambda_{17} \sim \lambda_{100}$ seem to be unnatural, because their magnitude is almost same.

Table. 2: Eigenvalues of the Hilbert matrix in double precision

matrix size: $n=100$

	Real part	Imaginary part
λ_1	0.218269609775742E+01	0.000000000000000E+00
λ_2	0.821445560556198E+00	0.000000000000000E+00
λ_3	0.218595882370696E+00	0.000000000000000E+00
$\vdots$	$\vdots$	$\vdots$
λ_{15}	0.456986377749665E−10	0.000000000000000E+00
λ_{16}	0.521223882655702E−11	0.000000000000000E+00
λ_{17}	0.100217547714874E−12	0.192798275536923E−17
λ_{19}	0.107363474464636E−12	0.143209038847983E−17
λ_{21}	0.110942509461211E−12	0.000000000000000E+00
$\vdots$	$\vdots$	$\vdots$
λ_{98}	0.930601959363224E−13	0.000000000000000E+00
λ_{99}	0.613157780640225E−14	0.000000000000000E+00
λ_{100}	0.630907998468590E−15	0.000000000000000E+00

Table. 3: Eigenvalues of the Hilbert matrix in multiple precision

matrix size: $n=100$ # digits = 300

λ_1	2.1826960E +0	λ_{26}	2.6173449E−22	λ_{51}	3.2340872E−54	λ_{76}	2.3887789E −95
λ_2	8.2144556E −1	λ_{27}	2.0250747E−23	λ_{52}	1.1330678E−55	λ_{77}	3.1234093E −97
λ_3	2.1859588E −1	λ_{28}	1.5166509E−24	λ_{53}	3.8408823E−57	λ_{78}	3.8765971E −99
λ_4	4.9292251E −2	λ_{29}	1.0997826E−25	λ_{54}	1.2593740E−58	λ_{79}	4.5588509E−101
λ_5	1.0031812E −2	λ_{30}	7.7233052E−27	λ_{55}	3.9929580E−60	λ_{80}	5.0696739E−103
λ_6	1.8850632E −3	λ_{31}	5.2536401E−28	λ_{56}	1.2237932E−61	λ_{81}	5.3195286E−105
λ_7	3.3086781E −4	λ_{32}	3.4621983E−29	λ_{57}	3.6244390E−63	λ_{82}	5.2538963E−107
λ_8	5.4645302E −5	λ_{33}	2.2107547E−30	λ_{58}	1.0368774E−64	λ_{83}	4.8711734E−109
λ_9	8.5362805E −6	λ_{34}	1.3679747E−31	λ_{59}	2.8641142E−66	λ_{84}	4.2268760E−111
λ_{10}	1.2661665E −6	λ_{35}	8.2036351E−33	λ_{60}	7.6355256E−68	λ_{85}	3.4211009E−113
λ_{11}	1.7887224E −7	λ_{36}	4.7682332E−34	λ_{61}	1.9636724E−69	λ_{86}	2.5727901E−115
λ_{12}	2.4126491E −8	λ_{37}	2.6862998E−35	λ_{62}	4.8692490E−71	λ_{87}	1.7899102E−117
λ_{13}	3.1133493E −9	λ_{38}	1.4669365E−36	λ_{63}	1.1635461E−72	λ_{88}	1.1461868E−119
λ_{14}	3.8502295E−10	λ_{39}	7.7648552E−38	λ_{64}	2.6778314E−74	λ_{89}	6.7162863E−122
λ_{15}	4.5698647E−11	λ_{40}	3.9839826E−39	λ_{65}	5.9318818E−76	λ_{90}	3.5764767E−124
λ_{16}	5.2122262E−12	λ_{41}	1.9813085E−40	λ_{66}	1.2639324E−77	λ_{91}	1.7165587E−126
λ_{17}	5.7190022E−13	λ_{42}	9.5503168E−42	λ_{67}	2.5886262E−79	λ_{92}	7.3519486E−129
λ_{18}	6.0423965E−14	λ_{43}	4.4615596E−43	λ_{68}	5.0921195E−81	λ_{93}	2.7753614E−131
λ_{19}	6.1525525E−15	λ_{44}	2.0198685E−44	λ_{69}	9.6129590E−83	λ_{94}	9.0907113E−134
λ_{20}	6.0420119E−16	λ_{45}	8.8610078E−46	λ_{70}	1.7400590E−84	λ_{95}	2.5311009E−136
λ_{21}	5.7263067E−17	λ_{46}	3.7662991E−47	λ_{71}	3.0172384E−86	λ_{96}	5.8243350E−139
λ_{22}	5.2407021E−18	λ_{47}	1.5508081E−48	λ_{72}	5.0067135E−88	λ_{97}	1.0634224E−141
λ_{23}	4.6339730E−19	λ_{48}	6.1850682E−50	λ_{73}	7.9417696E−90	λ_{98}	1.4443909E−144
λ_{24}	3.9606773E−20	λ_{49}	2.3888963E−51	λ_{74}	1.2027870E−91	λ_{99}	1.2973462E−147
λ_{25}	3.2735442E−21	λ_{50}	8.9336950E−53	λ_{75}	1.7370402E−93	λ_{100}	5.7797008E−151

The result in multiple precision is shown in Table.3. All the eigenvalues are real . From this result, the condition number $\mathbf{cond}A = ||A|| \cdot ||A^{-1}|| = \dfrac{|\lambda_1|}{|\lambda_n|}$ is about 10^{150}. From these two results, double precision is not proper to this case. Multiple precision is necessary for the Hilbert matrices with large dimension.

Mathematica is widely used for algebraic calculation. We compared our results with Mathematica's results. However, Mathematica 3.0 could not get algebraically eigenvalues of matrices whose dimensions are greater than 12 in reasonable time. So we used Mathematica's numeric mode and measured computation time(Table.4). PC used here is equipped with Pentium II 300MHz CPU and 224 MB memory.

Table. 4: Computational time

FORTRAN Program   (sec)

Precision (# digits)	Dimension n			
	10	20	100	200
Double Precision	0	0	0	3
100	0	1	90	1323
200	0	3	186	1897
300	1	5	340	2578

Mathematica   (sec)

Precision (# digits)	Dimension n			
	10	20	100	200
15	0	0	1	4
100	0	2	138	1385
200	1	4	222	1672
300	1	6	361	2445

FORTRAN program is not so slow. This means it is superior both in facilities and in improvement on speed by parallelization.

4.2 Perturbation

We compute eigenvalues of the perturbed matrix B for $n = 100$, $\varepsilon = 10^{-20}$, and compare with the exact eigenvalues $\lambda_k = 10^{-\frac{20}{100}}(\cos\dfrac{2k\pi}{100} + i\sin\dfrac{2k\pi}{100})$ computed by Mathematica 3.0.

Table. 5: Eigenvalues of the perturbed matrix B in double precision

matrix size: $n = 100$, $\varepsilon = 1E - 20$

	Real part	Imaginary part
λ_1	0.6309@701763531598	0.000000000000000@
λ_2	0.6297@515968499192	0.0396@3719563725086
λ_3	0.6259@450172025149	0.079@15440946703962
λ_4	0.619@6797828387999	0.118@1638305383951
$\vdots$	$\vdots$	$\vdots$
λ_{23}	0.118@3960020963865	0.619@9558071208230
λ_{24}	0.07@896951553309539	0.62@61205138493846
λ_{25}	0.039@47718337829974	0.629@6808384037713
λ_{26}	-0.0000@4873355560028325	0.630@7801471677452
$\vdots$	$\vdots$	$\vdots$

Table. 6: Eigenvalues of the perturbed matrix B in multiple precision

matrix size $n = 100$, $\varepsilon = 1E - 20$, # digits=300

λ_1	Re:0.6309573444801932494343601366223438646729452571882287245277295288334949432977686 80757291406774365226487327346730988364659067642396464880448569818546555924659850 36241859191339523915193186595632068892720998767238331147096889970166794020026058 48115012327035845249311315549845097992743041198103120640@952408
	Im:0.00000000000000000000000000000000000000000000000000000000000000000000000000000000000000 00000000000000000000000000000000000000000000000000000000000000000000000000000000000000000000 00000000000000000000000000000000000000000000000000000000000000000000000000000000000000000000 00000000000000000000000000000000000000000000000000000000000000000@
λ_2	Re:0.6297122942893572169864932971530560393503258402569549269068573251357094777785915 60148630667904388074737180685546540687471304439885790375919317854457189325671847 55877254610235617371439057342093103816616321763013272464537732643672000708031450 54248239322523280535633142956529859558014162809010850078 8@52150
	Im:0.0396181394607472815191511193681085575203658333800090396581737454138386948237809 11970865266265717350921704570224804179053767685434224321663821793122701304710785 40696786691783067475296510408927145885846112051960083386877021420217021970983004 67914108411481330268104387103913851309999381928379471693@7081351
$\vdots$	$\vdots$
λ_{25}	Re:0.0396181394607472815191511193681085575203658333800090396581737454138386948237809 11970865266265717350921704570224804179053767685434224321663821793122701304710785 40696786691783067475296510408927145885846112051960083386877021420217021970983004 67914108411481330268104387103913851309999381928379471693@4938175
	Im:0.6297122942893572169864932971530560393503258402569549269068573251357094777785915 60148630667904388074737180685546540687471304439885790375919317854457189325671847 55877254610235617371439057342093103816616321763013272464537732643672000708031450 54248239322523280535633142956529859558014162809010850078 8@81210
λ_{26}	Re:-0.00000000000000000000000000000000000000000000000000000000000000000000000000000000000000 00000000000000000000000000000000000000000000000000000000000000000000000000000000000000000000 00000000000000000000000000000000000000000000000000000000000000000000000000000000000000000000 00000000000000000000000000000000000000000000000000000000000@75578874627077156696
	Im:0.6309573444801932494343601366223438646729452571882287245277295288334949432977686 80757291406774365226487327346730988364659067642396464880448569818546555924659850 36241859191339523915193186595632068892720998767238331147096889970166794020026058 48115012327035845249311315549845097992743041198103120640 7@51620
$\vdots$	$\vdots$

The result in double precision is shown in Table.5. The mark '@' shows the first position where the digit of the computed eigenvalue differs from that of the exact eigenvalue.

The result in multiple precision with 300 digits is shown in Table.6. Over 290 digits coincide with those of the exact value. The result is satisfactory.

This case also shows multiple precision is necessary to get the accurate eigenvalues.

5 Conclusion

We developed FORTRAN subroutines for calculation of eigenvalues and eigenvectors in multiple precision and applied to some ill-conditioned matrices. Numerical methods which are used here are traditional. However, the newest and free libraries which are written in

FORTRAN are used for multiple precision arithmetic. Numerical results are very satisfactory. Moreover, our subroutines realize such advanced calculation on PC. They are easily improved to be faster by using the parallel computing environment which can be easily realized by the technology PVM[8].

In the near future, our subroutines are used in infinite numerical simulation[1, 2].

References

[1] T. Takeuchi, H. Imai, Tarmizi, Y. Shinohara, H. Sakaguchi and T. Miyakoda. "On Numerical Simulation of Partial Differential Equations in Arbitrary Precision" *Science International(Lahore)* Vol.10 No.4 (1998)

[2] H. Imai, T. Takeuchi, H. Sakaguchi, Y. Shinohara and Tarmizi. "On Numerical Simulation of Partial Differential Equations in Arbitrary Precision" *RIMS Kokyuroku, Kyoto Univ.* Vol.1040 (1998) ,in Japanese

[3] D. S. Watkins. *Fundamentals of Matrix Computations.* John Wiley & Sons (1991)

[4] D. E. Knuth. *The Art of Computer Programming.* Addison-Wesley (1981)

[5] D. M. Smith. "A FORTRAN Package For Floating-Point Multiple-Precision Arithmetic". *Transactions on Mathematical Software.* 17 (1991)

[6] A. Ralston, P. Rabinowitz. *A First Course in Numerical Analysis.* McGraw-Hill. (1978)

[7] J. H. Wilkinson. *Rounding Errors in Algebraic Processes.* Her Britannic Majesty's Stationery Office. (1963)

[8] A. Geist et al. . *PVM: Parallel Virtual Machine.* The MIT Press. (1994)

偏微分方程式汎用数値計算プログラム構築の試み

Unified Algorithm for Partial Differential Equations
and
Examples of Numerical Computation

文部省核融合合科学研究所　　渡辺二太

WATANABE Tsuguhiro
National Institute for Fusion Science

Abstract

A new unified algorithm is proposed to solve partial differential equations which describe nonlinear boundary value problems, eigenvalue problems and time developing boundary value problems. The algorithm is composed of implicit difference scheme and multiple shooting scheme and is named as HIDM (Higher order Implicit Difference Method). A new prototype computer programs for 2-dimensional partial differential equations is constructed and tested successfully to several problems. Extension of the computer programs to 3 or more higher order dimension problems will be easy due to the direct product type difference scheme.

Keywords: partial differential equation, implicit difference scheme, multiple shooting scheme, eigenvalue problem, evolutionary problem

1　序

プラズマ・核融合研究で直面する問題の解決には多次元空間で記述されている偏微分方程式を解くことが, しばしば, 必要となる. プラズマの平衡を解く問題は偏微分方程式で記述された境界値問題を解く問題に帰着される. 通常この境界値問題は平衡を規定する未定の定数を含むので, 非線形固有値問題の性質も抱えている. 平衡状態にあるプラズマの安定性を解析する問題は典型的な固有値問題であり, また, プラズマの効率的高周波加熱法を特定するためにも固有値問題の数値解析を必要とする. プラズマを生成・加熱し, 各種の輸送過程による粒子損失, エネルギー散逸を取り入れながらプラズマの大局的挙動を予測するには, 時間発展境界値問題の数値計算を行わなければならない. プラズマは各種の不安定性を内包しているので, この数値計算には線形不安定な場合でも正しく計算ステップを刻むことのできるアルゴリズムを必要とする.

上記を背景とし, 偏微分方程式に対する新しいあリゴリズムを構築した. このときには,

- 常微分方程式 (初期値問題) 並みの容易さで偏微分方程式を解けるようにしたい.
- 多次元問題への拡張が容易な計算手続きで実現したい.
- 多重並列処理可能な計算手続きで実現したい.
- 線形不安定な非線形問題の時間発展も追跡可能な計算手続きで実現したい.

等の要求を実現できることを目標とした.

1 次元問題 (常微分方程式) の場合には, 陰的差分化技法とトーナメント式多分割シューティング法式との組み合わせで構築されたプログラム (HIDMAS [1], HIDMEG [2], [3]) は,

- 初期値問題
- 非線形境界値問題
- 固有値問題

等に対してほぼ満足すべき性能の発揮できることを実証してきた．初期値問題に対しては，微分代数方程式で記述されている場合，固い微分方程式の場合，シンプレクティックな特質を要求される場合等にも適用できることが示されている [3]．境界値問題を解くプログラムは，LHD の密度計測を念頭に置いた，シア磁場中プラズマにおけるマイクロ波の線形モード変換の数値解析にも成功している [4].

陰的差分化技法とトーナメント式多分割シューティング法式との組み合わせで構築されたプログラム (非線形境界値問題を解くプログラム) に手を加え 1 次元境界値問題の時間発展を記述する方程式 (独立変数が (x, t) である偏微分方程式) を解くプログラム HIDMTD([5], [6], [7], [8]) が開発されている．HIDMTD は，高電力マイクロ波発生装置の解析に適用され ([6], [7]) ，さらに，線形不安定なシステムでも時間ステップ幅可変で計算可能なことを実証した [8].

HIDMTD を 2 次元境界値問題を解けるようにすること，あるいは，より一層の多次元空間で記述された偏微分方程式にも適用可能であるものに拡張する試みには成功しなかった．そこで今回は，多次元化実現を第 1 の目標として新たな計算手続きを組み立てた．

HIDMEG および HIDMTD は，微分代数方程式にも適用可能であることを目的として，区間端点 (両端) の高階微係数も用いる差分化技法を採用した ([2], [3])．このことが多次元化を進める上での壁となった．よってここでは，格子点上の関数値のみを用いる差分化技法を採用する．HIDMEG および HIDMTD で実証された陰的差分化技法と多分割シューティング法の組み合わせはそのまま踏襲する．

偏微分方程式はその構造によって数学的特性が大きく異なる．例えば，初期値問題として設定される双曲型偏微分方程式には特性曲線によって決定される影響域，依存域が存在し，境界条件の設定にはこれらのことを考慮に入れなければならない．滑らかな初期条件から出発しても時間の経過につれて不連続解に到達することもある．これに対して，楕円型偏微分方程式は，通常，閉じた領域内で解が一意に決定され領域内の全ての関数値が互いに関連しあっている．楕円型偏微分方程式が初期値問題として定式化されることはない．多様な数学的特性を内包する偏微分方程式を対象とする汎用プログラムを構築するための方策は 3 点に要約される．

(1) 人工的粘性項等を内包せず，且つ，数値不安定性を引き起こすことのない高精度差分化技法の採用．

(2) シューティング法による境界条件への高い適応性の確保．

(3) シューティング法に伴う数値発散を回避するための多重分割法の併用．

局所的差分化誤差が如何に小さくても数値不安定が発生する状況の下では，数値計算結果は，たちまちにして，真の解とは無縁のものとなる．逆に，数値不安定等が発生せず，且つ人工粘性項等を含まぬ高精度差分化方程式の解が得られたならば，もとの偏微分方程式の解に十分近いものと期待する．方策 (1) を実現するには陰的差分化技法の採用が必然と思われる．陽的差分化技法を採用するときには,CFL(Courant-Friedrics-Lewy) 条件に代表される強い制約を受け，さらに数値粘性項等の導入が普遍的に行われる．このようなことでは，多様な型の偏微分方程式を適用対象とする汎用プログラムの構築はできない．

具体的問題に対面したときには，境界条件の設定方法が問題解決の鍵という場合も多々ある．このようなときには種々の境界条件を試行錯誤的に採用し数値計算する必要性に迫られる．このような状況に対応するには，境界の関数値および微分値で書き下された境界条件に即座に対応可能なプログラムとなっている必要がある．方策 (2) に記したように，シューティング法であるならばこのような汎用プログラムの作成が可能である．

シューティング法では境界の格子点上の関数値 (あるいは微分値) のパルスが境界上の他の地点にどのように伝搬するかを数値的に解く必要がある．この計算を汎用的に行うには，全ての場合を機械的に初期値問題として解くのが簡便である．このときには不適切条件 (ill posed condition) のもとで，方程式を解くことも要求される．双曲型偏微分方程式では，依存関係の存在しない 2 点間のパルス伝達を解く必要にも直面する．これらのときには数値計算は急速な成長と 1 格子毎の振動を繰り返す解となるので，あまりに遠い 2 点をシューティングの対象とすることはできない．このため方策 (3) が必然である．また，方策 (3) は，今後急速な発展が見込まれる多重並列処理計算機による高速処理に適していることも期待できる．

第 2 節では HIDM の採用する陰的差分化技法について述べる．第 3 節では HIDM のアルゴリズムで組

み立てられた2独立変数の偏微分方程式の汎用数値計算プログラム HIDM2D の概要を記す. HIDM2D の数値計算例は第4節, まとめと討論は第5節に記す.

2 HIDM の陰的差分化技法
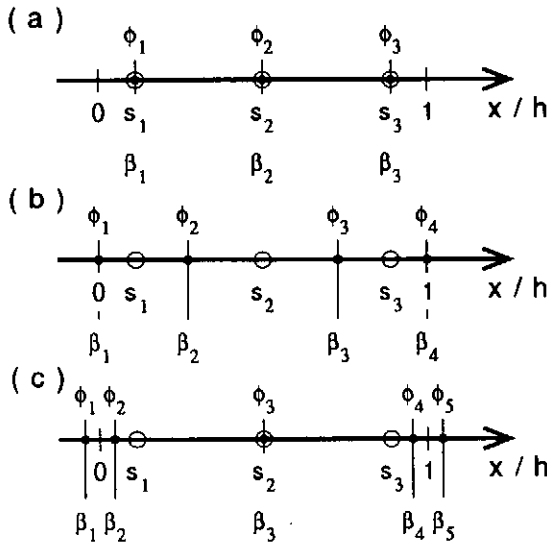
Fig.1 HIDM の差分化技法: 微分方程式を解く地点 (分点) を白抜きの ○ で記し, 微分方程式の解の関数値が埋め込まれている地点 (格子点) を小さな黒丸 ● で記す. (a) は代数方程式で解が決定される場合 (階数 $r = 0$) を示し, (b) は1階微分方程式で解が決定される場合 (階数 r=1) を示し, (c) は2階微分方程式で解が決定される場合 (階数 $r = 2$) を示している. 連立微分方程式の場合は階数の異なる関数が混在するので, 微分方程式を解く地点の位置 (図の s_1, s_2, s_3) は共通である. 関数値 (ϕ_i, $\{i = 1, 2, \cdots m\}$) が埋め込まれる格子点位置 (β_i, $\{i = 1, 2, \cdots m\}$) は変数の階数に応じて, 個数も位置も異なる.

微分方程式を解くには関数値から微分値を表現する表式 — 差分化表現 — が必要である. 常微分方程式を対象として, HIDMEG および HIDMTD は区間端点 (両端) の高階微係数も用いる差分化技法を開発してきた. しかしながら, 区間端点の高階微係数も用いる差分化技法を, 独立変数が2個以上となる偏微分方程式に適用可能な形に拡張する簡単・明瞭な手続きは見いだすことができない. よってここでは, 多次元化の実現を第一目標として, 関数値のみを用いる差分化技法を採用しよう. 簡単のため, 説明は独立変数が1個の場合について行う (独立変数を

x と記す). 階数 r の常微分方程式

$$L(\phi(x), \phi'(x), \cdots, \phi^{(r)}(x), x) = 0 \qquad (1)$$

を $x = 0$ から $x = h$ まで解くことを考える. 但し, h は積分の1ステップ幅を表し, この範囲内では解 $\phi(x)$ の変化は充分に小さく, この区間内の関数は $x = 0$ でのテーラ展開級数で近似できると仮定する. 階数 r の常微分方程式は初期値として, r 個の独立な条件を任意に設定できるので, $\phi(h)$ を計算するための必要な格子点数 m と方程式を解く地点 (以下では分点と記す) の個数 n との間には

$$m = n + r \qquad (2)$$

の関係が必要である (Fig.1). なお, 微分方程式の解となる関数値の埋め込まれる離散点を格子点と称する. n 個の微分方程式と r 個の初期条件で m 個の格子点上の関数値を数値的に解く. この m 個の格子点を抱える区間 $0 \le x \le h$ を以下では単位胞と称する. HIDM は単位胞内の少数格子点上の関数値をニュートン法で解くので, 陰的差分法に原因する計算負荷は高くない. 単位胞を適当個数並べて1個のブロックと称し, ブロックの集合で全計算領域が構成される. ブロック境界での滑らかな接続と境界条件を満足させる手続きはシューティング法で構成される.

常微分方程式の場合は1階の微分方程式を対象にした計算プログラムを用意すれば高階の微分方程式に対しても直ちに対応可能である. 高階微分を新しい変数に置き換えれば簡単に1階微分方程式に帰着できる. しかしながら独立変数が2個以上となる偏微分方程式の場合にはこのような (高階微分方程式を1階の微分方程式に帰着する) 手続きは自明ではない. また, 新しい変数を導入して1階の微分方程式に帰着した場合でも, 高階の微分方程式を直接解いた場合よりも, 計算効率の点で劣ると思われる. よってここでは2階の微分方程式で決定される方程式も直接解くことを念頭に置く差分化技法を展開する. 多くの物理システムは2階の微分方程式で記述されている.

通常, 解くべき方程式には複数個の未知関数が含まれており, それらの階数は多様である. よって, 微分方程式を解く地点 (分点) は変数の階数とは独立に設定されている. 分点を s_i, $\{i = 1, 2, \cdots, n\}$) と記す. n が打ち切り誤差精度 (次数) を決定する. 微分方程式を解く地点 ($= sh$ と記す) の関数値と微分値を,

$$\phi''(sh) = \frac{1}{h^2}\sum_{j=1}^{m} E_j(s)\phi(\beta_j h) + Tr_2 , \quad (3)$$

$$\phi'(sh) = \frac{1}{h}\sum_{j=1}^{m} D_j(s)\phi(\beta_j h) + Tr_1 , \quad (4)$$

$$\phi(sh) = \sum_{j=1}^{m} C_j(s)\phi(\beta_j h) + Tr_0 , \quad (5)$$

と表現する $(Tr_2, Tr_1, Tr_0$は打ち切り誤差を表し以下の議論では無視する). 打ち切り誤差がもっとも大きくなる $r = 2$ の場合の$\phi''(sh)$ を考察する. (3)式の右辺を $x = sh$ の周りでテーラ展開すると次の関係式を得る.

$$\delta_{k,2} = \sum_{j=1}^{m} E_j(s)\frac{(\beta_j - s)^k}{k!} , \quad (k = 0, 1, \cdots, m)$$
$$(6)$$

$$Tr_2 = \sum_{j=1}^{m} E_j(s)\frac{(\beta_j - s)^{m+1}}{(m+1)!}h^{m-1} + (O(h^m)) \quad (7)$$

方程式 (6) の左辺の δ はクロネッカーのデルタである. (6) の $k = 0, 1, \cdots, m-1$ を連立させれば, E_j, $\{j = 0, 1, \cdots, m\}$ を s, β_j で表す表式が得られる. この, E_j, $\{j = 1, 2, \cdots, m\}$ を残された最後の関係式 (連立方程式 (6) における $k = m$ の式) に代入すると s と β_j に関する代数方程式が導かれる. 例えば, $n = 3$ の場合は

$$\left.\begin{array}{rcl} \beta_1 &=& -\sqrt{(10s^2 - 10s + 1)/6} \\ \beta_2 &=& \sqrt{(10s^2 - 10s + 1)/6} \\ \beta_3 &=& 1/2 \\ \beta_4 &=& 1 - \sqrt{(10s^2 - 10s + 1)/6} \\ \beta_5 &=& 1 + \sqrt{(10s^2 - 10s + 1)/6} \end{array}\right\} \quad (8)$$

但し, ここでは数値計算の対称性の観点から積分ステップの中間地点は自動的に格子点, 分点に設定されるとし上記の s は中間点以外の分点を表す $(s \neq 1/2)$. さらに, 効率的数値計算実行の観点から, $\beta_1 = -\beta_2$, $\beta_4 = 1 + \beta_1$, $\beta_5 = 1 + \beta_2$ を要請して決定した. このときには, 当該ステップで計算されたϕ_4, ϕ_5 が次のステップのϕ_1, ϕ_2 の値に利用できるからである. この時点では分点 s には自由度が残されているが, この自由度を用いて打ち切り誤差に対する精度をさらに高めることはできない. また, $\beta_2 = s$ が成立すると偏微分方程式を解くことが不可能となる場合が発生するので,

$$0 < \beta_2 < s$$

すなわち,

$$0.1043\cdots = \frac{5 - \sqrt{21}}{4} < s < \frac{5 - \sqrt{15}}{10} = 0.1127\cdots$$
$$(9)$$

の条件が必要である. β_2 があまりに 0 に近いと丸め誤差の影響が厳しくなるので, 以下では $s = 1/9$, すなわち, 方程式を解く分点には

$$s_1 = 1/9 , \quad s_2 = 1/2 , \quad s_3 = 8/9 \quad (10)$$

の数値を採用する. よって, 階数が 2 $(r = 2)$ の変数に対する格子点は (8) より,

$$(\beta_1, \beta_2, \beta_3, \beta_4, \beta_5) = \left(-\frac{\sqrt{6}}{54}, \frac{\sqrt{6}}{54}, \frac{1}{2}, 1 - \frac{\sqrt{6}}{54}, 1 + \frac{\sqrt{6}}{54}\right)$$

となる. 階数が 1 $(r = 1)$ の変数に対する格子点は同様の考察から

$$(\beta_1, \beta_2, \beta_3, \beta_4) = \left(0 , \frac{9 - \sqrt{17}}{18} , \frac{9 + \sqrt{17}}{18} , 1\right)$$

と導かれる. 階数が 0 $(r = 0)$ の変数に対する格子点は分点と同一が最適なので

$$(\beta_1 , \beta_2 , \beta_3) = \left(\frac{1}{9} , \frac{1}{2} , \frac{8}{9}\right)$$

である. 格子点と分点とが定まれば差分化公式 (3,4,5) の係数 E_j, D_j, C_j は差分化誤差を最小にするという条件で一意に決定される.

次に, 差分化公式の特性を要約しよう. 階数が 0 $(r = 0)$ の変数に対しては, この変数に対する微分値が方程式の中に現れてこないならば. 差分化誤差は発生しない.

階数が 1 $(r = 1)$ の変数にする特性を調べるために,

$$\phi'(x) + \lambda\phi(x) = 0 , \quad \phi(0) = 1 \quad (11)$$

に差分化公式を適用し, $\phi(h)$ を求める.

$$\phi(h) = \frac{972 + 486(\lambda h) + 97(\lambda h)^2 + 8(\lambda h)^3}{972 - 486(\lambda h) + 97(\lambda h)^2 - 8(\lambda h)^3} \quad (12)$$

この関係式は,

$$|\phi(h)| < 1 , \text{ for } \Re\lambda < 0$$

を直ちに導くので, この差分化技法は絶対安定であり, さらに,

$$|\phi(h)| = 1 , \text{ for } \Re\lambda = 0$$

も証明できるので, 線形的シンプレクテイックな特性を有していることも示される. 打ち切り誤差は,

$$\phi(h) - exp(\lambda h) = -\frac{(\lambda h)^5}{58320} + O(h^6); \quad (13)$$

となる. 階数が 2 ($r = 2$) の変数にする特性を調べるために,

$$\phi''(x) + \omega^2 \phi(x) = 0 , \quad \phi(0) = 1 , \phi'(0) = 0 \quad (14)$$

に差分化公式を適用し, $\phi(h)$ を求めると次のようになる (Fig.2) .

$$\phi(h) = \frac{1889568 - 873342(\omega h)^2 + 44644(\omega h)^4 - 420(\omega h)^6}{1889568 + 71442(\omega h)^2 + 1633(\omega h)^4 + 32(\omega h)^6} \quad (15)$$

$|\phi(h)| > 1$ のときは数値不安定が発生し得る. この条件は上式より,

$$3.125843\cdots < |\omega h| < 3.1655\cdots$$

と導かれ,1 ステップで振幅が反転 ($\omega h = \pi$) するほどにステップ幅 h が大きい場合 (あるいは現象が急変化する場合) に限られる. 解の変化に追随できるステップ幅なら数値的に安定と思われる. 差分化誤差は

$$\phi(h) - \cos(\omega h) = \frac{(\omega h)^6}{155520} + O(h^8) \quad (16)$$

となる.
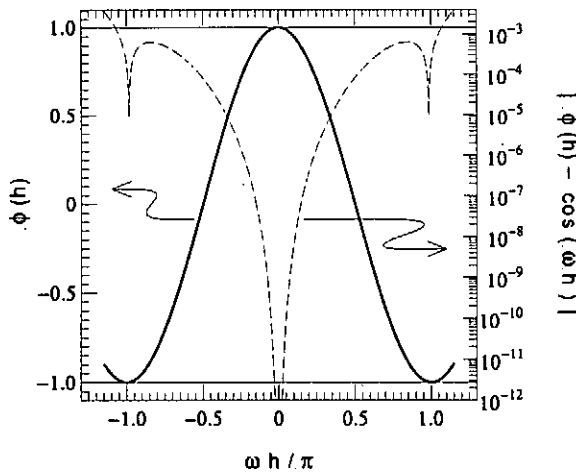
Fig.2　HIDM の差分化技法の安定性係数と誤差: 線形調和振動子 (14) を HIDM で解いたときの関数値 $\phi(h)$ (15) と誤差. 関数値 $\phi(h)$ は太い実線, 誤差は細い破線で示されている. $|\phi(h)| > 1$ となるときには数値不安定が発生する.

3　HIDM2D の概要

　ここでは HIDM の計算手続きを多次元化する方法を, 2 独立変数の偏微分方程式の汎用数値計算プログラム HIDM2D で具体的に示す. まず最初に微小長方形領域 (単位胞)

$$0 \le x \le h_x , \quad 0 \le y \le h_y , \quad (17)$$

で偏微分方程式

$$L(\phi, \phi_x, \phi_y, \phi_{xy}, x, y) = 0 \quad (18)$$

を解くことを考えよう. 長方形領域 (17) の (x, y) に Fig.1 に示したと同様の格子点, 分点を配置する. 微分方程式 (18) を解く分点 $(s_k h_x , s_l h_y)$ 上の関数値, 微分値は差分化公式 (3,4,5) を直接的に多次元化した公式で表現できる ($k, l = 1, \cdots, n$).

$$\phi(s_k h_x, s_l h_y) = \sum_{i,j=1}^{m} C_i(s_k) C_j(s_l) \phi(\beta_i h_x, \beta_j h_y) \quad (19)$$

$$\phi_x(s_k h_x, s_l h_y) = \frac{1}{h_x} \sum_{i,j=1}^{m} D_i(s_k) C_j(s_l) \phi(\beta_i h_x, \beta_j h_y) \quad (20)$$

$$\phi_y(s_k h_x, s_l h_y) = \frac{1}{h_y} \sum_{i,j=1}^{m} C_i(s_k) D_j(s_l) \phi(\beta_i h_x, \beta_j h_y) \quad (21)$$

$$\phi_{xy}(s_k h_x, s_l h_y) = \frac{1}{h_x h_y} \sum_{i,j=1}^{m} D_i(s_k) D_j(s_l) \phi(\beta_i h_x, \beta_j h_y) \quad (22)$$

未知の関数値が埋め込まれている格子点の総数は $(n+1)^2$ 個あり, 微分方程式を解く地点 (分点) の総数は n^2 個あるので, 解を一意に決定するには

$$(n+1)^2 - n^2 = 2n + 1$$

個の境界条件・初期条件が必要である. この条件は, $x = 0$ 軸, および $y = 0$ 軸上に設定される. この手続きを繰り返せば,

$$\phi(0, y), \quad \phi(x, 0) \quad (23)$$

を境界条件・初期条件としたときの偏微分方程式 (18) の解

$$\phi(x, y), \quad (0 \le x \le x_1, \quad 0 \le y \le y_1) \quad (24)$$

が求まるはずである. 但し, 通常の偏微分方程式は境界条件が (23) の様な形で与えられることはなく, $\phi(0, y), \phi(x, 0)$ の中には必ず未知の関数値が含まれ, それれらの値は, 他の境界上で与えられている条件を満たすように定める必要がある. このときには, 境界条件 (23) に推定値を設定して計算し, 物理的に設定されている境界条件を満たすようにニュートン法を用いて修正することで解に到達する (シューティング法).

(a)

(b)
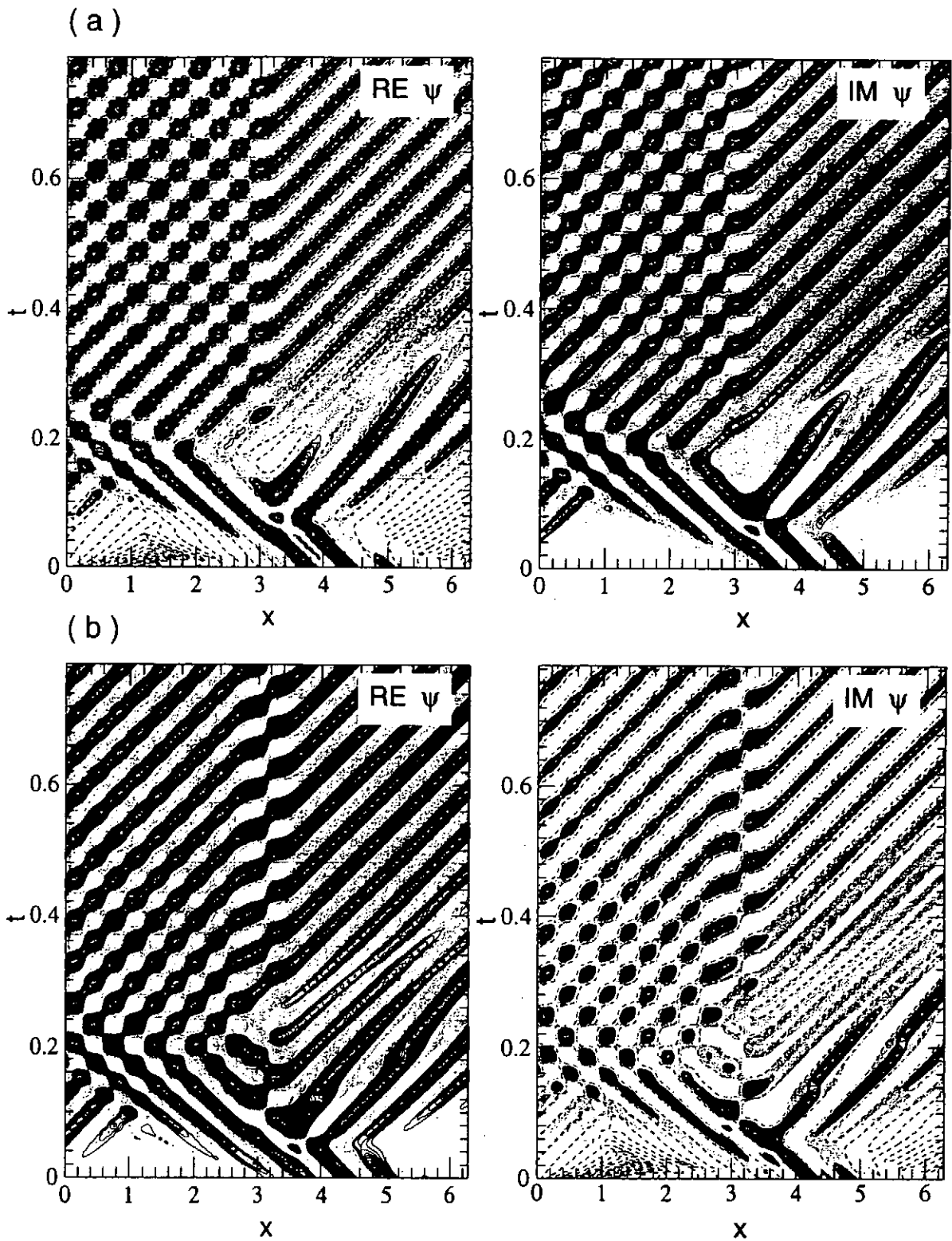
Fig.3　HIDM2D によるシュレディンガー方程式の数値計算: x 方向を 8 個のブロックに分割し (等分割) 各々のブロックは 4 個の単位胞から構成されている. 時間, 空間のステップ幅は $h_x = 2\pi/32$, $h_t = 2\pi/1600$ である. 初期条件, 境界条件は本文に述べられている. $\psi(x,t)$ の実部 (左側) と虚部 (右側) の高さが (x,t) 空間で等高線表示されている. 黒色の点線が $\psi(x,t) = 0$ を示している. (a) は, ポテンシァルが単峰, (b) は, ポテンシァルが双峰の場合を示す. 単峰では, 波を反射するポテンシァルでも, それを隣接して 2 個整列配置すれば, 波の超透過現象の起こり得ることを示している.

このシューティング計算を行うときには, 数値解の急激な成長と, 激しい振動が発生する. よって計算機で正しく処理できる範囲内で計算を進めるためには, 計算領域を小さなブロックに分割する必要がある (多重分割をした上でのシューティング法 — 多分割シューティング法 —).

偏微分方程式に対する汎用数値計算プログラムとして, 十分な実用性を確保するには高階の微分を含む場合にも効率的に計算できる必要がある. よってHIDM2D は,

$$L(\phi, \phi_x, \phi_y, \phi_{xy}, \phi_{xx}, x, y) = 0$$

$$L(\phi, \phi_x, \phi_y, \phi_{xy}, \phi_{xx}, \phi_{yy}, x, y) = 0$$

等, 高階微係数を含む場合にも対処できるように組み立てられた. また実用性をさらに高めるため固有値問題も計算可能とした.

4 HIDM2D の数値計算例

HIDM の計算手続きの有効性を確認するために, 2 独立変数の偏微分方程式を解く汎用プログラム HIDM2D を構築した. 計算手続きの有効性をできるだけ幅広く, 1 個のプログラムで検査できるようにするため, 関数値, 固有値はともに複素数数であることを許している.

保存系の時間発展境界値問題への適応性, 衝撃波解への適応性, 2 次元空間における固有値問題への適応性を確かめた数値計算結果を以下に述べよう.

4.1 シュレディンガー方程式の数値計算

保存系の時間発展境界値問題への適応性を確かめるためにシュレディンガー方程式

$$i\frac{\partial \psi}{\partial t} = -\frac{\partial^2 \psi}{\partial x^2} + V(x)\psi, \quad (0 \le x \le 1) \quad (25)$$

を解く. 初期条件は波数が $-k_0$ $(k_0 = 20\pi)$ の波束とする.

$$\psi(x, 0) = 3\exp\left(-ik_0 x - \frac{k_0^2}{100}(x - 0.7)^2\right) \quad (26)$$

境界条件には,

$$0 = \psi_t(0, t) - 2k_0\psi_x(0, t) - i\omega_0\psi(0, t)$$
$$+ 4i\omega_0 \exp(-i\omega_0 t)\left(1 - \exp(-100t^2)\right) \quad (27)$$

$$0 = \psi_t(1, t) + 2k_0\psi_x(1, t) - i\omega_0\psi(1, t) \quad (28)$$

を採用する. ただし, ω_0 $(= k_0^2)$ は, 波数 $\pm k_0$ に対応する真空中での振動数である. この境界条件は中心波数が k_0 となる波束の外向きへの自由な通過と, $x = 0$ 境界からの波数 k_0 の波の入射を表している (付録 A) 参照). ポテンシャル $V(x)$ としては, 次の 2 例を採用した.

$$V(x) = V_1(x) \equiv k_0^2 \exp\left(-50(x - 0.50)^2\right)$$
$$V(x) = V_2(x) \equiv k_0^2 \left[\exp\left(-50(x - 0.45)^2\right) \right.$$
$$\left. + \exp\left(-50(x - 0.55)^2\right)\right]$$

ポテンシャル $V_1(x)$ の高さは波数 k_0 の波のエネルギーと等しいので波束の部分的透過と部分的反射とが生ずるはずである. これに対してポテンシャル $V_2(x)$ は, $V_1(x)$ を隣接して 2 個並べたものであり, 波束の超透過現象の発生を期待したものである. 数値計算結果を Fig.3 に示す. Fig.3(b) には, 反射波の存在を示す干渉波形の減少が示されており, 斥力ポテンシャルの整列配置で超透過現象を実現できることを予測させている.

4.2 バーガーズ方程式の数値計算

衝撃波を形成する偏微分方程式への適応可能性を確かめるために, バーガーズ方程式

$$\frac{\partial \phi}{\partial t} + \phi\frac{\partial \phi}{\partial x} = \nu\frac{\partial^2 \phi}{\partial x^2}, \quad (0 \le x \le 1) \quad (29)$$

を HIDM2D で解こう. 方程式は移流拡散方程式とも呼ばれ, 弱い衝撃波の構造を表すことができる. 初期条件と境界条件は次のようにとる.

$$\phi(x, 0) = 0$$

$$\phi(0, t) = \left(1 - \exp(-15t^2)\right)^2$$

$$\phi(1, t) = -0.8\left(1 - \exp(-15t^2)\right)^2$$

計算結果を Fig.4 に示す. 衝撃波の形成と伝搬・衝突の過程が数値的に再現されている.
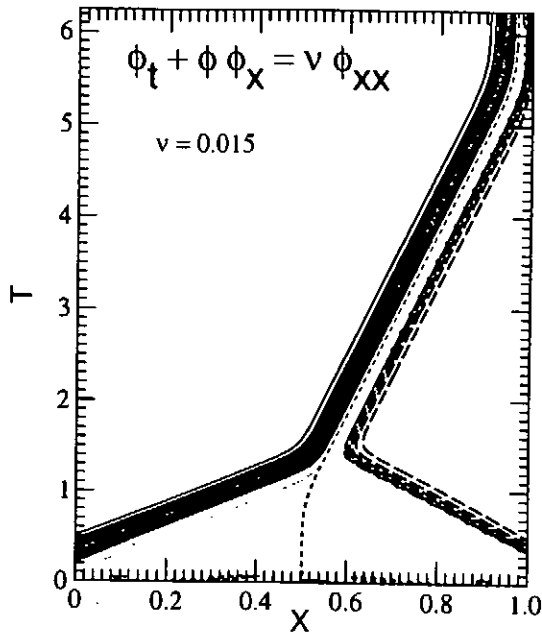
Fig.4　HIDM2D によるバーガーズ方程式の数値計算. x 方向を 25 のブロックに分割し (等分割) 各々のブロックは 4 個の単位胞から構成されている. 時間, 空間のステップ幅は $h_x = 1/100$, $h_t = 1/16$ である. 初期条件, 境界条件は本文に述べられている. $\phi(x,t)$ の高さが (x,t) 空間で等高線表示されている. 実線は正, 破線は負の関数値を表し, 黒色の点線が $\phi(x,t) = 0$ を示して. 衝撃波の形成と伝搬・衝突の過程がきれいに再現されている.

4.3　2次元固有値問題への適用

HIDM2D が, 固有値問題へも適用可能であることを確認するために, 周期的ポテンシャルの存在する下でのシュレディンガー方程式を固有値問題として解いた.

$$\frac{\partial^2 \psi}{\partial x^2} + \frac{\partial^2 \psi}{\partial y^2} = (V - \lambda)\psi \tag{30}$$

$$(-\infty \leq x \leq \infty, \quad 0 \leq y \leq 2\pi)$$

ポテンシャルとしては次の関数形を仮定した.

$$V(x,y) = 5 \exp\left(-5\sin^2(x/2) - 2\sin^2(y/2)\right) \tag{31}$$

λ はエネルギー固有値を表す. エネルギーバンド構造を求めるために, 波数ベクトル k_x に対応するブロッホ関数 $u(x,y)$ を HIDM2D で計算した.

$$\psi(x,y) = \exp(ik_x x) u(x,y)$$

ブロッホ関数 $u(x,y)$ を支配する方程式は

$$\frac{\partial^2 u}{\partial x^2} + \frac{\partial^2 u}{\partial y^2} = (V - \lambda + k_x^2)u - 2ik_x \frac{\partial u}{\partial x} \tag{32}$$

$$(0 \leq x \leq 2\pi, \quad 0 \leq y \leq 2\pi)$$

となる. ブロッホ関数 $u(x,y)$ に対する境界条件は

$$u(x,0) = u(x,2\pi) = 0 ,$$

$$u(0,y) = u(2\pi, y) ,$$

$$\frac{\partial u(0,y)}{\partial x} = \frac{\partial u(2\pi, y)}{\partial x}$$

で与えられる. 数値計算結果を Fig.5 に示す. Floquet の定理によれば, エネルギー固有値 λ は波数 k_x の周期関数になることが導かれる. HIDM2D の計算はこの要請を満たしていることが Fig.5 に示されている. (x,y) に関する 2 階の偏微分方程式は連立 1 階の偏微分方程式にも帰着できる.

$$\left.\begin{array}{c} \frac{\partial \psi}{\partial x} + i\frac{\partial \psi}{\partial y} = \phi \\ \frac{\partial \phi}{\partial x} - i\frac{\partial \phi}{\partial y} = (V - \lambda)\psi \end{array}\right\} \tag{33}$$

連立 1 階の偏微分方程式 (33) に HIDM2D を適用した結果は 2 階の偏微分方程式 (30) に HIDM2D を適用した結果と同一の結果となったことを念のため書き加えておこう.

5　まとめと討論

陰的差分化技法と多分割シューティング法式との組み合わせで構築されたプログラム HIDM2D は, 独立変数が 2 個に限定された偏微分方程式に対してであるが,

- 常微分方程式 (初期値問題) 並みの容易さで偏微分方程式を解けるようにしたい.

という要求をほぼ実現できることを示した. このプログラムの実用性を高めるには,

- 多分割シューティング法にともなうニュートン法の計算に使われる線形計算の効率化

が必要である. 現行の HIDM2D は, 計算手続きの有効性を確認するためのプロトタイプとして構築されているので, 全ての線形計算は稠密な行列を持つことを前提としたサブルーチンプログラムで処理している. しかしながら, 多分割シューティング法にともなうニュートン法の計算時の線形計算は疎行列を係数とする線形計算なので, 必要な主記憶量, および計算時間を現行に比べ大幅に節約可能な道があると思われる. 2 次元を超え, HID2D の 3 次元化, 4 次元化を実現するにはこの効率化が本質的に重要となるであろう.

謝辞

HIDM2D のプログラムが期待通りの動作を示すまでには，アルゴリズムの欠陥に起因するのか，あるいは，単なるバグに起因するのか，様々な可能性を予想しながらのプログラム訂正作業を必要とした．この作業中に手詰まり状態を感じたときには，核融合科学研究所の等々力二郎教授と議論することで，新しい展開を開くことができた．

参考文献

[1] 渡辺二太，高木益雄：常微分方程式初期値問題の数値計算プログラムHIDMAS，日本応用数理学会論文誌 1 (1991) 135-163.

[2] T.Watanabe: A New numerical scheme to solve algebraic-differential equations: Annals of Numerical Mathematics 1 (1994) 293-306.

[3] T.Watanabe and G.Gnudi: A New Algolitm for Differential — Algebraic Equations Based on HIDM, Numerical Analysis of Ordinary Differential Equations and its Applications, edited by T.Mitsui and Y.Shinohara (World Scientific Publishing Co., Singapole, 1995) 91-111.

[4] K.Minami, A.Ejiri, K.Tanaka and T.Watanabe: Linear Mode Conversion between Ordinary and Extrordinary Waves in Plasma with Large Magnetic Shear, JJAP 37,(1998) 6601-6608.

[5] T.Watanabe: HIDM, a General Purpose Algorithm for Nonlinear Problems Described by Partial D ifferential Equations: GAKUTO International Series, Mathematical Science and Applications 1 (1993) 189.

[6] T.Watanabe, K.Ogura, S.Watanabe and K.Minami: High-Power Backward Wave Oscillator Driven by an Intense Relativistic Electron Beam with Tapered Slow Wave Structure for Improved Performaces, Nucl. Inst. and Meth. A331 (1993) 134-139.

[7] 渡辺二太，小椋一夫: 高品質・高電力マイクロ波発生装置（後進波発振器）の計算機解析，シミュレーション 12 (1993) 107-118.

[8] 渡辺二太：時間刻み幅自動調節方式の微分方程式汎用ソルバーの試みと Cahn-Hilliard 方程式への応用，

付録 A)

無限領域に展開する偏微分方程式を有限領域に限定された数値計算で解析するには境界条件の設定法が重要である．ここでは，波動方程式の計算で必要となる外向き進行波の自由通過と特定な振動数，波数を持つ波の入射を指定する境界条件の設定法を述べる．簡単のため 1 次元空間の波動 $\psi(x,t)$ について記す．波の分散関係を

$$\omega = \omega(k) \qquad (34)$$

とする．考察対象の媒質中に複数個のモードが混在するときの場合に対する拡張は容易と思われるのでここでは，単一のモードのみが存在する場合について述べる．

外向き進行波となることを要請するものは，

$$(k, \omega) = (k_o, \omega_o), \quad (\omega_o \equiv \omega(k_o))$$

を中心波数，中心振動数とする波束であるとする．入射波の振幅を $a(t)$ とし，中心波数，中心振動数を

$$(k, \omega) = (k_i, \omega_i)$$

とし，境界の位置を

$$x = x_b$$

とすると，境界条件は次のようになる．

$$\psi_t + \left.\frac{\partial\omega}{\partial k}\right|_{k=k_o} \psi_x - ik_o^2 \frac{\partial}{\partial k}\left(\frac{\omega}{k}\right)\Big|_{k=k_o} \psi$$
$$= -i\left\{ \omega_i - k_i \frac{\partial\omega}{\partial k}\Big|_{k=k_o} + k_o^2 \frac{\partial}{\partial k}\left(\frac{\omega}{k}\right)\Big|_{k=k_o} \right\}$$
$$\times a(t)\exp(ik_i x_b - i\omega_i t) \qquad (35)$$

シュレディンガー方程式 (25) の場合の分散式は

$$\omega = k^2$$

となるので，境界条件 (35) は，(27, 28) に帰着する．
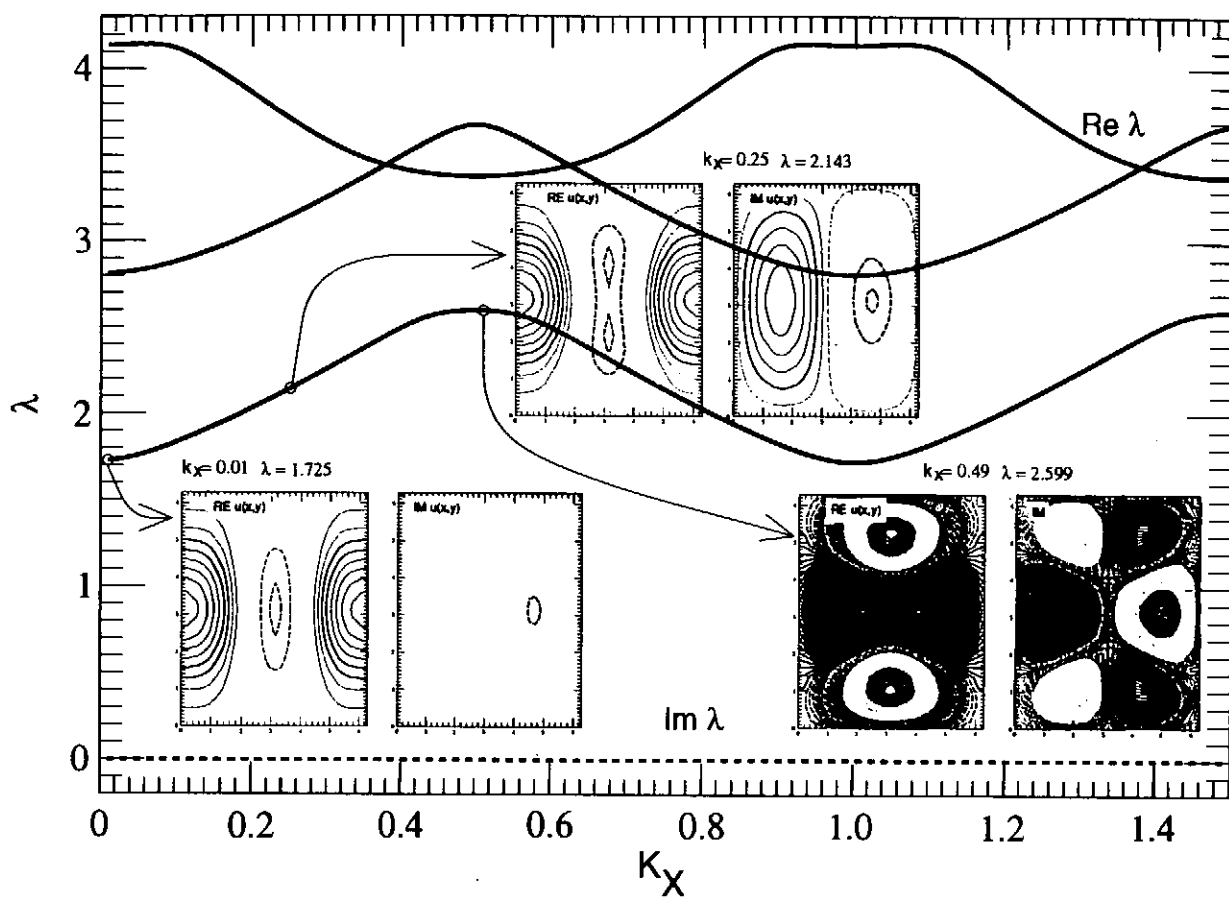
Fig.5 HIDM2D による 2 次元固有値問題 (32) の計算例: 計算領域を x 方向,y 方向を共に 4 等分し, 合計 16 個のブロックに分割した. 各ブロックは 4 (= 2 × 2) 個の単位胞から構成されている. 横軸は波数 k_x 縦軸はエネルギー固有値 λ を表す. ポテンシァルの周期構造に原因するエネルギーバンド構造が計算されている. y 方向に関して偶関数構造の波動関数を持つバンドが 2 本, 奇関数構造の波動関数を持つバンドが 1 本示されている. ブロッホ関数 $u(x, y)$ の代表例も等高線表示されている.

Magnetic Shielding Analysis of Axisymmetric HTS Plate by Flux Flow Creep Model

Atsushi Kamitani*, Shigetoshi Ohshima* and Takafumi Yokono**

*Department of Electrical and Information Engineering, Yamagata University
Yonezawa, Yamagata 992-8510, Japan
**Institute of Information Sciences and Electronics, University of Tsukuba
Tsukuba, Ibaraki 305-8573, Japan

Abstract

The magnetic shielding performance of the high-Tc superconducting (HTS) plate is numerically investigated by assuming the flux flow creep model as a constitutive relation representing a mixed state. In order to reduce the number of variables, both the axisymmetry of the plate shape and the isotropy of the applied magnetic field are introduced. Under these assumptions, the shielding factor and the damping coefficient are calculated as functions of time and the frequency of the applied magnetic field. The results of computations show that an increase in the frequency will weaken the time dependence of the shielding factor and will enhance the shielding performance. In addition, the magnetic shielding performance in the low-frequency range and in the high-frequency range is shown to be strongly influenced by the flux creep and the flux flow, respectively.

Keywords: magnetic shielding, superconductor, YBCO, flux flow, flux creep

I. INTRODUCTION

Recently, the application of the high-Tc superconductor (HTS) has been proposed in many engineering fields. The magnetic shielding is one of the most important and promising applications of the HTS. Although high-conductivity or high-permeability materials have been so far used as magnetic shielding materials, they cannot cut off magnetic fields with the low frequency below 10Hz. In this contrast, the HTS is expected to have a frequency-independent magnetic shielding ability because of its shielding mechanism, i.e., the Meissner effect. For this reason, the HTS has attracted great attention as a new type of the magnetic shielding material and experimental studies on its magnetic shielding performance have been performed intensively [1]–[4]. However, in these studies, the applied magnetic field is much smaller than the lower critical one and, hence, the HTS does not remain in a mixed state but in a pure superconducting one. On the other hand, the high upper critical magnetic field is one of the excellent advantages of the HTS. In this sense, the next stage is to investigate the magnetic shielding performance of the HTS plate in a mixed state.

The purpose of the present study is to develop the numerical code for analyzing the time evolution of the shielding current density and to numerically investigate the magnetic shielding performance of the axisymmetric HTS plate in a mixed state. In the next section, we introduce the governing equation of the shielding current density in the axisymmetric HTS plate by taking account of the strong anisotropy of the critical current density. The numerical

method for the solution of the equation is also explained there. In the third section, the time and the frequency dependence of the magnetic shielding performance of the HTS plate are investigated by using the method explained in the third section. Furthermore, the influence of the flux creep and the flux flow on the magnetic shielding performance is studied quantitatively. Conclusions are summarized in the final section.

The SI units are used throughout the present study.

II. MATHEMATICAL FORMULATION

In this section, we introduce the governing equation of the shielding current density in the HTS plate. The schematic view of the magnetic shielding measurements is shown in Fig. 1. Throughout the present study, the shape of the HTS plate is assumed to be a disk of radius a and of thickness b. Let us use the cylindrical coordinate system (ρ, θ, z), and take the symmetry axis as z-axis and the center of gravity of the plate as the origin. The magnetic flux density B_0 is generated by a couple of Helmholtz coils and, therefore, it is spatially homogeneous and its magnitude B_{0z} changes as $B_{0z} = B_0 \sin \omega t$.

As is well known, the MPMG-YBCO superconductor has a crystallographic anisotropy in the critical current density: its component parallel to the a-b plane is negligibly small as compared with that along the c axis [5]. By taking this fact into account, we assume that the HTS plate is composed of K pieces of thin layers and that the shielding current density does not flow across the interface of every
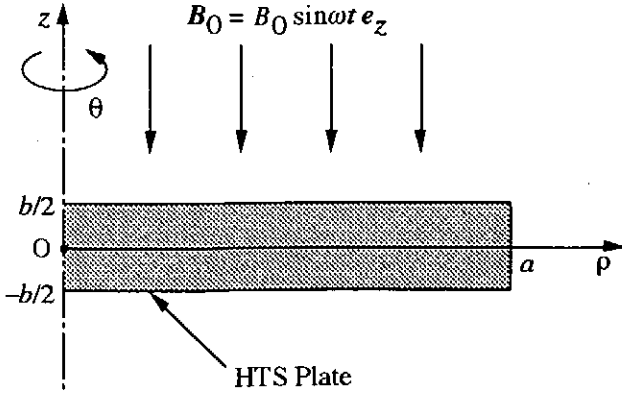
Fig. 1. Schematic view of the magnetic shielding measurements.

two layers. When the thickness of each layer is much smaller than the radius a of the HTS plate, the variation of physical quantities in the z-direction can be neglected as compared with their variation in the ρ-direction. Thus, it is also assumed that neither the shielding current density nor the electric field depends on z in each layer.

Under the above assumptions, the behavior of the shielding current density can be expressed by the following equation [6]:

$$\mu_0 \partial_t \sum_{q=1}^{K} \int_0^a S_q(\rho', t) \, Q^*{}_{pq}(\rho, \rho') \, \rho' \, d\rho' + \frac{\mu_0}{\varepsilon_p} \partial_t S_p$$
$$= - \partial_t B_{0z} - \frac{1}{\rho} \frac{\partial}{\partial \rho} (\rho \, E_{p\theta}) \ , \tag{1}$$

where $E_{p\theta}$ denotes θ-component of an electric field E_p in the pth layer and μ_0 represents permeability of vacuum. The scalar function $S_p(\rho, t)$ is z-component of a current vector potential and is associated with the shielding current density j_p in the pth layer through the relation:

$$j_p = -\frac{1}{\varepsilon_p} \frac{\partial S_p}{\partial \rho} e_\theta \ . \tag{2}$$

Here the thickness of the pth layer is denoted by $2\varepsilon_p$. The explicit form of the function $Q^*{}_{pq}$ in (1) is written as

$$Q^*{}_{pq}(\rho, \rho') = -(4\pi \, \varepsilon_p \, \varepsilon_q)^{-1} (\rho \, \rho')^{-1/2}$$
$$\times \sum_{m=0}^{1} \sum_{n=0}^{1} (-1)^{m+n} k_{pq}^{mn} \, K(k_{pq}^{mn}) \ , \tag{3}$$

where $K(x)$ is a complete elliptic integral of the first kind and its parameter k_{pq}^{mn} is given by

$$\left(k_{pq}^{mn}\right)^2 \equiv 4\rho\rho'$$
$$\times [(\rho + \rho')^2 + \{[z_p + (-1)^m \varepsilon_p] - [z_q + (-1)^n \varepsilon_q]\}^2]^{-1} \ .$$

Here z_p denotes z-coordinate of the central plane in the pth layer.

The effect of electromagnetic characteristics of the HTS is included by assuming the following J-E constitutive relation:

$$E_{p\theta} = E(|j_{p\theta}|) \, \text{sgn}(j_{p\theta}) \ . \tag{4}$$

For $E(j)$, we adopt two kinds of functions: the Bean model [7]-[11] and the flux flow creep model [6], [12]-[14]. The former represents the balance between the pinning and the Lorentz force, whereas the movement of fluxoids is included in the latter. The explicit form of $E(j)$ for the Bean model is given by

$$E(j) = j / \sigma[j] \ , \tag{5}$$

where σ denotes a virtual conductivity and is a functional of j. In order to determine σ at each time step, we employ the following iterative procedure [8]-[11]. At first, the initial value $\sigma^{(0)}$ of a virtual conductivity is assumed sufficiently large, e.g., $\sigma_{Cu} \times 10^8$. Here σ_{Cu} denotes an electric conductivity of copper at the room temperature. In the nth cycle, (1) is solved together with the associated boundary conditions after the substitution of $\sigma^{(n)}$ into σ. Then, the spatial distribution $j_{p\theta}^{(n)}(\rho, t)$ of the shielding current density is obtained and, subsequently, the virtual conductivity is corrected by

$$\sigma^{(n+1)} = \sigma^{(n)} \, \text{Min}(j_C / |j_{p\theta}^{(n)}|, 1) \ , \tag{6}$$

where j_C denotes a critical current density and the superscript (n) represents an iteration number label. The above cycle is repeated until the shielding current density does not exceed j_C all over the HTS plate. On the other hand, the function $E(j)$ for the flux flow creep model [6], [12]-[14] can be written in the form,

$$E(j) = \begin{cases} 2 \, \rho_c \, j_C \, \sinh\left(\dfrac{U_0}{k_B T} \dfrac{j}{j_C}\right) \exp\left(-\dfrac{U_0}{k_B T}\right) & ; j < j_C \\[2ex] \rho_c \, j_C \left[1 - \exp\left(-\dfrac{2 \, U_0}{k_B T}\right)\right] + \rho_f \, (j - j_C) & ; j > j_C \end{cases}$$

where ρ_c and ρ_f are the creep and the flow resistivity, respectively, and U_0, k_B, and T denote the pinning potential, the Boltzmann constant and the temperature, respectively.

As the initial and the boundary conditions to (1), we assume that the shielding current density does not have a normal component on each layer surface and that it vanishes at $t = 0$. In terms of S_p, these assumptions are rewritten as follows: $S_p(a, t) = 0$ and $S_p(\rho, 0) = 0$. By solving (1) together with these conditions, we can follow the time evolution of the shielding current density.

If the finite element method and the θ-method are applied to the discretization of (1) and the associated boundary conditions, the resulting equation becomes a nonlinear matrix equation. Thus, the iterative scheme is employed to solve the equation. As the methods for its solution, the successive substitution method and the Newton-Raphson method are used for the Bean model and the flux flow creep model, respectively. The numerical code for solving the initial-boundary-value problem of (1) has been developed by using the method explained above [6] and, by means of the code, we can investigate the magnetic shielding performance of the HTS plate.

III. MAGNETIC SHIELDING ANALYSIS

In this section, we investigate the magnetic shielding performance of the HTS plate by using the code explained in the previous section. As the measure of the shielding performance, we adopt the damping coefficient defined by $\alpha = 10 \log_{10}(\langle B^2\rangle/\langle B_0^2\rangle)$ and the shielding factor defined by $\lambda = B_z/B_{0z}$. Here B and B_z denote the total magnetic flux density and its z-component, respectively. In addition, the square bracket means a time average. Throughout the present study, the geometrical and the physical parameters are assumed as follows: $a = 20\times10^{-3}$m, $b = 2\times10^{-3}$m, $B_0 = 1\times10^{-2}$T, $T = 77$K, $j_C = 1.5\times10^6$A/m^2, $U_0 = 92$meV.

First, let us investigate the time dependence of the shielding performance of the HTS plate. The shielding factors λ are calculated by using the flux flow creep model and are depicted as functions of time in Fig. 2. We see from this figure that the shielding performance strongly
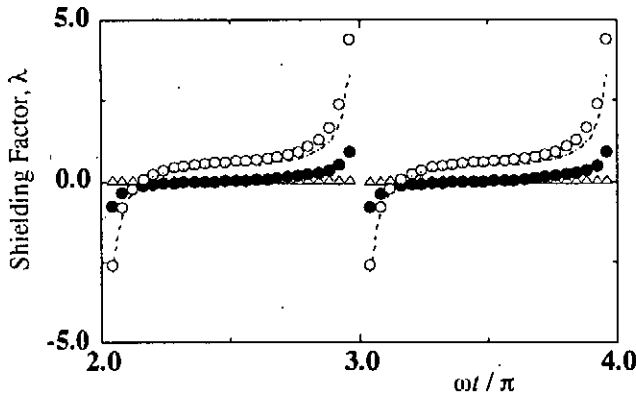
Fig. 2. Time dependence of the shielding factor λ at $(\rho/a, z/a) = (0.0, -0.06)$. The symbols, $\bigcirc$, $\bullet$ and $\triangle$, denote the values for the flux flow creep model with $\omega = 1$, 10^2 and 10^4Hz, respectively, and the dashed curve represents those for the Bean model. The values of the creep and the flow resistivity are assumed as $\rho_c = 6.666\times10^{-11}\Omega$m and $\rho_f = 7.620\times10^{-10}\Omega$m, respectively.
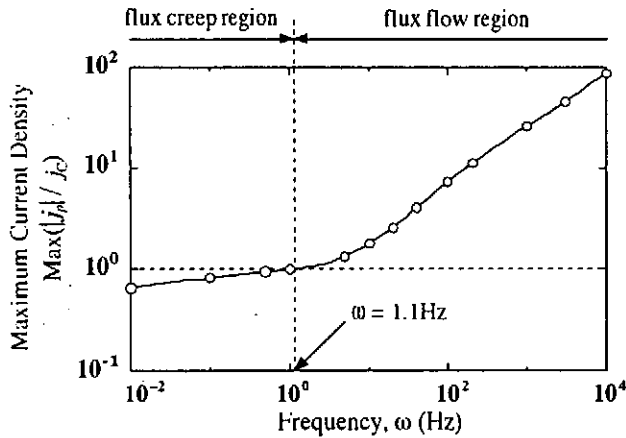
depends on time for the case with $\omega = 1$Hz. In this contrast, the shielding performance is almost time-independent for the case with $\omega = 10^2$ and 10^4Hz. This tendency is attributable to the phase difference between the applied and the induced magnetic field. With an increase in the frequency, the phase difference increases and approaches gradually to π. In fact, an increase in ω raises the maximum absolute value of the shielding current density until the flux flow becomes dominant for $\omega \gtrsim 10^2$Hz (see Fig. 3). In such a high-frequency region that $\omega \gtrsim 10^2$Hz, the effect of the flux creep can be neglected as compared with that of the flux flow and, hence, the J-E constitutive relation is written as $E(j) = \rho_f j$. Since the governing equation (1) becomes linear in this case, the phase difference is equal to π. The shielding factors are also calculated by use of the Bean model and are depicted in Fig. 2. In case of the Bean model, the shielding factor does not change its value for the frequency range from 10^{-2} to 10^4Hz.

Next, we investigate the influence of the frequency on the shielding performance of the HTS plate. Figure 4 shows the frequency dependence of the damping coefficient for the flux flow creep model. The damping coefficient α decreases slightly with an increasing frequency for $\omega \lesssim 1$Hz, whereas it diminishes drastically with ω for 1Hz $\lesssim \omega \lesssim 10^2$Hz. This is mainly because the flux flow becomes dominant as compared with the flux creep in the frequency range from 1 to 10^2Hz. With a further increase in ω, the damping coefficient will approach to a constant value.

Finally, we investigate the influence of the flux flow and the flux creep on the shielding performance of the HTS plate. For this purpose, the damping coefficients are calculated as functions of either the creep or the flow resistivity. In Fig. 5, we show the dependence of the damping coefficient α on the creep resistivity ρ_c. This figure indicates that, in case of $\omega \leq 10$Hz, a decrease in the creep resistivity will lessen the damping coefficient to its value for the Bean model. In this contrast, the dependence of α on ρ_c is relatively weak in case of $\omega = 10^2$Hz because the flux flow dominates the flux creep. From this result, we might conclude that the flux creep affects only the shielding

Fig. 3. Maximum absolute value of the shielding current density as a function of the frequency ω in case that the flux flow creep model is used. The values of the creep and the flow resistivity are the same as those used in Fig. 2.
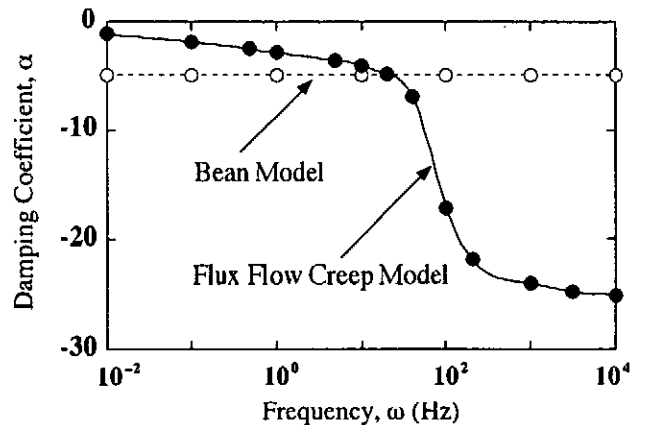

Fig. 4. Frequency dependence of the damping coefficient α at $(\rho/a, z/a) = (0.0, -0.06)$. The values of the creep and the flow resistivity are the same as those used in Fig. 2.
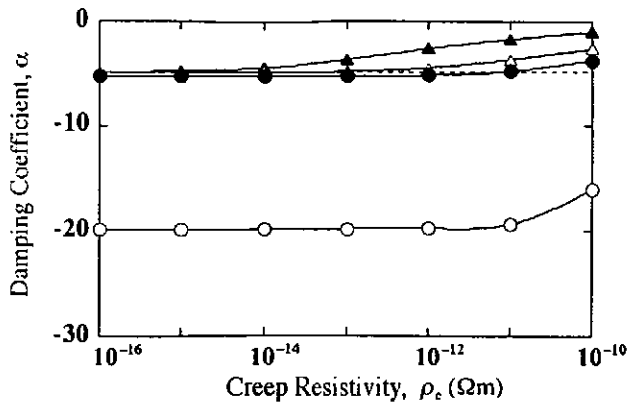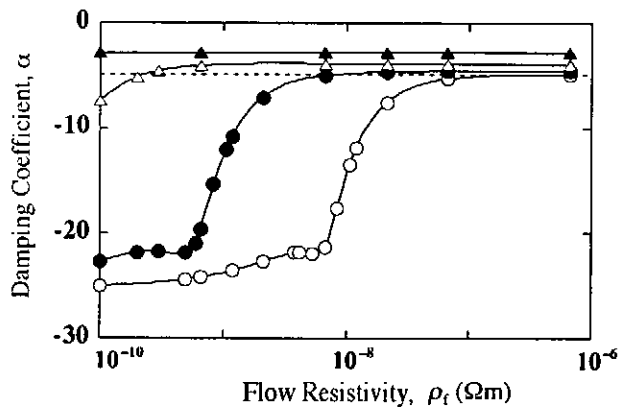
Fig. 5. Damping Coefficient α at $(\rho/a, z/a) = (0.0, -0.06)$ as functions of the creep resistivity ρ_c. The value of ρ_f is fixed as $\rho_f = 7.620\times10^{-10}\Omega m$. The symbol ▲ is for the case of $\omega = 10^{-2}Hz$, △ for $\omega = 1Hz$, ● for $\omega = 10Hz$, ○ for $\omega = 10^2Hz$, and the dashed line indicates the value for the Bean model.

Fig. 6. Damping Coefficient α at $(\rho/a, z/a) = (0.0, -0.06)$ as functions of the flow resistivity ρ_f. The value of ρ_c is fixed as $\rho_c = 6.666\times10^{-11}\Omega m$. The symbol ▲ is for the case of $\omega = 1Hz$, △ for $\omega = 10Hz$, ● for $\omega = 10^2Hz$, ○ for $\omega = 10^3Hz$, and the dashed line indicates the value for the Bean model.

performance against the low-frequency magnetic field. In Fig. 6, we show the dependence of α on the flow resistivity ρ_f. We see from this figure that, for the case with $\omega = 10^2$ and 10^3Hz, an increase in the flow resistivity will raise the damping coefficient up to the value for the Bean model. On the other hand, for the cases with $\omega = 1$ and $10Hz$, the damping coefficient remains almost constant and does not approach to the value for the Bean model. This tendency indicates that the flux flow influences on the magnetic shielding performance only in the high-frequency range.

IV. CONCLUSION

We have developed the numerical code for analyzing

the time evolution of the shielding current density on the basis of the flux flow creep model. By means of the code, we have numerically investigated the magnetic shielding performance of the HTS plate in a mixed state. Conclusions obtained in the present study are summarized as follows.

1) With an increasing frequency, the time dependence of the shielding performance becomes weak. The reason for this is that the phase difference between the induced and the applied magnetic field increases up to π with an increase in the frequency.

2) If the frequency is small enough to suppress the flux flow, the damping coefficient takes a small value. However, once the flux flow occurs, the shielding performance is considerably improved until the damping coefficient approaches to a constant value.

3) The flux creep influences on the magnetic shielding performance against the low-frequency magnetic field, whereas the flux flow has an influence on the high-frequency magnetic shielding.

REFERENCES

[1] S. Ohshima and K. Okuyama: *Jpn. J. Appl. Phys.*, vol. 29, pp. 2403-2406 (1990).
[2] A. Hussain and M. Sayer: *Cryogenics*, vol. 32, pp. 64-68 (1992).
[3] S. Ohshima, H. Ohtsu, A. Kamitani, S. Kambe, and K. Okuyama: *Advances in Superconductivity* V, pp. 1273-1276 (1993).
[4] G. Mizuochi, S. Ohshima, K. Okuyama, A. Kamitani, and S. Ohshima: *Advances in Superconductivity* VII, pp. 1321-1324 (1995).
[5] M. Murakami, S. Gotoh, H. Fujimoto, K. Yamaguchi, N. Koshizuka, and S. Tanaka: *Supercond. Sci. Technol.*, vol. 4, pp. S43-S50 (1991).
[6] A. Kamitani, and S. Ohshima: to be published in *IEICE Trans. Electron.*
[7] C. P. Bean: *Phys. Rev. Lett.*, vol. 8, pp. 250-253 (1962).
[8] H. Hashizume, T. Sugiura, K. Miya, Y. Ando, S. Akita, S. Torii, Y. Kubota, and T. Ogasawara: *Cryogenics*, vol. 31, pp. 601-606 (1991).
[9] A. Kamitani, T. Yokono, M. Shibata, G. Mizuochi, and S. Ohshima: *Advances in Superconductivity* VIII, pp. 1349-1352 (1996).
[10] A. Kamitani, M. Shibata, S. Seki, and S. Ohshima: *Advances in Superconductivity* IX, pp. 1451-1454 (1997).
[11] A. Kamitani, M. Shibata, and S. Ohshima: *IEEE Trans. Appl. Superconductivity*, vol. 7, pp. 2562-2565 (1997).
[12] M. Uesaka, Y. Yoshida, and K. Miya: *Trans. Jpn. Soc. Mech. Eng.*, vol. 60, no. 570C, pp. 126-133 (1994).
[13] M. Uesaka, A. Suzuki, N. Tanaka, Y. Yoshida, and K. Miya: *Cryogenics*, vol. 35, pp. 243-247 (1995).
[14] Y. Yoshida, M. Uesaka, and K. Miya: *IEEE Trans. Magn.*, vol. 30, pp. 3503-3506 (1994).

Numerical Solution for Hybrid of Homogeneous and Inhomogeneous Linear Elliptic PDEs
- Application of Combination Method of FDM and BEM -

Soichiro Ikuno*, Atsushi Kamitani** and Makoto Natori*

*University of Tsukuba

**Yamagata University

The numerical method for solving the hybrid boundary-value problem composed of the homogeneous and the inhomogeneous linear elliptic partial differential equations (PDEs) has been developed. The hybrid problem often appears when the realistic MHD equilibria are determined by solving the Grad-Shafranov equation numerically. Although the combination method of FDM and BEM has been proposed as the method for the solution of the hybrid problem, it takes much CPU time to solve the problem by using the combination method. This is mainly because the iterative method is employed to satisfy the interface conditions precisely. In order to overcome this disadvantage, the non-iterative new method is proposed as the method for solving the hybrid problem. In the new method, the combination method of FDM and BEM is formulated into a set of the simultaneous equations and the equations are directly solved by the Gauss elimination method. The new method is compared with the original one for the simple hybrid problem. The results of computations show that the CPU time required for the new method is about 60 times as small as that for the original method.

Keywords: hybrid of homogeneous and inhomogeneous, PED, FDM, BEM, MHD equilibrium

1. はじめに

　　異媒質がある界面を隔てて接するような物理現象や磁場の表皮時間が領域によって異なる物理現象は2階楕円方偏微分方程式で記述され，同方程式の境界値問題は同次・非同次混合問題に帰着される．姫路工業大学のHIST装置では，プラズマを定常維持するためにダイバータ・コイルを用いて静電的にヘリシティを注入し，プラズマ電流の駆動を行っている．また，同装置ではコイルとプラズマの接触を避けるためにコイルは遮蔽板によって覆われている．そのため，軸対称プラズマの電磁流体力学的平衡の支配方程式であるGrad-Shafranov方程式は領域によって同次方程式，または，非同次方程式となり，同方程式の境界値問題は同次・非同次混合問題に帰着される．そのため，同問題では界面条件や界面情報を高精度で表現するのは必要不可欠となる．

　　本研究の目的は，HIST装置内低アスペクト比トロイダル・プラズマの電磁流体力学的平衡問題を例に取り上げ，有限差分・境界要素併用法を用いて同次・非同次混合問題を数値的に解くことである．さらに，HIST装置内プラズマを無限円柱プラズマと仮定しモデルを簡単化することにより，有限差分・境界要素併用法の高速化についても考える．

　　本研究では，真空の透磁率が $\mu_0 = 1.0$ となる MKS 単位系を用いている．

2. HIST 装置内プラズマの MHD 平衡

　　HIST 装置では，Marshall gun により生成されたプラズマが，flux conserver (FC) と呼ばれる金属製容器内に射出され，同容器内で平衡配位を形成する．その際，プラズマが射出される充分前に，バイアス・コイルにプラズマ電流と同方向の電流を流し，中心対称軸に沿って電流（中心対称軸電流）を流しておく．これらの2種類の電流が生成するバイアス・ポロイダル磁場とトロイダル磁場は，gun から FC に打ち込まれたプラズマの作る磁場との相互作用により，平衡配位を形成するのである．

2.1 解析モデル

HIST 装置では半径 500mm の球形 FC を用いている．FC にはヘリシティ・インジェクタが結合し，その中には矩形断面バイアス・コイルを配置してある．バイアス・コイルはプラズマとの接触を避けるために遮蔽板で覆われている．また，中心対称軸電流を流すため中心対称軸上に沿って半径 57mm の中心導体が挿入されている．本章を通して使用する FC のモデルを Fig. 2.1 に示す．以下では，解析領域を互いに重複しない部分領域 Ω_1, Ω_2 及び Ω_3 に分割する．部分領域 Ω_1 は FC の境界 Γ_1 と遮蔽板 Γ_s と中心導体表面 Γ_3 及び Γ_E に囲まれた領域であり，部分領域 Ω_2 は Γ_s, Γ_2 とバイアス・コイル表面 Γ_D に囲まれる 2 重連結領域を示す．さらに，中心導体の断面領域を Ω_3 とする．

2.2 支配方程式と境界条件

HIST 実験では Mashall gun からプラズマが射出される充分前にバイアス・コイルに電流を流している．この事実を考慮して，平衡配位が形成されたときバイアス・ポロイダル磁場は全空間に拡がっていると仮定する．また，バイアス・コイルは完全導体でできており，磁場はコイル断面内には浸透しないと仮定する．さらに，プラズマの寿命は遮蔽板の表皮時間と比べ充分長く，FC 壁や中心導体の表皮時間に比べ充分短い．故に，平衡状態でのプラズマ電流の作る磁場は遮蔽板の内側領域 Ω_2 には浸透するが，FC 壁の外部及び中心導体内部には浸透しないと仮定できる．また，遮蔽板と鎖交する磁力線上にあるプラズマは磁力線方向の熱伝導のため冷却され消え去る．この事実を反映するため，高温プラズマは遮蔽板と鎖交しない磁力線上にのみ存在すると仮定する．

一般に，トロイダル・プラズマは軸対称であるため，中心対称軸を z 軸とする円柱座標系 (z, r, φ) を用いると，上記仮定のもとで，Grad-Shafranov 方程式は以下のように書き表せる．

$$-\hat{L}\psi = \chi_{\Omega_1}(z, r) f(\lambda, r, \psi) . \tag{2.1}$$

但し，$\chi_{\Omega_1}(z, r)$ は

$$\chi_{\Omega_1}(z, r) \equiv \begin{cases} 1 ; & (z, r) \in \Omega_1 , \\ 0 ; & (z, r) \notin \Omega_1 , \end{cases} \tag{2.2}$$

で定義される特性関数であり，プラズマが領域 Ω_1 内にのみ存在することを特徴づけている．

Browning 等[2]はプラズマの圧力効果を無視し，トロイダル磁場関数 $I(\psi)$ として ψ に関する 2 次関数を採用することにより，低アスペクト比トロイダル・プラズマの平衡配位を求めた．しかしながら，彼らと同じトロイダル磁場関数を用いた場合，プラズマ表面でポロイダル，トロイダルの両電流密度は有限の値をもつ．本研究ではプラズマ表面での電流密度が滑らかに変化するように，参考文献[2]の $I(\psi)$ を改良した．さらに圧力効果を取り入れるため，Gautier 等[3]が用いたプラズマ圧力 $p(\psi)$ を採用し，その $p(\psi)$ にも電流密度の連続性を課した改良を加えた．即ち，$I(\psi)$ 及び $p(\psi)$ として次式を採用した．

$$I(\psi) = \frac{\lambda}{L}(\psi_{axis} - \psi_s)\Theta(\Psi)\left[\sqrt{\Psi^2 + \delta^2}(1 + \sigma\Psi) - \delta^2\sigma\log\left(\Psi + \sqrt{\Psi^2 + \delta^2}\right) - \delta + \delta^2\sigma\log\delta\right] + \frac{I_s}{2\pi} , \tag{2.3}$$

$$\frac{dp}{d\psi} = \frac{\varepsilon}{L^4}(\psi_{axis} - \psi_s)(1 - \Psi) \, \Theta(\Psi) \, S(\Psi) . \tag{2.4}$$
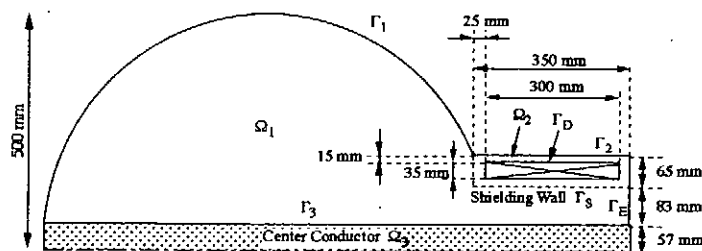
Fig. 2.1 解析モデル．
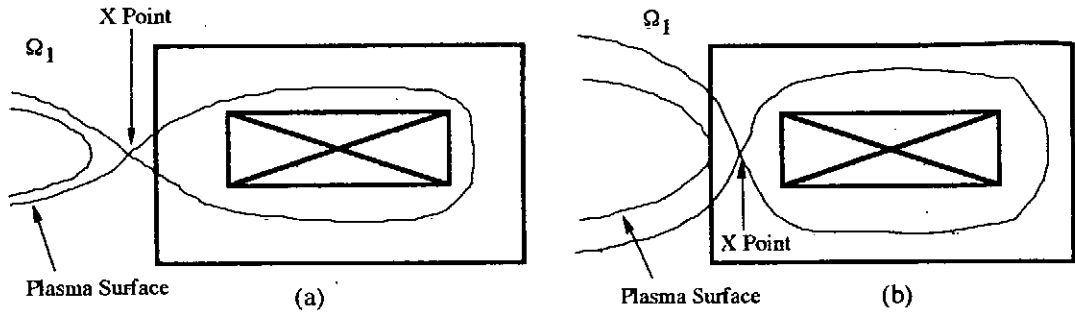
Fig. 2.2　プラズマ表面の磁束関数 ψ_s の決定方法. (a)セパラトリックスが Ω_1 内に存在する場合. (b)セパラトリックスが Ω_1 内に存在しない場合.

但し, I_s は中心対称軸電流を示し, λ, σ, δ は定数である. ここで, σ は磁気軸近傍のポロイダル電流を増加させるパラメタであり, ε はプラズマのベータ値に関連するパラメタである. ここで, L は代表的な長さを示し, 本研究ではFCの半径を採用している. (2.3), (2.4)に現れる Ψ は $\Psi = (\psi - \psi_s)/(\psi_{axis} - \psi_s)$ で定義される規格化された磁束関数であり, ψ_s, ψ_{axis} はそれぞれプラズマ表面及び磁気軸上の ψ の値である. さらに, $\Theta(x)$ 及び $S(x)$ はそれぞれ

$$\Theta(x) \equiv \begin{cases} 1 & ; \quad x > 0 , \\ 0 & ; \quad x < 0 , \end{cases} \tag{2.5}$$

$$S(x) \equiv \frac{x}{\sqrt{x^2 + \delta^2}} , \tag{2.6}$$

で定義される関数である. (2.5)は ψ_s の内部にのみプラズマが存在するという事実を特徴づける関数である. 尚, $\psi_s = \delta = 0$ の場合, (2.3)及び(2.4)は参考文献[4]で用いていたプラズマ圧力及びトロイダル磁場関数の仮定と一致する. 前述したように, 本研究では, 遮蔽板と鎖交しない磁力線上にのみプラズマが存在すると仮定している. この仮定を満足させるため, プラズマ表面上の ψ の値 ψ_s を次式を用いて決定する.

$$\psi_s \equiv \begin{cases} \psi_X; & \text{in case that a X point exists in } \Omega_1 , \\ \underset{(z,r) \in \Gamma_s}{\text{Max}} \psi(z, r); & \text{otherwise.} \end{cases}$$

ここで, ψ_X はX point上での ψ の値を示す. 即ち, Fig. 2.2(a)のようにX pointが領域 Ω_1 内に現れる場合には, セパラトリックスをプラズマ表面とみなし, Fig. 2.2(b)のようにX pointが領域 Ω_1 内に存在しない場合には, 遮蔽板 Γ_s に接する磁気面をプラズマ表面とみなすのである.

次に, (2.1)の境界条件を考えよう. 上述の仮定より Γ_1, Γ_2, Γ_3 及び Γ_B 上での境界条件は,

$$\psi = \psi_D , \tag{2.7}$$

である. 但し, ψ_D はバイアス・コイルの作る磁束を示す. さらに, バイアス・コイルは完全導体であると仮定すると, 境界 Γ_D 上では ψ は未知定数であり, その値はAmpère の法則:

$$\oint_{\Gamma_D} \frac{1}{r} \frac{\partial \psi}{\partial n} d\ell = \frac{I_D}{I_p} \iint_{\Omega_1} \frac{1}{r} f(\lambda, r, \psi) \, dz \, dr , \tag{2.8}$$

により決定される. ここで, I_D 及び I_p はそれぞれバイアス・コイル電流及びプラズマ電流を示し, n は Γ_D 上の外向き単位法線ベクトルを示す.

上記境界条件のもとでGrad-Shafranov方程式(2.1)を解くことにより, HIST装置内プラズマの平衡配位を決定できる.

2.3　Grad-Shafranov 方程式(2.1)の数値解法
2.3.1　非線形固有値問題

支配方程式(2.1)とその境界条件はパラメタ λ, σ, ε, δ, I_s/I_p 及び I_D/I_p をもつ. パラメタ σ, ε, δ, I_s/I_p, I_D/I_p を固定した場合, (2.1)とその境界条件は固有値 λ をもつ非線形固有値問題をなす. 平衡配位は最小固有値に属する固有関数を求めることによって決定できる. 本研究では, プラズマ電流 I_p を一定とする反復法を用いて非線形固有値問題を解いている. 第 m 回目の反復では(2.1)の線形化方程式:

$$-\hat{L}\psi^{(m)} = \chi_{\Omega_1}(z,r)f(\lambda^{(m-1)}, r, \psi^{(m-1)}) \equiv rj_\varphi^{(m-1)}(z,r) , \tag{2.8}$$

の境界値問題を解いて m 回目の近似関数 $\psi^{(m)}$ を決定した後,

$$I_{p0} = \iint_{\Omega_1} \frac{1}{r}f(\lambda^{(m)}, r, \psi^{(m)}) \, dz \, dr , \tag{2.9}$$

を解くことにより m 回目の近似固有値 $\lambda^{(m)}$ を決定する.

　線形化方程式 (2.8) の境界値問題を解く際には, $\psi^{(m)}$ をプラズマ電流 $j_\varphi^{(m-1)}$ が作る磁束 $\psi_p^{(m)}$ とバイアス・ポロイダル磁束 ψ_D の和として

$$\psi^{(m)} = \psi_D + \psi_p^{(m)} ,$$

のように分解し, $\psi_p^{(m)}$, ψ_D を別々に求めている.

2.3.2　バイアス・ポロイダル磁束 ψ_D の決定法

　バイアス・コイル電流はコイル断面内だけを流れるため, コイル断面を除く半開領域内で ψ_D は

$$-\hat{L}\psi_D = 0 , \tag{2.10}$$

を満足する. バイアス・コイル電流 I_D の影響は, 境界条件を通して反映されることになる. 即ち, 境界 Γ_D 上で ψ_D は未知定数であり, その値は Ampère の法則:

$$\oint_{\Gamma_D} \frac{1}{r}\frac{\partial \psi_D}{\partial n} d\ell = \frac{I_D}{I_p}I_{p0} , \tag{2.11}$$

から決定される. (2.10) と上記境界条件は開領域問題を成す. 本研究では, 開領域問題が比較的容易に扱える境界要素法を用いて ψ_D を決定している. ψ_D は I_D/I_p 及び I_{p0} を与えれば決定できる. 即ち, 非線形固有値問題の反復の間 ψ_D の値は変化しない. このため, 非線形固有値問題を解く際には, 前もって ψ_D を一度だけ求めておけばよい.

2.3.3　$\psi_p^{(m)}$ の決定法

　(2.8) から (2.10) を引くことにより, $\psi_p^{(m)}$ の支配方程式:

$$-\hat{L}\psi_p^{(m)} = \chi_{\Omega_1}(z,r)f(\lambda^{(m-1)}, r, \psi^{(m-1)}) \equiv rj_\varphi^{(m-1)}(z,r) , \tag{2.12}$$

を得る. 全く同様に, $\psi^{(m)}$ の境界条件から ψ_D の境界条件を差し引くことにより, $\psi_p^{(m)}$ の境界条件が得られる. その結果, Γ_1, Γ_2, Γ_3 及び Γ_E 上での境界条件は,

$$\psi_p^{(m)} = 0 , \tag{2.13}$$

となる. さらに, Γ_D 上では $\psi_p^{(m)}$ は未知定数となり, その値は

$$\oint_{\Gamma_D} \frac{1}{r}\frac{\partial \psi_p^{(m)}}{\partial n} d\ell = 0 , \tag{2.14}$$

から決定されることになる.

　上記境界条件のもとで, (2.12) を解けば, $\psi_p^{(m)}$ を決定できる. しかしながら, (2.12) は特性関数 (2.2) を含むため, (2.12) の境界値問題は同次・非同次混合問題をとなり界面条件を高精度で表現することが必要不可欠となる. 本研究では, この難点を克服するために支配方程式 (2.12) が 2 階の楕円型偏微分方程式であることに着目して, 関数値 $\psi_p^{(m)}$ とその法線微係数 $\partial\psi_p^{(m)}/\partial n$ が境界 Γ_s を横切って連続に変化するとし, 以下に示す 2 つのステップからなる有限差分・境界要素併用法 [5, 6] を用いて (2.12) の境界値問題を数値的に解いている.

　第 k 回目の反復では, 先ず, 領域 Ω_2 内で境界要素法を用いて同次方程式:

$$-\hat{L}\psi_p^{(m,k)} = 0 , \tag{2.15}$$

の境界値問題を解く. その結果得られた境界 Γ_s 上の $\partial\psi_p^{(m,k)}/\partial n$ の値を境界条件の一部とし, 領域 Ω_1 内で有限差分法を用いて非同次方程式:

$$-\hat{L}\psi_p^{(m,k)} = f(\lambda^{(m-1)}, r, \psi^{(m-1)}) , \tag{2.16}$$

の境界値問題を解く. 但し, 上付き文字 k は有限差分・境界要素併用法での反復回数を示す. この際, 領域 Ω_1 は複雑形状をしているため, 境界適合型曲線座標系 [7] を生成し, 同座標系に基づく差分法を用いている. 上

<div align="center">(a)</div>
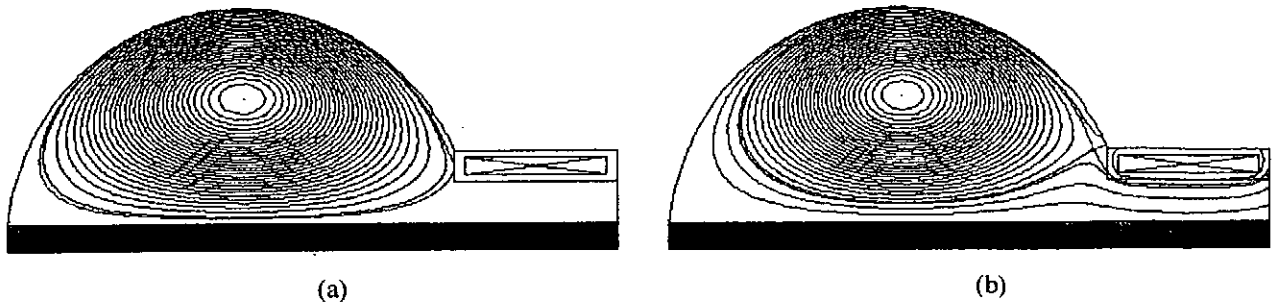<div align="center">(b)</div>

<div align="center">Fig. 2.3　HIST 装置内プラズマの平衡配位. 但し, $\beta_0 = 0.0$, $\sigma = 0.1$, $I_s/I_p = 0.15$.</div>
<div align="center">(a) $I_D/I_p = 0.05$, (b) $I_D/I_p = 0.50$.</div>

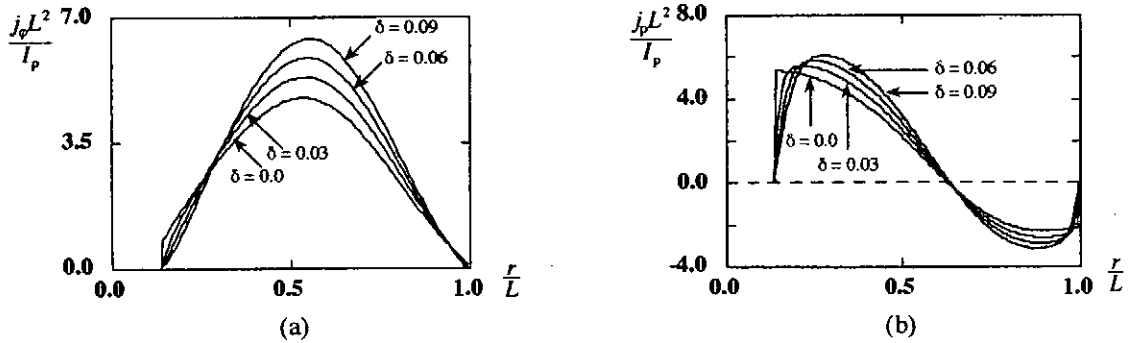
<div align="center">(a)</div>
<div align="center">(b)</div>

Fig. 2.4　$z = z_{axis}$ 平面における (a) トロイダル電流密度と (b) ポロイダル電流密度の分布. 但し, $\beta_0 = \sigma = 0.0$, $I_s/I_p = 0.15$, $I_D/I_p = 0.05$.

記 2 ステップを境界 Γ_s 上の $\psi_p^{(m,k)}$ の値が収束するまで反復すれば, (2.12) の境界値問題の解 $\psi_p^{(m)}$ が得られることになる.

2.3.4　平衡配位

　　上記手法を用いて求めた HIST 装置内プラズマの典型的な平衡配位を Fig. 2.3 に示す. Fig. 2.3(a) では, 遮蔽板と接する磁気面がプラズマ表面となっているのに対し, Fig.2.3(b) ではセパラトリックスがプラズマ表面となっている.

　　Fig. 2.4 に $z = z_{axis}$ におけるトロイダル電流密度 j_φ 及びポロイダル電流密度 j_p の分布を示す. 但し, z_{axis} は磁気軸の z 座標を示す. δ の増加にともない, トロイダル電流密度はプラズマ中心近傍でピーキングしていく. 一方, ポロイダル電流密度は $\delta = 0.0$ の場合, プラズマ表面で不連続となるが, δ が増加するにつれてプラズマ表面で滑らかに変化していく. 即ち, 2.2 節で導入したパラメタ δ は電流分布をプラズマ表面で滑らかに変化させる役割をもっている. このパラメタ δ を導入することにより, 現実的な電流分布を実現することが可能になったと云えよう.

3. 有限差分・境界要素併用法の高速化

　　HIST 装置内低アスペクト比トロイダル・プラズマの MHD 平衡は Grad‐Shafranov 方程式 (2.1) のなす非線形固有値問題を数値的に解くことによって決定できる. しかしながら, 非線形固有値問題の解法では線形化された方程式 (2.8) の境界値問題を解いており, (2.8) の右辺が特性関数 (2.2) を含むため, 同境界値問題は同次・非同次混合問題をなす. 第 2 章では界面条件を精度良く表現するため有限差分・境界要素併用法を導入した.

　　有限差分・境界要素併用法は反復法であり, 第 k 回目の反復は, 以下の 2 つのステップから成る.

1）第 ($k-1$) 回目の反復で得られた近似関数を界面上の境界条件として, 境界要素法を用いて同次問題を解く.

2）1）で得られた近似関数の法線微係数を界面上の新たな境界条件として, 有限差分法を用いて非同次問題を解く. 但し, 解析領域が複雑形状である場合, 領域内に境界適合型曲線座標系を生成し, 同座標系に

<div align="center">— 76 —</div>

基づく有限差分法を用いる.

上記2ステップを界面上の近似関数の値が収束するまで繰り返せば，同次・非同次混合問題の解が得られることになる．有限差分・境界要素併用法は，界面形状が複雑な場合に特に有効な数値解法である．しかしながら，同手法は反復解法であるため，計算時間を消費し過ぎるという難点をもつ．また，各反復で界面上の近似関数の急激な変化を防ぐため，不足緩和を用いている．そのため，反復回数が増大してしまう危険性もある．

本章の目的は，有限差分・境界要素併用法を根本的に見直すことにより，同法の高速化を行うことである．さらに，省メモリ化も議論する．本章では，Grad-Shafranov方程式(2.1)を解くのではなく，無限円柱プラズマであると仮定し，2次元Poisson方程式の同次・非同次混合問題を例として取り上げ，同問題に対する有限差分・境界要素併用法の高速化，省メモリ化を考える．

3.1 Poisson方程式の同次・非同次混合問題

前述したように，本章では2次元Poisson方程式の同次・非同次混合問題を考え，同問題を高速に解く手法を開発する．解析領域は幅2，高さ1の(x, y)平面内の矩形領域である．以下では，線分$x = 1$ $(0 < y < 1)$ を界面Γとし，Γに区切られた左側及び右側の領域をそれぞれΩ_1，Ω_2とする．さらに，領域Ω_1，Ω_2の境界をそれぞれ$\partial\Omega_1$及び$\partial\Omega_2$とし，全領域$\Omega = \Omega_1 \cup \Omega_2$の境界を$\partial\Omega$とする（Fig. 3.1参照）．

全領域Ω内で

$$-\Delta u = \chi_{\Omega_1}(x, y)\, f(x, y)\ , \tag{3.1}$$

が成り立つとし，(3.1)の境界条件としては$\partial\Omega$上で同次ディリクレ条件：

$$u = 0\ , \tag{3.2}$$

を与える．但し，$\chi_{\Omega_1}(x, y)$は，

$$\chi_{\Omega_1}(x, y) = \begin{cases} 1; & (x, y) \in \Omega_1\ , \\ 0; & \text{otherwise}\ , \end{cases}$$

で定義される特性関数であり，非同次項中の関数$f(x, y)$は

$$f(x, y) = 1 - x^2\ ,$$

で与えられるものとする．

(3.1)はΩ_1，Ω_2内でそれぞれ同次，非同次方程式となるため，上記境界値問題(3.1), (3.2)は同次・非同次混合問題をなす．故に，同問題を有限差分・境界要素併用法を用いて解くことができる．以下では記法を簡単にするため，法線微係数$\partial u / \partial n$をqと書くことにする．

3.2 高速化

従来の有限差分・境界要素併用法は反復法であるため計算時間を消費しすぎるという難点をもつ．本節では，従来法を根本から見直し，非反復法を用いて有限差分・境界要素併用法を再定式化しよう．

有限差分・境界要素併用法は，大別すると以下の3つの操作を伴っている．

(a) 同次問題を境界要素法を用いて解く．

(b) 非同次問題を有限差分法を用いて解く．

(c) 界面上で関数値及び法線微係数を合わせる．
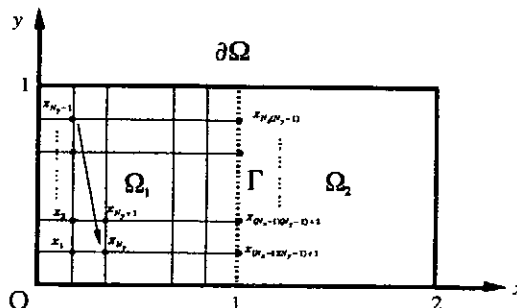
Fig. 3.1 解析領域$\Omega \equiv \Omega_1 \cup \Omega_2$.

従来法では，反復法を用いて(c)の操作を実現している．本節では，上記3つの操作をそれぞれ境界要素法，有限差分法，片側差分法を用いて離散化した後，連立一次方程式にまとめることにより高速化を図る．

先ず，同次問題の境界要素法による離散化について考えよう．領域 Ω_2 内では，

$$-\Delta u = 0 , \tag{3.3}$$

が成立している．(3.3) と等価な境界積分方程式は，

$$c(x_i, y_i) u(x_i, y_i) = \oint_{\partial\Omega_2} \left(u^* q - u \frac{\partial u^*}{\partial n} \right) d\ell , \tag{3.4}$$

で与えられる．但し，u^* は基本解を示し，次式で与えられる．

$$u^*(x, y; x_i, y_i) = \frac{1}{2\pi} \ln\left(\frac{1}{r}\right) .$$

ここで，$r^2 = (x - x_i)^2 + (y - y_i)^2$ である．境界 $\partial\Omega_2$ を N_{BEM} 個の節点をもつ N_{BEM} 個の線形一次要素に分割すると(3.4)は

$$H' u_{\partial\Omega_2} = G q_{\partial\Omega_2} , \tag{3.5}$$

と離散化できる．但し，H', G は影響行列を示し，$u_{\partial\Omega_2}$ 及び $q_{\partial\Omega_2}$ は境界 $\partial\Omega_2$ 上の関数値及び法線微係数に対応する節点ベクトルであり，

$$u_{\partial\Omega_2} \equiv \left[u_1^{BEM}, u_2^{BEM}, \cdots, u_{N_{BEM}}^{BEM} \right]^T , \quad q_{\partial\Omega_2} \equiv \left[q_1^{BEM}, q_2^{BEM}, \cdots, q_{N_{REM}}^{BEM} \right]^T ,$$

で定義する．
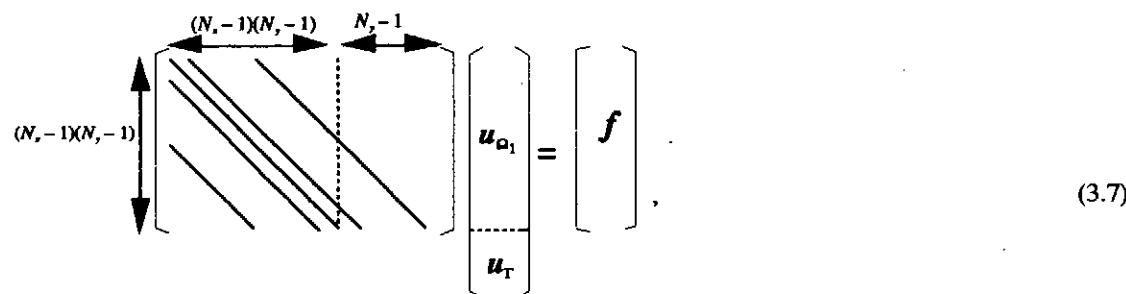
次に，非同次問題の有限差分法による離散化を考えよう．領域 Ω_1 を x, y 方向にそれぞれ N_x, N_y 等分割することにより，Ω_1 内に $(N_x - 1)(N_y - 1)$ 個の格子点を生成する．格子点には辞書的に節点番号を付け（Fig. 3.1参照），さらに，界面 Γ を y 方向に N_y 等分割することにより Γ 上に $N_y - 1$ 個の格子点を生成し，各格子点には y 座標が大きくなる順に，$(N_x - 1)(N_y - 1) + 1, (N_x - 1)(N_y - 1) + 2, \cdots, N_x(N_y - 1)$ と節点番号を付ける（Fig. 3.1参照）．第 j 番目の節点 x_j における u の値を u_j とし，ベクトル u_{Ω_1} 及び u_Γ を

$$u_{\Omega_1} \equiv \left[u_1, u_2, \cdots, u_{(N_x-1)(N_y-1)} \right]^T , \quad u_\Gamma \equiv \left[u_{(N_x-1)(N_y-1)+1}, u_{(N_x-1)(N_y-1)+2}, \cdots, u_{N_x(N_y-1)} \right]^T ,$$

で定義する．有限差分法を用いて Ω_1 内での支配方程式：

$$-\Delta u = f(x, y) , \tag{3.6}$$

を離散化すると，

$$\tag{3.7}$$

を得る．但し，f は

$$f \equiv \left[f(x_1), f(x_2), \cdots, f(x_{(N_x-1)(N_y-1)}) \right]^T ,$$

で定義されるベクトルを示す．ここで，注意しなければならないのは，$(N_x - 2)(N_y - 1) < i \leq (N_x - 1)(N_y - 1)$ を満たす i に対して u_i を計算する際，ベクトル u_Γ を用いていることである．そのため，(3.7)の係数行列は非正方行列となる．

最後に，(c)を離散化しよう．支配方程式(3.1)が2階偏微分方程式であるから，界面 Γ を横切る際に関数値 u とその法線微係数 $\partial u / \partial n$ が連続に変化するとし，界面条件を課す．即ち，

$$q_k^{BEM} = -\frac{1}{\Delta x}(u_{k+(N_x-1)(N_y-1)} - u_{k+(N_x-2)(N_y-1)}) , \quad (k = 1, 2, \cdots, N_y - 1) \tag{3.8}$$

$$u_k^{BEM} = u_{k+(N_x-1)(N_y-1)} , \quad (k = 1, 2, \cdots, N_y - 1) \tag{3.9}$$

が成立する．但し，Δx は領域 Ω_1 内の x 方向の刻み幅であり，$\Delta x = 1 / N_x$ で与えられる．但し，(3.8)の右辺では q を求めるのに1次精度の後退差分を用いて離散化している．(3.8), (3.9)を書き直すことにより，

$$
\begin{bmatrix}
 & & & & & \\
 & & & & E & \\
 & & & & &
\end{bmatrix}
\begin{bmatrix}
u_{(N_x-2)(N_y-1)+1} \\
\vdots \\
u_{(N_x-1)(N_y-1)} \\
\hline
u_\Gamma \\
\hline
q_1^{\mathrm{BEM}} \\
\vdots \\
q_{N_y-1}^{\mathrm{BEM}}
\end{bmatrix}
=
\begin{bmatrix}
0
\end{bmatrix}
\tag{3.10}
$$

を得る．ここで，境界節点を定義する際に，Γ上の $x_{(N_x-1)(N_y-1)+1}$ を始点とし，時計周りに番号付けをしている．この番号付けをすると，(3.7) の係数行列と (3.10) の係数行列の帯幅が等しくなり，(3.7)，(3.10) 各々の係数行列を一つにまとめる際に都合がよい．さらに，次節で説明する省メモリ化でも非常に有効となる．

以上で求めた (3.5)，(3.7)，(3.10) をまとめると，連立一次方程式：

$$
\begin{bmatrix}
 & & & & O \\
 & & & N_y-1 & \\
 & & & & \\
 & & & E & \\
O & H & -G &
\end{bmatrix}
\begin{bmatrix}
u_{\Omega_1} \\
\hline
u_\Gamma \\
\hline
q_{\partial\Omega_2}
\end{bmatrix}
=
\begin{bmatrix}
f \\
\hline
0 \\
\hline
0
\end{bmatrix}
\tag{3.11}
$$

を得る．但し，E は単位行列を示し，H は (3.5) 内の影響行列 H′ に対して境界条件 (3.2) を考慮することによって得られる行列である．即ち，H は $1 \le i \le N_y-1$, $1 \le j \le N_{\mathrm{BEM}}$ を満たす H′ の i 行 j 列を取り出した部分行列である．(3.11) を数値的に解くことにより領域 Ω_1 内の関数値，界面 Γ 上の関数値及び境界 $\partial\Omega_2$ 上の法線微係数が決定できる．即ち，反復することなく関数値及び法線微係数が決定できる．

(3.7) の係数行列は有限差分法によって離散化された行列であるため対角優位性をもつのに対し，(3.10) の係数行列は対角優位性をもたない．これらの性質を考慮することにより，前進消去を行う際に対角優位性及び非対角優位性をもつ部分にそれぞれ部分軸選択無し及び部分軸選択付き Gauss の消去法を用いている．

3.3 省メモリ化

(3.11) を数値的に解けば同次・非同次混合問題 (3.1)，(3.2) の解を得ることができる．しかしながら，(3.7) の係数行列は半帯幅 N_y-1 をもつ帯行列であるため，領域 Ω_1 の分割数を増加するにともない (3.11) の係数行列は大型疎行列となる．その結果，係数行列を格納するためのメモリ使用量は莫大なものとなる．本節では，この難点を克服するために省メモリ化 [8] について考えよう．

先ず，有限差分法で離散化された (3.7) の係数行列は半帯幅が N_y-1 の帯行列であるので，$(N_x-1)(N_y-1)\times(2N_y-1)$ 行列 B を用意し，(3.7) の係数行列の帯内部の要素を行列 B に格納する．係数行列と行列 B の要素をそれぞれ $a_{i,j}$, $b_{i,j}$ とすると，(3.7) の係数行列と行列 B の対応関係は，

$$
a_{i,j}=
\begin{cases}
b_{i,j-i+N_y}; & i \le j \le i+N_y-1 , \\
b_{i,i-j+1}; & j \le i \le j+N_y-1 ,
\end{cases}
\tag{3.12}
$$

となる．(3.10) の係数行列も半帯幅が N_y-1 の帯行列である．全く同様に (3.12) 関係を用いて (N_y-1) 行 $(2N_y-1)$ 列の行列 F に格納する．ここで，行列 B の前進消去を行う場合，$f_{i,j}$（但し，$1 \le i,j \le N_y-1$）の情報は必要不

可欠である．ここで，$f_{i,j}$は行列Fの要素を示す．本研究では，行列B，Fを一つにまとめて計算を行っている．その具体形は

$$
\qquad (3.13)
$$

となる．3.2節で述べたように，$(N_x - 1)(N_y - 1)$ 行までは対角優位性があるため部分軸選択無しGaussの消去法により前進消去を行う．

　次に，境界要素法を用いて離散化した後に得られる影響行列について考えよう．連立方程式 (3.11) で $(N_x - 1)(N_y - 1)$ 段まで前進消去が終了したとき，$(N_x - 1)(N_y - 1) < i \leq N_x(N_y - 1)$，$(N_x - 2)(N_y - 1) < j \leq (N_x - 1)(N_y - 1)$ を満たす i 行 j 列には全て零が入っている．この事実を考慮し，行列Fと影響行列を以下に示すように格納する．

$$
\qquad (3.14)
$$
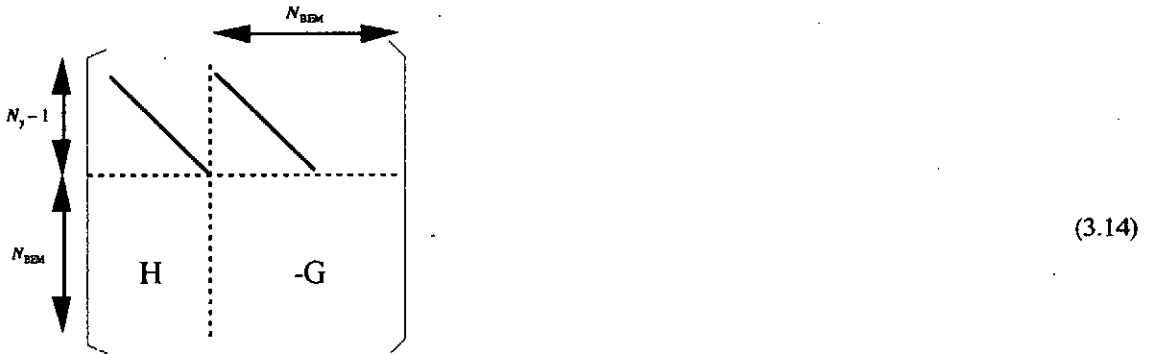
(3.14) は対角優位性がないため軸選択付きGaussの消去法を用いて前進消去を行う．

　(3.13) 及び (3.14) を用いれば改良された有限差分・境界要素併用法の省メモリ化を行うことができる．加えて，零要素に対して不要な計算をしないため，省メモリ化が高速化にもつながる．次節では，従来法と改良法とを比較することにより，本章で導入した手法の有効性を調べる．

3.4　結果

　本節では，改良された有限差分・境界要素併用法の有効性を示すために，解析領域 Ω 全体を有限差分法のみで解いた関数値 u と比較する．

　Fig. 3.2 に同次・非同次混合問題 (3.1)，(3.2) を有限差分法，従来の有限差分・境界要素併用法，高速化された有限差分・境界要素併用法の3つの方法で解いた場合のCPU時間を非同次問題領域 Ω_i の分割数 $N(= N_x = N_y)$ の関数として示す．Fig. 3.2から分かるように，高速化を施した有限差分・境界要素併用法は従来法に比べて，分割数 N には関係なく，常に計算時間は短い．特に $N = 60$ の場合は，従来の方法に比べて約70倍程度の速度向上が得られている．また，Fig. 3.3 に有限差分・境界要素併用で得られた解と有限差分法で得られた解の相対誤差の分割数 N に対する変化を示す．Fig. 3.3 より，分割数の増加とともに解の精度が向上していることが分かる．即ち，第2章で用いた有限差分・境界要素併用法は同次・非同次混合問題に対して有効な解法であると云えるであろう．
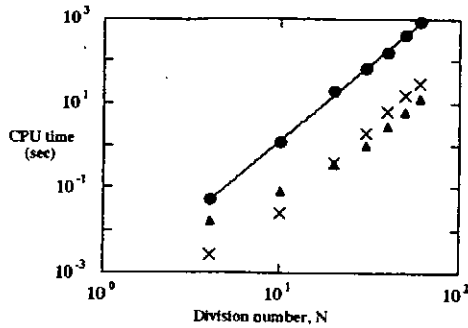
Fig. 3.2 　Ω$_1$内の分割数Nに対するCPU時間の変化.
●：有限差分・境界要素併用法, ×：有限差分法,
▲：高速化された有限差分・境界要素併用法.
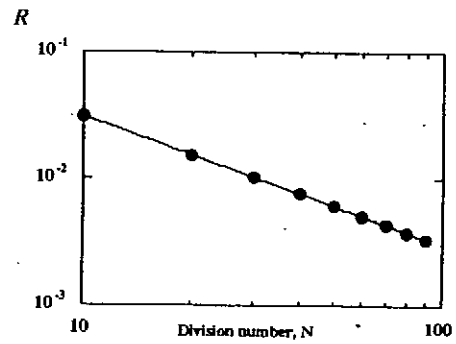
Fig. 3.3 　有限差分・境界要素併用法で得られた解
u_{combi}と有限差分法だけで得られた解u_{full}の相対誤差R
の 分 割 数 N に 対 す る 変 化. 但 し ,
$R = \left\| u_{full} - u_{combi} \right\| / \left\| u_{full} \right\|$ である.

4 　結論

本研究では, HIST装置内低アスペクト比トロイダル・プラズマの現実的な電磁流体力学的平衡を数値的
に求めるため, トロイダル磁場関数とプラズマ圧力に改良を加え, 定常維持部を現実的にモデル化した. 導入
したGrad-Shafranov方程式は非線形固有値問題を成すため, 線形化された後, 同方程式の境界値問題は同次・
非同次混合問題となる. 本研究では, 有限差分・境界要素併用法を用いて, 同次・非同次混合問題を数値的に
解いた. さらに, 無限円柱プラズマと仮定することによりモデルを簡単化し, 有限差分・境界要素併用法の高
速化についても考えた. 本研究で得られた結果をまとめると以下のようになる.

1. 　有限差分・境界要素併用法の２つの手続きである同次問題の境界要素法による解法と非同次問題の有限
差分法による解法を１つにまとめることによって高速化を行った.
2. 　有限差分法で離散化された係数行列は対角優位性をもつため, 部分軸選択無しGaussの消去法を用いて
前進消去を行い, 界面条件を離散化した後に得られる係数行列と境界要素法で得られる影響行列は対角
優位性がないため部分軸選択Gaussの消去法で前進消去を行った.
3. 　有限差分法, 境界要素法で得られた２つの行列を別々に格納し, メモリの節約を図った.
4. 　従来の有限差分・境界要素併用法に比べ, 高速化された有限差分・境界要素併用法は約７０倍の速度向
上が得られた.

本研究で解いた同次・非同次混合問題は, 非線形固有値問題の反復解法の中に含まれているため, 連立一
次方程式(3.11)の左辺係数行列は反復の間変化することはない. 即ち, １回だけLU分解をしておけば非線形
固有値問題の反復の間, 後退代入の手続きだけでよいため, さらなる速度向上が期待できる. また, 境界適合
型曲線座標系[7]に基づいた有限差分法を用いた場合, 連立一次方程式(3.11)の左辺係数行列は非対称行列と
なるが, 同問題に拡張するのは容易であると考えられる.

参考文献

[1] 　M. Nagata, N. Fukumoto, M. Haruoka, T. Kanki, K. Kuramoto and T. Uyama: Proc. US-Japan Workshop on the
Spherical Torus and Low Aspect Ratio Tokamaks 2 (1996) 717-730.
[2] 　P. K. Browning, L. R. Clegg, R. C. Duck and M. G. Rusbridge:Plasma Phys. Control. Fusion 35 (1993) 1563-1583.
[3] 　P. Gautier, R. Gruber and F. Troyon: Nucl. Fusion 21 (1981) 1399 - 1407.
[4] 　生野壮一郎, 神谷淳, 名取亮 : 日本 AEM 学会誌 6 (1998) 63 - 68.
[5] 　A. Kamitani, T. Kanki, M. Nagata and T. Uyama: Periodica Polytechnica Ser. El. 38 (1994) 257 - 266.
[6] 　T. Kanki, M. Nagata, T. Uyama, S. Ikuno and A. Kamitani: J. Phys. Soc. Jpn. 67 (1998) 140 - 146.
[7] 　J. F. Thompson, F. C. Thames and C. W. Mastin: J. Comp. Phys. 24 (1977) 274 - 302.
[8] 　菊池文雄著 :『有限要素法概説』(サイエンス社, 東京, 1980) p.78 - p.80.

ニューマーク法に対するエネルギー評価を用いた安定性解析と誤差解析

(Stability and error analyses by energy estimate for Newmark's method)

CHIBA, Fumihiro* and KAKO, Takashi†

*Doctor Course Student, Dep. Computer Science and Information Mathematics,

The University of Electro-Communications

†Dep. Computer Science and Information Mathematics,

The University of Electro-Communications

Abstract

For the second order time evolution equation with a general dissipation term, we consider the condition of stability for Newmark's method[10]. We treat the case that a coefficient linear operator C in the dissipation term is constant in time and nonnegative: $C \geq 0$. We give the proofs of stability and convergence of the scheme by an energy method. We apply the results to a model resistive MHD equation[6].

Keywords: Newmark's method, second order time evolution equation, dissipation term, stability, error analysis, energy estimate, recurrence relation

1. Newmark's method

We consider Newmark's method for the second order time evolution equation in $\mathbf{R}^n$. Let C and K be linear operators on $\mathbf{R}^n$ and constants in time t, and $f(t)$ be a given function on $[0, \infty)$. We consider the following second order time evolution equation:

$$\frac{d^2}{dt^2}u(t) + C\frac{d}{dt}u(t) + Ku(t) = f(t). \tag{1}$$

Let $A(t)$, $V(t)$ and $U(t)$ be approximations of $\frac{d^2}{dx^2}u(t)$, $\frac{d}{dx}u(t)$ and $u(t)$ respectively, then Newmark's method for (1) is described as

$$\begin{cases} A(t) + CV(t) + KU(t) = f(t) \\ U(t+\tau) = U(t) + \tau V(t) + \frac{1}{2}\tau^2 A(t) + \beta\tau^2(A(t+\tau) - A(t)) \\ V(t+\tau) = V(t) + \tau A(t) + \gamma\tau(A(t+\tau) - A(t)). \end{cases} \tag{2}$$

2. Iteration scheme of Newmark's method

In Newmark's method, the approximation sequence $U(t), t = t_0, t_0 + \tau, \cdots, t_0 + n\tau$, is generated by the following iteration scheme:

*chiba@im.uec.ac.jp

†kako@im.uec.ac.jp

- 1. For $t = t_0$, compute $A(t)$ from initial data $U(t)$ and $V(t)$:

$$A(t) = f(t) - (C\,V(t) + K\,U(t)).$$

- 2. Compute $A(t + \tau)$ from $f(t + \tau)$, $U(t)$, $V(t)$ and $A(t)$:

$$A(t+\tau) = (I + \gamma\tau C + \beta\tau^2 K)^{-1}$$
$$\times[-KU(t) - (C + \tau K)V(t) + \{(\gamma - 1)\tau C + (\beta - \tfrac{1}{2})\tau^2 K\}A(t) + f(t+\tau)].$$

- 3. Compute $U(t + \tau)$ from $U(t)$, $V(t)$, $A(t)$ and $A(t + \tau)$:

$$U(t+\tau) \;=\; U(t) + \tau V(t) + \tfrac{1}{2}\tau^2 A(t) + \beta\tau^2(A(t+\tau) - A(t)).$$

- 4. Compute $V(t + \tau)$ from $V(t)$, $A(t)$ and $A(t + \tau)$:

$$V(t+\tau) = V(t) + \tau A(t) + \gamma\tau(A(t+\tau) - A(t)).$$

- 5. Replace t by $t + \tau$, and return to 2.

3. Recurrence relation of Newmark's method

Newmark's method (2) for (1) is reformulated as follows in the recurrence relation([1],[2] and Chaix-Leleux[12]). Eliminating V and A from (2), we have

$$(I + \gamma\tau C + \beta\tau^2 K)U(t+\tau) + \{-2I + \tau(1 - 2\gamma)C + \frac{1}{2}\tau^2(1 - 4\beta + 2\gamma)K\}U(t)$$
$$+\{I + \tau(-1 + \gamma)C + \tfrac{1}{2}\tau^2(1 + 2\beta - 2\gamma)K\}U(t - \tau) \tag{3}$$
$$= \beta\tau^2 f(t+\tau) + \tfrac{1}{2}\tau^2(1 - 4\beta + 2\gamma)f(t) + \tfrac{1}{2}\tau^2(1 + 2\beta - 2\gamma)f(t - \tau).$$

By using difference operators, (3) is represented as

$$(I + \beta\tau^2 K)D_{\tau\bar{\tau}}U(t) + \gamma C D_\tau U(t) + \{(1 - \gamma)C + \tau(\gamma - \tfrac{1}{2})K\}D_{\bar{\tau}}U(t) + KU(t) \tag{4}$$
$$= \{I + \tau(\gamma - \tfrac{1}{2})D_{\bar{\tau}} + \beta\tau^2 D_{\tau\bar{\tau}}\}f(t),$$

where

$$\begin{cases} D_\tau U(t) = \frac{1}{\tau}(U(t + \tau) - U(t)) \\ D_{\bar{\tau}}U(t) = \frac{1}{\tau}(U(t) - U(t - \tau)) \\ D_{\tau\bar{\tau}}U(t) = \frac{1}{\tau}(D_\tau U(t) - D_{\bar{\tau}}U(t)). \end{cases} \tag{5}$$

Especially, in the case $\gamma = \tfrac{1}{2}$, we have:

$$(I + \beta\tau^2 K)D_{\tau\tau}U(t) + \frac{1}{2}C(D_\tau + D_{\bar{\tau}})U(t) + KU(t) = (I + \beta\tau^2 D_{\tau\bar{\tau}})f(t).$$

These recurrence relations are useful for the stability and error analyses of Newmark's method. See [8] and [11] for the case with $C \equiv 0$.

4. Stability analysis by energy estimate

Taking a scalar-product between (4) and $(D_\tau + D_{\bar{\tau}})U(t)$, we can derive an energy inequality for Newmark's method. From this inequality, we obtain the stability conditions for Newmark's method. In the following, we use the usual Euclidean scalar product $(\cdot, \cdot)$ and the corresponding the norm $\| \cdot \|$ in $\mathbf{R}^n$.

4.1 Derivation of an energy inequality

From now on, let $C, K \geq 0$ and $f(t) \equiv 0$. We also assume that

$$\gamma \geq \frac{1}{2}. \tag{6}$$

Using (4), we derive an energy inequality(see [1],[2] for the case $\gamma = \frac{1}{2}$). Rearranging (4), we have

$$(I + \beta\tau^2 K)D_{\tau\bar{\tau}}U(t) + \frac{1}{2}C(D_\tau + D_{\bar{\tau}})U(t) + (\gamma - \frac{1}{2})C(D_\tau - D_{\bar{\tau}})U(t) \\ + \tau(\gamma - \frac{1}{2})KD_{\bar{\tau}}U(t) + KU(t) = 0. \tag{7}$$

We take a scalar-product between (7) and $(D_\tau + D_{\bar{\tau}})U(t)$. Since C is nonnegative, we have

$$((I + \beta\tau^2 K)D_{\tau\bar{\tau}}U(t), (D_\tau + D_{\bar{\tau}})U(t)) + (\gamma - \frac{1}{2})(C(D_\tau - D_{\bar{\tau}})U(t), (D_\tau + D_{\bar{\tau}})U(t)) \\ + \tau(\gamma - \frac{1}{2})(KD_{\bar{\tau}}U(t), (D_\tau + D_{\bar{\tau}})U(t)) + (KU(t), (D_\tau + D_{\bar{\tau}})U(t)) \\ = -(\frac{1}{2}C(D_\tau + D_{\bar{\tau}})U(t), (D_\tau + D_{\bar{\tau}})U(t)) \leq 0. \tag{8}$$

We estimate each term in the left hand of (8) as follows. The first term is written as follows:

$$((I + \beta\tau^2 K)D_{\tau\bar{\tau}}U(t), (D_\tau + D_{\bar{\tau}})U(t)) \\ = \frac{1}{\tau^2}((I + \beta\tau^2 K)(D_\tau U(t) - D_{\bar{\tau}}U(t)), (U(t + \tau) - U(t)) + (U(t) - U(t - \tau))) \\ = \frac{1}{\tau^3}((I + \beta\tau^2 K)(U(t + \tau) - U(t)), U(t + \tau) - U(t)) \\ - \frac{1}{\tau^3}((I + \beta\tau^2 K)(U(t) - U(t - \tau)), U(t) - U(t - \tau)). \tag{9}$$

The second term is transformed as follows:

$$(\gamma - \frac{1}{2})(C(D_\tau - D_{\bar{\tau}})U(t), (D_\tau + D_{\bar{\tau}})U(t)) \\ = (\gamma - \frac{1}{2})\{(CD_\tau U(t), D_\tau U(t)) - (CD_{\bar{\tau}}U(t), D_{\bar{\tau}}U(t))\} \\ = (\gamma - \frac{1}{2})\{(CD_\tau U(t), D_\tau U(t)) - (CD_\tau U(t - \tau), D_\tau U(t - \tau))\}. \tag{10}$$

For the third term, we decompose $D_{\bar{\tau}}U(t)$ into a symmetric part and an anti-symmetric part with respect to D_τ and $D_{\bar{\tau}}$:

$$\tau(\gamma - \frac{1}{2})(KD_{\bar{\tau}}U(t), (D_\tau + D_{\bar{\tau}})U(t)) \\ = \tau(\gamma - \frac{1}{2})(K\{\frac{1}{2}(D_\tau + D_{\bar{\tau}})U(t) - \frac{1}{2}(D_\tau - D_{\bar{\tau}})U(t)\}, (D_\tau + D_{\bar{\tau}})U(t)) \\ = \frac{1}{2}\tau(\gamma - \frac{1}{2})(K(D_\tau + D_{\bar{\tau}})U(t), (D_\tau + D_{\bar{\tau}})U(t)) \\ - \frac{1}{2}\tau(\gamma - \frac{1}{2})(K(D_\tau - D_{\bar{\tau}})U(t), (D_\tau + D_{\bar{\tau}})U(t)) \\ = \frac{1}{2}\tau(\gamma - \frac{1}{2})\|K^{1/2}(D_\tau + D_{\bar{\tau}})U(t)\|^2 - \frac{1}{2}\tau(\gamma - \frac{1}{2})(KD_\tau U(t), D_\tau U(t)) \\ + \frac{1}{2}\tau(\gamma - \frac{1}{2})(KD_\tau U(t - \tau), D_\tau U(t - \tau)). \tag{11}$$

The fourth term is deformed as

$$(KU(t), (D_\tau + D_{\bar{\tau}})U(t)) \\ = (K^{1/2}U(t), K^{1/2}U(t + \tau)) - (K^{1/2}U(t), K^{1/2}U(t - \tau)) \\ = (K^{1/2}U(t + \tau), K^{1/2}U(t)) - (K^{1/2}U(t), K^{1/2}U(t - \tau)). \tag{12}$$

Multiplying (8) by τ^3 and using the above formulas, we have

$$((I + \beta\tau^2 K)(U(t + \tau) - U(t)), U(t + \tau) - U(t)) + (\tau^2 K^{1/2}U(t + \tau), K^{1/2}U(t)) \\ \quad + \tau(\gamma - \frac{1}{2})(C(U(t + \tau) - U(t)), U(t + \tau) - U(t)) \\ \quad + \frac{1}{2}\tau^4(\gamma - \frac{1}{2})\|K^{1/2}(D_\tau + D_{\bar{\tau}})U(t)\|^2 - \frac{1}{2}\tau^4(\gamma - \frac{1}{2})(KD_\tau U(t), D_\tau U(t)) \\ \leq ((I + \beta\tau^2 K)(U(t) - U(t - \tau)), U(t) - U(t - \tau)) + (\tau^2 KU(t), U(t - \tau)) \\ \quad + \tau(\gamma - \frac{1}{2})(C(U(t) - U(t - \tau)), U(t) - U(t - \tau)) \\ \quad - \frac{1}{2}\tau^4(\gamma - \frac{1}{2})(KD_\tau U(t - \tau), D_\tau U(t - \tau)). \tag{13}$$

Since $\gamma - \frac{1}{2} \geq 0$, we can omit $\frac{1}{2}\tau^4(\gamma - \frac{1}{2})\|K^{1/2}(D_\tau + D_{\bar\tau})U(t)\|^2$ from the left hand side of (13). So, we have

$$
\begin{aligned}
&((I + \beta\tau^2 K)(U(t+\tau) - U(t)), U(t+\tau) - U(t)) + \tau^2(KU(t+\tau), U(t)) \\
&\quad + \tau(\gamma - \tfrac{1}{2})(C(U(t+\tau) - U(t)), U(t+\tau) - U(t)) - \tfrac{1}{2}\tau^4(\gamma - \tfrac{1}{2})(KD_\tau U(t), D_\tau U(t)) \\
&\leq ((I + \beta\tau^2 K)(U(t) - U(t-\tau)), U(t) - U(t-\tau)) + \tau^2(KU(t), U(t-\tau)) \\
&\quad + \tau(\gamma - \tfrac{1}{2})(C(U(t) - U(t-\tau)), U(t) - U(t-\tau)) - \tfrac{1}{2}\tau^4(\gamma - \tfrac{1}{2})(KD_\tau U(t-\tau), D_\tau U(t-\tau)).
\end{aligned}
\tag{14}
$$

Dividing (14) by τ^2, we obtain

$$
\begin{aligned}
&((I + \beta\tau^2 K)D_\tau U(t), D_\tau U(t)) + (KU(t+\tau), U(t)) \\
&\quad + \tau(\gamma - \tfrac{1}{2})(CD_\tau U(t), D_\tau U(t)) - \tfrac{1}{2}\tau^2(\gamma - \tfrac{1}{2})(KD_\tau U(t), D_\tau U(t)) \\
&\leq ((I + \beta\tau^2 K)D_\tau U(t-\tau), D_\tau U(t-\tau)) + (KU(t), U(t-\tau)) \\
&\quad + \tau(\gamma - \tfrac{1}{2})(CD_\tau U(t-\tau), D_\tau U(t-\tau)) - \tfrac{1}{2}\tau^2(\gamma - \tfrac{1}{2})(KD_\tau U(t-\tau), D_\tau U(t-\tau)).
\end{aligned}
\tag{15}
$$

Using (15) repeatedly, we have

$$
\begin{aligned}
&((I + \beta\tau^2 K)D_\tau U(t), D_\tau U(t)) + (KU(t+\tau), U(t)) \\
&\quad + \tau(\gamma - \tfrac{1}{2})(CD_\tau U(t), D_\tau U(t)) - \tfrac{1}{2}\tau^2(\gamma - \tfrac{1}{2})(KD_\tau U(t), D_\tau U(t)) \\
&\leq ((I + \beta\tau^2 K)D_\tau U(0), D_\tau U(0)) + (KU(\tau), U(0)) \\
&\quad + \tau(\gamma - \tfrac{1}{2})(CD_\tau U(0), D_\tau U(0)) - \tfrac{1}{2}\tau^2(\gamma - \tfrac{1}{2})(KD_\tau U(0), D_\tau U(0)).
\end{aligned}
\tag{16}
$$

Rearranging the right hand of (16), we define

$$
\begin{aligned}
C_0 &\equiv ((I + \beta\tau^2 K)D_\tau U(0), D_\tau U(0)) + (KU(\tau), U(0)) \\
&\quad + \tau(\gamma - \tfrac{1}{2})(CD_\tau U(0), D_\tau U(0)) - \tfrac{1}{2}\tau^2(\gamma - \tfrac{1}{2})(KD_\tau U(0), D_\tau U(0)) \\
&= \|D_\tau U(0)\|^2 + \tau^2(\beta - \tfrac{1}{2}\gamma + \tfrac{1}{4})\|K^{1/2}D_\tau U(0)\|^2 \\
&\quad + \tau(KD_\tau U(0), U(0)) + \|K^{1/2}U(0)\|^2 + \tau(\gamma - \tfrac{1}{2})\|C^{1/2}D_\tau U(0)\|^2.
\end{aligned}
\tag{17}
$$

Rearranging the left hand side of (16) and using the identity:

$$
(KU(t+\tau), U(t)) = \tau(KD_\tau U(t), U(t)) + (KU(t), U(t)),
$$

we get

$$
\begin{aligned}
&((I + \beta\tau^2 K)D_\tau U(t), D_\tau U(t)) + (KU(t+\tau), U(t)) \\
&\quad + \tau(\gamma - \tfrac{1}{2})(CD_\tau U(t), D_\tau U(t)) - \tfrac{1}{2}\tau^2(\gamma - \tfrac{1}{2})(KD_\tau U(t), D_\tau U(t)) \\
&= \|D_\tau U(t)\|^2 + \tau^2(\beta - \frac{1}{2}\gamma + \frac{1}{4})\|K^{1/2}D_\tau U(t)\|^2 \\
&\quad + \tau(K^{1/2}D_\tau U(t), K^{1/2}U(t)) + \|K^{1/2}U(t)\|^2 + \tau(\gamma - \tfrac{1}{2})\|C^{1/2}D_\tau U(t)\|^2.
\end{aligned}
\tag{18}
$$

So, we have

$$
\begin{aligned}
&\|D_\tau U(t)\|^2 + \tau^2(\beta - \frac{1}{2}\gamma + \frac{1}{4})\|K^{1/2}D_\tau U(t)\|^2 \\
&\quad + \tau(K^{1/2}D_\tau U(t), K^{1/2}U(t)) + \|K^{1/2}U(t)\|^2 + \tau(\gamma - \tfrac{1}{2})\|C^{1/2}D_\tau U(t)\|^2 \leq C_0.
\end{aligned}
\tag{19}
$$

We now estimate the third term of (19). For a positive α, we have

$$
\begin{aligned}
&|\tau(K^{1/2}D_\tau U(t), K^{1/2}U(t))| \\
&\leq \tau \|K^{1/2}D_\tau U(t)\| \times \alpha \times \frac{1}{\alpha} \times \|K^{1/2}U(t)\| \leq \frac{1}{2}\{\alpha^2\tau^2\|K^{1/2}D_\tau U(t)\|^2 \frac{1}{\alpha^2}\|K^{1/2}U(t)\|^2\}.
\end{aligned}
\tag{20}
$$

Applying this inequality to (19), we get

$$\|D_\tau U(t)\|^2 + \tau^2\{\beta - \frac{1}{2}\tau^2(\gamma - \frac{1}{2})\}\|K^{-1/2}D_\tau U(t)\|^2 + \tau(\gamma - \frac{1}{2})\|C^{1/2}D_\tau U(t)\|^2 + \|K^{1/2}U(t)\|^2$$
$$\leq C_0 - \tau(K^{-1/2}D_\tau U(t), K^{1/2}U(t)) \leq C_0 + \frac{1}{2}\{\alpha^2\tau^2\|K^{-1/2}D_\tau U(t)\|^2 + \frac{1}{\alpha^2}\|K^{1/2}U(t)\|^2\}. \tag{21}$$

So, we have

$$\|D_\tau U(t)\|^2 + \tau^2\{\beta - \frac{1}{2}(\gamma - \frac{1}{2}) - \frac{1}{2}\alpha^2\}\|K^{-1/2}D_\tau U(t)\|^2$$
$$+\tau(\gamma - \frac{1}{2})\|C^{1/2}D_\tau U(t)\|^2 + (1 - \frac{1}{2\alpha^2})\|K^{1/2}U(t)\|^2 \leq C_0. \tag{22}$$

Since $\tau(\gamma - \frac{1}{2}) \geq 0$, we can neglect $\tau(\gamma - \frac{1}{2})\ \|C^{1/2}D_\tau U(t)\|^2$ and get the estimate

$$C_0 \geq \|D_\tau U(t)\|^2 + \tau^2\{\beta - \frac{1}{2}(\gamma - \frac{1}{2}) - \frac{1}{2}\alpha^2\}\|K^{-1/2}D_\tau U(t)\|^2$$
$$+\tau(\gamma - \frac{1}{2})\|C^{1/2}D_\tau U(t)\|^2 + (1 - \frac{1}{2\alpha^2})\|K^{1/2}U(t)\|^2 \tag{23}$$
$$\geq \quad \|D_\tau U(t)\|^2 + \tau^2\{\beta - \frac{1}{2}(\gamma - \frac{1}{2}) - \frac{1}{2}\alpha^2\}\|K^{-1/2}D_\tau U(t)\|^2 + (1 - \frac{1}{2\alpha^2})\|K^{1/2}U(t)\|^2.$$

Finally we obtain the energy estimate:

$$\|D_\tau U(t)\|^2 + \tau^2\{\beta - \frac{1}{2}(\gamma - \frac{1}{2}) - \frac{1}{2}\alpha^2\}\|K^{-1/2}D_\tau U(t)\|^2 + (1 - \frac{1}{2\alpha^2})\|K^{1/2}U(t)\|^2 \leq C_0. \tag{24}$$

4.2 Stability conditions

In this section, using (24) we derive stability conditions for Newmark's method under the condition $\gamma \geq \frac{1}{2}$. With respect to a parameter β, we consider the following two cases.

4.2.1 Case 1 ($\beta \geq \frac{1}{2}\gamma$)

We consider the case $\beta \geq \frac{1}{2}\gamma$. In (24), we look for the condition:

$$\beta - \frac{1}{2}(\gamma - \frac{1}{2}) - \frac{1}{2}\alpha^2 = 0 \text{ and } 1 - \frac{1}{2\alpha^2} \geq 0.$$

This implies that

$$\beta - \frac{1}{2}(\gamma - \frac{1}{2}) = \frac{1}{2}\alpha^2 \geq \frac{1}{4}$$

and hence

$$\beta \geq \frac{1}{2}\gamma \geq \frac{1}{4}. \tag{25}$$

Conversely, if $\beta \geq \frac{1}{2}\gamma \geq \frac{1}{4}$ and $\alpha^2 = 2\beta - (\gamma - \frac{1}{2})$, then $2\alpha^2 \geq 1$. So, from (24) we have, for this α,

$$\|D_\tau U(t)\|^2 + (1 - \frac{1}{2\alpha^2})\|K^{1/2}U(t)\|^2 \leq C_0. \tag{26}$$

Furthermore, in this case we have

$$\|D_\tau U(t)\|^2 \leq C_0,$$

which implies that

$$\|U(t)\| \leq \|U(t - \tau)\| + \sqrt{C_0}\tau.$$

Hence we have the stability estimate:

$$\|U(t)\| \leq \|U(0)\| + \sqrt{C_0}t. \tag{27}$$

Note that we need no restriction for the time step $\tau > 0$.

4.2.2 Case 2 ($0 \leq \beta < \frac{1}{2}\gamma$)

Under the condition that $\frac{1}{2} \leq \gamma$ and $0 \leq \beta < \frac{1}{2}\gamma$, we need a restriction on τ for the stability. Putting $\alpha^2 = \frac{1}{2}$, we have

$$\|D_\tau U(t)\|^2 + \tau^2(\beta - \frac{1}{2}\gamma)\|K^{1/2}D_\tau U(t)\|^2 \leq C_0.$$

Using the definition of operator norm and the condition $\beta - \frac{1}{2}\gamma < 0$, we have

$$\{1 - \tau^2(\frac{1}{2}\gamma - \beta)\|K^{1/2}\|^2\}\|D_\tau U(t)\|^2 \leq C_0.$$

In order that this inequality makes sense as the estimate for an upper bound of $\|D_\tau U(t)\|$, the following inequality must be satisfied:

$$0 < 1 - \tau^2(\frac{1}{2}\gamma - \beta)\|K^{1/2}\|^2.$$

Solving this inequality with respect to τ, we have

$$\tau < \sqrt{\frac{1}{(\frac{1}{2}\gamma - \beta)\|K^{1/2}\|^2}}. \tag{28}$$

Similarly to Case 1, we obtain

$$\tau < \sqrt{\frac{1}{(\frac{1}{2}\gamma - \beta)\|K^{1/2}\|^2}} \implies \|U(t)\| \leq \|U(0)\| + \sqrt{\frac{C_0}{1 - \tau^2(\frac{1}{2}\gamma - \beta)\|K^{1/2}\|^2}}\, t. \tag{29}$$

4.3 Theorem on the stability of Newmark's method

Combining the above considerations, we obtain the following result.

Theorem 1 *Let $C \geq 0$ and $K \geq 0$, and let $f(t) \equiv 0$. Under the common condition that $\frac{1}{2} \leq \gamma$, Newmark's method for (1) with time step τ is stable as follows:*

Case 1: $\frac{1}{2}\gamma \leq \beta$ *and for any* $\tau \implies \|U(t)\| \leq \|U(0)\| + \sqrt{C_0}\,t.$

Case 2: $0 \leq \beta < \frac{1}{2}\gamma$ *and for* $\tau < \sqrt{\frac{1}{(\frac{1}{2}\gamma - \beta)\|K^{1/2}\|^2}} \implies \|U(t)\| \leq \|U(0)\| + \sqrt{\frac{C_0}{1 - \tau^2(\frac{1}{2}\gamma - \beta)\|K^{1/2}\|^2}}\,t.$

Here,

$$\begin{aligned}
C_0 &= \|D_\tau U(0)\|^2 + \tau^2(\beta - \frac{1}{2}\gamma + \frac{1}{4})\|K^{1/2}D_\tau U(0)\|^2 + \tau(KD_\tau U(0), U(0)) \\
&\quad + \|K^{1/2}U(0)\|^2 + \tau(\gamma - \frac{1}{2})\|C^{1/2}D_\tau U(0)\|^2.
\end{aligned}$$

5. Convergence of Newmark's method

We show the proof of convergence of Newmark's method using the stability theorem in the previous section.

5.1 Convergence theorem

Theorem 2 *Let T be a finite positive real number, τ be a time step, $C, K \geq 0$, and $f(t) \equiv 0$ (1). If $\beta \geq 0$ and $\gamma \geq \frac{1}{2}$, Newmark's method for (1) converges on $[0, T]$ with the order $O(\tau^2)$ when $\tau \downarrow 0$.*

5.2 Proof of the theorem

Let $u(t)$ be the solution of (1), $U(t)$ be the solution of (4), and put $\tau = T/n$ for $n \in \mathbf{N}$. We define the error $E(t)$ for $t = j\tau (1 \le j \le n)$ as follow:

$$E(t) = U(t) - u(t).$$

From (17) and Theorem 1, we consider the following quantity $L[E]$:

$$
\begin{aligned}
L[E] \equiv & \ \|D_\tau E(0)\|^2 + \tau^2(\beta + \tfrac{1}{4} - \tfrac{1}{2}\gamma)\|K^{1/2}D_\tau E(0)\|^2 + (K^{1/2}D_\tau E(0), K^{1/2}E(0)) \\
& + \|K^{1/2}E(0)\|^2 + \tau(\gamma - \tfrac{1}{2})\|C^{1/2}D_\tau E(0)\|^2.
\end{aligned}
$$

Since $E(0) = 0$, we have

$$L[E] = \tfrac{1}{\tau^2}\|E(\tau)\|^2 + (\beta + \tfrac{1}{4} - \tfrac{1}{2}\gamma)\|K^{1/2}E(\tau)\|^2 + \tfrac{1}{\tau}(\gamma - \tfrac{1}{2})\|C^{1/2}E(\tau)\|^2.$$

By using the Taylor expansion of $u(\tau)$ at 0 and the definition of $U(\tau)$, we have

$$E(\tau) = O(\tau^3), \quad L[E] = O(\tau^4).$$

Next, by using (3), we define a time shift operator N_τ which appears in a formulation of Newmark's method:

$$
\begin{aligned}
N_\tau v(t) \equiv & \ -(I + \gamma\tau C + \beta\tau^2 K)^{-1} \times [\{-2I + \tau(1 - 2\gamma)C + \tfrac{1}{2}\tau^2(1 - 4\beta + 2\gamma)K\}v(t) \\
& + \{I + \tau(\gamma - 1)C + \tfrac{1}{2}\tau^2(1 + 2\beta - 2\gamma)\}v(t - \tau)], \quad t \ge \tau,
\end{aligned}
\tag{30}
$$

where $v(\tau)$ is calculated from $v(0)$, $\frac{d}{dt}v(0)$ and (2). When $v(\tau) = U(\tau)$, we apply N_τ to $U(\tau)$ $j-1$ times, and obtain the expression:

$$U(t) = N_\tau^{j-1}U(\tau).$$

Before estimating $E(t) = U(t) - u(t)$, we treat the following expression:

$$
\begin{aligned}
N_\tau^{j-1}u(\tau) - u(t) = & \ N_\tau^{j-1}u(\tau) - N_\tau^{j-2}u(2\tau) + N_\tau^{j-2}u(2\tau) - \cdots \\
& - N_\tau^{j-i}u(i\tau) + N_\tau^{j-i}u(i\tau) - N_\tau^{j-i-1}u((i+1)\tau) \\
& + \cdots - N_\tau u(t - \tau) + N_\tau u(t - \tau) - u(t).
\end{aligned}
$$

For the estimate of this expression, we define $\tilde{U}_i(k\tau)$ as follows:

$$\tilde{U}_i(k\tau) \equiv N_\tau^{k+1}u(i\tau) - N_\tau^k u((i+1)\tau) = N_\tau^k\{N_\tau u(i\tau) - u((i+1)\tau)\},$$

where

$$
\begin{cases}
0 \le k, \\
\tilde{U}_i(0) = N_\tau u(i\tau) - u((i+1)\tau), \\
\tilde{U}_i(\tau) = N_\tau^2 u(i\tau) - N_\tau u((i+1)\tau).
\end{cases}
$$

So, we obtain

$$N_\tau^{j-1}u(\tau) - u(t) = \sum_{i=1}^{j-1} \tilde{U}_i((j - i - 1)\tau).$$

Using Theorem 1, we estimate each $\tilde{U}_i((j - i - 1)\tau)$. From Theorem 1, we consider a quantity $L[\tilde{U}_i]$ which corresponds to C_0 in Theorem 1:

$$
\begin{aligned}
L[\tilde{U}_i] \equiv & \ \|D_\tau\tilde{U}_i(0)\|^2 + \tau^2(\beta + \tfrac{1}{4} - \tfrac{1}{2}\gamma)\|K^{1/2}D_\tau\tilde{U}_i(0)\|^2 \\
& + \tau(\gamma - \tfrac{1}{2})\|C^{1/2}D_\tau\tilde{U}_i(0)\|^2 + \tau(K^{1/2}D_\tau\tilde{U}_i(0), K^{1/2}\tilde{U}_i(0)) + \|K^{1/2}\tilde{U}_i(0)\|^2.
\end{aligned}
$$

Using the Taylor expansion of $u((i+1)\tau)$ at $i\tau$ and the definition of N_τ, we have

$$\tilde{U}_i(0) = \beta\tau^2\{u''((i+1)\tau) - u''(i\tau)\} - \frac{1}{6}\tau^3 u'''(i\tau) - \frac{1}{12}\tau^4 u''''(i\tau) + O(\tau^5)$$
$$\tilde{U}_i(\tau) = N_\tau[\beta\tau^2\{u''((i+1)\tau) - u''(i\tau)\} - \frac{1}{6}\tau^3 u'''(i\tau) - \frac{1}{12}\tau^4 u''''(i\tau) + O(\tau^5)]$$

where $' = \frac{d}{dt}$. Then we have

$$\tilde{U}_i(0) = O(\tau^3), \quad \tilde{U}_i(\tau) = O(\tau^3), \quad D_\tau\tilde{U}_i(0) = O(\tau^3), \quad L[\tilde{U}_i] = O(\tau^6).$$

Using these estimates and Theorem 1, we have

$$
\begin{aligned}
\|\tilde{U}_i((j-i-1)\tau)\| &= \|N_\tau^{j-i-1}\{N_\tau u(i\tau) - u((i+1)\tau)\}\| \\
&\leq \|\tilde{U}_i(0)\| + \sqrt{L[\tilde{U}_i]}(j-i-1)\tau \\
&\leq \|\tilde{U}_i(0)\| + \sqrt{L[\tilde{U}_i]}T = O(\tau^3) + TO(\tau^3) = O(\tau^3).
\end{aligned}
$$

So, we obtain

$$N_\tau^{j-1}u(\tau) - u(t) = \sum_{i=1}^{j-1}\tilde{U}_i((j-i-1)\tau) = O(\tau^2),$$

and

$$E(t) = U(t) - u(t) = N_\tau^{j-1}U(\tau) - N_\tau^{j-1}u(\tau) + O(\tau^2) = N_\tau^{j-1}E(\tau) + O(\tau^2).$$

Applying Theorem 1 to this we obtain, for small enough τ,

$$\|E(t)\| \leq O(\sqrt{L[E]}) \times t + O(\tau^2) = O(\tau^2), \quad when \ \frac{1}{2} \leq \gamma \ and \ 0 \leq \beta.$$

Therefore, we obtain Theorem 2.

6. Numerical experiments

We compare Newmark's method with the second order explicit Runge-Kutta method and the second order implicit Runge-Kutta method. We apply those methods to the finite element approximation of the following model resistive MHD(MgnetoHydroDynamics) equation[6]:

$$
\begin{cases}
\frac{d^2}{dt^2}u(t) + C\frac{d}{dt}u(t) + Ku(t) = 0, \\
C = -\eta\frac{\partial^2}{\partial x^2}, \ K = (2 + \sin 2\pi x)^2, \\
0 \leq \eta, \ 0 \leq x \leq 1, \ 0 \leq t < \infty, \\
u(0) = \sin 2\pi x, \ \frac{d}{dt}u(0) = 0,
\end{cases}
\tag{31}
$$

where η is the electric resistivity, and K is the so-called Alfvén frequency.

We discretize C and K by the finite element method using piecewise linear continuous functions for the equipartition of $(0, 1)$ with a mesh size Δx. From now on $\eta = 0.0001$, and mesh size of x-direction is $\Delta x = 1/128$.

6.1 Newmark's method vs. Runge-Kutta methods

For applying Runge-Kutta methods to (31), we rewrite (31) as the first order equation:

$$
\frac{d}{dt}Y(t) = AY(t),
$$
$$
A = \begin{pmatrix} 0 & I \\ -K & -C \end{pmatrix}, \quad Y(0) = \begin{pmatrix} u(0) \\ \frac{d}{dt}u(0) \end{pmatrix}.
\tag{32}
$$

Then, using (32), we can represent the second order explicit Runge-Kutta with a time step τ as follows:

$$\begin{cases} k_1 = \tilde{A}\tilde{Y}(t), \\ k_2 = \tilde{A}(\tilde{Y}(t) + \tau k_1), \\ \tilde{Y}(t + \tau) = \tilde{Y}(t) + \frac{1}{2}\tau(k_1 + k_2), \end{cases}$$

where $\tilde{A}$ and $\tilde{Y}$ are the approximations of A and Y. Using (32), we can also represent the second order implicit Runge-Kutta with a time step τ as follows:

$$\begin{cases} k_1 = \tilde{A}(\tilde{Y}(t) + \frac{1}{2}\tau k_1), \\ \tilde{Y}(t + \tau) = \tilde{Y}(t) + \tau k_1. \end{cases}$$

Using the time evolution of the energy of solutions, we compare the result of Newmark's method with those of the Runge-Kutta methods. Here the energy of solutions are calculated as follows:

$$\mathcal{E}(t) = \frac{1}{2}\int_0^1 \{(\frac{d}{dt}u(t))^2 + Ku(t)^2\}dx \simeq \frac{1}{2}\{(V(t), V(t)) + (\tilde{K}U(t), U(t))\}\Delta x,$$

where $U(t)$, $V(t)$ and $\tilde{K}$ are approximations of $u(t)$, $\frac{d}{dt}u(t)$ and K. We calculate the energy for t from $t = 0$ to 100. We calculate two cases. The first case is shown in Figure 1 where $\tau = 0.1$ and the second case with $\tau = 0.2$ is shown in Figure 2. Figure 2 has a log-scale with respect to energy. In Figure 1 and Figure 2 we set parameters as follows:

curve name	method	τ in Fig 1	τ in Fig 2	β	γ	η	Δx
line 1	Newmark	0.01	0.01	1/6	1/2	0.0001	1/128
line 2	Newmark	0.1	0.2	1/12	1/2	0.0001	1/128
line 3	Explicit Runge-Kutta	0.1	0.2			0.0001	1/128
line 4	Implicit Runge-Kutta	0.1	0.2			0.0001	1/128

Here 'line 1' corresponds to a basic curve for the comparison with a small $\tau = 0.01$. Others correspond to curves for different methods. Figure 1 and Figure 2 show that, although the equation (31) is stiff, Newmark's method gives a good result.

References

[1] Chiba, F. and Kako, T., 'On the stability of Newmark's β method', *RIMS Kokyuroku 1040*, Research Institute of Mathematical Sciences, Kyoto University, pp.39–44, 1998.

[2] _____ , 'On the stability and convergence of Newmark's β method', *The Institute of Statistical Mathematics Cooperative Report 110 Proceedings of 1997-Workshop on MHD Computations —Numerical methods and optimization techniques in controlled thermonuclear fusion research—*. pp.196–202, 1998.

[3] Fujii, H., 'Finite-Element Galerkin Method for Mixed Initial-Boundary Value Problems in Elasticity Theory', Center for Numerical Analysis, The University of Texas at Austin, October 1971.

[4] _____ , 'A Note on Finite Element Approximation of Evolution Equations', *RIMS Kokyuroku 202*, Research Institute of Mathematical Sciences, Kyoto University, pp.96–117, 1974.

[5] John, F., *Lectures on Advanced Numerical Analysis*, Courant Institute of Mathematical Sciences, New York University, 1967.

[6] Kako, T., 'Spectral and numerical analysis of resistive linearized magnetohydrodynamic operators', Series on Applied Mathematics Vol.5, Proceedings of the First China-Japan Seminar on Numerical Mathematics (eds. Z.-C. Shi and T. Ushijima), pp. 60–66, 1993.

[7] Kato, T., *Perturbation Theory for Linear Operators*, Springer, 1976.

[8] Matsuki, M. and Ushijima, T., 'Error estimation of Newmark method for conservative second order linear evolution', *Proc. Japan Acad.*, Vol. 69, Ser A, pp. 219–223, 1993.

[9] 三井斌友 (Mitsui, T.), 数値解析入門 *(Introduction to Numerical Analysis)*, 朝倉書店 (Asakurasyoten), 1985.

[10] Newmark, N. M., 'A method of computation for structural dynamics', *Proceedings of the American Society of Civil Engineers*, Journal of the Engineering Mechanics Division, Vol.85, No. EM 3, pp. 67–94, July, 1959.

[11] Raviart, P. A. and Thomas, J. M., *Introduction à l' Analyse Numérique des Equations aux Dérivées Partielles*, Masson, Paris, 1983.

[12] Wood, W. L., 'A further look at Newmark, Houbolt, etc., time-stepping formulate', *International Journal for Numerical Methods in Engineering*, Vol. 20, pp. 1009–1017, 1984.
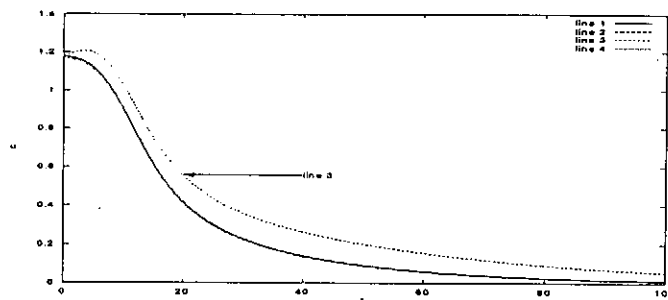
Figure 1: $\tau = 0.1$
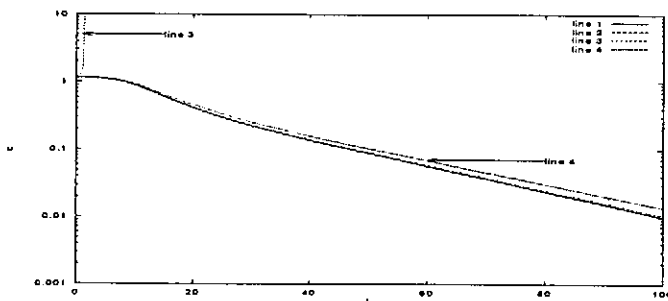
Figure 2: $\tau = 0.2$

Linear global analysis of slab ion temperature gradient mode in negative shear tokamaks

Y. Idomura, S. Tokuda[t], and M. Wakatani.

Graduate School of Energy Science, Kyoto University, Uji, Kyoto, 611-0011, Japan.
[tt] *Department of Fusion Plasma Research, Naka Fusion Research Establishment,*
Japan Atomic Energy Research Institute, Naka, Ibaraki, 311-0193, Japan.

In a slab configuration modeling the negative shear tokamak, the ion temperature gradient (ITG) mode is analyzed numerically based on a gyrokinetic integral eigenvalue equation. Numerical results show that characteristics of the ITG mode are greatly changed depending on the number of mode-rational surfaces. When a single mode-rational surface exists at the q_{min}-surface, the finite Larmor radius (FLR) effect produces an asymmetric mode structure with respect to the mode-rational surface. Since the magnetic shear is weak near the q_{min}-surface, two separate unstable regions appear in both sides of the mode-rational surface. Also, the ion temperature gradient is steep in these regions. Therefore, two independent modes become unstable depending on k_y regions; one is a low-k_y mode which exists in the high-T_i side, and the other is a high-k_y mode which is in the low-T_i side. When double mode-rational surfaces exist near the q_{min}-surface, it is found that the ITG mode becomes unstable in the interior region between the two mode-rational surfaces. Since the shear stabilization disappear in this region, the unstable region spreads up to a high-k_y value or $k_y \rho_{ti} \leq 10$, where ρ_{ti} is the ion Larmor radius.

Keywords: ion temperature gradient mode, negative shear tokamak, gyrokinetic theory, linear global analysis.

I. INTRODUCTION

In recent tokamak experiments with the negative-sheared magnetic configuration, the internal transport barrier (ITB) was formed, and significant improvement of particle and energy confinement at the ITB was observed [1–3]. Here, the ITB is characterized by a steep density and temperature gradient near the q_{min}-surface, and often, sheared poloidal and toroidal flows are observed. As one of the theoretical models for explaining these experimental results, a model based on the drift wave turbulence was proposed [4]. Here, the main result is the stabilization of toroidal drift modes and suppression of the associated anomalous transport by the negative magnetic shear. However, even in such a situation, a slab drift mode remains to be a possible unstable mode, because the sign of magnetic shear has a little effect on the stability of a slab drift mode. In recent years, comprehensive parameter studies for the ion temperature gradient (ITG) mode have been performed for the purpose of evaluating the anomalous ion transport in tokamak plasmas with the normal magnetic shear. Since the scale length ordering between the characteristic perpendicular wavelength and equilibrium quantities has been assumed to be valid for conventional tokamak discharges with the normal magnetic shear, Wentzel-Kramers-Brillouin (WKB) method [5] has been adopted in the linear stability analysis of micro-instabilities. However, as is shown in recent works using the gyrokinetic global spectral code [9,10] or the gyrokinetic particle-in-cell simulation [11], the linear eigenfunction of the ITG mode has a global radial mode structure, especially in a weak magnetic shear region of the negative-sheared magnetic configuration. Therefore, the WKB approximation or the ballooning representation may not be a good approximation for the ITB region, which is characterized by a steep density and temperature gradient at the weak magnetic shear region. Although several Vlasov or gyrokinetic global codes, which solve an integral eigenmode equation, have been developed both for a slab geometry [6,7,9] and for a toroidal geometry [8,10], numerical results for clarifying properties of the ITG mode in the negative-sheared magnetic configuration were very limited.

In the present work, we concentrate on the negative shear configuration with a steep density and temperature gradient to study the ITG mode. In analyzing the ITG mode under these conditions, it is important to retain the full finite Larmor radius (FLR) effect. Thus we have developed a gyrokinetic integral eigenvalue code [7,9,10] in a sheared slab geometry. In the framework of the ballooning representation [12], a weak magnetic shear around the q_{min}-surface suppresses the driving force of the toroidal ITG mode due to the toroidal guiding-center drift in a region other than $\theta_b \sim 0$, where θ_b denotes the ballooning angle. In addition, the toroidal mode coupling diminishes in a weak shear region. Hence, it is probable that the ITG mode has a slab-like feature in the negative shear configuration [10], and a slab model is useful as a model for the negative shear tokamak. Also, a slab model is advantageous in regard to an analytical treatment of the eigenmode equation, as well as a numerical resolution in solving the gyrokinetic integral eigenmode equation.

The negative-sheared slab ITG (NS-ITG) mode is characterized by following features: the shear stabilization disappear around the q_{min}-surface; the variation of the magnetic shear, q'', generates a potential well in the linear eigenmode equation; and two mode-rational surfaces appear in both sides of the q_{min}-surface when $k_z \neq 0$, where k_z is a wavenumber in the direction of the magnetic field at the q_{min}-surface. In the previous works [13,14], the NS-ITG modes have been studied by the fluid type linear eigenmode equation, which is solved with the corresponding WKB shooting code [5]. However, as is mentioned above, this treatment requires the assumption of a relatively weak density and temperature gradient or $k_\perp^{-1}/L_n \sim k_\perp^{-1}/L_{ti} \ll 1$, where $k_\perp$ is a wavenumber in the perpendicular direction to the dominant magnetic field, and L_n and L_{ti} are scale lengths of the density and temperature gradients respectively. In our analysis using the gyrokinetic integral eigenvalue code, we will study properties of the NS-ITG mode under the assumption of a steep density and temperature gradient or $k_\perp^{-1}/L_n \sim k_\perp^{-1}/L_{ti} \leq 1$, with including full kinetic effects such as the higher order FLR effect and the Landau resonance.

The NS-ITG modes are classified in two cases. One is the single mode-rational surface case with $k_z = 0$, and the other is the double mode-rational surface case with $k_z \neq 0$. The former corresponds to the weak shear limit [15] of the slab ITG mode. Its property is significantly affected by a steep ion temperature gradient which produces an asymmetric eigenmode structure with respect to the q_{min}-surface through the FLR effect. The latter appears only in the negative shear configuration. In the fluid limit described by the Weber type equation, the problem of the double mode-rational surface case reduces to a harmonic oscillator in a parabolic potential well perturbed by a fourth order potential, in contrast to the ITG mode in the standard sheared slab model, which is characterized by a parabolic potential hill. Thus, the NS-ITG mode with the double mode-rational surfaces is strongly destabilized around the q_{min}-surface and has a global eigenmode structure bounded by the two mode-rational surfaces. The stability of this mode is determined locally at the q_{min}-surface since $q' \simeq 0$. As a result, the unstable region in the k_y space widely spreads over the high-k_y region with $k_y \rho_{ti} \leq 10$. This is a remarkable feature of the NS-ITG mode obtained from the gyrokinetic integral eigenvalue code which enable to analyze micro-instabilities with $k_\perp \rho_{ti} \gg 1$.

The reminder of this paper is organized as follows. In Sec. II, the linearized gyrokinetic Vlasov-Maxwell system is formulated to obtain an integral eigenvalue equation. In Sec. III, the integral eigenvalue equation is reduced to the Weber type differential eigenmode equation under the fluid limit with the long perpendicular wavelength approximation where $k_\perp \rho_{ti} < 1$. Here the analytic solution of the NS-ITG mode is presented. In Sec. IV, numerical results obtained from the gyrokinetic integral eigenvalue code are shown and the properties of the NS-ITG modes are discussed. Finally, in Sec. V, we show the validity of the present analysis by comparing both the analytic and numerical results of the NS-ITG modes.

II. GYROKINETIC INTEGRAL EIGENVALUE EQUATION

In this section, we derive an integral eigenvalue equation based on the gyrokinetic Vlasov-Maxwell system. We also give a numerical method for solving the linear eigenvalue problem described as a transcendental equation.

In the present study of the ITG mode, we consider a sheared slab geometry, where the x-direction corresponds to the radial direction, the z-direction is chosen in the direction of the magnetic field at $x = 0$, and the y-direction is chosen to be normal to both the x and z-direction. We assume the periodic boundary condition in the y and z-direction, and the fixed boundary condition with conducting walls in the x-direction. By expanding the q-profile around the position $x = 0$, we write the q-profile as $q(x) = q_0 + q_0'x + \frac{1}{2}q_0''x^2 + \cdots$, where q_0, q_0' and q_0'' are evaluated at $x = 0$. The corresponding slab magnetic field configuration for the normal shear case with $q_0' \neq 0$ is

$$\mathbf{B}(x) = B_0[\mathbf{z} - x/L_s \mathbf{y}], \tag{1}$$

where $L_s = (q_0^2 R)/(q_0' r_0)$, R is the major radius of a toroidal plasma, r_0 is the minor radius at the position $x = 0$, and $x = 0$ is the position of the mode-rational surface. For the negative shear case with $q_0' = 0$, we choose the model magnetic configuration as

$$\mathbf{B}(x) = B_0[\mathbf{z} - (x/L_{ns})^2 \mathbf{y}], \tag{2}$$

where $L_{ns} = \sqrt{(2q_0^2 R)/(q_0'' r_0)}$, and $x = 0$ corresponds to the position of the q_{min}-surface. Here, it is noted that an inclusion of the first order shear term [14] in Eq. (2) just shifts the position of the q_{min}-surface, and changes the minimum value of q from q_0. Thus, only the second order derivative term is retained in Eq. (2). In these model configurations, the asymmetry of the configuration which is produced by q_0''' is ignored for simplicity.

In analyzing a relatively low frequency fluctuation in tokamak plasmas, we can apply the usual gyrokinetic ordering: $\omega/\Omega \sim k_\parallel/k_\perp \sim e\phi/T \sim \rho/L_n \sim \mathcal{O}(\epsilon)$, where ω is the characteristic frequency of the fluctuation; the gyro-frequency

is $\Omega = qB_0/mc$; m and q are the mass and the charge of particle, respectively; the Larmor radius is $\rho = |\mathbf{b} \times \mathbf{v}|/\Omega$; the direction of the dominant magnetic field is $\mathbf{b} = \mathbf{B}_0/B_0$; $k_\parallel$ and $k_\perp$ are wavenumbers in the parallel and perpendicular directions to $\mathbf{b}$, respectively; T is the temperature; L_n is the density characteristic scale length, and ϕ is the perturbed electrostatic potential. Under this ordering, a fast non-secular perturbation relating to the gyration of a charged particle is removed from the Vlasov-Maxwell system. We then have the gyrokinetic Vlasov-Maxwell system [16–19] in the gyro-averaged coordinates, $\bar{\mathbf{Z}} = (t; \bar{\mathbf{R}}, \bar{v}_z, \bar{M}, \bar{\theta})$, where the definitions of each independent variables follow those given in the gyro-center coordinates. In the gyro-center coordinates, $\mathbf{R}$ is the position of guiding center; $v_z = \mathbf{v} \cdot \mathbf{b}$; $v_\perp = |\mathbf{v} \times \mathbf{b}|$; M is defined as $M \equiv mv_\perp^2/2\Omega$; c is the velocity of light; the gyro-phase angle is given by $\theta \equiv \tan^{-1}(\mathbf{v} \cdot \mathbf{e}_1/\mathbf{v} \cdot \mathbf{e}_2)$; and $\mathbf{e}_1$, $\mathbf{e}_2$ are the unit vector in the x and y-directions. By linearizing the guiding-center distribution function as $\bar{F} = \bar{F}_0 + \bar{F}_1$, we obtain the linearized gyrokinetic equations:

$$\frac{\partial \bar{F}_1}{\partial t} + \frac{\bar{v}_z}{B_0}\mathbf{B} \cdot \nabla_{\bar{\mathbf{R}}} \bar{F}_1 + \frac{c}{B_0}\mathbf{b} \times \nabla_{\bar{\mathbf{R}}}\langle \phi \rangle_{\bar{\theta}} \cdot \nabla_{\bar{\mathbf{R}}} \bar{F}_0 - \frac{q}{mB_0}\mathbf{B} \cdot \nabla_{\bar{\mathbf{R}}}\langle \phi \rangle_{\bar{\theta}} \frac{\partial \bar{F}_0}{\partial \bar{v}_z} = 0, \tag{3}$$

$$n_1(\mathbf{x}) = \int \bar{F}_1 \delta([\bar{\mathbf{R}} + \bar{\rho}] - \mathbf{x})\bar{D}d^6\bar{\mathbf{Z}} - \frac{qn_0}{T}\sum_{\mathbf{k}}\left[1 - I_0(k_\perp^2\rho_t^2)\exp(-k_\perp^2\rho_t^2)\right]\phi_{\mathbf{k}}\exp(i\mathbf{k}\cdot\mathbf{x}), \tag{4}$$

$$-\nabla^2\phi = 4\pi e\left[n_{i1}(\mathbf{x}) - n_{e1}(\mathbf{x})\right], \tag{5}$$

where the Jacobian of the gyro-averaged coordinates is $\bar{D} = qmB_0/c$, ρ_t is the Larmor radius evaluated with the thermal velocity, and I_0 is the zeroth order modified Bessel function.

Since the system is symmetric in the y and z-direction, we assume the $\bar{R}_y$ and $\bar{R}_z$-dependence of a linear perturbation $\bar{F}_1$ as a plane wave with specified k_y and k_z:

$$\bar{F}_1(\bar{\mathbf{R}}, \bar{v}_z, \bar{M}, t) = \bar{F}_1(\bar{R}_x, \bar{v}_z, \bar{M})\exp(ik_y\bar{R}_y + ik_z\bar{R}_z - i\omega t), \tag{6}$$

where the time dependence is also assumed as $\exp(-i\omega t)$ with a frequency ω. By expanding the radial eigenfunction into Fourier series, we write a perturbed guiding-center distribution function and an electrostatic potential in a form:

$$\bar{F}_1(\bar{\mathbf{R}}, \bar{v}_z, \bar{M}, t) = \sum_{k_x}\bar{F}_{1k_x}(\bar{v}_z, \bar{M})\exp(ik_x\bar{R}_x + ik_y\bar{R}_y + ik_z\bar{R}_z - i\omega t), \tag{7a}$$

$$\bar{F}_{1k_x}(\bar{v}_z, \bar{M}) = \frac{1}{2L_x}\int_{-L_x}^{L_x}\bar{F}_1(\bar{R}_x, \bar{v}_z, \bar{M})\exp(-ik_x\bar{R}_x)d\bar{R}_x, \tag{7b}$$

and

$$\phi(\bar{\mathbf{R}}, t) = \sum_{k_x}\phi_{k_x}\exp[ik_x\bar{R}_x + ik_y\bar{R}_y + ik_z\bar{R}_z - i\omega t], \tag{8a}$$

$$\langle\phi(\bar{\mathbf{R}} + \bar{\rho}, t)\rangle_{\bar{\theta}} = \sum_{k_x}\phi_{k_x}J_0(k_\perp\bar{\rho})\exp[ik_x\bar{R}_x + ik_y\bar{R}_y + ik_z\bar{R}_z - i\omega t], \tag{8b}$$

$$\phi_{k_x} = \frac{1}{2L_x}\int_{-L_x}^{L_x}\phi(\bar{R}_x)\exp(-ik_x\bar{R}_x)d\bar{R}_x, \tag{8c}$$

where L_x denotes the system size in the x-direction. In the Fourier series representation, the gyro-average of a perturbed quantity is written using the zeroth order Bessel function, J_0. By substituting these expressions into Eq. (3), we have the perturbed guiding-center distribution function as,

$$\bar{F}_1(\bar{R}_x, \bar{v}_z, \bar{M}) = \frac{q}{T}\bar{F}_0\frac{\omega^*\left[1 - \eta\{\frac{3}{2} - (\bar{M}\Omega + \frac{1}{2}m\bar{v}_z^2)/T\}\right] - k_\parallel\bar{v}_\parallel}{k_\parallel\bar{v}_\parallel - \omega}\sum_{k_x}\phi_{k_x}J_0(k_\perp\bar{\rho})\exp(ik_x\bar{R}_x), \tag{9}$$

where $k_\parallel = \mathbf{k} \cdot \mathbf{B}/B$, $\bar{v}_\parallel = \bar{v}_z B/B_0$, $\eta = d\ln T/d\ln n_0$, and the diamagnetic drift frequency is $\omega^* = (k_y T/m\Omega)(d\ln n_0/d\bar{R}_x)$. Using a local Maxwellian for the unperturbed guiding-center distribution function, we obtain the perturbed density from Eq. (4):

$$n_1(x) = \frac{1}{2L_x}\sum_{k_x}\sum_{k_x'}\int_{-L_x}^{L_x}dx'\exp(ik_x(x - x') + ik_x'x')$$

$$\times \frac{qn_0}{T}\phi_{k_x'}\left[\left\{\Gamma_0 - \eta\left(\frac{1}{2} + b_a\right)\Gamma_0 + \eta b_g\Gamma_1\right\}\xi^* Z + \Gamma_0(\eta\xi^*\xi - 1)(1 + \xi Z)\right]$$

$$- \frac{qn_0}{T}\sum_{k_x'}[1 - I_0(b')\exp(-b')]\phi_{k_x'}\exp(ik_x'x). \tag{10}$$

The definitions of quantities in Eq. (10) are given as follows: $Z = Z(\xi)$ is the Fried-Conte plasma dispersion function; $\xi = \omega/(\sqrt{2}|k_\parallel|v_t)$; $\xi^* = \omega^*/(\sqrt{2}|k_\parallel|v_t)$; $b = (k_x^2 + k_y^2)\rho_t^2$; $b' = (k_z'^2 + k_y^2)\rho_t^2$; $b_a = (b + b')/2$, $b_g = \sqrt{bb'}$; $\Gamma_0(b_a, b_g) = \exp(-b_a)I_0(b_g)$; $\Gamma_1(b_a, b_g) = \exp(-b_a)I_1(b_g)$; and I_n is the n-th order modified Bessel function. Finally, by imposing the self-consistency condition or the Poisson equation, Eq. (5), in the Fourier space, we derive the linear integral equation for the Fourier amplitude, ϕ_{k_x},

$$\sum_{k_l} \mathcal{L}_{k_m, k_l}(\omega)\phi_{k_l} = 0 \tag{11}$$

$$\mathcal{L}_{k_m, k_l}(\omega) \equiv \frac{1}{2L_x} \int_{-L_x}^{L_x} dx \exp[i(k_l - k_m)x] \times \left[-(k_l^2 + k_y^2 + k_z^2) \right.$$

$$+ \sum_s \frac{1}{\lambda_{D_s}^2} \left[\left\{ \Gamma_0 - \eta_s \left(\frac{1}{2} + b_{a_s} \right) \Gamma_0 + \eta_s b_{g_s} \Gamma_1 \right\} \xi_s^* Z_s \right.$$

$$\left. \left. + \Gamma_0 (\eta_s \xi_s^* \xi_s - 1)(1 + \xi_s Z_s) - \{1 - I_0(b_s') \exp(-b_s')\} \right] \right], \tag{12}$$

where $\mathcal{L}_{k_m, k_l}(\omega)$ are elements of the complex matrix $\mathcal{L}(\omega)$, $\lambda_{D_s}^2 = T_s/(4\pi n_{s0} q_s^2)$, and s denotes the particle species. Thus, the linear stability problem of low frequency micro-instabilities in the sheared magnetic field is formulated as the integral eigenvalue equation. Since our interest is not only in the ITG mode, but also in the short wavelength electron temperature gradient driven (ETG) mode [20], we have used the general dielectric tensor including the electron kinetic effects in Eq. (12). An analysis of the ETG mode will be reported in elsewhere.

The matrix form of the integral eigenvalue equation, Eq. (11), can be reduced to the problem of finding eigenvalues, $\{\omega_i\}_{i=1, N}$, of the complex matrix $\mathcal{L}$, which satisfy

$$\det \mathcal{L}(\omega_i) = 0. \tag{13}$$

In finding a root of Eq. (13), first, we plot the contour lines of $\mathrm{Re}(\det \mathcal{L}) = 0$ and $\mathrm{Im}(\det \mathcal{L}) = 0$ in a complex ω-plane, and obtain guesses for the eigenfrequencies, $\{c_i\}_{i=1...N}$, in a region where the eigenfrequency with the maximum growth rate exists. We then refine guesses using a method based on the algorithm developed by Davies [21]. Although the original algorithm can treat multiple roots simultaneously, we apply the algorithm only for a single root case. Let us set a closed positively oriented contour, $C : |\omega - c_i| = r_i$, so that there exists a single root, ω_i, in the region limited by C. Applying the residue theorem, the eigenfrequency, ω_i, is written by the following integral:

$$\omega_i = \frac{1}{2\pi i} \oint_C \omega \frac{g'(\omega)}{g(\omega)} d\omega, \tag{14}$$

where $g(\omega) = \det \mathcal{L}(\omega)$. In order to avoid the numerical calculation of $g'(\omega)$, we use integration by parts to estimate Eq. (14). Here, since $\ln[g]$ is not single-valued along the contour, C, we rewrite the integral, Eq. (14), into the following form:

$$\omega_i = \frac{1}{2\pi i} \oint_C \omega \frac{G'(\omega)}{G(\omega)} d\omega + c_i,$$

$$= -\frac{1}{2\pi i} \oint_C \ln[G(\omega)] d\omega + c_i \tag{15}$$

where $G(\omega) = g(\omega)/(\omega - c_i)$, and $\ln[G]$ is single-valued along the contour, C. The integral, Eq. (15), is evaluated using a numerical quadrature to obtain the eigenfrequency, ω_i. Finally, the corresponding eigenfunction is solved using the usual inverse iterative method.

As a benchmark test, we have compared numerical results of our gyrokinetic integral eigenvalue code with our former numerical results of the gyrokinetic particle simulation [19], which solve the gyrokinetic Vlasov-Maxwell system as an initial value problem. And, we have seen a good agreement between the linear eigenfunctions and the linear growth rates of these numerical results in a shearless slab plasma. Also, for the standard sheared slab case, we have confirmed that our gyrokinetic integral eigenvalue code recovers the eigenfunction and the dispersion relation of the ITG mode [22] and the ETG mode ($\beta = 0$ case in Ref. [20]), which were also obtained by solving the integral eigenmode equation.

III. NON-LOCAL ANALYSIS USING DIFFERENTIAL EIGENMODE EQUATION

Before showing numerical results of the gyrokinetic integral eigenvalue code, we provide an analytical result of the differential eigenmode equation [23,24] in order to show qualitative characteristics of the NS-ITG mode.

We try an analytical treatment of the gyrokinetic Vlasov-Maxwell system under the ordering for the phase velocity, $v_{ti} < |\text{Re}(\omega)/k_\parallel| \ll v_{te}$. Hence, the differential eigenmode equation is obtained from the quasi-neutrality condition with the gyrokinetic ion response and the adiabatic electron response. We also apply a long perpendicular wavelength approximation, $b \sim b' \ll 1$, to the ion gyrokinetic response, Eq. (10). We then have the second order ordinary differential equation,

$$\frac{\partial^2 \tilde{\phi}}{\partial \tilde{x}^2} + Q(\tilde{x})\tilde{\phi} = 0, \tag{16a}$$

$$Q(\tilde{x}) \equiv -\tilde{k}_y^2 + \tau \frac{\tau + 1 + \{(\tau + 1/\tilde{\Omega} - \eta_i/(2\tilde{\Omega})\}\xi_i Z_i + (\eta_i/\tilde{\Omega})\xi_i^2(1 + \xi_i Z_i)}{\{\tau + 1/\tilde{\Omega} + \eta_i(2\tilde{\Omega})\}\xi_i Z_i + (\eta_i/\tilde{\Omega})\xi_i^2(1 + \xi_i Z_i)}, \tag{16b}$$

where $\tau \equiv T_e/T_i$, $\rho_s = \sqrt{\tau}\rho_{ti}$, and each variables are normalized as follows: $\tilde{\Omega} \equiv \omega/\omega_e^*$; $\tilde{x} \equiv x/\rho_s$; $\tilde{k}_y \equiv k_y\rho_s$; and $\tilde{\phi} \equiv e\phi/T_e$. Here, it is noted that in this normalization, radial variation of the temperature within an analysis domain is assumed to be weak, $T \sim \bar{T}$, even for a finite η, where $\bar{T}$ is an average temperature. This assumption is valid for a case with a relatively weak density and temperature gradient. Using the asymptotic expansion for the plasma dispersion function, $Z_i \sim -\xi_i^{-1} - \frac{1}{2}\xi_i^{-3} - \frac{1}{4}\xi_i^{-5} - \cdots$, under the fluid limit, $\xi_i > 1$, we have a reduced form of the eigenmode equation [24],

$$\frac{d^2 \tilde{\phi}}{d\tilde{x}^2} + \left(-\tilde{k}_y^2 + \frac{1 - \tilde{\Omega}}{\tilde{\Omega} + K} + \frac{\bar{L}_n^2 |\tilde{k}_\parallel|^2}{\tilde{k}_y^2 \tilde{\Omega}^2}\right) \tilde{\phi} = 0, \tag{17}$$

where $K = (1 + \eta_i)/\tau$.

For the normal shear case with $q_0' \neq 0$ or the model magnetic field, Eq.(1), the eigenmode equation is rewritten in a form of the well-known Weber equation:

$$\frac{d^2 \tilde{\phi}}{d\zeta^2} + (\epsilon - \zeta^2)\tilde{\phi} = 0, \tag{18}$$

where

$$\zeta = a\tilde{x}, \quad a = \sqrt{\frac{i\bar{L}_n}{\bar{L}_s\tilde{\Omega}}}, \quad \epsilon = \frac{\bar{L}_s\tilde{\Omega}}{i\bar{L}_n}\left(-\tilde{k}_y^2 + \frac{1 - \tilde{\Omega}}{\tilde{\Omega} + K}\right).$$

In Eq. (18), $\tilde{k}_z$ is set to zero, because $\tilde{k}_z$ does not affect the stability but just shift the mode-rational surface from $x = 0$. From the bounded solution in the ζ space and the corresponding quantization condition for ϵ, we have the eigenfunction and the dispersion relation as follows,

$$\tilde{\phi}_l(\tilde{x}) = \left[a/\left(\sqrt{\pi}2^l l!\right)\right]^{1/2} H_l(\zeta)\exp(-\zeta^2/2), \tag{19}$$

$$\epsilon = 2l + 1, \tag{20}$$

where l denotes a radial mode number, H_l is the l-th order Hermite polynomials, and the eigenfunction, Eq. (19), is normalized as $\int \tilde{\phi}_l^2 d\tilde{x} = 1$. If we assume that the eigenfrequency satisfies $|\text{Re}(\tilde{\Omega})| \gg |\text{Im}(\tilde{\Omega})|$, a potential of the Weber equation, Eq. (18), is recognized as a parabolic potential hill and the eigenfunction, Eq. (19), shows an oscillating feature in the $\tilde{x}$ space. The asymptotic solution of Eq. (18) is then given as

$$\lim_{|x|\to 0} \tilde{\phi} = C \exp\left(-i\frac{\bar{L}_n}{2\bar{L}_s\tilde{\Omega}}\tilde{x}^2\right), \tag{21}$$

where C is a constant. By comparing Eq. (21) with an eikonal form of WKB solution, $\exp(\int \tilde{k}_x d\tilde{x})$, the group velocity is evaluated as $\tilde{v}_g = \partial\tilde{\Omega}/\partial\tilde{k}_x = [\bar{L}_n/(\tilde{k}_x^2 \bar{L}_s)]\tilde{x}$. Hence, the asymptotic solution, Eq. (21), behaves as the outgoing wave which takes a wave energy away from an unstable region around the mode-rational surface to a stable region where

the wave energy is absorbed by the ion Landau damping. This stabilizing mechanism is so-called the shear convective damping [25].

For the negative shear case with $q'_0 = 0$ or the model magnetic field, Eq. (2), the eigenmode equation becomes

$$\frac{d^2\tilde{\phi}}{d\zeta^2} + (\epsilon - \zeta^2 - \alpha\zeta^4)\tilde{\phi} = 0, \tag{22}$$

where

$$\zeta = a\tilde{x}, \quad a = \left(\sqrt{\frac{2\tilde{k}_z}{\tilde{k}_y}} \frac{\tilde{L}_n}{\tilde{L}_{n,}\bar{\Omega}}\right)^{1/2}, \quad \alpha \equiv -\left(\frac{\tilde{k}_y}{2\tilde{k}_z}\right)^{3/2} \frac{\bar{\Omega}}{\tilde{L}_n \tilde{L}_{n,}},$$

$$\epsilon = \left(\frac{\tilde{k}_y}{2\tilde{k}_z}\right)^{1/2} \frac{\tilde{L}_{n,}\bar{\Omega}}{\tilde{L}_n} \left[-\tilde{k}_y^2 + \frac{1-\bar{\Omega}}{\bar{\Omega}+K} + \left(\frac{\tilde{L}_n\tilde{k}_z}{\bar{\Omega}\tilde{k}_y}\right)^2\right].$$

Here, we have assumed the double mode-rational surface case with $k_z \neq 0$. Assuming α as a perturbation parameter, the perturbation theory [26] can be applied to Eq. (22). Solving the perturbed eigenfunction $\tilde{\phi}_l^{(1)}$ and the perturbed energy level $\epsilon_l^{(1)}$ yields the eigenfunction,

$$\tilde{\phi}_l = \tilde{\phi}_l^{(0)} + \tilde{\phi}_l^{(1)}, \tag{23a}$$

$$\tilde{\phi}_l^{(0)} = \left[a/\left(\sqrt{\pi}2^l l!\right)\right]^{1/2} H_l(\zeta)\exp(-\zeta^2/2), \tag{23b}$$

$$\tilde{\phi}_l^{(1)} = \sum_{j\neq l} \frac{\epsilon_l^{(1)}}{\epsilon_l^{(0)} - \epsilon_j^{(0)}} \tilde{\phi}_j^{(0)}, \tag{23c}$$

and the dispersion relation,

$$\epsilon = \epsilon_l^{(0)} + \epsilon_l^{(1)} \tag{24a}$$

$$\epsilon_l^{(0)} = 2l + 1, \tag{24b}$$

$$\epsilon_l^{(1)} = \int \tilde{\phi}_l^{(0)*} \alpha\zeta^4 \tilde{\phi}_l^{(0)} d\tilde{x}, \tag{24c}$$

where $\tilde{\phi}_l^{(0)*}$ denotes a complex conjugate of $\tilde{\phi}_l^{(0)}$. Again, for the case satisfying $|\text{Re}(\tilde{\Omega})| \gg |\text{Im}(\bar{\Omega})|$, a potential in Eq. (22) is recognized as a parabolic potential well with a fourth order perturbation, and the eigenfunction, Eq. (23a), becomes a bounded solution in the $\tilde{x}$ space. Accordingly, the linear stability problem of the NS-ITG mode with the double mode-rational surfaces, which is described by Eq. (22), is recognized as a harmonic oscillator perturbed by a fourth order potential. In the negative shear case, when there are two neighboring mode-rational surfaces at $\tilde{x}_{r\pm} = \pm\sqrt{\tilde{k}_z/\tilde{k}_y}\tilde{L}_{n,}$, a potential well is formed between these mode-rational surfaces, $\tilde{x}_{r-} < \tilde{x} < \tilde{x}_{r+}$. For this situation, the width of the eigenfunction is evaluated as $\Delta\tilde{x} \sim a^{-1}$. From comparison between the width of the eigenfunction and that of the potential well, we obtain a relation, $\Delta\tilde{x}/(\tilde{x}_{r+} - \tilde{x}_{r-}) = \sqrt{\alpha} < 1$, i.e., the eigenfunction, Eq. (23a), becomes localized within the potential well. Therefore, in the negative shear case, the shear convective damping does not work, and the NS-ITG mode becomes unstable easily around the $q_{\min}$-surface.

IV. NUMERICAL RESULTS

Using the gyrokinetic integral eigenvalue code, we have analyzed the ITG modes both in the normal shear case and in the negative shear case. Use of the gyrokinetic integral eigenvalue code enable us to analyze a global mode with $k_x\rho_{ti} < 1$ as well as a short perpendicular wavelength mode with $k_\perp\rho_{ti} > 1$, where the full FLR effect becomes significant.

Parameters used in the present analysis are chosen based on plasma parameters in Tokamak Fusion Test Reactor (TFTR): $R = 2.6$m, $r_0 = 0.3$m; $\bar{n}_e = \bar{n}_i \sim 2 \times 10^{19}$m^{-3}; $L_n = 0.38$m; $\bar{T}_e \sim 3.9$keV; $\bar{T}_i = 12.8$keV; $B_0 = 4.6$T; and $\bar{\rho}_{ti} = 2.52$mm, where $\bar{}$ denotes a quantity averaged over the region of the $q_{\min}$-surface. Here, we have considered a relatively steep temperature gradient case corresponding to the ITB region of the negative shear discharges. Also, we

have adopted the steep ion temperature gradient $L_{ti} \sim 0.076$m corresponding to $\eta_i = 5$ in this section. For the negative shear case, we have chosen a model configuration with $q_0 = 2$, $q_0' = 0$m^{-1}, and $q_0'' = 142$m^{-2}, which corresponds to $L_{n_s} = 0.883$m. In the former works [13–15,24], plasma parameters were described with non-dimensional parameters with the normalization as in the previous section. In this section, in order to explicitly show relations among the scale lengths of equilibrium quantities such as the density, temperature and magnetic shear, the ion Larmor radius, and the scale length of the eigenmode structure, we have described the plasma parameters with dimensional quantities. Also, in the present analysis, the non-adiabatic electron response is included for completeness.

In the numerical calculation, in order to exclude spurious solutions, we have used 128 modes for the k_x spectrum corresponding to the system size, $L_x = 60.3\bar{\rho}_{ti}$, the grid size of $\Delta x \simeq 0.471\bar{\rho}_{ti}$, and the wavenumber of $k_x\bar{\rho}_{ti} \leq 7$. Also, we have adopted a sine series expansion to satisfy the conducting wall boundary condition in the x-direction. Thus, even and odd modes appear alternately with the increase of k_x.

First, we will show the result of the conventional slab ITG mode, where the shear parameter, L_s, is chosen as $L_s = L_{n_s}$ ($L_n/L_s \simeq 0.43$). The eigenfunction and the k_x spectrum of $l = 0$ mode are shown in Figs. 1 (a) and 1 (b). In Fig. 1 (a), the mode-rational surface, x_r, the ion resonance point, x_i, and the electron resonance point, x_e, are also shown with arrows, where x_r, x_i, and x_e are defined as $k_\parallel(x_r) = 0$, $\mathrm{Re}(\omega)/k_\parallel(x_i) = v_{ti}$, and $\mathrm{Re}(\omega)/k_\parallel(x_e) = v_{te}$, respectively. Since the eigenfunction has a finite amplitude on the ion resonance point, the conventional slab ITG mode shows the kinetic feature [24]. In Fig. 1 (b), we see that odd modes are close to zero and the eigenmode structure has even symmetry. Since the mode width is relatively narrow, $\Delta x/\bar{\rho}_{ti} \sim 4.7$, the effect due to the radial variation of equilibrium quantities is relatively weak. Here, the mode width, Δx, is defined as $\Delta x \equiv (\bar{k}_x/2\pi)^{-1} = (\sum_{k_x} k_x|\phi_{k_x}|/2\pi \sum_{k_x} |\phi_{k_x}|)^{-1}$ [7]. Also, since the k_x spectrum has large amplitude components for $k_x\bar{\rho}_{ti} \leq 2$, the long wavelength approximation, $k_\perp\rho_{ti} < 1$, is not a good approximation in analyzing this mode.

In the negative shear configuration, there are two types of NS-ITG modes. One is for the single mode-rational surface case with $k_z = 0$, and the other is for the double mode-rational surface case with $k_z \neq 0$, which is discussed analytically in the previous section. While the double mode-rational surface case is specific to the negative shear configuration, the single mode-rational surface case is recognized as the weak shear limit [15] of the slab ITG mode in the normal shear configuration, because the perturbed density response, Eq. (10), does not depend on the sign of the shear in the sheared slab geometry.

In the single mode-rational surface case, there are several unstable branches both in a low-k_y region and in a high-k_y region. In Figs. 2 and 3, the eigenfunction and the k_x spectrum of two characteristic branches are shown for the low-k_y case with $k_y\bar{\rho}_{ti} \simeq 0.348$, and the high-$k_y$ case with $k_y\bar{\rho}_{ti} \simeq 0.9$, respectively. Since the magnetic shear is weak around the mode-rational surface, which is equivalent to the q_{min}-surface in this case, an unstable region satisfying $v_{ti} \leq |\mathrm{Re}(\omega)/k_\parallel| \ll v_{te}$, is divided into two separate regions which are located in both sides of the q_{min}-surface. Between these regions, the ion Larmor radius varies due to the variation of the ion temperature, and the FLR effect, which is most effective at $k_\perp\rho_{ti} \sim 1$, produces the asymmetry of the mode structure. As is shown in Figs. 2 (b) and 3 (b), these modes do not have spatial parity. Therefore, the eigenfunction of the low-k_y (high-k_y) mode peaks in the high (low) temperature side. In Figs. 2 (b) and 3 (b), we also see that these modes have a relatively oscillating mode structure whose k_x spectrum peaks at $k_x\bar{\rho}_{ti} \sim 1.3$, and the radial correlation length is evaluated as $\Delta x/\bar{\rho}_{ti} \sim 5$.

In the double mode-rational surface case, k_z determines a depth of the potential well and a distance between the two mode-rational surfaces. In this section, we have chosen k_z as $k_z \sim 3 \times 2\pi/(q_0 R) \sim 0.00849\bar{\rho}_{ti}$, so that the double mode-rational surface NS-ITG mode gives the approximately maximum growth rate at $\eta_i = 5$. In Figs. 4 and 5, the eigenfunctions and the k_x spectrums of the double mode-rational surface NS-ITG modes are shown for $l = 0$ and $l = 1$, respectively. In the figures, it is noted that, while the electron resonance points appear in both sides of two mode-rational surfaces, the ion resonance points exist but do not appear in the interior region between these surfaces, because of the weak magnetic shear. And, a wide unstable region satisfying $v_{ti} < |\mathrm{Re}(\omega)/k_\parallel| \ll v_{te}$ exists around the q_{min}-surface. This fact implies the validity of the fluid approximation used in the analytic treatment of the differential eigenmode equation, Eqs. (16). As is predicted in the analytic solution, Eqs. (24), the double mode-rational surface NS-ITG mode has the mode structure which is localized around the q_{min}-surface. In Figs. 4 (b) and 5 (b), we see that the k_x spectrum of the $l = 0$ ($l = 1$) mode shows approximately even (odd) symmetry. However, also for the double mode-rational surface case, weak asymmetric components are observed because of a relatively broad mode structure, e.g., $\Delta x/\bar{\rho}_{ti} \sim 15$ for the $l = 0$ mode. Here, it is noted that for the NS-ITG modes which are analyzed in this section, the ratio of the radial correlation length Δx to the scale length of an ion temperature gradient L_{ti} reaches at $\Delta x/L_{ti} \sim 0.5$ and, therefore, the WKB procedure may not be appropriate for the analysis of these modes. Since the k_x spectrum of these modes peaks in a long wavelength region, $k_x\bar{\rho}_{ti} < 1$, the long wavelength approximation, $k_\perp\rho_{ti} < 1$, which is used in the analytic calculation, may be valid for the double mode-rational surface NS-ITG mode with $k_y\bar{\rho}_{ti} \leq 1$.

Figure 6 (a) shows the k_y-dependence of a real frequency of the above three types of ITG modes. For $k_y \bar{\rho}_{ti} < 1$, the absolute value of real frequency increases linearly with k_y and the dispersive feature behaves as $\mathrm{Re}(\omega) \sim \omega_e^*$ except for the high-k_y branch of the single mode-rational surface NS-ITG mode, which becomes unstable in a low temperature region. For $k_y \bar{\rho}_{ti} > 1$, the absolute value of real frequency of the double mode-rational surface NS-ITG modes reduces again. This feature is also seen in the k_y-dependence obtained from the local dispersion relation for the shearless slab ITG mode, Fig. 7 (a).

In Fig. 6 (b), the k_y-dependence of the growth rate of these modes is shown. As was seen in the previous works [6,22], an unstable region of the conventionsl slab ITG mode exists for $k_y \bar{\rho}_{ti} < 1$. For the single mode-rational surface NS-ITG modes, there are two unstable regions corresponding to the low-k_y mode with $k_y \bar{\rho}_{ti} \leq 0.5$, and the high-$k_y$ mode with $k_y \bar{\rho}_{ti} \geq 0.5$. Compared with these three branches, the double mode-rational surface NS-ITG modes are strongly unstable and their unstable region includes the high-k_y region with $k_y \bar{\rho}_{ti} > 1$. In order to explain this unique feature of the NS-ITG modes, we have analyzed the k_y-dependence, Fig. 7 (a), and the $k_{\parallel}$-dependence, Fig. 7 (b), of the local dispersion relation for the shearless slab ITG mode at the $q_{\min}$-surface. As shown in Fig. 7 (b), the ITG mode is basically the ion sound wave which is modified by the density and temperature gradient, and its stability is very sensitive to $k_{\parallel}$. Whereas, in Fig. 7 (a), we see that with a constant $k_{\parallel}$, the k_y-dependence of the growth rate is weak for $k_y \bar{\rho}_{ti} > 1$. It is noted that the non-adiabatic ion response contributes to the stability of ITG mode in the high-k_y limit, while the contribution vanishes exponentially in the high-$k_\perp$ or k_x limit. This is because the non-adiabatic part of the ion response, Eq. (10), is proportional to $k_y \rho_{ti} \Gamma_0(b)$ or $k_y \rho_{ti} \Gamma_1(b)$, and in the high-$k_y$ limit, these functions are approximated [27] as $\sqrt{b}\Gamma_0(b) \sim 0.399 + 0.0133b^{-1}$, and $\sqrt{b}\Gamma_1(b) \sim 0.399 - 0.0399b^{-1}$, respectively. Therefore, what is significant in stabilizing the ITG mode is not the variation of k_y but the variation of $k_{\parallel}$, which generates the ion Landau damping in a high-$k_{\parallel}$ region. In the sheared slab geometry, k_y and $k_{\parallel}$ are closely related by the magnetic shear. If the magnetic shear exist in an unstable region, $k_{\parallel}$ increases along with the increase of k_y, and the mode is then stabilized by the ion Landau damping for $k_y \bar{\rho}_{ti} > 1$. This is the kinetic stabilizing mechanism of the slab ITG mode and the single mode-rational surface NS-ITG mode. However, if the mode arises in a low magnetic shear region around the $q_{\min}$-surface, which corresponds to the double mode-rational surface NS-ITG mode, $k_{\parallel}$ is independent of k_y and the k_y-dependence of the stability is almost determined by the local stability for the shearless slab ITG mode which is shown in Fig. 7 (a). Thus, an unstable region with $k_y \bar{\rho}_{ti} > 1$ is allowed for the double mode-rational surface NS-ITG mode.

Figures 8 (a) and 8 (b) show the η_i-dependence of the real frequency and the growth rate, where k_y and k_z are chosen so that the critical temperature gradient parameter, η_{ic}, approximately becomes the minimum value. For the conventional slab ITG mode, $\eta_{ic} \sim 3$ is obtained, and this value is consistent with the analytical estimation of η_{ic}, which is obtained from the analysis of the differential eigenmode equation, Eq. (16), in the kinetic limit [24]. Compared with the slab ITG mode, the NS-ITG modes give considerably lower critical values around $\eta_{ic} = 1 \sim 1.5$. As for the real frequency, the slab ITG mode and the double mode-rational surface NS-ITG mode have a finite real frequency at their marginally stable state, while real frequencies of the single mode-rational surface NS-ITG modes become close to zero at $\eta_i \sim \eta_{ic}$.

V. SUMMARY

In the present paper, we have analyzed the NS-ITG modes using the gyrokinetic integral eigenvalue code. In the negative shear configuration, several types of ITG modes exist because of the peculiar properties of the magnetic configuration: the magnetic shear is very weak around the $q_{\min}$-surface; and the configuration is determined by q_0'', which forms a potential well in the eigenmode equation. Also, the double mode-rational surfaces appear when $k_z \neq 0$.

In the single mode-rational surface case with $k_z = 0$, two separate unstable regions, which widely spread in both sides of the mode-rational surface, appear because of a very weak magnetic shear. In these unstable regions, the ion temperature and the ion Larmor radius vary considerably, and the FLR effect provides the asymmetric mode structure. Thus, the low-k_y (high-k_y) mode becomes unstable in the high (low) temperature side of the mode-rational surface.

We have shown both the analytic and numerical results for the double mode-rational surface case with $k_z \neq 0$. In an analytical treatment, the linear stability problem described by the differential eigenmode equation is recognized as a harmonic oscillator perturbed by a fourth order potential. Using the perturbation theory, we have obtained a bounded solution which is localized around the $q_{\min}$-surface. This solution is also obtained from the gyrokinetic integral eigenvalue code. These analyses have shown an existence of a broad unstable region in the interior region between the two mode-rational surfaces, and this feature is also explained by either kinetic and fluid pictures. In the kinetic picture, the appearance of the unstable mode in the interior region between the two mode-rational surfaces

is explained by an absence of the ion resonance points in this region. In the fluid picture, the driving mechanism is explained by a trapping of wave energy in the potential well generated by variation of the magnetic shear, q_0''. Thus, the eigenfunction is bounded by the two mode-rational surfaces and has a relatively broad mode structure. Here, it should be noted that for the analysis of this kind of global modes, the WKB approximation or the ballooning representation seems inappropriate, because the scale length ordering, $\Delta x/L_n \sim \Delta x/L_t \sim \mathcal{O}(\epsilon)$, does not hold for the steep density and temperature profiles. Another particular feature of this mode is that the unstable region spreads over the high-k_y region, $k_y \bar{\rho}_{ti} \leq 10$. Unlike the conventional slab ITG modes and the single mode-rational surface NS-ITG modes, in the double mode-rational surface case, the magnetic shear vanishes in the unstable region, where the eigenfunction peaks, and $k_{\parallel}$ becomes independent of k_y. Hence, the k_y-dependence of the growth rate is essentially determined by the local stability at the q_{min}-surface. This numerical result may explain the short wavelength fluctuation with $k_\theta \rho_{ti} \sim 5$, based on the NS-ITG mode, which is observed in the TFTR enhanced reversed shear (ERS) experiment [28]. In order to identify this short wavelength fluctuation, a linear stability calculation of the ETG mode remains to be done for comparison with the data.

From evaluation of the radial correlation length and the growth rate for these three types of NS-ITG modes, the double mode-rational surface NS-ITG mode may occupy a significant contribution to the anomalous transport, provided that η_i is sufficiently larger than its critical value, η_{ic}. Also, for the plasma parameters used in Sec. IV, these NS-ITG modes give considerably lower critical temperature gradient parameter, $\eta_{ic} = 1 \sim 1.5$, compared with the conventional slab ITG mode which gives $\eta_{ic} \sim 3$.

In the present analysis, we have considered only the slab ITG modes, which is driven by the resonant interaction between transit particles and electrostatic waves. Thus, the present results may not be appropriate for a quantitative comparison with tokamak experiments, if the driving force due to the toroidal effects such as toroidal guiding center drift, trapped particles, and the toroidal mode coupling, are essential. However, we believe that the toroidal effects tend to become weak for the negative shear configuration and the slab-type drift waves are relevant to understand experimental results. Future work will be directed to the development of the gyrokinetic integral eigenvalue code for a realistic toroidal configuration.

ACKNOWLEDGMENTS

[1] F. M. Levinton, M. C. Zarnstorff, S. H. Batha, M. Bell, R. E. Bell, R. V. Budny, C. Bush, Z. Chang, E. Fredrickson, A. Janos, J. Manickam, A. Ramsey, S. A. Sabbagh, G. L. Schmidt, E. J. Synakowski, and G. Taylor, Phys. Rev. Lett. **75**, 4417 (1995).

[2] E. J. Strait, L. L. Lao, M. E. Mauel, B. W. Rice, T. S. Taylor, K. H. Burrell, M. S. Chu, E. A. Lazarus, T. H. Osborne, S. J. Thompson, and A. D. Turnbull, Phys. Rev. Lett. **75**, 4421 (1995).

[3] T. Fujita, S. Ide, H. Shirai, M. Kikuchi, O. Naito, Y. Koide, S. Takeji, H. Kubo, and S. Ishida, Phys. Rev. Lett. **78**, 2377 (1997).

[4] C. Kessel, J. Manickam, G. Rewoldt, and W. M. Tang, Phys. Rev. Lett. **72**, 1212 (1994).

[5] R. B. White, J. Comput. Phys. **31**, 409 (1979).

[6] W. M. Tang, G Rewolt, and E. A. Frieman, Phys. Fluids **23**, 2454 (1980).

[7] M. Artun and W. M. Tang, Phys. Fluids B **4**, 1102 (1992).

[8] W. M. Tang and G. Rewoldt, Phys. Fluids B **5**, 2451 (1993).

[9] S. Brunner and J. Vaclavik, Phys. Plasmas **5**, 365 (1998).

[10] S. Brunner, M. Fivaz, T. M. Tran, and J. Vaclavik, Phys. Plasmas **5**, 3929 (1998).

[11] R. D. Sydora, V. K. Decyk, and J. M. Dawson, Plasma Phys. Control. Fusion **38**, A281 (1996).

[12] W. Horton, Jr., D. I. Choi, and W. M. Tang, Phys. Fluids **24**, 1077 (1981).

[13] J. Li, W. Qu, L. Huang, and J. Zhang, Phys. Lett. A **233**, 85 (1997).

[14] J. Li, L. Huang, and W. Qu, Phys. Plasmas **5**, 959 (1998).

[15] J. Q. Dong, Y. Z. Zhang, and S. M. Mahajan, Phys. Plasmas **4**, 3334 (1997).

[16] D. H. E. Dubin, J. A. Krommes, C. Oberman, and W. W. Lee, Phys. Fluids **26**, 3524 (1983).

[17] T. S. Hahm, Phys. Fluids **31**, 1940 (1988).

[18] T. S. Hahm, Phys. Fluids **31**, 2670 (1988).

[19] Y. Idomura, S. Tokuda, and M. Wakatani, to be published in J. Plasma and Fusion Res.

[20] Y. C. Lee, J. Q. Dong, P. N. Guzdar, and C. S. Liu, Phys. Fluids **30**, 1331 (1987).

[21] B. Davies, J. Comput. Phys. **66**, 36 (1986).

[22] R. D. Sydora, U.S.-Japan Workshop on ITG Turbulent Transport (AIP Press, New York, 1993), p 224.

[23] B. Coppi, M. N. Rosenbluth, and R. Z. Sagdeev, Phys. Fluids **10**, 582 (1967).

[24] T. S. Hahm and W. M. Tang, Phys. Fluids B **1**, 1185 (1989).

[25] L. Chen, *Waves and Instabilities in Plasmas* (World Scientific, Singapore and New Jersey, 1987), Chap. IV.

[26] L. D. Landau and E. M. Lifshitz, *Quantum Mechanics, Non-relativistic Theory* (Pergamon Press, Oxford, 1977), Chap. VI.

[27] M. Abramowitz and I. A. Stegun, *Handbook of Mathematical Functions with Formulas, Graphs, and Mathematical Tables* (Dover Publications, New York, 1965), p378.

[28] K. L. Wong, N. L. Bretz, T. S. Hahm, and E. Synakowski, Phys. Lett. A **236**, 339 (1997).
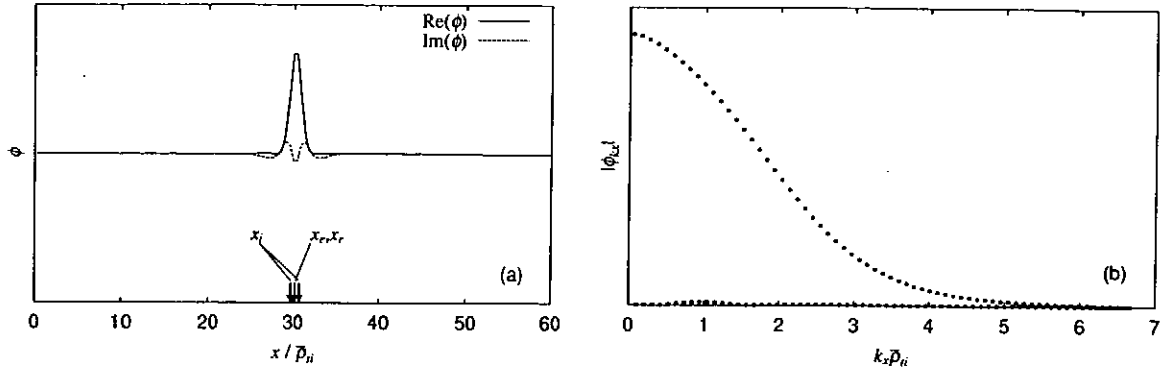
FIG. 1. (a) shows the eigenfunction of the $l = 0$ branch of the slab ITG mode for $k_y \bar{\rho}_{ti} \simeq 0.4$ and $\eta_i = \eta_e = 5$. Also, positions of the mode-rational surface, x_r, the ion resonance point, x_i, and the electron resonance point, x_e are indicated by arrows. (b) shows the corresponding k_x spectrum of the eigenfunction. Here, odd modes have almost zero amplitudes.
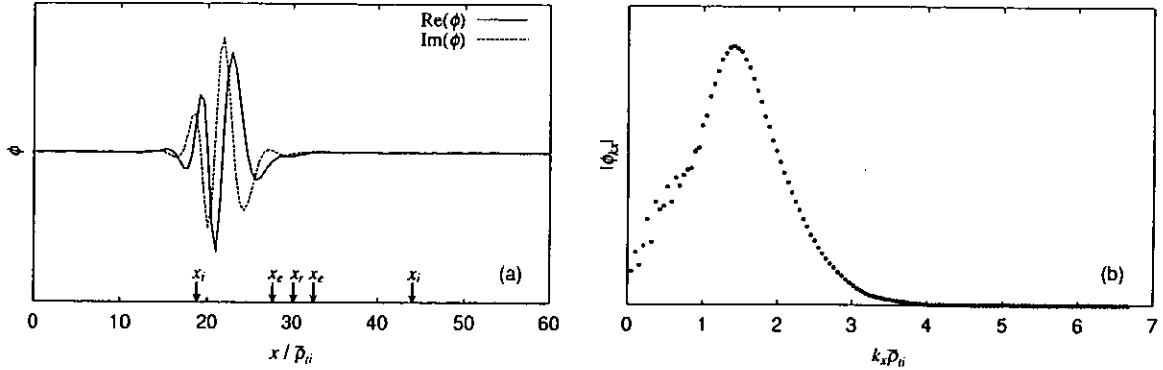
FIG. 2. (a) shows the eigenfunction of the single mode-rational surface NS-ITG mode for the low-k_y branch with $k_y \bar{\rho}_{ti} \simeq 0.348$ and $\eta_i = \eta_e = 5$. (b) shows the corresponding k_x spectrum of the eigenfunction.
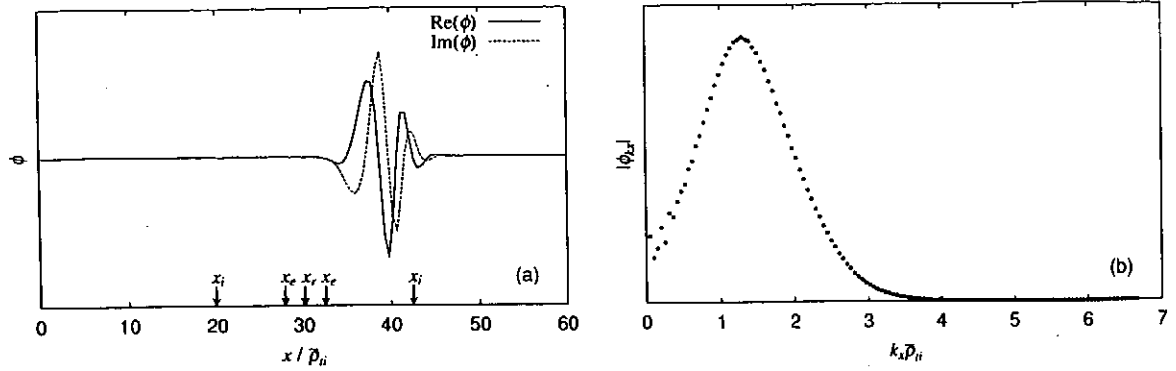
FIG. 3. (a) shows the eigenfunction of the single mode-rational surface NS-ITG mode for the high-k_y branch with $k_y \bar{p}_{ti} \simeq 0.9$ and $\eta_i = \eta_e = 5$. (b) shows the corresponding k_x spectrum of the eigenfunction.
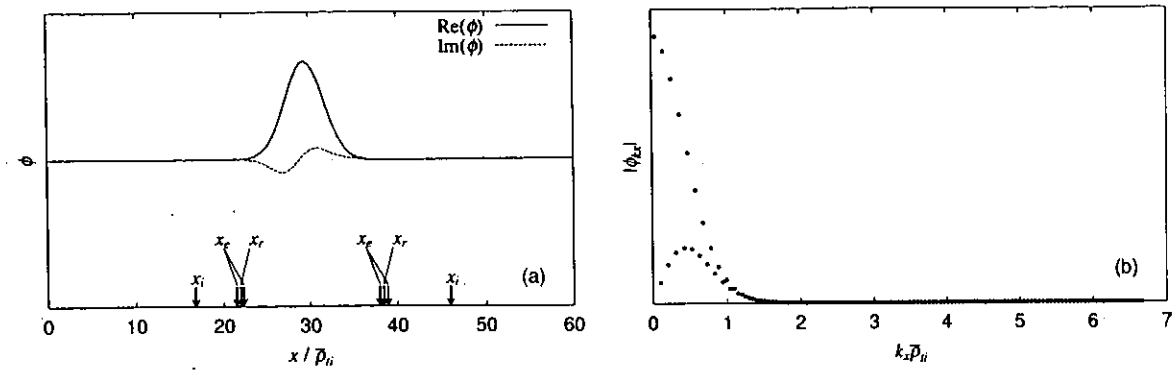
FIG. 4. (a) shows the eigenfunction of the $l = 0$ branch of the double mode-rational surface NS-ITG mode for $k_y \bar{p}_{ti} \simeq 1.5$, $k_x \bar{p}_{ti} \simeq 0.00849$, and $\eta_i = \eta_e = 5$. (b) shows the corresponding k_x spectrum of the eigenfunction. Here, the eigenfunction has even parity and even modes are dominant in the k_x spectrum.
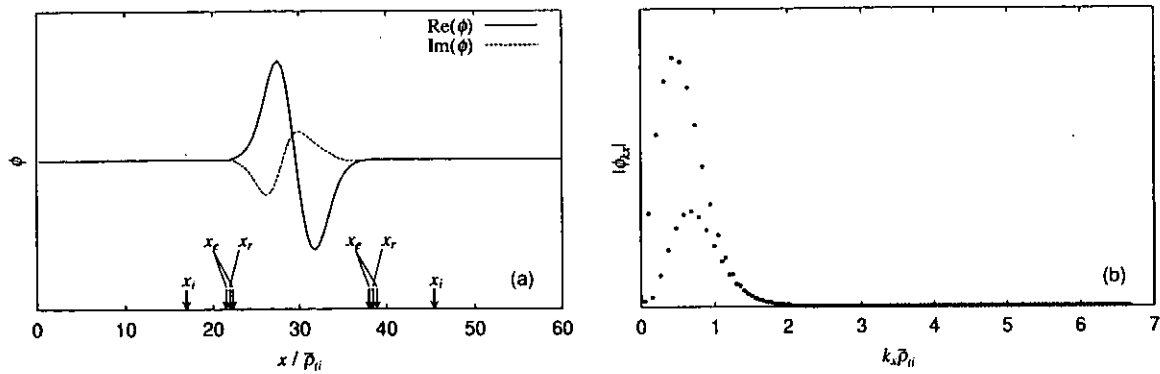
FIG. 5. (a) shows the eigenfunction of the $l = 1$ branch of the double mode-rational surface NS-ITG mode for $k_y \bar{p}_{ti} \simeq 1.5$, $k_x \bar{p}_{ti} \simeq 0.00849$, and $\eta_i = \eta_e = 5$. (b) shows the corresponding k_x spectrum of the eigenfunction. Here, the eigenfunction has odd parity and odd modes are dominant in the k_x spectrum.
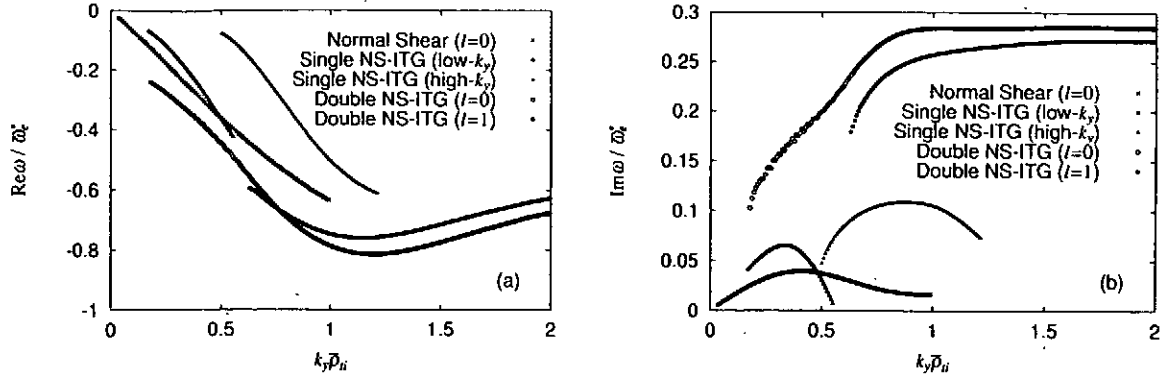
FIG. 6. (a) Real frequency and (b) growth rate are plotted for the $l = 0$ branch of sheared slab ITG mode (crosses), the low-k_y (open triangles) and high-k_y (closed triangles) branches of the single mode-rational surface NS-ITG mode, and the $l = 0$ (open circles) and $l = 1$ (closed circles) branches of the double mode-rational surface NS-ITG mode. Here, parameters are same as numerical results in Figs. 1-5, except for $k_y \bar{\rho}_{ti}$.
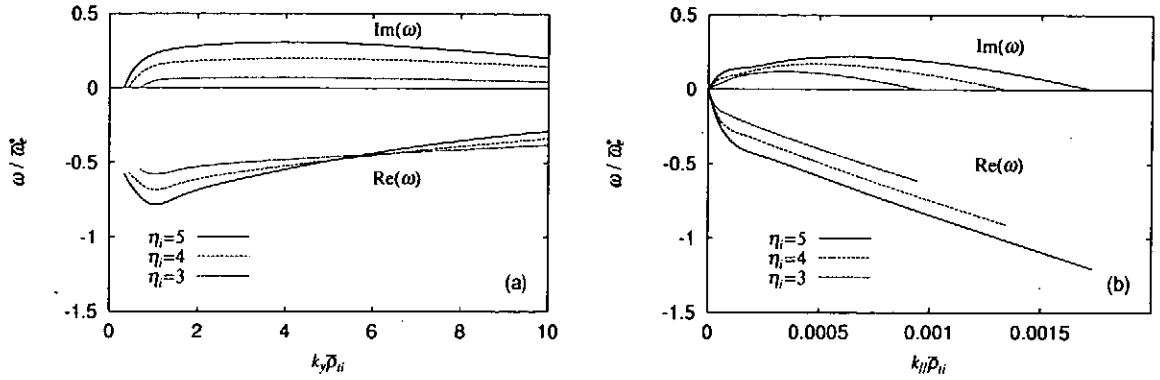
FIG. 7. (a) k_y-dependence and (b) k_z-dependence of the local dispersion relation of the shearless slab ITG mode are plotted under conditions with (a) $k_z \bar{\rho}_{ti} \simeq 0.00849$ and (b) $k_y \bar{\rho}_{ti} \simeq 0.4$, and $\eta_i = \eta_e$.
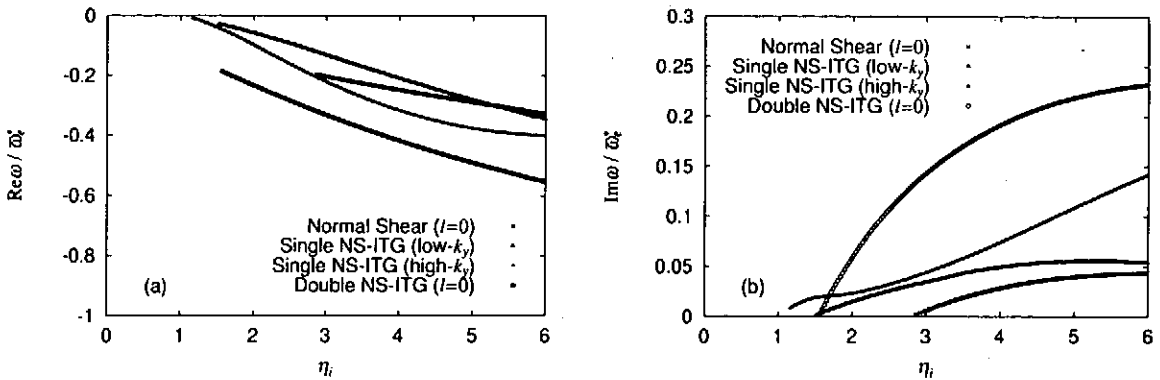
FIG. 8. (a) Real frequency and (b) growth rate versus η_i is plotted for the slab ITG mode and the NS-ITG modes. The parameters are chosen as follows: the slab ITG mode with $k_y \bar{\rho}_{ti} = 0.399$ (crosses); the low-k_y branch with $k_y \bar{\rho}_{ti} = 0.424$ (open triangles) and the high-k_y branch with $k_y \bar{\rho}_{ti} = 0.849$ (closed triangles) of the single mode-rational surface NS-ITG mode; and the double mode-rational surface NS-ITG mode with $k_y \bar{\rho}_{ti} = 0.849$ and $k_z \bar{\rho}_{ti} = 0.000424$ (open circles).

MHD Stability Analysis Using Higher Order Spline Functions

IDA Akihiro, TODOROKI Jiro[1] and SANUKI Heiji[1]

Department of Energy Engineering and Science,
Graduate School of Engineering,
Nagoya University, Nagoya 464-01, Japan
[1] *National Institute for Fusion Science, Toki 509-5292, Japan*

Abstract

The eigenvalue problem of the linearized magnetohydrodynamic(MHD) equation is formulated by using higher order spline functions as the base functions of Ritz-Galerkin approximation. When the displacement vector normal to the magnetic surface (in the magnetic surface) is interpolated by B-spline functions of degree p_1 (degree p_2) which is continuously c_1-th (c_2-th) differentiable on neighboring finite elements, the sufficient conditions for the good approximation is given by $p_1 \geq p_2 + 1$, $c_1 \leq c_2 + 1$, ($c_1 \geq 1, p_2 \geq c_2 \geq 0$). The influence of the numerical integration upon the convergence of calculated eigenvalues is discussed.

1 Introduction

MHD stability is an essential issue for the magnetic confinement of fusion plasmas. Spectrum analyzing codes of the linearized MHD equation with higher accuracy is required to analyze the localized modes with small growth rate.

The finite element method based on the variational energy principles has been applied to the analysis of MHD spectrum, and a lot of codes have been constructed [1, 2, 3, 4, 5]. Most of these codes are of second order accuracy, i.e., the numerical errors in the eigenvalues scale as N^{-2}, N being the number of elements in one dimension. Although fourth order accuracy is achieved in NOVA code [6] which does not depend on variational energy principles, by utilizing the third order spline functions, the nonlinear eigenvalue problem is involved. In the present paper, higher order spline functions are used as the base functions of the finite element method which applied to the Lagrangian of the linearized MHD equation.

In the present method, the 2-D (or 3-D) stability problem is reduced to 1-D problem with many variables by using the Fourier expansions with respect to poloidal (and toroidal) angles. Then the finite element method is applied to the minor radius direction. When the displacement vector normal to the magnetic surface is represented by X and the displacement vector in the magnetic surface is represented by Y, there appear the differential of X with respect to the minor radius direction, but not the differential of Y. The component vectors X and Y belong to the different function spaces. The operator which is defined by the energy integral is not compact; the spectrum pollution can occur. In order to avoid the spectrum pollution most of variational codes employ piecewise linear functions and step functions in hybrid. In this paper, the properties of "good approximation" is defined as the properties which the

approximated spectrum should possess, and the sufficient condition for the base functions that "good approximation" is derived is given with mathematical proof.

Most of theories of the finite element method depend on an assumption that the integral is carried out exactly. However, most of the spectrum analyzing codes utilize the numerical integration for calculating energy integral. Effect of numerical integration on convergence property of eigenvalues is one of the key problems, but only few discussions have so far been made. If the energy function is integrated exactly, the lowest eigenvalue is necessarily approximated from above. In ERATO code [1, 2], however, the lowest eigenvalue is approximated from below in most calculations against the ordinary theory. This problem is also discussed in this article.

The bilinear form which defines the linearized MHD operator is introduced in section 2. In section 3, the properties required for the approximated spectrum are defined. The theorem which determines the function spaces of the Ritz-Galerkin approximation is presented in section 4. The outline of the proof of the theorem is given in section 5 (the detail is shown in Appendix II). In section 6, the numerical errors in the eigenvalues are estimated. In section 7, the influence of the numerical integration upon the convergence of calculated eigenvalues is discussed. The numerical examples in the case of the clyndrical plasma are shown in section 8. Section 9 is devoted to the conclusions.

2 Linearized MHD Operator

We consider tours plasma configurations such that there exists a magnetic axis and around the magnetic axis there exist the magnetic surfaces which do not intersect each other.

Let ξ be the plasma displacement. When we assume the time dependence $\xi(r,t) = \xi(r)\exp(-i\omega t)$, the ideal linearized MHD equations are written as

$$-\lambda\rho_0\xi = F[\xi],\tag{1}$$

with

$$F[\xi] = \{\nabla(\xi\cdot\nabla p_0 + \gamma p_0\nabla\cdot\xi) + \nabla\times Q(\xi)\times B_0 + J_0\times Q(\xi)\}\tag{2}$$

where $\lambda = \omega^2$, $Q(\xi) = \nabla\times(\xi\times B_0)$ and ρ_0, J_0, B_0 and p_0 are the mass density, the current density, the magnetic field and the pressure in the equilibrium. In general ρ_0 may be a function of r. In follow, we assume that ρ_0 is a positive constant ($\rho_0 = 1$) for simplicity. Since we assume that the plasma is bounded by a conducting shell, the boundary condition at the plasma surface is expressed by

$$\xi\cdot n = 0,\tag{3}$$

where n denotes the vector normal to the plasma surface. The eigenvalue problem (1) can be formulated in the weak form as

$$W[\xi,\eta] = \lambda K[\xi,\eta], \text{ for any } \eta,\tag{4}$$

where

$$W[\xi,\eta] \equiv \int\{Q(\xi)\cdot Q(\eta) + J_0\times\eta\cdot Q(\xi) + (\xi\cdot\nabla p_0)\nabla\cdot\eta + \gamma p_0\nabla\cdot\xi\nabla\cdot\eta\}d\tau,\tag{5}$$

$$K[\xi,\eta] \equiv \int\xi\cdot\eta d\tau\tag{6}$$

with volume element $d\tau$. From the symmetricity of $W[\xi,\eta]$ we can see that λ is real number.

We introduce the coordinate system (ψ,θ,ζ) where ψ is a magnetic surface label, while θ and ζ are angular coordinates on a toroidal surface. If we deal with 2-D equilibria, we can take ψ as the poloidal magnetic flux within a magnetic surface and ζ as the toroidal angle ϕ which appears in the geometric cylindrical coordinate (R,ϕ,Z), while θ is determined by the condition that the lines of force are straight in the $\theta-\zeta$ plane.

We decompose the displacement vector ξ as

$$\xi = \xi_\psi \frac{\nabla\psi}{|\nabla\psi|^2} + \xi_s \frac{B \times \nabla\psi}{B^2} + \xi_b B. \tag{7}$$

Furthermore we expand ξ_ψ, ξ_s and ξ_b into Fourier series with respect to θ and ζ

$$
\begin{aligned}
\xi_\psi &= \sum_{m,n} \xi_\psi^{mn}(\psi) \exp\{i(m\theta + n\zeta)\} \\
\xi_s &= \sum_{m,n} \xi_s^{mn}(\psi) \exp\{i(m\theta + n\zeta)\} \\
\xi_b &= \sum_{m,n} \xi_b^{mn}(\psi) \exp\{i(m\theta + n\zeta)\}.
\end{aligned}
\tag{8}
$$

We also define the vectors X and Y as

$$X \equiv (\xi_\psi^{mn})^T, \quad Y \equiv (\xi_s^{mn}, \xi_b^{mn})^T. \tag{9}$$

X denotes the plasma displacement vectors normal to the magnetic surface and Y in the magnetic surface. When we truncate the Fourier series at $-m_0 \le m \le m_0$ and $-n_0 \le n \le 0$, the vectors X and Y have $M_X = 2m_0n_0 + n_0 + m_0 + 1$ and $M_Y = 2(2m_0n_0 + n_0 + m_0 + 1)$ components, respectively.

Let $V = \left(H_0^1(0, a; d\psi)\right)^{M_X} \times \left(L^2(0, a; d\psi)\right)^{M_Y}$, where H^l denotes the Sobolev space of the order of l. We introduce $Z \in V$, and we use the notation $Z = (X, Y)$ for an element of Z. For any trial function $W = (U, V) \in V$, eq.(4) reduces to the following bilinear form

$$a[Z, W] = \lambda b[Z, W], \tag{10}$$

where

$$a[Z, W] = \int_0^1 \begin{pmatrix} U'^H & U^H & V^H \end{pmatrix} \begin{pmatrix} D & C_1^H & C_2^H \\ C_1 & A_{11} & A_{21}^H \\ C_2 & A_{21} & A_{22} \end{pmatrix} \begin{pmatrix} X' \\ X \\ Y \end{pmatrix} d\psi \tag{11}$$

and

$$b[Z, W] = \int_0^1 \{U^H \cdot B_1 \cdot X + V^H \cdot B_2 \cdot Y\} d\psi. \tag{12}$$

Here the prime indicates the derivative with respect to ψ and the superscript H refers the Hermitian conjugate. D, A_{11}, A_{22}, B_1 and B_2 are Hermitian matrices. We assume that coefficients in eqs.(11) and (12) are sufficiently smooth. The bilinear form $a[Z, W]$ is continuous and coercive; $b[Z, W]$ is continuous and positive definite. The boundary conditions are given by

$$X(0) = 0, \quad X(1) = 0. \tag{13}$$

We note that the bilinear form $a[Z, W]$ is related to the Fourier Expanded operator of the linearized MHD $\hat{F}$ as

$$a[Z, W] = b[\hat{F}Z, W]. \tag{14}$$

3 Definition of the Good Approximation

The spectra of the linearized MHD operator F in eq.(2) are to be approximated by means of a finite element method. We here define properties that the approximated spectrum should possess.

Let $\sigma(F) \subset R$ be the spectrum of the operator F, and $\sigma(F_h) \subset R$ the spectrum of the operator F_h, where F_h is the operator approximating F. It should be noted that the ideal linearized MHD operator

F is non-compact. Therefore, the approximated spectrum $\sigma(F_h)$ can be polluted, i.e. there exists the series of eigenvalues of F_h which, converges to a value which belongs to the spectrum of F. We say that $\sigma(F_h)$ is "a good approximation" of $\sigma(F)$ when the approximated spectrum $\sigma(F_h)$ satisfies the following properties to the spectrum $\sigma(F)$;

i)For all $\mu \in \sigma(A)$, there exist the series of eigenvalues of A_h which converges to μ.

ii) There do not exist the series of eigenvalues of F_h which, converges to an eigenvalue which belongs to the spectrum of F(Non-pollution property).

iii) The numerical errors in the eigenvalue scale as $N^{-2(p_2+1)}$, where N is the number of elements and p_2 refers the degree of base function for the unknown function Y. If the coefficients belong to $H^{\alpha}(\alpha < 2(p_2+1)+1)$ but not to $H^{\alpha+1}$, the numerical errors scale as $N^{-(\alpha+1)}$.

4   Approximation of Function Spaces

When we apply the finite element method to eq.(10) the mathematical problem is that unknown functions X and Y belongs to different function spaces, i.e., there does not exists Y' in eq.(10). We here discuss the approximation of function spaces.

The integral region $[0,1]$ is divided into N intervals. There are $N+1$ points $\psi_0 = 0 < \psi_1 < \cdots < \psi_N = 1$ in $[0,1]$. The $i-$th interval is written as (ψ_{i-1}, ψ_i). For a given integer p we introduce the following finite dimensional function space K_h^p;

$$K_h^p = \{f \mid f \text{ is a polynomial of degree } \leq p \text{ on } (\psi_{i-1}, \psi_i) \quad i = 1, 2, ..., N\}.$$

Furthermore the following two kinds of finite dimensional function spaces $S_h^{p_1,c_1}$ and $T_h^{p_2,c_2}$ are defined; For given integers $p_1, p_2, c_1 (1 \leq c_1 \leq p_1)$ and $c_2 (0 \leq c_2 \leq p_2)$

$$S_h^{p_1,c_1} = \{f | f \in K_h^{p_1} \cap H^{c_1}, f(0) = f(1) = 0\}, \tag{15}$$

$$T_h^{p_2,c_2} = \{f | f \in K_h^{p_2} \cap H^{c_2}\}. \tag{16}$$

Here $c_2 = 0$ denotes that base functions are discontinuous on borders of intervals. The dimensions n_X (of the function space $S_h^{p_1,c_1}$) and n_Y (of the function spaces $T_h^{p_2,c_2}$) are given by

$$n_X = (p_1 + 1)N - c_1(N-1) - 2 = (p_1 - c_1 + 1)N + c_1 - 2, \tag{17}$$

$$n_Y = (p_2 + 1)N - c_2(N-1) = (p_2 - c_2 + 1)N + c_2. \tag{18}$$

We should note that the term -2 in eq. (17) is concerned with the boundary condition.

We apply Ritz-Galerkin method and define the finite element subspace V_h of the function space V as $V_h = (S_h^{p_1,c_1})^{M_X} \times (T_h^{p_2,c_2})^{M_Y}$ i.e. X and Y in eqs. (11) and (12) are expanded with $S_i \in S_h^{p_1,c_1}$ and $T_i \in T_h^{p_2,c_2}$ in the forms

$$X(\psi) = \sum_i^{n_X} X_i S_i(\psi), \quad Y(\psi) = \sum_i^{n_Y} Y_i T_i(\psi). \tag{19}$$

We can state the following theorem.

[THEOREM]

V_h described above is applied for the finite element subspace of the Ritz-Galerkin approximation of the linearized MHD operator. It is assumed that D is positive definite at almost everywhere in $[0,1]$, that $\det(D)$ is not zero at almost everywhere in $[0,1]$, and that there exists $\hat{C}_2^H$ such that $\hat{C}_2^H \cdot C_2^H = 1$.

The sufficient conditions to obtain the good approximation property are

$$p_1 \geq p_2 + 1, \quad c_1 \leq c_2 + 1, \quad (c_1 \geq 1, p_2 \geq c_2 \geq 0) \tag{20}$$

Base functions which have been used in most of linearized MHD stability codes correspond to the parameters $p_1 = 1, p_2 = 0, c_1 = 1$ and $c_2 = 0$. In [9], it has been pointed out that the combination of the Hermite functions of the third order and of the second order prevents spectrum pollution, i.e. $p_1 = 3, p_2 = 2, c_1 = 3$ and $c_2 = 2$. It has been proved by J.Rappaz in [8] that the sufficient condition for the non-pollution property is $p_1 = p, p_2 = p - 1, c_1 = 1, c_2 = 0, p \geq 1$. We note that all these conditions satisfy the conditions (20).

5 Proof of the Theorem for the Good Approximation Property

In this section we shall prove the theorem described in the previous section.

In section 2 we introduced the eigenvalue problem of MHD equation in the bilinear form eq.(10): $a[Z, W] = \lambda b[Z, W]$. We here consider $\hat{a}[Z, W] = \hat{\lambda} b[Z, W]$ instead of $a[Z, W] = \lambda b[Z, W]$ where $\hat{a} = a + \lambda_s b$ and $\hat{\lambda} = \lambda + \lambda_s$ with a positive constant λ_s. If the constant λ_s is large enough, we can define the linear bounded non-compact operator $\hat{F}_{\lambda_s}^{-1}$ where $\hat{F}_{\lambda_s} = \hat{F} + \lambda_s$. On the other hand, $\hat{a}$ is the positive and continuous bilinear form on $V = (H_0^1(0, a; d\psi))^{M_X} \times (L^2(0, a; d\psi))^{M_Y}$, so that according to the Lax-milgram theorem, there exists an unique operator $T : V \to V$ such that

$$\hat{a}[TZ, W] = b[Z, W], \text{ for any } Z, W \in V. \tag{21}$$

Indeed the operator T accords with the resolvent $\hat{F}_{\lambda_s}^{-1}$. In the following, we consider the spectral approximation of T.

The linear bounded operator T is the non-compact operator. Therefore, the approximation of T has the difficulty associated with spectral pollution [10]. Descloux-Nassif-Rappaz [7] have verified the mathematical conditions which ensure the efficiency of approximations of the spectrum for a non-compact operator including the linearized MHD operator.

[THEOREM(Descloux-Nassif-Rappaz)]

Let U be a Banach space with norm $\| \ \|$. Let A be linear bounded operators in U. Then sufficient conditions for the good approximation properties are the following two conditions,

$$P2 : \forall u \in U, \lim_{h \to 0} \delta(u, U_h) = 0,$$

$$P3 : \lim_{h \to 0} \sup_{\substack{u \in U_h \\ \|u\| = 1}} \delta(Au, U_h) = 0. \tag{22}$$

We apply this theorem to the operator T. Let $V = (H_0^1(0, a; d\psi))^{M_X} \times (L^2(0, a; d\psi))^{M_Y}$ and $V_h = (S_h^{p_1, c_1})^{M_X} \times (T_h^{p_2, c_2})^{M_Y}$ where $S_h^{p_1, c_1}$ and $T_h^{p_2, c_2}$ are the function spaces introduced in the previous section. Then we shall verify that the conditions $P2$ and $P3$ are satisfied.

The property $P2$ is the basic property of the finite elements. We entrust the proof of $P2$ to textbooks [11]. It remains to verify the $P3$ property.

As an example Descloux-Nassif-Rappaz have referred to the two-dimensional linearized MHD eigenvalue problem with three components in [7]. We trace the way of the their proof of $P3$ property in our case.

We consider the region $\Omega = \{\psi | \psi \in [0,1]; \forall v \in C^{M_X}, (v, D(\psi)v) > 0, |D| \neq 0\}$. In Ω, $\hat{a}[Z, W]$ which is introduced in section 5 is coercive, so that according to the Lax-milgram theorem, there exists an unique operator $T : V \to V$ such that

$$\hat{a}[TZ, W] = b[Z, W], \text{ for any } Z, W \in V. \tag{23}$$

We supposed $V_h = (S_h^{p_1, c_1})^{M_X} \times (T_h^{p_2, c_2})^{M_Y} \subset (H_0^{c_1})^{M_X} \times (H^{c_2})^{M_Y}, Z \in V_h, \bar{Z} \equiv (\tilde{X}, \tilde{Y}) = TZ$, i.e.

$$\hat{a}[\bar{Z}, W] = b[Z, W] \text{ for any } W \in V. \tag{24}$$

Setting $U = 0$ in eq.(24), we obtain

$$\tilde{Y} = \bar{A}_{22}^{-1} \cdot (B_2 \cdot Y - C_2 \cdot \tilde{X}' - A_{21} \cdot \bar{X}), \tag{25}$$

where $\bar{A}_{22} = A_{22} + \lambda_s B_2$. Substituting this relation for $\tilde{Y}$ into eq.(24) and setting $V = 0$, we obtain for any $U \in (H_0^{c_1})^{M_Y}$

$$
\begin{aligned}
c[\tilde{X}, U] = \int_\Omega [& U \cdot B_1 \cdot X + U \cdot \{A_{21}^H \cdot \bar{A}_{22}^{-1} \cdot A_{21} - (A_{11} + \lambda_s B_1) + C_1' \\
& - (A_{21}^H \cdot \bar{A}_{22}^{-1} \cdot C_2 + A_{21}^H \cdot \hat{C}_2^H \cdot G)'\} \cdot \bar{X} \\
& + U' \cdot \{C_2^H \cdot \bar{A}_{22}^{-1} \cdot A_{21} - A_{21}^H \cdot \bar{A}_{22}^{-1} \cdot C_2 + C_1 - C_1^H - A_{21}^H \cdot \hat{C}_2^H \cdot G\} \cdot \bar{X} \\
& - U' \cdot C_2^H \cdot \bar{A}_{22}^{-1} \cdot B_2 \cdot Y - U \cdot A_{21}^H \cdot \bar{A}_{22}^{-1} \cdot B_2 \cdot Y] \mathrm{d}\psi
\end{aligned}
\tag{26}
$$

with

$$c[\phi_X, \phi_Y] = \int_\Omega \{\phi_Y' \cdot G \cdot \phi_X' + \phi_Y \cdot A_{21}^H \cdot \hat{C}_2^H \cdot G \cdot \phi_X' \mathrm{d}\psi \tag{27}$$

where $\hat{C}_2^H$ is the matrix satisfying $\hat{C}_2^H \cdot C_2^H = 1$ and $G = D - C_2^H \cdot \bar{A}_{22}^{-1} \cdot C_2$. Here G is positive definite because D and B_2 are positive definite and the constant λ_s included in $\bar{A}_{22}$ is selected large enough. Hence $c[\phi_X, \phi_Y]$ is a continuous and coercive bilinear form on $(H_0^{c_1})^{M_X}$. We here introduce a function $w \in (H_0^{c_1})^{M_X}$ and a function $\phi \in (S_h^{p_2+1, c_2+1})^{M_Y}$. Under the condition (20), $\phi \in (S_h^{p_2+1, c_2+1})^{M_Y} \subseteq (S_h^{p_1, c_1})^{M_Y}$ and $\phi' \in (T_h^{p_2, c_2})^{M_Y}$. Substituting $\bar{X} = w - G^{-1} \cdot C_2^H \cdot \bar{A}_{22}^{-1} \cdot B_2 \cdot \phi$ and $Y = \phi' \in (T_h^{p_2, c_2})^{M_Y}$ into eq.(26), we get

$$
\begin{aligned}
c[w, U] = \int_\Omega [& U \cdot B_1 \cdot X + U \cdot \{A_{21}^H \cdot \bar{A}_{22}^{-1} \cdot A_{21} - (A_{11} + \lambda_s B_1) + C_1' - (A_{21}^H \cdot \bar{A}_{22}^{-1} \cdot C_2)' \\
& - (A_{21}^H \cdot \hat{C}_2^H \cdot G)'\} \cdot (w - G^{-1} \cdot C_2^H \cdot \bar{A}_{22}^{-1} \cdot B_2 \cdot \phi) \\
& + U' \cdot \{C_2^H \cdot \bar{A}_{22}^{-1} \cdot A_{21} - A_{21}^H \cdot \bar{A}_{22}^{-1} \cdot C_2 + C_1 - C_1^H \\
& - A_{21}^H \cdot \hat{C}_2^H \cdot G\} \cdot (w - G^{-1} \cdot C_2^H \cdot \bar{A}_{22}^{-1} \cdot B_2 \cdot \phi) \\
& - U' \cdot G \cdot (G^{-1} \cdot C_2^H \cdot \bar{A}_{22}^{-1} \cdot B_2)' \cdot \phi \\
& - U \cdot A_{21}^H \cdot \hat{C}_2^H \cdot G \cdot (G^{-1} \cdot C_2^H \cdot \bar{A}_{22}^{-1} \cdot B_2)' \cdot \phi] \mathrm{d}\psi
\end{aligned}
\tag{28}
$$

for any $U \in (H_0^{c_1})^{M_X}$. Then the right member depends on ϕ, but not on ϕ'. We note that the mapping $V \to (H_0^{c_1})^{M_X}, Z \to w$ is compact, so that there exists $p \in (S_h^{p_1, c_1})^{M_X}$ with $\|p - w\|_{(H^{c_1})^{M_X}} \leq \epsilon_h \|Z\|$, where ϵ_h denotes a genetic sequence converging to zero. Since $S_h^{p_1, c_1}$ satisfies the Nitsche-Schatz property (see appendix I), there exists $q \in (S_h^{p_1, c_1})^{M_X}$ with $\|G^{-1} \cdot C_2^H \cdot \bar{A}_{22}^{-1} \cdot B_2 \cdot \phi - q\|_{(H^{c_1})^{M_X}} \leq ch \|\phi\|_{(H^{c_1})^{M_Y}}$; setting $r = p + q$, we have $\|\tilde{X} - r\|_{(H^{c_1})^{M_X}} \leq \epsilon_h \|Z\|$. In order to approximate $\tilde{Y}$, we approximates $\tilde{X}$ in eq.(25) by r. Since $T_h^{p_2, c_2}$ satisfies the Nitsche-Schatz property, there exists $s \in (T_h^{p_2, c_2})^{M_Y}$ such that $\|\tilde{Y} - s\|_{(H^{c_2})^{M_Y}} \leq \epsilon_h \|Z\|$. Setting $g = (r, s) \in V_h$, we have $\|\bar{Z} - g\| \leq \epsilon_h \|Z\|$, which proves the $P1$ property. Finally, we extend the region Ω to [0,1] by analytic continuation.

6 Convergence Property

We here estimate the errors included in the energy integral $a[Z, W]$. It is assumed that the coefficients are sufficiently smooth, i.e., the coefficients belong to $H^{2(p_2+1)+1}$. If the solution $Z = (X, Y)$ is sufficiently smooth, i.e., $X \in H^{p_1+1}, Y \in H^{p_2}$, Galerkin approximations of the solution $X_h \in S_h^{p_1, c_1}$ and $Y_h \in T_h^{p_2, c_2}$ satisfy the following relations

$$\|X - X_h\|_1 \leq CN^{-p_1}\|X\|_{p_1+1}, \tag{29}$$

$$\|Y - Y_h\|_0 \leq CN^{-p_2+1}\|Y\|_{p_2}. \tag{30}$$

Here C is a constant and $\|. \|_l$ denotes the Sobolev's norm of the order of l. The errors included in the energy integral $a[Z, W]$ is determined by the order of base functions of Y because of the condition $p_1 \geq p_2 + 1$. When we select $Z = (X, Y)$ itself as the trial function $W = (U, V)$, the errors in the eigenvalues scale as

$$|\mu - \mu^*| \leq CN^{-2(p_2+1)}, \tag{31}$$

where μ and μ^* denote the eigenvalue and the approximated one, respectively.

If the coefficients are not sufficiently smooth, however, the estimation (31) tends to

$$|\mu - \mu^*| \leq CN^{-(\alpha+1)}, \tag{32}$$

provided that the coefficients belong to $H^\alpha(\alpha < 2(p_2 + 1) + 1)$ but not to $H^{\alpha+1}$.

7 Influence of the Numerical Integration

The integration in eq.(10) is numerically carried out by using the Gaussian quadrature formula over each element. We shall select Z itself as the trial function W. If the polynomials of degree p are employed as the base functions of X in eq.(10) and the condition (20) is satisfied, the highest degree which appears in the integrand in eq.(10) is $2p$. It is not required that every polynomial which appears be integrated exactly. According to the theory of the finite element method, the condition for the converge of the calculated lowest eigenvalue is that the quadrature formula should be correct at least through degree $2(p-1)$ in the present problem. If we use the $q(> p)$-point quadrature formula, every polynomial must be integrated exactly. Then it is found by the minimax principle that the lowest eigenvalue is approximated from above. But if we employ the just p-point quadrature formula, the term of the highest order is not estimated correctly. Although the convergence of the calculated lowest eigenvalue is ensured, the lowest eigenvalue is no longer approximated from above. Whether the eigenvalue is approximated from above or from below will depend on the situation.

It is reported that the lowest eigenvalue is approximated from below in most calculations of ERATO code and TERPSICHORE code [14]. This will be caused by the fact that the quadrature formula which can not integrate exactly the polynomials is applied in ERATO code and TERPSICHORE code.

8 Numerical Example

In order to show the applicability of the present scheme, we applied it to the eigenvalue problem of the cylindrical uniform plasma bounded by a conducting shell. We consider the only one Fourier component

with the dependence of $\exp[i(nz + m\theta)]$. Equations (11) and (12) reduce to the following quadratic form

$$a[Z,Z] = \int_0^1 \left(X'\ X\ Y_1\ Y_2 \right) \begin{pmatrix} B^2 + \gamma p & -\frac{2B_\theta^2}{r^2} & -\frac{(B^2+\gamma p)G}{B^2} & -\gamma p F \\ -\frac{2B_\theta^2}{r^2} & \frac{F^2}{r^2} + \frac{2B_\theta^2}{r^3} - \frac{2B_\theta B_\theta'}{r^2} & -\frac{2nB_\theta}{r} & 0 \\ -\frac{(B^2+\gamma p)G}{B^2} & -\frac{2nB_\theta}{r} & n^2 + \frac{m^2}{r^2} + \frac{\gamma p G^2}{B^4} & \frac{\gamma p G F}{B^2} \\ -\gamma p F & 0 & \frac{\gamma p G F}{B^2} & \gamma p F^2 \end{pmatrix} \begin{pmatrix} X' \\ X \\ Y_1 \\ Y_2 \end{pmatrix} dr$$

(33)

$$b[Z,Z] = \lambda \int_0^1 \{ \frac{X^2}{r} + r(\frac{Y_1^2}{B^2} + B^2 Y_2^2) \} dr$$

(34)

where $F = \frac{mB_\theta}{r} + nB_z,\ G = \frac{mB_z}{r} - nB_\theta$.

We shall examine that the coefficients in (33) satisfy the conditions for coefficients in present theorem (see section 4).

$$D = B^2 + \gamma p > 0 \qquad \text{allmost everwhere in } [0,1]$$

We determine the equilibrium by giving two profile functions, i.e., the pressure $p(r)$ and the safety factor $q(r)$. Here we consider the case that profile functions are taken as

$$p(r) = p(0)(1 - r^2),$$

(35)

$$q(r) = q(0)(1 + cr),\ c = \frac{q(1)}{q(0)} - 1$$

(36)

where the parameters are $p(0) = 0.1, q(0) = 1/6$ and $q(1) = 2/13$. Hereafter we deal with only the case that $m = 2$ and $n = 1$. This equilibrium is chosen so that the following three spectra — the Alfvén continuum, the slow continuum, the Sturmian discrete spectrum of fast waves which clusters at the infinity — do not overlap. The schematic picture of these spectra is shown in Fig.1 [12].
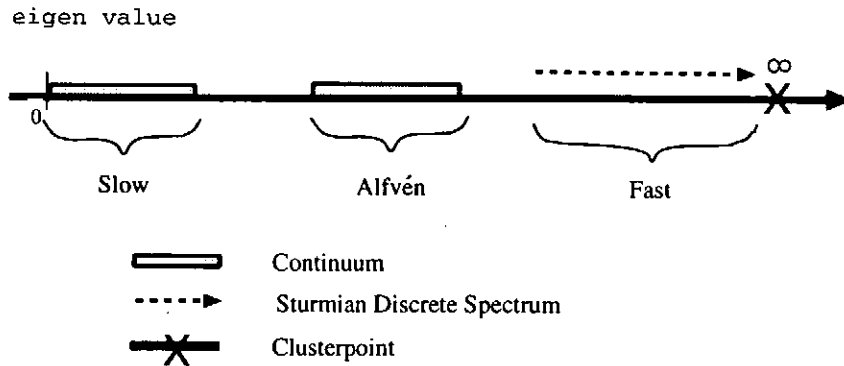
Figure 1: Schematic picture of the spectrum.

First the non-pollution property of the present method is examined. The number of the point of the Gaussian quadrature formula is fixed for $q = p + 1$. When we fix the parameter $p_1 = 2$, we can take the four kinds of combinations of base functions under the condition (20);

[a] $p_1 = 2, p_2 = 0, c_1 = 1, c_2 = 0,$
[b] $p_1 = 2, p_2 = 1, c_1 = 1, c_2 = 0,$
[c] $p_1 = 2, p_2 = 1, c_1 = 1, c_2 = 1,$
[d] $p_1 = 2, p_2 = 1, c_1 = 2, c_2 = 1.$

Figures 2 and 3 show the numerically calculated spectrum for the cases [b] and [d] versus the number of intervals. From figures 2 and 3, we can see two eigenvalues of fast waves, as well as the spectra associated with the continua of the Alfvén waves and the slow waves. Figures shows that the spectral pollution does not occur. Similar results are obtained for the cases [a] and [c].

Next, we investigate the convergence property. The results of the numerical convergence are shown in Fig.6 for the minimum Sturmian discrete eigenvalue. The logarithm of numerical errors versus $\log_{10} N^{-1}$ is presented. In Fig.6 [a], the parameters are chosen as $p_1 = p, p_2 = p - 1, c_1 = 1$ and $c_2 = 0$ for a integer $p(= 1, 2, 3)$. The line with the symbols o represents the case $(p_1 = 1, p_2 = 0, c_1 = 1, c_2 = 0)$, while the line with the symbols □ and ◇ represent the case $(p_1 = 2, p_2 = 1, c_1 = 1, c_2 = 0)$ and $(p_1 = 3, p_2 = 2, c_1 = 1, c_2 = 0)$, respectively. The inclinations of these convergence curves are about $2(p_2 + 1)$. In Fig.4 [b] the parameters are selected as $p_1 = p, p_2 = p - 1, c_1 = 2$ and $c_2 = 1$. The line with the symbols o represents the case $(p_1 = 2, p_2 = 1, c_1 = 2, c_2 = 1)$ and the line with the symbols □ represents the case $(p_1 = 3, p_2 = 2, c_1 = 2, c_2 = 1)$. The inclinations of these convergence curves are also about $2(p_2 + 1)$. In both cases the numerical errors are in agreement with analytical one : $|\lambda - \lambda^*| = O(N^{-2(p_2+1)})$.

Thirdly, we discuss the influence of the numerical integration. In the equilibrium considered above, the lowest eigenvalue belongs to the continuum, so that it is difficult to discuss about the convergence of the lowest eigenvalue. Hence we consider the other equilibrium characterized by the following profile functions

$$p(r) = p(0)(1 - r^2)^2, \quad q(r) = q(0) + r(q(1) - q(0) + \frac{(r^2 - 1)(q'(1) - q(1) + q(0))(1 - y_s)}{(r^2 - y_s)}) \qquad (37)$$

where $y_s = (q'(1) - q(1) + q(0))/(q'(0) + q'(1) - 2(q(1) - q(0)))$ and the parameters are $p(0) = 0.0015, q(0) = 1.45, q(1) = 1.65, q'(0) = 0.2$ and $q'(1) = 0.2$. When we select the Fourier modes as $m = 3$ and $n = -2$, the interchange mode becomes unstable. Figure 5 shows the numerically calculated eigenvalue versus N^{-4}. The parameters associated with base functions are chosen as $p_1 = 2, p_2 = 1, c_1 = 2$ and $c_2 = 1$. The symbol o represents the numerically calculated eigenvalues in the case of using two point quadrature formula, while the symbol □ in the case of using three point formula. We note that in this case the eigenvalue is approximated from below under the influence of the quadrature formula which can not integrate exactly the polynomials.
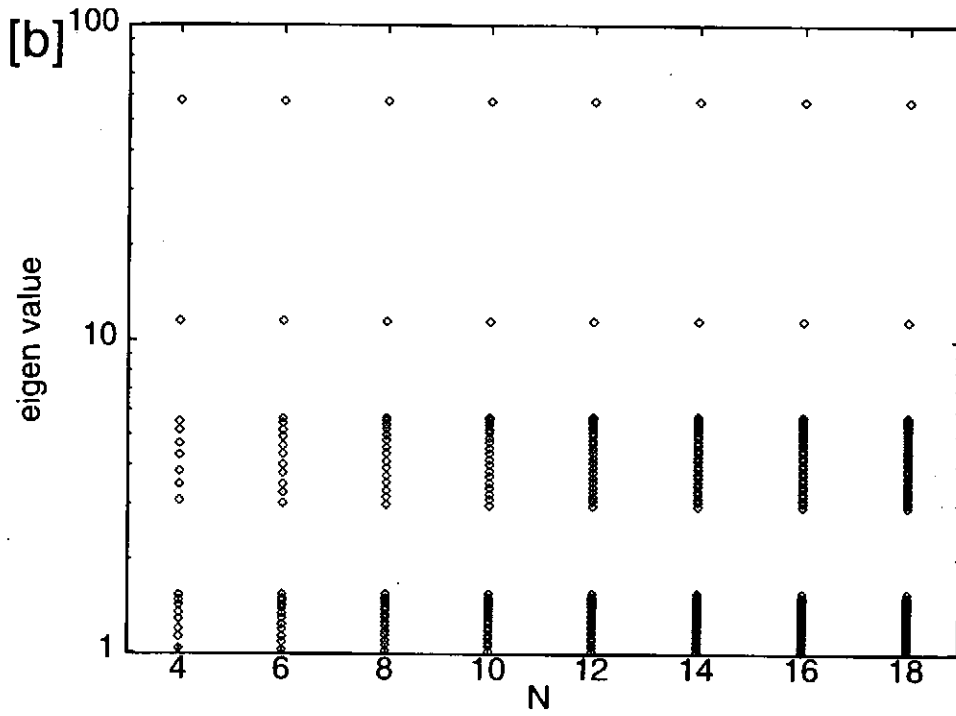
Figure 2: The numerically calculated spectrum in case of the cylinder model by using the present method as a function of the number of intervals N. The parameters are $p_1 = 2, p_2 = 1, c_1 = 1, c_2 = 0$ and $q = 3$.
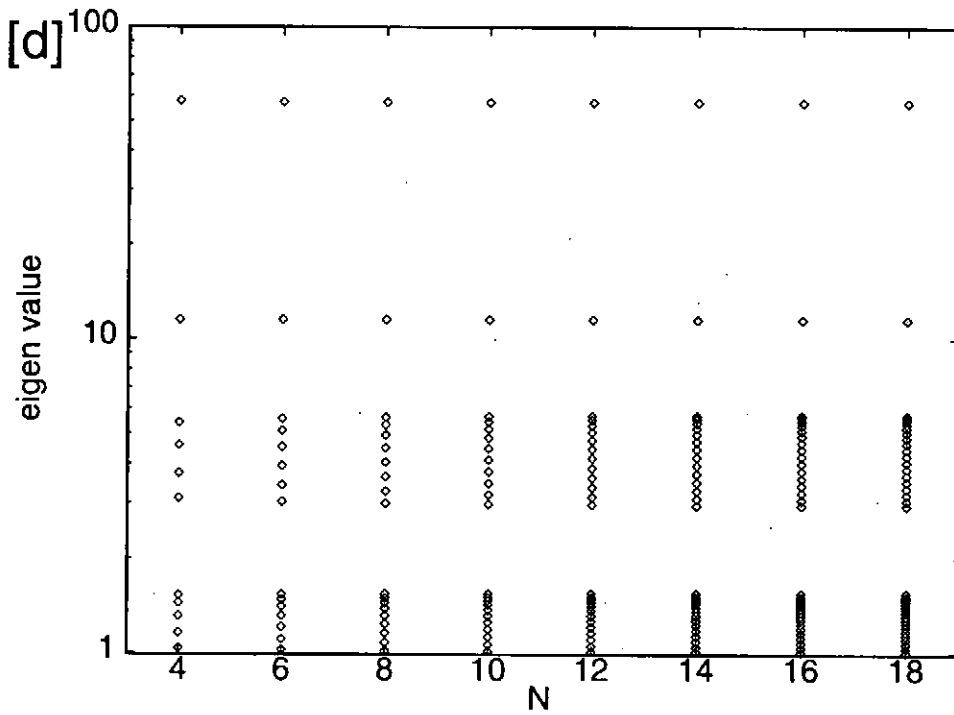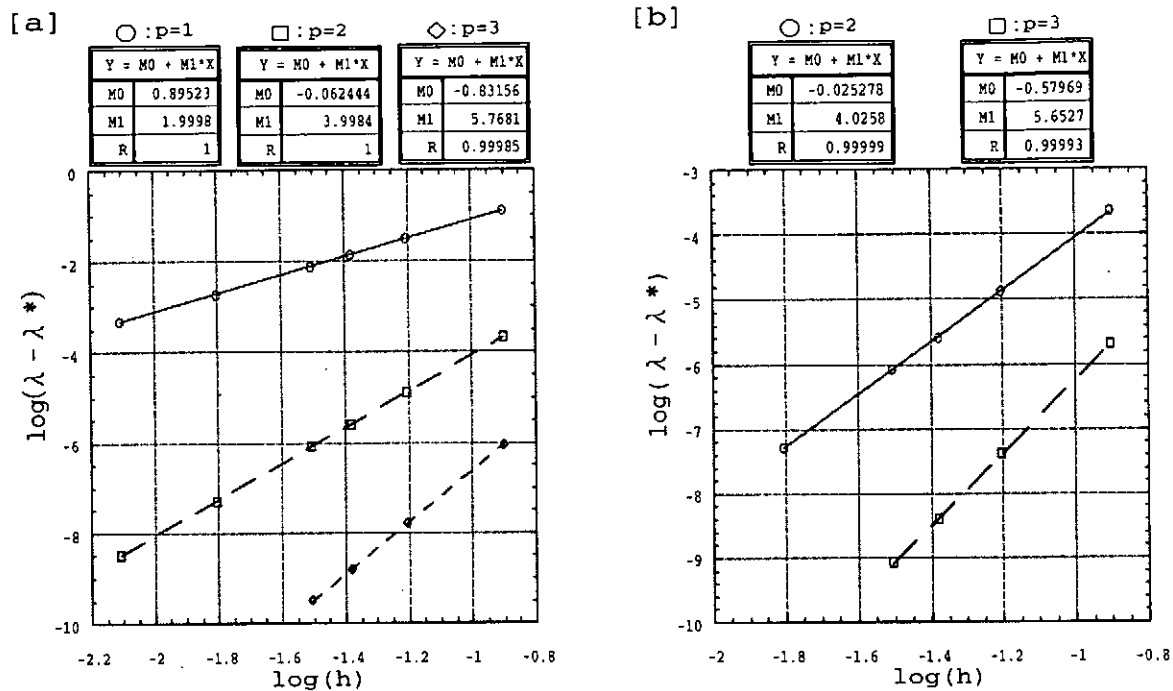

Figure 3: The numerically calculated spectrum in case of the cylinder model by using the present method as a function of the number of intervals N. The parameters are $p_1 = 2, p_2 = 1, c_1 = 2, c_2 = 1$ and $q = 3$.

Figure 4: Numerical convergence for the minimum discrete eigenvalue in the cylinder model. In [a], $p_1 = p, p_2 = p - 1, c_1 = 1, c_2 = 0, q = p + 1$, { $\circ$: $p = 1$ }, { $\square$: $p = 2$ }, { $\diamond$: $p = 3$ }. In [b], $p_1 = p, p_2 = p - 1, c_1 = 2, c_2 = 1, q = p + 1$, { $\circ$: $p = 2$ }, { $\square$: $p = 3$ }.
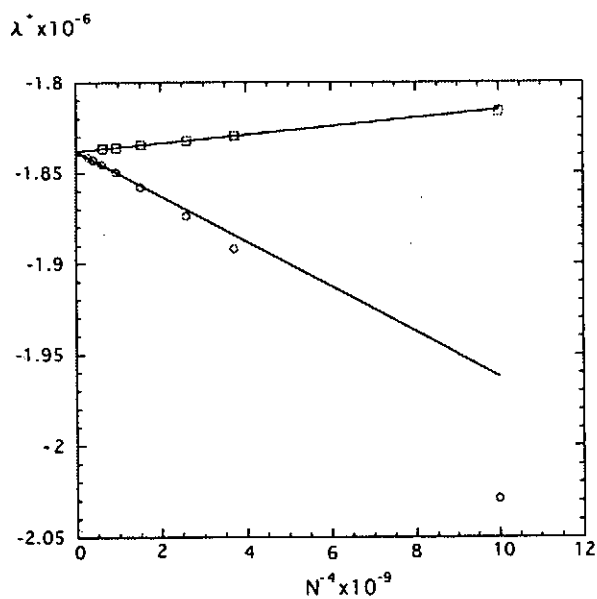
Figure 5: The numerically calculated eigenvalue of the interchange mode as a function of the number of intervals N^{-4}. The symbols $\circ$($\square$) represent the case of using two(three) point quadrature formula. The parameters associated with base functions are $p_1 = 2, p_2 = 1, c_1 = 2$ and $c_2 = 1$.

9 Conclusion

In this paper we have discussed a scheme to calculate the spectrum of the linearized MHD equations with higher accuracy. In the present method, 2-D (or 3-D) stability problem is reduced to 1-D multi-variable problem by using the Fourier expansions with respect to poloidal and toroidal angles. Then the finite element method is applied to the minor radius direction. The two kinds of spline functions are employed as the base functions of Ritz-Galerkin approximation; the sufficient conditions (20) for the spline functions to obtain the good approximation property is presented. In most actual calculations the integral can not be carried out exactly because the equiliblium is given numerically. The present method makes use of the Gaussian quadrature formula to evaluate the integral over each elements. The influence of the numerical integration upon the convergence of calculated eigenvalues is discussed.

As an example the present method is applied to the eigenvalue problem of the cylindrical plasma. The good approximation has been obtained, i.e., the spectral pollution is not observed and the numerical errors in the discrete eigenvalues are in agreement with analytical one :$|\lambda - \lambda^*| = O(N^{-2(p_2+1)})$. The eigenvalue of the interchange mode is approximated from below when we use the quadrature formula which can not integrate exactly the base functions. This is a typical example that the calculated lowest eigenvalues is approximated from below under the influence of the numerical integration.

Acknowledgments

References

[1] R.Gruber, F.Troyon, D.Berger, Comput. Phys. commun. **21**, 323(1981)

[2] R.Gruber, S. Semenzato, F.Troyon, T. Tsunematsu, Comput. Phys. commun. **24**, 363(1981)

[3] R.C.Grimm, R.L.Dewar and J.Manickam, J.Comput.Phys. **49**, 94(1983)

[4] D.V.Anderson, W.A.Cooper, R.Gruber, S.Merazzi and U.Schwenn, Int. J. Supercomput. Appl. **4**, 3(1990)

[5] C.Schwab, Phys.Fluids **B5**, 9(1993)

[6] C.Z.Cheng, M.S.Chance, J. Comput. Phys. **71**,124(1987)

[7] J.Descloux, N.Nassif, J.Rappaz, RAIRO Anal. Numér. **12**,97(1978)

[8] J.Rappaz, Numer. Math. **28**,15(1977)

[9] T.Tsunematsu,*Handbook of Numerical Calculation (New Version) ed. by Ohno and Isoda,* (Ohm Express, Tokyo, 1990) §4.10.3 p.434 [in japanese]

[10] K.Appert, D.Berger, R.Gruber, and F.Troyon, J. Appl. Math. and Phys. (ZAMP) **25**, 229(1974)

[11] G.Strang and J.Fix, *An Analysis of the Finite Element Method,* (Prentice-Hall, New Jersey, 1973) §3.2

[12] J. P. Goedbloed, Phys. of Fluids **18**, 1258(1975)

[13] K.Appert, D.Berger, R.Gruber, and J.Rappaz, J. Comput. Phys. **18**,284(1975)

[14] D.V.Anderson, W.A.Cooper, S.Merazzi, U.Schwenn, R.Gruber, Supercomputer **8**,32(1991)

Stability analysis of a hollow electron column in a sheared magnetic field

Shigeo Kondoh

Department of Quantum Engineering and Systems Science,
University of Tokyo, 7-3-1 Hongo, Bunkyo-ku, Tokyo 113, Japan

Abstract

Stability of the diocotron modes of a hollow cylindrical electron cloud in a sheared magnetic field is analytically investigated. For the first step of the stability analysis, we analyze electrostatic behavior of an electron column. It is found that, under the electrostatic limitation, the azimuthal magnetic field makes the electron column unstable.

Key Words: non-neutral plasma, diocotron instability, magnetic shear

1 Introduction

Proto-RT (Prototype Ring Trap) is a new-type toroidal device for non-neutral plasma confinement[1]. In this device, the magnetic field is produced by the internal ring, six toroidal coils, and two vertical field coils. The ultimate purpose of this experimental device is to investigate the possibility of high-β plasma confinement due to the hydrodynamic pressure of the $\boldsymbol{E} \times \boldsymbol{B}$ flow[2].

One of the most common instabilities of non-neutral plasmas is the diocotron instability[3]. It is known that[4] two surface waves on the both sides of a non-neutral plasma sheet interact with each other through the electrostatic field and the consequent $\boldsymbol{E} \times \boldsymbol{B}$ drift of charged particles, and this interaction causes the two surface waves to grow, which results in instability. In the cylindrical geometry, it is also known that hollow density profiles tend to be unstable[3, 5–7]. Proto-RT provides hollow electron plasmas surrounding the internal ring, therefore the diocotron modes can be potentially unstable.

Fortunately, Proto-RT has a sheared magnetic field, because the poloidal magnetic field decreases as the distance from the internal ring increases but the toroidal magnetic field is almost uniform around the plasma region. Such a magnetic shear has been shown[8] to have a stabilizing effect on the diocotron instability for the special case that electrons form a relativistic beam and the azimuthal magnetic field is much weaker than the axial magnetic field. However, effects of the magnetic shear are still unknown for general cases including the case of Proto-RT, where electrons are non-relativistic.

The purpose of this research is to analytically investigate the effect of the magnetic shear on the diocotron instability especially for the case of Proto-RT. For the first step of the analysis,

we electrostatically examine how the hollow electron column behaves if we apply the poloidal magnetic field as well as the toroidal magnetic field.

The analysis reported in this paper is an extention of two previous articles on the diocotron instability[3, 5], which consider hollow electron plasmas in the uniform axial magnetic field. We add the poloidal magnetic field to the two previous analyses.
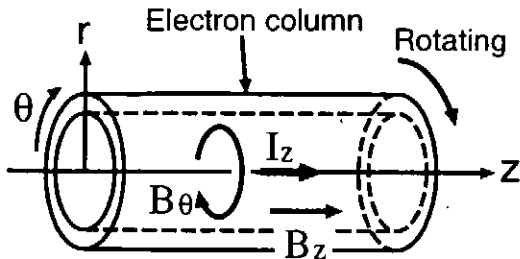
2   Assumed configuration

Figure 1 : The assumed hollow electron plasma.

We assume a hollow cylindrical electron plasma as shown in Fig.1. We consider the limit of the infinite aspect ratio $(R/a \to \infty)$, thus any toroidal effects are neglected. The toroidal magnetic field B_z is assumed to be uniform and straight in the z-direction, and there is a linear line current at the center of axisymmetry, which provides the azimuthal (poloidal) magnetic field given by

$$B_\theta = \frac{\mu_0 I_z}{2\pi r},$$

(1)

where I_z is the linear line current at the axis of symmetry and r is the distance from it.
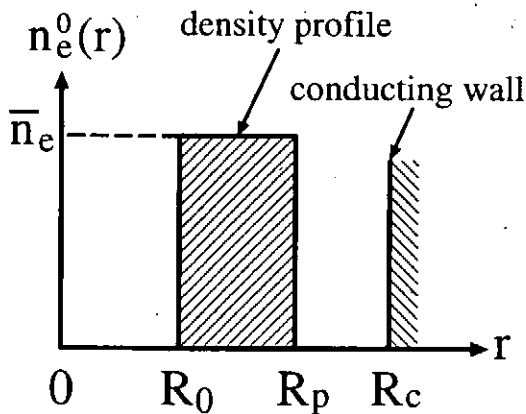
Figure 2 : The assumed rectangular density profile.

The electron column is assumed to be infinitely long in the z-direction. The density profile is assumed to be rectangular in the r-direction as shown in Fig.2. The radii of the inner and outer plasma surfaces are defined as R_0 and R_p, respectively, and it is assumed that a conducting wall is placed at $r = R_c$. The electron density on the flat top is assumed to be $\bar{n}_e$, and no background ions and neutral particles are assumed.

3   Fluid equations and equilibria

The fluid equations for non-neutral electron plasmas are

$$\frac{\partial}{\partial t} \boldsymbol{v} + (\boldsymbol{v} \cdot \nabla) \boldsymbol{v} = -\frac{e}{m} \left(-\nabla \phi - \frac{\partial \boldsymbol{A}}{\partial t} + \boldsymbol{v} \times \boldsymbol{B} \right),$$

(2)

$$\frac{\partial n_e}{\partial t} + \nabla \cdot (n_e \boldsymbol{v}) = 0, \tag{3}$$

$$\nabla^2 \phi = \frac{e n_e}{\varepsilon_0}, \tag{4}$$

$$\boldsymbol{E} = -\nabla \phi - \frac{\partial \boldsymbol{A}}{\partial t}, \tag{5}$$

where $\boldsymbol{v}$ is the fluid velocity, n_e is the density of particles, ϕ is the electrostatic potential, $-e$ and m are the charge and the mass of an electron, respectively. The pressure term $\nabla \cdot \vec{P} / (mn)$ has been neglected in Eq.(2), because we assume a cold plasma.

Under the assumed steady state described in Sec. 2, the r-component of Eq.(2) is identical to

$$-\frac{m v_\theta^2}{r} = -e(E_r + v_\theta B_z - v_z B_\theta), \tag{6}$$

and Eq.(4) can be written as

$$\frac{1}{r}\frac{d}{dr}\left(r\frac{d\phi_0}{dr}\right) = \begin{cases} 0 & (0 \le r < R_0) \\ \dfrac{e\overline{n}_e}{\varepsilon_0} & (R_0 \le r \le R_p) \\ 0 & (R_p < r \le R_c) \end{cases} \tag{7}$$

in the cylindrical polar coodinates. Integrating Eq.(7) gives

$$E_r = -\frac{d\phi}{dr} = \begin{cases} 0 & (0 < r \le R_0) \\ -\dfrac{e\overline{n}_e}{2\varepsilon_0}\left(r - \dfrac{R_0^2}{r}\right) & (R_0 \le r \le R_p) \\ -\dfrac{e\overline{n}_e}{2\varepsilon_0 r}(R_p^2 - R_0^2) & (R_p \le r \le R_c) \end{cases} \tag{8}$$

Substituting Eq.(8) and $\boldsymbol{v} \cdot \boldsymbol{B} = 0$, which can be expected since the $\boldsymbol{E} \times \boldsymbol{B}$ flow is perpendicular to $\boldsymbol{B}$, into Eq.(6), we obtain a quadratic equation for the angular velocity $\omega_e \equiv v_\theta / r$ as follows:

$$\omega_e^2(r) + \frac{\omega_{pe}^2}{2}\left(1 - \frac{R_0^2}{r^2}\right) - \left(\Omega_{ez}\omega_e(r) - \frac{v_z}{r}\Omega_{e\theta}\right) = 0 \quad (R_0 \le r \le R_p), \tag{9}$$

where $\omega_{pe} = \sqrt{e^2 \overline{n}_e / \varepsilon_0 m}$ is the electron plasma frequency, and $\Omega_{e\theta}(r) = e B_\theta(r)/m$ and $\Omega_{ez} = e B_z/m$ are the θ-component and the z-component of the cyclotron frequency, respectively. The solutions to Eq.(9) are

$$\omega_e^\pm(r) = \frac{\Omega_{ez}}{2}\left(1 + \frac{a^2}{r^2}\right)\left\{1 \pm \left[1 - \frac{2\omega_{pe}^2 r^2(r^2 - R_0^2)}{\Omega_{ez}^2(r^2 + a^2)}\right]^{\frac{1}{2}}\right\}, \tag{10}$$

where a is a constant defined by

$$a = \frac{\mu_0 I_z}{2\pi B_z} = r\frac{\Omega_{e\theta}(r)}{\Omega_{ez}}. \tag{11}$$

Under the condition $\omega_{\mathrm{pe}} \ll \Omega_{ez}$, the low-frequency mode ω_{e}^- in Eq.(10) can be approximated by

$$\omega_{\mathrm{e}}^-(r) \simeq \omega_{\mathrm{D}} \frac{r^2 - R_0^2}{r^2 + a^2}, \tag{12}$$

where $\omega_{\mathrm{D}} = \omega_{\mathrm{pe}}^2/2\Omega_{ez}$ is called the diocotron frequency. Equation (12) gives the equilibrium rotation frequency profile. Note that in the limit $a \to 0$, Eq.(12) is identical to Eq.(2.10.17) in Ref.[3].

4 Stability analysis

4.1 Equation for perturbed electrostatic potential

Now we consider stability of the equilibrium state derived in Sec. 3. All perturbed values $\Psi(r, t)$ are decomposed into equilibrium values $\Psi^0(r)$ and variations $\delta\Psi(r, t)$ from them:

$$\Psi = \Psi^0 + \delta\Psi. \tag{13}$$

Then the fluid equations Eq.(2)-(4) are linearized as

$$\frac{\partial}{\partial t}\delta n_{\mathrm{e}} + \nabla \cdot [n_{\mathrm{e}}^0 \delta v_{\mathrm{e}} + \delta n_{\mathrm{e}}(v_{\mathrm{e}\theta}^0 e_\theta + v_{\mathrm{e}z}^0 e_z)] = 0, \tag{14}$$

$$\frac{\partial}{\partial t}\delta v_{\mathrm{e}} + [(v_{\mathrm{e}\theta}^0 e_\theta + v_{\mathrm{e}z}^0 e_z) \cdot \nabla]\delta v_{\mathrm{e}} + (\delta v_{\mathrm{e}} \cdot \nabla)[v_{\mathrm{e}\theta}^0 e_\theta + v_{\mathrm{e}z}^0 e_z]$$

$$= \frac{e}{m_{\mathrm{e}}} \left\{ \nabla\delta\phi + \frac{\partial}{\partial t}\delta A - \delta v_{\mathrm{e}} \times (B_\theta^0 e_\theta + B_z^0 e_z) - (v_{\mathrm{e}\theta}^0 e_\theta + v_{\mathrm{e}z}^0 e_z) \times \delta B \right\} \tag{15}$$

$$\nabla \cdot \left(\nabla\delta\phi(x, t) + \frac{\partial}{\partial t}\delta A \right) = \frac{1}{\varepsilon_0}\delta n_{\mathrm{e}} e, \tag{16}$$

where we neglect $\partial(\delta A)/\partial t$ and δB in order to analyze electrostatically. Furthermore, we Fourier-decompose all the perturbation terms $\delta\Psi$ as

$$\delta\Psi(r, \theta, z, t) = \sum_{l=-\infty}^{\infty} \sum_{k_z=-\infty}^{\infty} \delta\Psi^l(r, k_z)\exp[i(l\theta + k_z z - \omega t)]. \tag{17}$$

Then some partial derivative operators and all the perturbed quantities can be replaced as follows:

$$\frac{\partial}{\partial t} \to -i\omega, \quad \frac{\partial}{\partial z} \to ik_z, \quad \frac{\partial}{\partial \theta} \to il, \quad \delta\Psi \to \delta\Psi^l. \tag{18}$$

Equation (15) can be expressed as

$$\begin{pmatrix} -i(\omega - l\omega_{\mathrm{e}} - k_z v_{\mathrm{e}z}^0) & \Omega_{ez} - 2\omega_{\mathrm{e}} & -\Omega_{e\theta} \\ \frac{1}{r}\frac{\partial}{\partial r}(rv_{\mathrm{e}\theta}^0) - \Omega_{ez} & -i(\omega - l\omega_{\mathrm{e}} - k_z v_{\mathrm{e}z}^0) & 0 \\ \frac{\partial v_{\mathrm{e}z}^0}{\partial r} + \Omega_{e\theta} & 0 & -i(\omega - l\omega_{\mathrm{e}} - k_z v_{\mathrm{e}z}^0) \end{pmatrix} \begin{pmatrix} \delta v_{\mathrm{e}r}^l \\ \delta v_{\mathrm{e}\theta}^l \\ \delta v_{\mathrm{e}z}^l \end{pmatrix} = \begin{pmatrix} \frac{e}{m}\frac{\partial\delta\phi^l}{\partial r} \\ \frac{e}{m}\frac{il\delta\phi^l}{r} \\ \frac{e}{m}ik_z\delta\phi^l \end{pmatrix}. \tag{19}$$

Making use of Eqs. (16) and (19), we eliminate δv^l and δn^l_e in favor of $\delta \phi^l$. Then we obtain the equation for the perturbed electrostatic potential:

$$\frac{1}{r}\frac{\partial}{\partial r}\left[\left(1-\frac{\omega_{\text{pe}}^2}{\nu_{\text{e}}^2}\right)r\frac{\partial}{\partial r}\delta\phi^l\right] - \frac{l^2}{r^2}\left\{1-\frac{\omega_{\text{pe}}^2}{\nu_{\text{e}}^2}\left[1-\frac{\Omega_{e\theta}\left(\dfrac{\partial v_z}{\partial r}+\Omega_{e\theta}\right)}{(\omega-l\omega_{\text{e}}-k_z v_z^0)^2}\right]\right\}\delta\phi^l$$

$$-k_z^2\left[1-\frac{\omega_{\text{pe}}^2}{(\omega-l\omega_{\text{e}}-k_z v_z^0)^2}\frac{\nu_{\text{e}}^2+\Omega_{e\theta}(\partial v_z^0/\partial r+\Omega_{e\theta})}{\nu_{\text{e}}^2}\right]\delta\phi^l$$

$$+\frac{k_z\partial\Omega_{e\theta}/\partial r}{\omega-l\omega_{\text{e}}-k_z v_z^0}\delta\phi^l + \frac{\Omega_{e\theta}k_z}{\omega-l\omega_{\text{e}}-k_z v_z^0}\left(1-\frac{\omega_{\text{pe}}^2}{\nu_{\text{e}}^2}\right)\frac{\partial\delta\phi^l}{\partial r}$$

$$=-\frac{l}{r}\delta\phi^l\frac{1}{\omega-l\omega_{\text{e}}-k_z v_z^0}\left\{\frac{\partial}{\partial r}\left[\frac{\omega_{\text{pe}}^2}{\nu_{\text{e}}^2}(-\Omega_{ez}+2\omega_{\text{e}})\right] + \frac{\Omega_{e\theta}k_z\omega_{\text{pe}}^2}{(\omega-l\omega_{\text{e}}-k_z v_z^0)^2\nu_{\text{e}}^2}\left[\frac{1}{r}\frac{\partial}{\partial r}(r^2\omega_{\text{e}})-\Omega_{ez}\right]\right.$$

$$\left.+\frac{(-\Omega_{ez}+2\omega_{\text{e}})k_z\omega_{\text{pe}}^2}{(\omega-l\omega_{\text{e}}-k_z v_z^0)\nu_{\text{e}}^2}\left(\frac{\partial v_z^0}{\partial r}+\Omega_{e\theta}\right)\right\}, \tag{20}$$

where $\nu_{\text{e}}^2(r)$ is the determinant of the matrix in the left-hand side of Eq.(19), which is given by

$$\nu_{\text{e}}^2(r) = (\omega-l\omega_{\text{e}}-k_z v_z^0)^2 + (\Omega_{ez}-2\omega_{\text{e}})\left[\frac{1}{r}\frac{\partial}{\partial r}(r^2\omega_{\text{e}})-\Omega_{ez}\right] - \Omega_{e\theta}\left(\frac{\partial v_z^0}{\partial r}+\Omega_{e\theta}\right). \tag{21}$$

Here we make further assumptions for simplicity as follows:

$$\omega_{\text{pe}}^2(r) \ll \Omega_{ez}^2, \tag{22}$$

$$\omega_{\text{pe}}^2(r) \ll \Omega_{e\theta}^2, \tag{23}$$

$$k_z = 0, \tag{24}$$

$$|\omega-l\omega_{\text{e}}(r)|^2 \ll \Omega_{ez}^2, \tag{25}$$

$$|\omega-l\omega_{\text{e}}(r)|^2 \ll \Omega_{e\theta}^2, \tag{26}$$

$$\omega_{\text{e}}(r) = \omega_{\text{e}}^-(r) \quad , \tag{27}$$

$$\frac{\partial v_z^0}{\partial r} \ll \Omega_{ez}. \tag{28}$$

Under the assumptions above, Eq.(20) is reduced to

$$\frac{1}{r}\frac{\partial}{\partial r}\left(r\frac{\partial}{\partial r}\delta\phi^l\right) - \frac{\omega^2}{(\omega-l\omega_{\text{e}})^2}\frac{\Omega_{e\theta}^2}{\Omega_{ez}^2+\Omega_{e\theta}^2}\frac{l^2}{r^2}\delta\phi^l = \frac{l}{r}\delta\phi^l\frac{1}{\omega-l\omega_{\text{e}}}\frac{\partial}{\partial r}\left(\frac{\omega_{\text{pe}}^2\Omega_{ez}}{\Omega_{e\theta}^2+\Omega_{ez}^2}\right). \tag{29}$$

Substituting $x \equiv r/R_0$, Eq.(12), and the assumed rectangular density profile (Fig.2) into Eq.(29) gives

$$\frac{1}{x}\frac{d}{dx}\left(x\frac{d}{dx}\delta\phi^l\right) - \frac{l^2}{x^2}\delta\phi^l = 0 \quad (0 < x < 1 \quad \text{or} \quad x_p < x < x_c), \tag{30}$$

$$\frac{d^2}{dx^2}(x^{\frac{1}{2}}\delta\phi^l) - \kappa^2\left\{\frac{\gamma^2}{(\alpha x^2+l)^2} + \frac{\beta}{x^2}\right\}(x^{\frac{1}{2}}\delta\phi^l) = 0 \quad (1 < x < x_p), \tag{31}$$

where $\kappa^2 = \Omega_{ez}^2/\varpi_{pe}^2$, $\alpha = \omega/\omega_D - l$, $\beta = (l^2 - 1/4)/\kappa^2$, $\gamma = 2al/R_0$, $x_p = R_p/R_0$, and $x_c = R_c/R_0$ are dimensionless parameters. These are the reduced equations for the perturbed electrostatic potential.
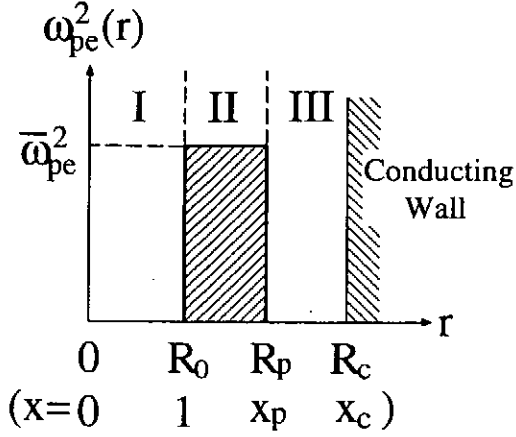
4.2 Dispersion relation

Figure 3 : The assumed density profile and regions I, II, and III.

While Eq.(30) can be analytically solved as

$$\delta\phi^l = Br^l + \frac{C}{r^l}, \tag{32}$$

where B and C are arbitrary constants, solutions to Eq.(31) are unknown. However, we can make use of the Wentzel-Kramers-Brillouin (WKB) method on Eq.(31), if $\kappa\gamma \gg 1$. Then an approximate solution to Eq.(31) is given by

$$x^{\frac{1}{2}}\delta\phi^l \simeq P(x)^{-\frac{1}{4}}(B'\exp(i\kappa\tau) + C'\exp(-i\kappa\tau)), \tag{33}$$

$$P(x) = -\left\{\frac{\gamma^2}{(\alpha x^2 + l)^2} + \frac{\beta}{x^2}\right\}, \tag{34}$$

$$\tau(x) = \int^x P(x)^{\frac{1}{2}}dx. \tag{35}$$

We have to connect Eqs. (32) and (33) at $x = 1$ and $x = x_p$ under certain boundary conditions. Boundary conditions for Eq.(32) are

$$\delta\phi^l(0) < \infty, \tag{36}$$

$$\delta\phi^l(x_c) = 0, \tag{37}$$

and that $\delta\phi^l$ is continuous at $x = 1$ and $x = x_p$, i.e. Eqs.(32) and (33) have the same values at $x = 1$ and $x = x_p$. Under these boundary conditions, Eqs.(32) and (33) become

$$\delta\phi^l = \begin{cases} \delta\phi^l_{\rm I} = \delta\phi^l_{\rm II}(1)x^l & (0 < x \leq 1) \\ \delta\phi^l_{\rm II} = (x^2 P(x))^{-\frac{1}{4}}[B'\exp(i\kappa\tau) + C'\exp(-i\kappa\tau)] & (1 \leq x \leq x_p) \\ \delta\phi^l_{\rm III} = \delta\phi^l_{\rm II}(x_p)\dfrac{x_p^l}{x_p^{2l} - x_c^{2l}}\left(x^l - \dfrac{x_c^{2l}}{x^l}\right) & (x_p \leq x \leq x_c) \end{cases} \tag{38}$$

where I, II, and III are the names of the regions as shown in Fig.3. Furthermore, there are jump conditions of $d\delta\phi^l/dx$ at $x = 1$ and $x = x_p$. Multiplying Eq.(29) by r, integrating from $R_0 - \varepsilon$ to $R_0 + \varepsilon$, and taking the limit $\varepsilon \to 0$ give

$$\left[\frac{d}{dx}\delta\phi^l_{\rm II}(1) - \frac{d}{dx}\delta\phi^l_{\rm I}(1)\right] = -2l\frac{\omega_D}{\omega}\delta\phi^l_{\rm II}(1)\frac{1}{1 + b^2}, \tag{39}$$

where $b = a/R_0$. Note that

$$\frac{d\omega_{\text{pe}}}{dr} = \overline{\omega}_{\text{pe}}(\delta(r - R_0) - \delta(r - R_p)). \tag{40}$$

In the same way, multiplying Eq.(29) by r, integrating from $R_p - \varepsilon$ to $R_p + \varepsilon$, and taking the limit $\varepsilon \rightarrow 0$ give

$$\left[\frac{d}{dx}\delta\phi_{\text{III}}^l(x_p) - \frac{d}{dx}\delta\phi_{\text{II}}^l(x_p)\right] = \frac{2l\omega_{\text{D}}x_p^2\delta\phi_{\text{II}}^l(x_p)}{(\omega - l\omega_e(x_p))(x_p^2 + b^2)} . \tag{41}$$

Substituting Eq.(38) into Eqs.(39) and (41), we obtain

$$\begin{bmatrix} A_{11} & A_{12} \\ A_{21} & A_{22} \end{bmatrix} \begin{bmatrix} B' \\ C' \end{bmatrix} = \begin{bmatrix} 0 \\ 0 \end{bmatrix} , \tag{42}$$

where

$$A_{11} = \exp(i\kappa\tau(1))\left\{\frac{1}{2} + \frac{P'(1)}{4P(1)} + l - \frac{2l\omega_{\text{D}}}{(1 + b^2)\omega} - i\kappa P(1)^{\frac{1}{2}}\right\} , \tag{43}$$

$$A_{12} = \exp(-i\kappa\tau(1))\left\{\frac{1}{2} + \frac{P'(1)}{4P(1)} + l - \frac{2l\omega_{\text{D}}}{(1 + b^2)\omega} + i\kappa P(1)^{\frac{1}{2}}\right\} , \tag{44}$$

$$A_{21} = \exp(i\kappa\tau(x_p))\left\{l\frac{x_p^{2l} + x_c^{2l}}{x_p^{2l} - x_c^{2l}} + \frac{1}{2} + \frac{x_pP'(x_p)}{P(x_p)} - \frac{2l\omega_{\text{D}}x_p^2}{(\omega - l\omega_e(x_p))(x_p^2 + b^2)} - i\kappa x_pP(x_p)^{\frac{1}{2}}\right\} , \tag{45}$$

$$A_{22} = \exp(-i\kappa\tau(x_p))\left\{l\frac{x_p^{2l} + x_c^{2l}}{x_p^{2l} - x_c^{2l}} + \frac{1}{2} + \frac{x_pP'(x_p)}{P(x_p)} - \frac{2l\omega_{\text{D}}x_p^2}{(\omega - l\omega_e(x_p))(x_p^2 + b^2)} + i\kappa x_pP(x_p)^{\frac{1}{2}}\right\} . \tag{46}$$

In order for Eq.(42) to have non-trivial solutions for B' and C', the following is required:

$$\det A_{ij} = A_{11}A_{22} - A_{12}A_{21} = 0, \tag{47}$$

which is identical to

$$\exp(\kappa\tau)(A_1 + \kappa Q(1)^{\frac{1}{2}})(A_2 - \kappa x_pQ(x_p)^{\frac{1}{2}}) - \exp(-\kappa\tau)(A_1 - \kappa Q(1)^{\frac{1}{2}})(A_2 + \kappa x_pQ(x_p)^{\frac{1}{2}}) = 0 , \tag{48}$$

where

$$Q(x) = -P(x) \tag{49}$$

$$A_1 = \frac{1}{2} + \frac{Q'(1)}{4Q(1)} + l - \frac{2l}{\dfrac{\omega}{\omega_{\text{D}}}(1 + b^2)} , \tag{50}$$

$$A_2 = \frac{1}{2} + \frac{x_pQ'(x_p)}{4Q(x_p)} + l\frac{x_p^{2l} + x_c^{2l}}{x_p^{2l} - x_c^{2l}} - \frac{2lx_p^2}{\dfrac{\omega}{\omega_{\text{D}}}(x_p^2 + b^2) - l(x_p^2 - 1)} . \tag{51}$$

Equation (48) is the dispersion relation.

4.3 Stability

Now we can analyze stability of the hollow electron column assumed in Sec. 2. Although we derived the dispersion relation Eq.(48) in the previous subsection, we make use of the equation for the perturbed electrostatic potential Eq.(31) directly and do not use the dispersion relation Eq.(48), because we cannot discuss about the limit $B_\theta \to 0$ using Eq.(48). It is a violation of the condition $\kappa\gamma \gg 1$ to take the limit $B_\theta \propto \gamma \to 0$ in Eq.(48).

Using the boundary conditions described in Sec. 4.2, i.e. Eqs.(36), (37), (39), and (41), we numerically calculate the eigenvalues ω for the characteristic equation given by Eq.(31). The numerical scheme we adopt is a combination of the Newton method and the fourth-order Runge-Kutta method. The Newton method is used to determine ω, and the Runge-Kutta method is used to solve the differential equation (31).

Figure 4 shows an example of the obtained eigenvalues normalized by ω_D plotted as a function of $a/R_0 \propto B_\theta$. Here $n_e = 10^{12} \text{m}^{-3}$, $B_z = 300\text{G}$, $\kappa = 294.4$, $l = 2$, $x_p = 1.3$, and $x_c = 1.5$. In the toroidal geometry, the quantity a/R_0 can be expressed as

$$\frac{a}{R_0} = \frac{\iota}{2\pi A},\tag{52}$$

where ι is the rotational transform, and A is the aspect ratio of the toroidal plasma. The real part of ω is the frequency of the diocotron mode, which is on the order ω_D, and the imaginary
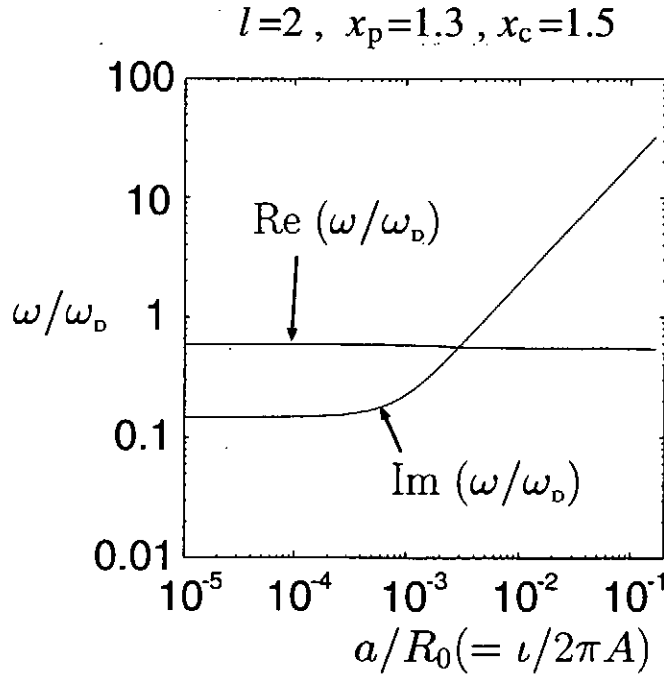
Figure 4 : The eigenvalues as functions of B_θ.

$$l = 2 \quad , \quad x_{\mathrm{p}} = 7.0 \quad , \quad x_{\mathrm{c}} = 10.0$$
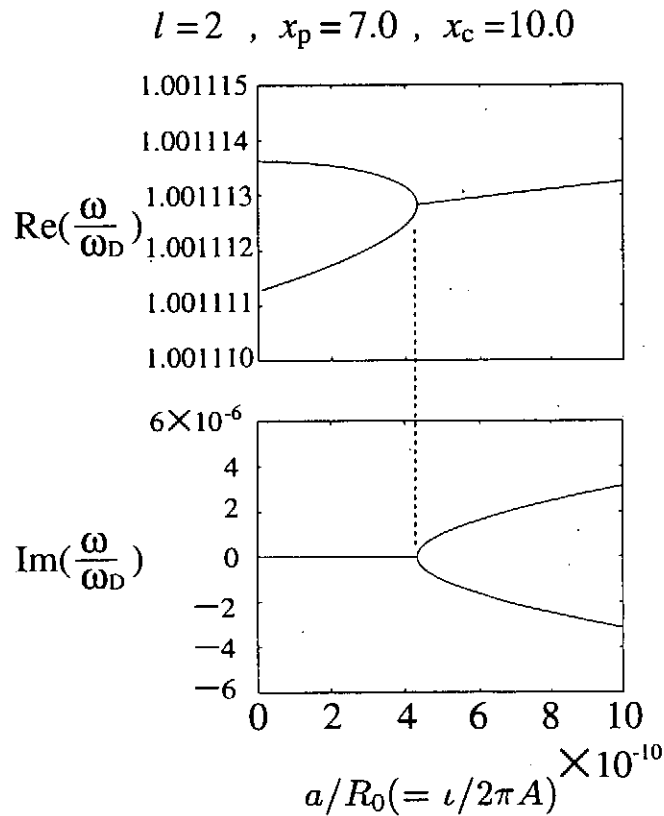
Figure 5 : The eigenvalues as functions of B_θ

part corresponds to the growth rate. As we can see from Fig.4, the imaginary part of ω, i.e. the growth rate, increases as the rotational transform of the magnetic field increases. In this case, therefore, the poloidal magnetic field B_θ makes the diocotron mode unstable in the electrostatic territory.

Another example of the eigenvalues is shown in Fig. 5. The parameters are $\kappa = 294.4$, $l = 2$, $x_p = 7.0$, and $x_c = 10.0$. The first figure in Fig. 5 expresses the real part of ω, which is the frequency, and the second one expresses the imaginary part, which is the growth rate. The transverse axis is $\iota/2\pi A$ again. In this case, the diocotron mode is stable in the limit of $\iota = 0$. However, a very small rotational transform makes the diocotron mode unstable, since the imaginary part becomes non-zero. Therefore, also in this case, the poloidal magnetic field makes the diocotron mode unstable.

From these two examples (Figs. 4 and 5), we can conclude that the diocotron mode tends to become unstable because of the poloidal magnetic field in the electrostatic territory. We do not know the physical reason why the diocotron mode becomes unstable if the poloidal magnetic field is applied. Note that we have ignored some important effects such as the electromagnetic effects, the existence of the inner conductor[5], the wave propagation in the z-direction k_z, etc. We have to consider these effects to know more practical behavior of the hollow electron column.

5 Summary

We have analyzed stability charactaristics of a hollow electron plasma placed in a sheared magnetic field. The magnetic field is a combination of the axial uniform magnetic field (i.e. the toroidal magnetic field) and the azimuthal magnetic field (i.e. the poloidal magnetic field) produced by a linear line current at the center of axisymmetry. We have determined the equilibrium state, linearized the fluid equations, derived the dispersion relation, and calculated the complex eigenfrequencies electrostatically. We have obtained the results that, in the electrostatic territory, the hollow electron column tends to become unstable due to the poloidal magnetic field.

References

[1] Z. Yoshida *et al.*, in *Proceedings of 17th IAEA Fusion Energy Conference* (IAEA), IAEA-CN-69/ICP/10(R)(1998).

[2] S. M. Mahajan and Z. Yoshida, Phys. Rev. Lett. (to be published).

[3] R. C. Davidson, *Theory of nonneutral plasmas* (Addison-Wesley, Massachusetts, 1989), pp. 66-73.

[4] W. Knauer, J. Appl. Phys. **37**, 602(1966).

[5] R. H. Levy, Phys. Fluids **8**, 1288(1965)

[6] R. L. Kyhl and H. F. Webster, IRE Trans. Electron Dev., **ED-3**, 172(1956).

[7] C. F. Driscoll *et al.*, Plasma Phys. Cont. Nucl. Fusion Res. 1988 (IAEA, Vienna, 1989), **3**, pp.507-514.

[8] E. Ott and J. M. Wersinger, Phys. Fluids **23**, 324(1980).

Ideal Non-resonant Pressure-driven Instabilities in Low Shear Stellarators with Magnetic Hill

Tomoya TATSUNO, Masahiro WAKATANI
Graduate School of Energy Science, Kyoto University,
Gokasho, Uji 611-0011, Japan

Katsuji ICHIGUCHI
National Institute for Fusion Science,
Oroshi-cho, Toki 509-5292, Japan

January 26, 1999

Abstract

There are two cases that Mercier criterion for localized interchange modes in stellarators is useless in ideal MHD plasma. One case is non-resonant pressure-driven instabilities with low mode numbers which become unstable even if the mode resonant surface does not exist inside the plasma column. The other case is interchange instabilities when the pressure gradient vanishes at the mode resonant surface due to small magnetic islands and so on. If the pressure becomes flat in a narrow region around the mode resonant surface, low mode number instabilities are suppressed and the beta limit at the particular resonant surface increases. Also radial mode structure at nearly marginal beta changes significantly. Properties of the resonant and non-resonant modes are clarified with a cylindrical plasma model for a low shear stellarator with a magnetic hill.

Key Words: ideal MHD, straight helical configuration, Mercier criterion, non-resonant instability

1 Introduction

While Mercier criterion is used for investigating interchange instabilities in tokamaks [1] and stellarators [2], there exist some cases for which the criterion does not predict the correct beta limit within the ideal MHD model. For deriving the Mercier criterion it is assumed that the unstable mode is radially localized near the mode resonant surface. However, this situation does not occur when the pressure gradient becomes locally flat at the mode resonant surface. Details of pressure profile effects on the interchange modes will be shown in this paper with use of a cylindrical plasma model for a low shear stellarator with a magnetic hill.

In order to destabilize the interchange mode, the resonant surface is not always necessary. It is reasonable that in a low shear region, non-resonant modes approximately satisfying the resonant condition can be destabilized. First non-resonant resistive modes were demonstrated for a Heliotron-E plasma with a highly peaked pressure profile [3]. Recently ideal non-resonant modes were shown unstable in the central region of Heliotron-E, which seems consistent with the $m = 2/n = 1$ mode triggering the sawtooth [4]. Non-resonant modes usually have global mode structures, which requires numerical analysis to clarify the property. We have studied the details of ideal non-resonant instabilities in the cylindrical configuration.

In section 2, we derive an eigenvalue equation for studying linear interchange modes in stellarators, which is derived from the reduced MHD equations [5]. In section 3, we first solve the eigenvalue equation analytically in the low shear limit, and discuss about the non-resonant mode. Next we solve the same eigenvalue equation numerically for a finite shear

case. In section 4 we show examples to clarify various properties for the resonant and non-resonant modes with standard pressure profiles. In section 5, we concentrate on the effect of the pressure flattening on the mode structures and the beta limits. Finally in section 6, we summarize the obtained results and give a physical interpretation for the behavior of non-resonant modes.

2 Eigenmode equations

For analyzing pressure-driven instabilities in stellarators, we use the ideal reduced MHD equations [5]. We will neglect the toroidal effect in the reduced MHD equations. In this case the equilibrium quantities do not depend on the poloidal angle θ. This assumption corresponds to the situation that the average flux surfaces have circular cross section in the large aspect ratio limit. Then the rotational transform is written as

$$\iota(r) \equiv \frac{R_0}{r B_0} \frac{d\psi_0}{dr}, \tag{1}$$

where the equilibrium poloidal flux function is given by $\psi_0(r)$. Since the correction due to the diamagnetic current becomes higher order, the rotational transform in this approximation includes only the vacuum helical field contribution.

After the appropriate normalization, the linearized reduced MHD equations in the cylindrical approximation can be written as

$$\gamma(\nabla_\perp^2 u) = -\frac{n - m\iota}{\gamma} \nabla_\perp^2 [(n - m\iota) u] - \frac{D_s}{\gamma} \frac{m^2}{r^2} u, \tag{2}$$

where D_s and the averaged helical curvature Ω are expressed as

$$D_s = -\frac{\beta_0}{2\epsilon^2} p' \Omega', \tag{3}$$

$$\Omega = \epsilon^2 N \left(r^2 \iota + 2 \int r\iota \, dr \right). \tag{4}$$

Here $\epsilon \equiv a/R_0$ denotes the inverse aspect ratio, $\beta_0 \equiv 2\mu_0 p_0(r = 0)/B_0^2$ the central plasma beta value, N the toroidal period number of the helical field, respectively. Also all perturbed quantities are assumed to be proportional to $\exp[\gamma t - i(m\theta + n\zeta)]$, where $m(n)$ denotes the poloidal(toroidal) mode number. Here and after, the prime denotes the derivative with respect to the normalized minor radius r. The perpendicular Laplacian operator in eq. (2) is shown as

$$\nabla_\perp^2 = \frac{1}{r} \frac{d}{dr} \left(r \frac{d}{dr} \right) - \frac{m^2}{r^2}. \tag{5}$$

Thus the O.D.E. (2) for the stream function u with the mode number (m, n) is written as

$$\frac{d^2 u}{dr^2} + \left[\frac{1}{r} - \frac{2m\iota'(n - m\iota)}{\gamma^2 + (n - m\iota)^2} \right] \frac{du}{dr}$$
$$- \left\{ \frac{m^2}{r^2} + \frac{1}{\gamma^2 + (n - m\iota)^2} \left[\left(\frac{m\iota'}{r} + m\iota'' \right)(n - m\iota) - \frac{D_s m^2}{r^2} \right] \right\} u = 0. \tag{6}$$

Here the boundary condition at the plasma surface $r = 1$ is $u = 0$ under the fixed boundary condition. At $r = 0$ we impose the boundary condition $u = 0$ from the regularity of the solution. With these boundary conditions we can set up an eigenvalue problem for the eigenvalue or growth rate γ^2 and the corresponding eigenfunction u.

3 Analytic solution of Eigenmode Equation

In this section we assume $\iota' = 0$ for obtaining an analytic solution, then eq. (6) is written as

$$\frac{d^2 u}{dr^2} + \frac{1}{r} \frac{du}{dr} + \frac{m^2}{r^2} \left[\frac{D_s}{\gamma^2 + (n - m\iota)^2} - 1 \right] u = 0. \tag{7}$$

For the parabolic pressure profile, $p = p_0(1 - r^2)$, the analytic solution is readily obtained with the transformation $\tilde{r} \equiv \{\widetilde{D}_s m^2/[\gamma^2 + (n - m\iota)^2]\}^{1/2}r$, where $\widetilde{D}_s = 4\beta_0 N\iota$. From the solution $u \propto J_m(\tilde{r})$ for the (m, n) mode and the boundary condition $u = 0$ at $r = 1$, the growth rate is written as

$$\gamma^2 = \frac{\widetilde{D}_s m^2}{Z^2(m, k)} - (n - m\iota)^2, \tag{8}$$

where $Z(m, k)$ is the kth zero point of the mth order Bessel function of the first kind $J_m(\tilde{r})$.

It is noted that, since there is no resonant surface for mode (m, n) in the plasma column, the unstable mode has a global structure without localizing in the radial direction unlike the resonant mode. Further we notice that, when there is no magnetic shear, the radial mode structure, $J_m(Z(m, k)r)$, is not affected by the beta value. The more unstable mode has the less node number, and the eigenvalue is discrete with respect to k for the specified (m, n), which is also shown in the case of $\iota' \neq 0$ in the Appendix. Since the LHS of eq. (8) is proportional to γ^2 and the RHS is linear with respect to the plasma beta, the relation (8) becomes parabolic in the (β, γ) space. Thus a small variation in β_0 from the marginal equilibrium may cause an abrupt increase of growth rate.

The beta limit for stability is obtained by substituting $\gamma^2 = 0$ into eq. (8), which yields

$$\beta_{0c} = \frac{Z^2(m, k)(n - m\iota)}{4N\iota m^2}. \tag{9}$$

In order to examine the beta limit of the higher harmonic modes with the same helicity, we use the transformation of the variables $(m, n) \mapsto l(m, n)$, which yields

$$\beta_{0c}^l = \frac{Z^2(lm, k)(n - m\iota)}{4N\iota m^2}. \tag{10}$$

Since $Z(lm, k) > Z(m, k)$ for $l \geq 2$, the beta limit of the higher harmonic mode, β_{0c}^l is higher than the $l = 1$ case, β_{0c}. This is different from the resonant modes with the same helicity, which give the same beta limit from the Suydam criterion [6].

4   Resonant and non-resonant eigenmode for standard pressure profiles

We have solved eq. (6) numerically by the shooting method using the fourth order Runge-Kutta formula. At first we picked up the same eigenvalue problem as shown in section 3 in order to validate the numerical code. The obtained growth rates for the $(m, n) = (2, 1)$ mode coincide well with the analytic solution, eq. (8), and the radial mode structures are described by the Bessel function $J_2(\tilde{r})$ seems to be unchanged by the variation of β_0. Since it is shown that the more unstable mode has the less node number with the specified (m, n) (see Appendix), we have concentrated on the most unstable mode without node.

Next we have investigated the effect of the magnetic shear on the non-resonant modes assuming the standard parabolic pressure profile. For the assumed rotational transform profile, $\iota = 0.51 + \sigma r^2$, σ is changed from 0.05 to 2.0. The rotational transform profile in the case of $\sigma = 1.69$ is approximately coincides with that in Heliotron-E. When the beta value is fixed, the growth rate of the non-resonant $(2, 1)$ mode is decreased as the magnetic shear intensity σ increased. Thus the beta limit is increased almost linearly with the increase of σ as shown in Fig. 1. The mode structure is shifted to inner region when σ is increased (see Fig. 1). This result can be interpreted in the following way. When σ is increased, the stabilizing effect is enhanced in the outer region, and the radial mode structure is shifted to the inner weak shear region at the same β_0. Also when β_0 is decreased, since the destabilizing effect due to the plasma pressure gradient becomes weak, the non-resonant mode can be excited only in the inner region. However, since there is no resonant surface, the radial mode structure is not highly localized and still has a global structure. The behavior of the growth rate near the marginal beta value for the non-resonant mode is different from that for the resonant mode as shown in Fig. 2. The growth rate of the non-resonant mode decreases suddenly to zero at $\beta_0 \gtrsim \beta_{0c}$, where β_{0c} is the beta limit for the non-resonant $(2, 1)$ mode.
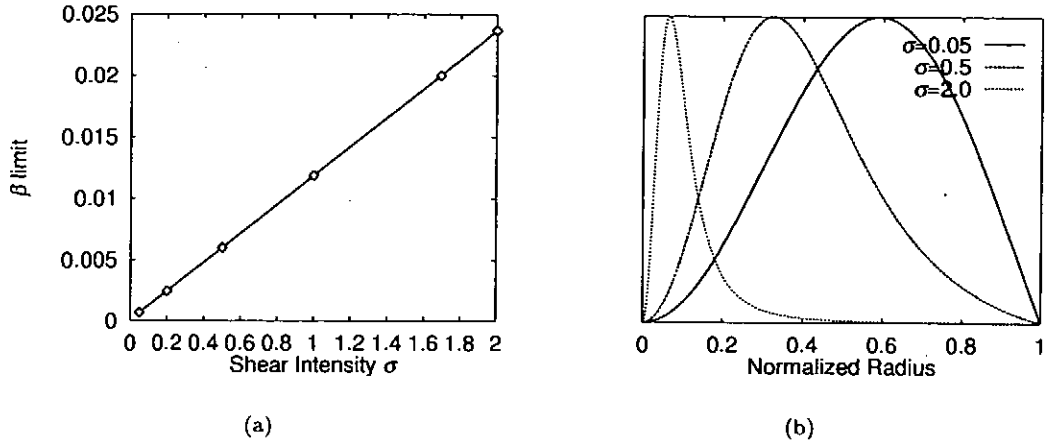
Figure 1: (a) Dependence of the beta limit on the magnetic shear parameter σ for the non-resonant $(2,1)$ mode. (b) Radial mode structures in case of $\sigma = 0.05$, 0.5, and 2.0 for the parabolic pressure profile with $\beta_0 = 0.03$.

Here we study transition from the resonant mode to the non-resonant one. For current-less plasmas in Heliotron-E, MHD equilibria show that the central rotational transform is increased with the increase of beta value. When the vacuum rotational transform at the plasma center is lower than 0.5, the resonant surface for the $(2,1)$ mode exists inside the plasma column. The resonant mode may not be excited due to the low beta value at the initial state. Experimental results show that the $(2,1)$ mode becomes unstable for $\beta_0 \gtrsim 0.7\%$ in the neutral beam heating plasma, which leads to the occurrence of sawtooth. However, when the ECRH is applied to the central region and the pressure profile becomes more peaked, the $(2,1)$ mode is stabilized. These data could be understood with disappearance of the $\iota = 0.5$ surface according to the increase of the central beta value. Linear stability of the ideal $(2,1)$ mode in the toroidal geometry shows that the resonant mode appears first, then it changes to the non-resonant mode with the increase of β_0. Finally the non-resonant mode becomes stable, when $\iota(0)$ is deviated far from 0.5 [4].

In the cylindrical model we simulate the above situation by changing the central value of the rotational transform artificially. Numerical results for both the resonant and non-resonant modes are shown in Fig. 2. Our aim is not to explain the experiment exactly, but to study the behavior of the non-resonant instabilities. Therefore we mainly consider a weak shear configuration where the resonant mode is hard to be excited. For clarifying the property of the non-resonant mode, we first consider a weak shear configuration with the resonant surface for the $(2,1)$ mode in the plasma column. Then we exclude the resonant surface of $\iota = 0.5$ by increasing $\iota(0)$. Figure 2 shows the numerical results for the parabolic pressure profile. White squares correspond to the growth rate for the equilibria with rotational transform profile, $\iota = 0.499 + 0.2r^2$, which has the resonant surface for the $(2,1)$ mode at the normalized radius $r \simeq 0.07$. Black squares correspond to the growth rate for the equilibria with $\iota = 0.501 + 0.2r^2$, which has no resonant surface for the $(2,1)$ mode. The beta limit in the resonant case seems to be 1.15×10^{-5} or less, while in non-resonant case it seems to be 2.51×10^{-4}. The difference between these beta limits comes from the role of resonant surface. In the small growth rate regime, when β_0 becomes small, the radial mode structure of the resonant mode becomes more localized. Thus the highly localized mode with an extremely small growth rate is possible as shown in Fig. 2(b). Thus, in the β-γ space the line showing the growth rate for the resonant case extends to the low beta side. On the contrary, since the non-resonant mode cannot be localized at a particular surface, the growth rate abruptly decreases to zero with the decrease of β_0. The dependence of the growth rate on β_0 is nearly parabolic as mentioned for the shearless case in the previous section.
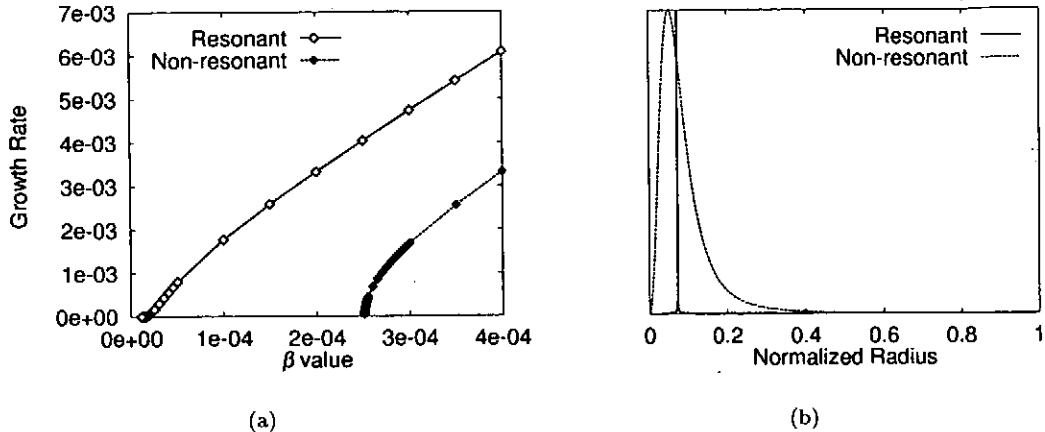
Figure 2: (a) Dependence of the growth rate of $(2,1)$ mode on the central beta value β_0 in case of parabolic pressure profile. Squares denote numerical results. The white ones correspond to the resonant case and the black ones to the non-resonant case. (b) Radial mode structures corresponding to the resonant $(\beta_0 = 1.25 \times 10^{-5})$, and to the non-resonant case $(\beta_0 = 2.51 \times 10^{-4})$.

We may apply the Suydam criterion for resonant modes, which can be derived from the indicial equation of eq. (6) at the singular point, or the resonant surface. It is written as

$$\frac{D_s}{\iota'^2 r_s^2} < \frac{1}{4}, \tag{11}$$

for stability, where D_s and ι' are evaluated at the resonant surface, $r = r_s$, for the corresponding mode. In the case of Fig. 2, the resonant surface of the $(m, n) = (2, 1)$ mode is $r_s \simeq 0.07$. Thus the beta limit obtained from the criterion (11) is $\beta_0 \simeq 1.05 \times 10^{-5}$. Generally the beta limit for the resonant mode is difficult to be calculated numerically. One reason is the extension of the small growth rate to the low beta side as mentioned above, and the other is the localization of the mode structure in the low beta regime. In Fig. 2, however, the difference between the analytic evaluation and the numerical calculation is less than 10%, and the growth rate of the mode at numerically calculated beta limit is 5.43×10^{-11}, which is normalized by poloidal Alfvén time.

5 Resonant modes for locally flattened pressure profiles

Here we will consider equilibria with the resonant surface of $\iota = 0.5$ in the plasma column, but without the pressure gradient on the resonant surface. In the experimental situation of Heliotron-E there may exist small magnetic islands due to resistive instabilities at the low order resonant surfaces [7], which may be nonlinearly saturated at low fluctuation levels [4]. In such a case the equilibrium may not be violated by the resistive mode, however, the local plasma profile will change and the pressure gradient becomes small near the resonant surface [4]. For this situation the Suydam criterion (11) predicts complete stability at the $\iota = 0.5$ surface. Here we will show that low m modes can be unstable due to the finite negative pressure gradient in the region different from the resonant surface. For simplicity the pressure profile is assumed as

$$p = 1 - r^2 + \lambda(r - r_s) \exp\left[-\frac{1}{2}\left(\frac{r - r_s}{W}\right)^2\right], \tag{12}$$

where r_s is the position of the mode resonant surface, and λ is determined to make the pressure gradient vanish at the resonant surface. The width of the flat region is controlled
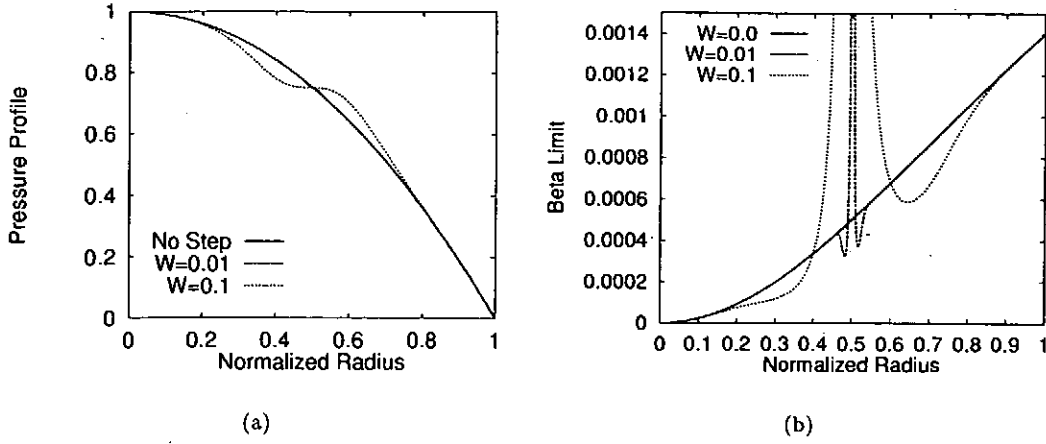
Figure 3: (a) Pressure profiles given by eq. (12) for $\lambda = 1$, and $W = 0.0$, $W = 0.01$, $W = 0.1$. (b) Suydam beta limit for the pressure profiles given by eq. (12) for $\lambda = 1$, and $W = 0.0$, $W = 0.01$, $W = 0.1$.
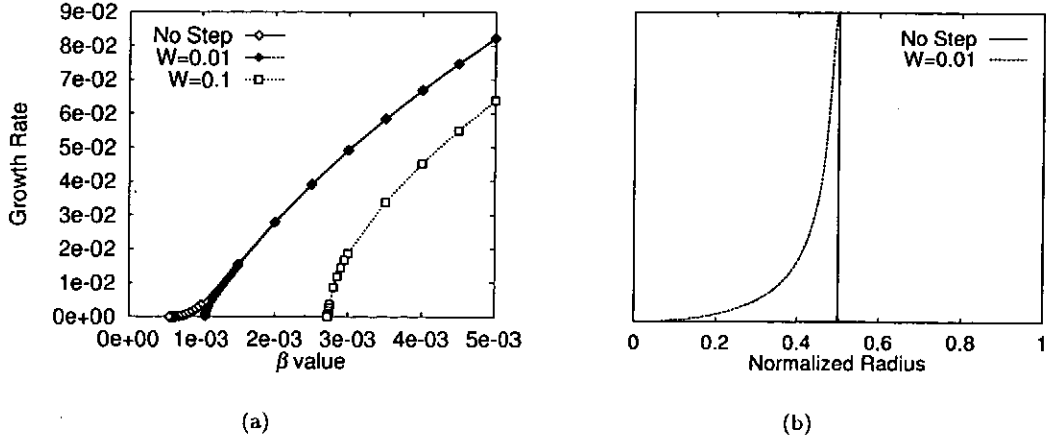

Figure 4: (a) Dependence of the growth rate of $(2,1)$ mode on the central beta value β_0 for $W = 0$, 0.01 and 0.1. (b) Radial mode structures for $W = 0$ ($\beta_0 = 5.62 \times 10^{-4}$), and $W = 0.01$ ($\beta_0 = 1.05 \times 10^{-3}$). The radial mode structures for $W = 0.1$ are shown in Fig. 5.

with the parameter W. Several pressure profiles given by eq. (12) are shown in Fig. 3(a). To investigate the effect of the pressure flattening we have calculated the Suydam beta limit for these pressure profiles (see Fig. 3(b)). In these cases the Suydam criterion shows stabilization in the flattened region, while the beta limit decreases in the neighborhood of the $(2, 1)$ mode resonant surface. We assume $\iota = 0.45 + 0.2r^2$ and consider the $(m, n) = (2, 1)$ mode again. The resonant surface exists at $r_s = 0.5$ where the pressure gradient vanishes. For three cases with $W = 0$, 0.01, and 0.1 shown in Fig. 3, growth rates are shown as a function of β_0 in Fig. 4. Although the highly localized mode structure is observed in the case of $W = 0$, it is not localized even in the case of $W = 0.01$, and the beta limit is increased with a factor of 2. Furthermore, in Fig. 4 the growth rate decreases to zero abruptly near the beta limit for $W = 0.01$, while the growth rate in the higher beta regime is not affected by the flattening of the pressure profile. The radial mode structure and the growth rate in the case of $W = 0.1$
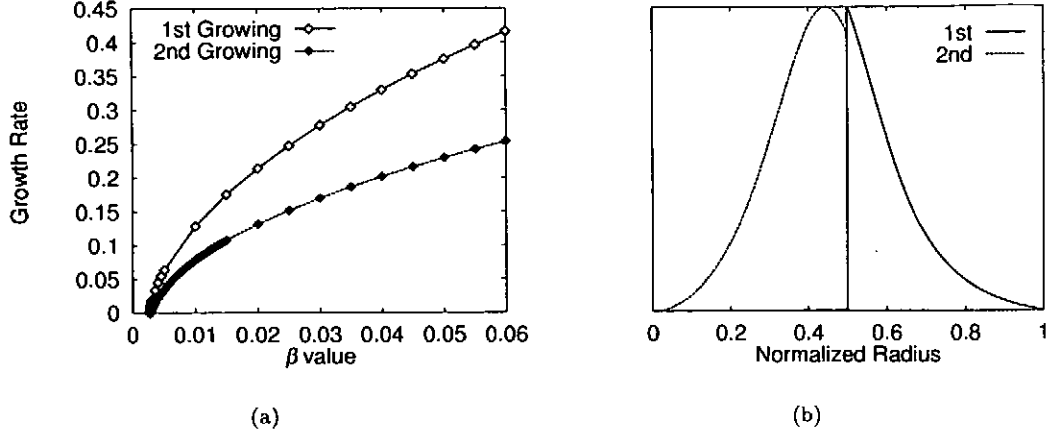
(a)   (b)

Figure 5: (a) Dependence of the growth rate of $(2,1)$ mode on the central beta value β_0 for $W = 0.1$. (b) Radial mode structure of the first growing mode $(\beta_0 = 2.72 \times 10^{-3})$ and that of the second growing mode $(\beta_0 = 2.76 \times 10^{-3})$. It is noted that the growth rates of the first growing mode are the same as those in Fig. 4(a).

are shown separately in Fig. 5. Also shown in Fig. 4(b) it can be seen that the radial mode structure is quite different from the case with no step. The mode structure is restricted in one side of the mode resonant surface, and sharply changes their value at the mode resonant surface in case of $W \neq 0$. It is considered that, since the average magnetic shear is weak in the inner side of the resonant surface, the first growing mode is restricted to the region $[0, r_s]$ in case of $W = 0.01$, whereas in case of $W = 0.1$, it is restricted to the outer region $[r_s, 1]$ since the average pressure gradient seems larger in the outer side. In the $W = 0.01$ case since the beta limit, $\beta_{0c} = 1.0 \times 10^{-3}$, is lower than that of $W = 0.1$ case, $\beta_{0c} = 2.7 \times 10^{-3}$, the destabilizing effect of the pressure gradient becomes weak in the outer region and the mode is considered to be excited in the inner region $[0, r_s]$. In both cases the second growing mode appears in the opposite region to the first growing mode.

To investigate why the steep mode structure appears at the resonant surface, we expand the coefficients in eq. (6) in the neighborhood of the mode resonant surface $r = r_s$. Since the rotational transform is expanded as $\iota(r) \approx \iota(r_s) + \iota'(r_s)(r - r_s) + \ldots$, the resonant denominator is expressed as

$$n - m\iota \approx -m\iota'(r_s)(r - r_s) + \ldots \quad (13)$$

Since the pressure becomes flat at the mode resonant surface, $p'(r_s)$ becomes zero, but $p'(r)$ is still negative in both sides of the mode resonant surface. Therefore p'' is also zero at $r = r_s$, thus p' is expanded in the neighborhood of the mode resonant surface as

$$p' \approx \frac{p'''(r_s)}{2}(r - r_s)^2 + \ldots, \quad (14)$$

where $p'''(r_s) < 0$. Substituting the leading terms of eqs. (13) and (14) into eq. (6) yields

$$\frac{d^2u}{dr^2} + \left[\frac{1}{r} + \frac{2m^2\iota'^2(r - r_s)}{\gamma^2 + m^2\iota'^2(r - r_s)^2}\right]\frac{du}{dr}$$
$$- \left[\frac{m^2}{r^2} - \frac{m\iota'(r - r_s)}{\gamma^2 + m^2\iota'^2(r - r_s)^2}\left(\frac{m\iota'}{r} + m\iota''\right)\right.$$
$$\left. + \frac{m^2\beta_0 N p'''(4r\iota + r^2\iota')}{4r^2[\gamma^2 + m^2\iota'^2(r - r_s)^2]}(r - r_s)^2\right]u = 0. \quad (15)$$
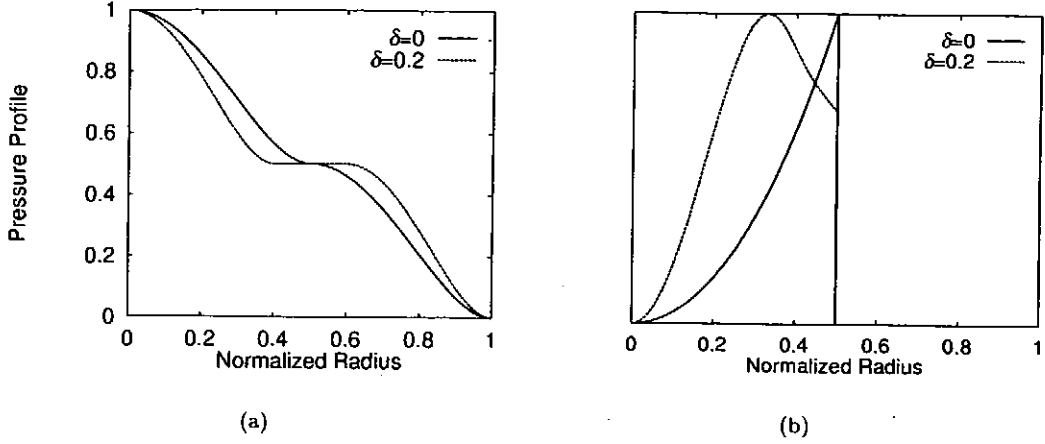
Figure 6: (a) Pressure profiles with the locally flat region around the mode resonant surface. The solid line corresponds to eq. (16) ($\delta = 0$) and the broken line to eq. (17) ($\delta = 0.2$). (b) Radial mode structure of $(m, n) = (2, 1)$ mode for the pressure profile corresponding to eq. (16) ($\delta = 0$) and to eq. (17) ($\delta = 0.2$).

As seen here, the effect of the pressure near the resonant surface is in the higher order with respect to $(r - r_s)$. Thus the pressure is negligible and does not affect the steep mode structure.

In order to confirm this situation, we have calculated the radial mode structure of nearly marginal mode for the following pressure profiles numerically. One is

$$
p = \begin{cases} \dfrac{1}{2}(1 - 4r^2)^2 + 0.5 & (r < 0.5), \\[2mm] \dfrac{1}{2}[1 - 4(r - 0.5)^2]^2 & (r > 0.5), \end{cases} \tag{16}
$$

and the other is

$$
p = \begin{cases} \dfrac{1}{2}\left(1 - \dfrac{25}{4}r^2\right)^2 + 0.5 & (r < 0.4), \\[2mm] 0.5 & (0.4 < r < 0.6), \\[2mm] \dfrac{1}{2}\left[1 - \dfrac{25}{4}(r - 0.5)^2\right]^2 & (r > 0.6). \end{cases} \tag{17}
$$

The latter pressure profile contains a completely flat region whose width is $\delta = 0.2$ at $[0.4, 0.6]$ in order to eliminate the effect of the pressure gradient. Equations (16) and (17) are shown in Fig. 6(a).

By assuming the same rotational transform profile as in Figs. 4 and 5, the obtained mode structures are shown in Fig. 6(b). It is interesting that the mode structure with the sharp decrease at $r = r_s$ is observed even though the pressure is completely flat in a region with a finite width around the mode resonant surface. This assures our conjecture that the steeply changing profile of the mode structure at $r = r_s$ such as seen in Figs. 5(b) and 6(b) is caused only by the profile of the magnetic shear, not by the pressure profile any more. We note that the non-resonant feature is seen in the radial mode structure for the second growing mode in Fig. 5(b) and the first growing mode for the pressure profile (17) in Fig. 6(b), since the peak is shifted from the resonant surface. This implies that the mode is driven by the negative pressure gradient roughly at the peak position of the mode structure.

6 Concluding remarks

We have clarified the properties of the non-resonant pressure driven instabilities and the relation to the resonant instabilities in the cylindrical plasma model. The behavior of the non-resonant mode depends strongly on the profile of both the pressure and rotational transform.

At first we have solved the eigenmode equation analytically with respect to the stream function for an equilibrium with a constant rotational transform and a parabolic pressure profile. It is noted that the non-resonant mode has a global structure, and the dependency of γ on β is parabolic (see eq. (8)). In this case it can be shown that the mode with less node number has the larger growth rate, and the higher harmonic mode with the same helicity has the higher beta limit.

With the numerical calculations, it is shown that the growth rate of the non-resonant type mode abruptly decreases to zero near the beta limit, while the resonant mode has a fairly wide small growth rate regime expressed as $\gamma \propto \exp[-\text{const.}/\sqrt{\beta_0 - \beta_0^c}]$ [6], where β_0^c denotes the central beta value given by the Suydam criterion. A physical interpretation is as follows. Although the resonant mode becomes localized at the resonant surface with the decrease of the beta value, the non-resonant type mode does not have such a surface in the plasma column. Therefore the free energy due to pressure gradient necessary to excite the non-resonant modes is always finite, although the parallel wave number along the magnetic field line is also finite. Thus the growth rate decreases to zero abruptly near the beta limit. In the resonant case, since the higher harmonic modes have larger poloidal and toroidal wave numbers than the fundamental one, they can be more localized in the radial direction. Thus the growth rates at the same beta value are larger than the fundamental mode. However, all modes can be highly localized at the resonant surface as the central beta value decreases, the beta limit does not depends on the mode numbers and agrees with the Suydam limit. On the contrary, in the non-resonant type case, since the parallel wave number of higher harmonic mode becomes larger than the fundamental mode in the region different from the resonant surface, the higher harmonics need more energy for excitation in low beta region. Thus the beta limit of the non-resonant type mode with higher harmonics is larger than the fundamental mode.

In case of the locally flattened pressure profiles around the resonant surface, the resonant mode shows the non-resonant feature. The beta limit in this case is doubled even with a small flat region. The nearly marginal mode structure is quite different from the case with $W = 0$, i.e. it is restricted to the one side of the resonant surface. Such non-resonant properties also appear in case of the nonzero but small pressure gradient at the resonant surface.

A Radial mode structure of the most unstable MHD mode

In this section we show that the more unstable mode has the less node number with the specified (m, n). We follow the proof shown by Goedbloed and Sakanaka [8, 9]. By introducing a variable $\xi = u/r$, the eigenmode equation (6) is written in the Sturmian form as

$$\frac{\mathrm{d}}{\mathrm{d}r}\left(K\frac{\mathrm{d}\xi}{\mathrm{d}r}\right) - G\xi = 0, \tag{A-1}$$

where

$$K(\gamma^2; r) = r^3[\gamma^2 + (n - m\iota)^2],$$
$$G(\gamma^2; r) = r\{(m^2 - 1)[\gamma^2 + (n - m\iota)^2] + (3m\iota' r + m\iota'' r^2)(n - m\iota) - D_s m^2\}.$$

Let two solutions corresponding to two neighboring growth rates, $\gamma^2 = \gamma_1^2$ and $\gamma_1^2 + \delta\gamma^2$ as ξ_1 and $\xi_1 + \delta\xi$, respectively, which only satisfy the boundary condition at $r = 0$. When we substitute the first solution ξ_1 corresponding to the parameter γ_1^2 in eq. (A-1), we obtain

$$\frac{\mathrm{d}}{\mathrm{d}r}\left(K(\gamma_1^2; r)\frac{\mathrm{d}\xi_1}{\mathrm{d}r}\right) - G(\gamma_1^2; r)\xi_1 = 0. \tag{A-2}$$

Substituting the second solution into eq. (A-1) and subtracting eq. (A-2) leads to

$$\frac{\mathrm{d}}{\mathrm{d}r}\left(K(\gamma_1^2;r)\frac{\mathrm{d}\delta\xi}{\mathrm{d}r}\right) - G(\gamma_1^2;r)\delta\xi = -\delta\gamma^2\left[\frac{\mathrm{d}}{\mathrm{d}r}\left(\frac{\partial K}{\partial\gamma^2}\bigg|_{\gamma_1^2}\frac{\mathrm{d}\xi_1}{\mathrm{d}r}\right) - \frac{\partial G}{\partial\gamma^2}\bigg|_{\gamma_1^2}\xi_1\right]. \qquad \text{(A-3)}$$

Assume now that $\xi_1(r_1) = 0$ at $0 < r_1 \leq 1$, which is possible for an unstable case. We make the product of $\delta\xi$ with eq. (A-2), ξ_1 with eq. (A-3) and integrate from 0 to r_1. Subtracting both sides leads to

$$K\delta\xi\frac{\mathrm{d}\xi_1}{\mathrm{d}r}\bigg|_{r_1} = -\delta\gamma^2\int_0^{r_1}\left[\frac{\partial K}{\partial\gamma^2}\left(\frac{\mathrm{d}\xi_1}{\mathrm{d}r}\right)^2 + \frac{\partial G}{\partial\gamma^2}\xi_1^2\right]\mathrm{d}r, \qquad \text{(A-4)}$$

after some partial integrations, where we have used the fact that $\delta\xi(0) = 0$, $K(\gamma_1^2;0) = 0$. Here K, G and their derivatives with respect to γ^2 are all evaluated at $\gamma^2 = \gamma_1^2$. Since $\partial K/\partial\gamma^2 = r^3$ and $\partial G/\partial\gamma^2 = r(m^2 - 1)$, the integrand is positive for $m \geq 1$ at all radial points. Provided that $\delta\gamma^2 > 0$, or $\xi_1 + \delta\xi$ is more unstable than ξ_1, the RHS of eq. (A-4) becomes negative. Since K is positive in $(0,1)$, the radial position of $\xi_1 + \delta\xi = 0$ moves to outer due to the increase of the parameter γ^2. Since K and G are monotonic functions of γ^2 for $m \geq 1$, we can conclude that the radial positions of all zeros move to the outer direction with the increase of the parameter γ^2. If we further impose another boundary condition at $r = 1$, it is confirmed that the eigenvalue is discrete and the more unstable mode has the less node number. In other words, the most unstable mode has no node.

References

[1] Shafranov, V. D. and Yurchenko, E. I.: Sov. Phys. JETP **26** (1968) 682.

[2] Shafranov, V. D.: Phys. Fluids **26** (1983) 357.

[3] Ichiguchi, K., Nakamura, Y., and Wakatani, M.: Nucl. Fusion **31** (1991) 2073.

[4] Carreras, B. A., Lynch, V. E., Zushi, H., Ichiguchi, K., and Wakatani, M.: Phys. Plasmas **5** (1998) 3700.

[5] Strauss, H. R.: Plasma Phys. **22** (1980) 733.

[6] Sugama, H. and Wakatani, M.: J. Phys. Soc. Jpn. **58** (1989) 1128.

[7] Furth, H. P., Killeen, J., and Rosenbluth, M. N.: Phys. Fluids **6** (1963) 459.

[8] Goedbloed, J. P. and Sakanaka, P. H.: Phys. Fluids **17** (1974) 908.

[9] Freidberg, J. P.: *Ideal Magnetohydrodynamics*, Plenum Press, New York (1987) 304.

Resistive interchange instability in reversed shear tokamaks

Masaru FURUKAWA, Yuji NAKAMURA and Masahiro WAKATANI

Graduate School of Energy Science, Kyoto University
Gokasho, Uji 611-0011, Japan

Abstract

Resistive interchange modes become unstable due to the magnetic shear reversal in tokamaks. In the present paper, the parameter dependences, such as q (safety factor) profile and the magnetic surface shape are clarified for improving the stability, using the local stability criterion. It is shown that a significant reduction of the beta limit is obtained for the JT-60U reversed shear configuration with internal transport barrier, since the local pressure gradient increases.

Keywords : resistive interchange instability, reversed shear tokamak, beta limit, stabilizing method

1 Introduction

Reversed shear configurations[1, 2, 3] are the recent topic in tokamak experiments. In such discharges, improved confinement is obtained with internal transport barrier. Furthermore large amount of bootstrap current is driven by the steep pressure gradient around the transport barrier, which is considered to be favorable for achieving a steady state operation of a tokamak. Thus it is important to investigate the properties of reversed shear configurations. We investigate the stability properties of reversed shear tokamak theoretically.

In terms of the ideal MHD modes, such as ballooning modes and kink modes, the stability study has been done by several authors[4]. It is shown that the beta limit due to ballooning modes can be increased by broadening the pressure profile. Also it is shown that kink modes are stabilized by placing a conducting wall at suitable position from the plasma column.

Our interest here is the resistive MHD modes, especially resistive interchange modes; the methods to stabilize the ideal modes are well investigated, and when the ideal modes are suppressed, the resistive modes become important, especially in long time discharges.

We found that resistive interchange modes become unstable in reversed shear configurations. The local stability of the equilibria calculated by the VMEC (Variational Moment Equilibrium Code)[5] is examined with the stability criterion derived by Glasser, Greene, and Johnson[6]. In Sec. 2, we show the procedures to calculate the MHD equilibria and to examine the local stability. In Sec. 3, it is shown that the resistive interchange modes become unstable in reversed shear configurations, and we investigate the parameter dependences, such as safety factor profile and flux surface shape, on the resistive interchange modes and discuss methods to improve the stability. Also we estimate the beta limit due to the resistive interchange modes. It is found that a low safety factor with a weak negative magnetic shear in a D-shaped tokamak seems to be favorable to stabilize the modes. As for a realistic example, we use the JT-60U reversed shear discharge with internal transport barrier, and the beta limit is estimated in Sec. 4. The beta limit is significantly lower than the that obtained in experiment. Concluding remarks are given in Sec. 5.

2 MHD equilibrium and local stability criterion

MHD equilibria for studying the local resistive stability are calculated by the VMEC (Variational Moment Equilibrium Code)[5]. An equilibrium can be calculated by specifying the plasma pressure and safety factor profiles. Also needed is the boundary condition. Although the VMEC can solve the free boundary problem, we use the fixed boundary condition in the present paper, because it is easier to study the resistive interchange modes in tokamaks with different cross-sections systematically.

The plasma pressure profile is assumed as,

$$p(s) = p_0(1 - s)^2 \tag{1}$$

for the most calculations, where $s \equiv \Phi_T / \Phi_{T\,edge}$ is the normalized toroidal magnetic flux and p_0 is the plasma pressure at the magnetic axis where $s = 0$. Note that the pressure profile used in Sec. 4 is different and is shown below. A typical pressure profile is plotted in Fig. 1.

For the fixed boundary condition, the outermost flux surface shape is given as follows,

$$R_b = R_{b0} + R_{b1} \cos\theta + R_{b2} \cos 2\theta, \tag{2}$$
$$Z_b = Z_{b1} \sin\theta, \tag{3}$$

where R and Z are usual coordinates in the cylindrical coordinate system, and θ is the poloidal angle used in the VMEC. The definitions of the aspect ratio A, the ellipticity κ, and the triangularity δ are similar to those given in Ref. [7]. In principle, more Fourier components must be retained for expressing the complicated plasma boundary shape, however, we retain only a few Fourier components for simplicity. We consider that the above components are sufficient to investigate the basic dependences of the instability on the outermost flux surface shape. Note that the ellipticity is determined by the ratio of R_{b1} and Z_{b1}, and the triangularity corresponds to R_{b2}.

The final assumption required for the MHD equilibrium calculation is the safety factor profile. This is shown in Figs. 2, 6, or 11.

Next we mention about the local MHD stability criteria used in the present study. They are derived by GGJ(Glasser, Greene and Johnson)[6], and given as

$$D_I \equiv E + F + H - \frac{1}{4} < 0, \tag{4}$$
$$D_R \equiv E + F + H^2 < 0, \tag{5}$$

where the subscripts 'I' and 'R' represent 'ideal' mode and 'resistive' mode, respectively. E, F, and H are defined as,

$$E \equiv \frac{\langle B^2/|\nabla V|^2\rangle}{\Lambda^2}\left(J'\psi'' - I'\chi'' + \Lambda\frac{\langle \sigma B^2\rangle}{\langle B^2\rangle}\right), \tag{6}$$

$$F \equiv \frac{\langle B^2/|\nabla V|^2\rangle}{\Lambda^2}\left(\langle \sigma^2 B^2/|\nabla V|^2\rangle - \frac{\langle \sigma B^2/|\nabla V|^2\rangle^2}{\langle B^2/|\nabla V|^2\rangle} + (p')^2\left\langle\frac{1}{B^2}\right\rangle\right), \tag{7}$$

$$H \equiv \frac{\langle B^2/|\nabla V|^2\rangle}{\Lambda}\left(\frac{\langle \sigma B^2/|\nabla V|^2\rangle}{\langle B^2/|\nabla V|^2\rangle} - \frac{\langle \sigma B^2\rangle}{\langle B^2\rangle}\right). \tag{8}$$

Here prime denotes the derivative with respect to the plasma volume V, B is the magnetic field strength, ψ and χ are the toroidal and poloidal fluxes respectively, I and J are the toroidal and poloidal current fluxes respectively, $\Lambda \equiv \psi'\chi'' - \chi'\psi''$ is the magnetic shear parameter, $\sigma \equiv \mathbf{j}\cdot\mathbf{B}/B^2$ is the parallel current, and the angular brackets denote the flux surface average. The factor $1/4$ in D_I represents the shear stabilization effect. The difference between D_I and D_R is seen by rewriting Eq. (5) as

$$D_R = D_I + \left(H - \frac{1}{2}\right)^2. \tag{9}$$

The stability criterion $D_R < 0$ means that the resistive mode is always more unstable than the ideal modes.

In the present study, we use the stability criteria normalized by $-(\iota')^2$, i.e.,

$$D_M(ideal) \equiv D_M(E) + D_M(F) + D_M(H) + D_M(shear) > 0, \tag{10}$$

$$D_M(resistive) \equiv D_M(E) + D_M(F) - \left(\frac{D_M(H)}{\iota'}\right)^2 > 0, \tag{11}$$

where $D_M(E)$, $D_M(F)$, $D_M(H)$, and $D_M(shear)$ are given by,

$$D_M(E) \equiv -\left(\imath'\right)^2 E,\tag{12}$$

$$D_M(F) \equiv -\left(\imath'\right)^2 F,\tag{13}$$

$$D_M(H) \equiv -\left(\imath'\right)^2 H,\tag{14}$$

$$D_M(shear) \equiv -\frac{1}{4}\left(\imath'\right)^2.\tag{15}$$

It should be noted that these criteria can be examined by the equilibrium quantities only. Although the beta limit estimated by these criteria, i.e., $D_M(ideal) > 0$ for ideal interchange modes or $D_M(resistive) > 0$ for resistive interchange modes, is considered to be optimistic, because the assumption of the localized plasma displacement is used in the derivation. It is pointed out that radially broadened modes, such as ballooning modes, become unstable even when the localized stability criteria are satisfied.

3 Resistive interchange instability in reversed shear tokamak

In this section, we show the numerical results. The resistive interchange mode becomes unstable in the shear reversal region in reversed shear tokamaks. It should be noted that all the MHD equilibria investigated in the present paper are stable with respect to the ideal interchange modes, i.e., $D_M(ideal) > 0$.

First we show the safety factor, q, profiles assumed in the MHD equilibrium calculations in Fig. 2. In this sequence of q profiles, $q_{min} = 3.8$ is fixed and q_0 is varied as shown in Fig. 2. The outermost flux surface shape is also fixed to be circular and the aspect ratio is $A = 3$. The pressure profile is given in Eq. (1) and $\beta_{T0} = 3\%$, where $\beta_{T0} \equiv 2\mu_0 p_0 / B_{T0}^2$, B_{T0} is the vacuum magnetic field at the plasma center $R = R_0$. The radial profiles of $D_M(resistive)$ is plotted in Fig. 3.

It can be seen that the resistive interchange modes become more unstable as q_0 is increased. This is explained as follows. When q_0 is increased, the Pfirsch-Schlüter current increases by which the geodesic curvature becomes large. In a conventional sense, the interchange stability is determined by the competition among the pressure gradient, the magnetic well, and normal curvature. Usually Pfirsch-Schlüter component, or $D_M(H)$, have a small contribution. In fact it is the case for the normal shear or monotonically increasing q profile equilibrium. However, the Pfirsch-Schlüter component has a significantly large contribution to the stability for the reversed shear equilibrium. This can be seen from Fig. 4.

Also we show the normalized beta, $\beta_N[\%\text{mT/MA}]$, limit of the resistive interchange modes is plotted versus q_0 in Fig. 5, where $\beta_N \equiv \langle\beta\rangle a B_{T0}/I_T$, $\langle\beta\rangle$ is the volume averaged beta, a is the horizontal minor radius on the midplane, and I_T is the toroidal plasma current.

Beta limit in Fig. 5 is estimated by $D_M(resistive) = 0$. It should be noted that the lower q_0 gives the higher β_N. Note that the $q_0 = 3.1$ case in Fig. 5 corresponds to a normal shear equilibrium. In this case, the violation of the stability condition occurs around $\langle r\rangle/\langle r\rangle_{edge} \simeq 0.3$, not near the magnetic axis. Since our interest here is in the reversed shear tokamak, we will not consider positive shear equilibria in the later part of this paper.

It is important to know how to stabilize these modes. In the following we propose two stabilizing methods. The one corresponds to the safety factor profile control, and the other to the outermost flux surface shape control.

First we show the safety factor dependence of the resistive interchange mode. Since q_0 dependence is already investigated for the fixed q_{min} in Fig. 5, here we investigate the q_{min} dependence. The q profiles assumed for the equilibrium calculations are shown in Fig. 6.

In this sequence, the ratios $q_0/q_{min} = 2.0$ and $q_{edge}/q_{min} = 1.8$ are fixed and q_{min} is varied. This corresponds to the situation that the current density profile is fixed and the total current is varied. The aspect ratio is $A = 3$, circular cross-section, and $\beta_{T0} = 3\%$ are also fixed. The corresponding $D_M(resistive)$ profiles are shown in Fig. 7. It can be seen that the resistive interchange modes become more stable when q_{min} is decreased.

Thus in terms of the q profile, lower q_0 and q_{min} are favorable to the resistive interchange mode. However, it should be noted that the ideal modes are stable if the q_{min} or q_0 are larger than a critical value, typically about unity in a low shear system from the Mercier criterion for circular tokamaks[7],

$$\left(\frac{rq'}{q}\right)^2 + 4r\beta'(1 - q^2) > 0,\tag{16}$$

where r is a minor radius, $\beta \equiv 2\mu_0 p/B_0^2$, and the prime denotes the derivative with respect to r. It seems to be possible to obtain an optimized q profile. This will be discussed in a separate paper.

Next we consider the outermost flux surface shaping. Since we retain only a few Fourier components to express the outermost flux surface shape, the possible shape is somewhat limited. However, we can treat three types of the deformation, i.e., ellipticity κ, triangularity δ, and aspect ratio A. First we mention about the effect of the ellipticity. In Fig. 8, the normalized beta limit is plotted versus κ for the equilibria with $A = 3$, $\delta = 0$, and the q profile with $q_0 = 5.35$ in Fig. 2. It should be noted that the excessively high κ leads to the vertical instability. Thus we consider the equilibria with $\kappa \lesssim 2$. Also, excessively small κ is unfavorable from the view point of the plasma volume, i.e., the plasma volume becomes smaller for such a small κ. By increasing κ, the Pfirsch-Schlüter current decreases although the magnetic well stabilization is not affected so much. Thus the resistive interchange modes become more stable and the higher beta limit can be obtained as κ is increased.

For the effect of the triangularity, it is expected that the magnetic well stabilization is enhanced and that the higher beta limit can be obtained. This is shown in Fig. 9. The considered equilibria has $A = 3$, $\kappa = 1.6$, and the q profile with $q_0 = 5.35$ in Fig. 2. The value of $\kappa = 1.6$ is chosen because it is close to an optimum value. The beta limit is higher for the larger δ configuration. It is noted that the range of δ is limited by the number of Fourier components in Eqs. (2) and (3). In our equilibrium calculations, maximum obtainable δ is about 0.4.

Finally we consider the effect of the aspect ratio. Similar to the triangular deformation, the magnetic well becomes deeper as the aspect ratio is decreased. The beta limit is plotted in Fig. 10 for the equilibria with circular cross-section and the q profile with $q_0 = 5.35$ in Fig. 2. For this sequence, the plasma minor radius a and the vacuum toroidal field at the plasma center B_{T0} are fixed and the major radius R_0 is varied. The normalized beta limit has a maximum around $A \simeq 2$, although marginal β_{T0} becomes larger as A is decreased. This is due to the normalization by the plasma current in β_N. It is noted that the plasma current becomes larger for the lower aspect ratio configuration. Thus the higher central plasma pressure can be obtained for lower aspect ratio when the toroidal field strength at the plasma center and the plasma minor radius are fixed.

In summary, though the parameter ranges are somewhat limited, the configuration with higher κ, higher δ, and $A \simeq 2$ is considered to be favorable for the stability of the resistive interchange modes. In addition, from the view point to obtain higher plasma pressure, low aspect configuration is attractive.

4 Beta limit estimation of JT-60U equilibrium with internal transport barrier

In this section, we study the stability of the MHD equilibrium using the JT-60U improved confinement discharge[1] profile with internal transport barrier (ITB). The pressure and q profiles are shown in Fig. 11. The parameters such as the major radius and the magnetic field are chosen to be consistent with JT-60U. The numerical result show that the normalized beta limit is $\beta_N \simeq 0.387[\%mT/MA]$, which is much lower than the value obtained in the experiment, $\beta_N \simeq 2.4$. The decrease of β_N is attributed to the steep pressure profile near the q_{min} surface. Thus it is considered that there are some stabilizing effects for the resistive interchange mode, such as finite Larmor radius effect. Also the growth rate of these modes should be compared to the experimental time scale. These are our future subject.

5 Conclusions

In this paper we investigate the parameter dependences of the beta limit for the resistive interchange modes. As mentioned in Sec. 3, the large amount of Pfirsch-Schlüter current produces large geodesic curvature, which leads to instability. Thus the beta limit can be increased by reducing the Pfirsch-Schlüter current, or reducing q_0 and q_{min} with an increase of κ. The magnetic well also has a stabilizing effect, thus larger δ and smaller A are favorable. Our studies show that for the equilibrium with $A = 3$, $\kappa = 1.6$, $\delta = 0.4$, $q_0 = 5.35$, $q_{min} = 3.8$, and $q_{edge} = 6.0$, the normalized beta limit $\beta_N \simeq 2.3$ is possible.

Also shown is the beta limit for the JT-60U reversed shear discharge with ITB. In this case the beta limit drastically decreases because of the presence of the steep pressure gradient. The obtained result of the beta limit is $\beta_N \simeq 0.387$ [%mT/MA] or $\beta_{T0} \simeq 0.8$ [%].

Acknowledgements

References

[1] T. Fujita, S. Ide, et al., Phys. Rev. Lett. **78**, 2377 (1997).

[2] E.J. Strait, L.L. Lao, et al., Phys. Rev. Lett. **75**, 4421 (1995).

[3] F.M. Levinton, M.C. Zarnstorff, et al., Phys. Rev. Lett. **75**, 4417 (1995).

[4] A.D. Turnbull, T.S. Taylor, M.S. Chu, R.L. Miller, and Y.R. Lin-liu, Nucl. Fusion **38**, 1467 (1998).

[5] S. P. Hirshman, W. I. van Rij and P. Merkel, Comp. Phys. Commun. **43**, 143 (1986).

[6] A. H. Glasser, J. M. Greene and J. L. Johnson, Phys. Fluids **18**, 875 (1975).

[7] J. P. Freidberg, "Ideal Magnetohydrodynamics" (Prenum Press, New York and London, 1987).
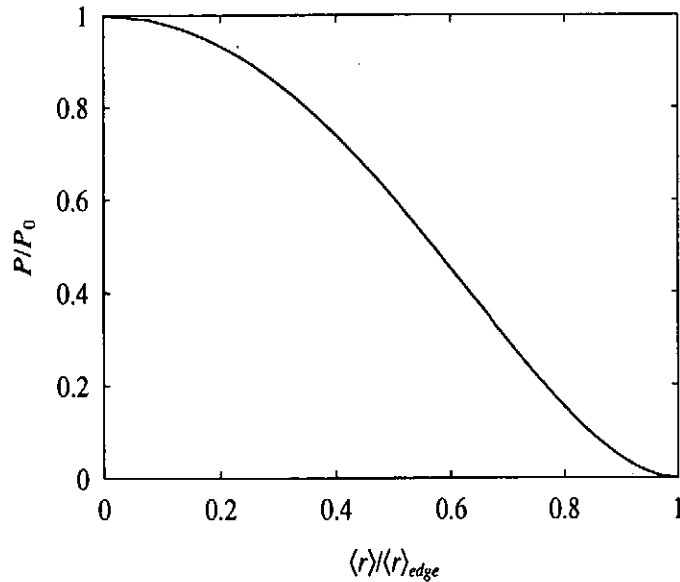
Fig. 1: Typical example of the pressure profile is plotted. The horizontal axis label $\langle r \rangle / \langle r \rangle_{edge}$ is the normalized average minor radius.
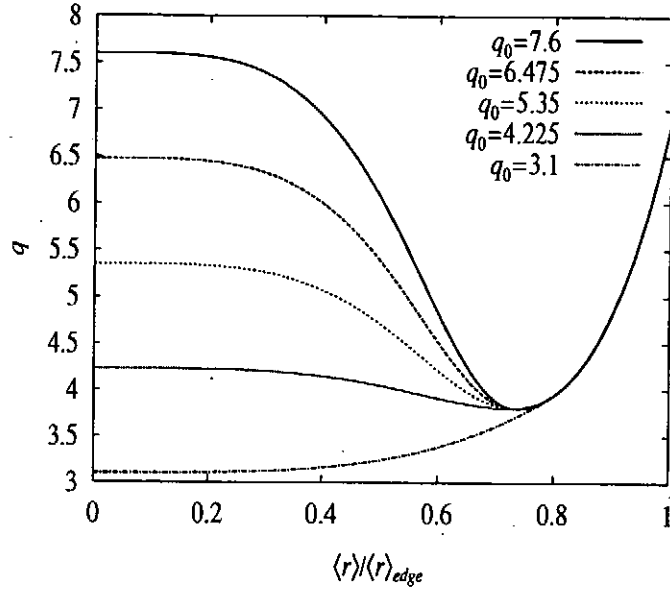
Fig. 2: Safety factor profiles assumed in the MHD equilibrium calculations are shown.
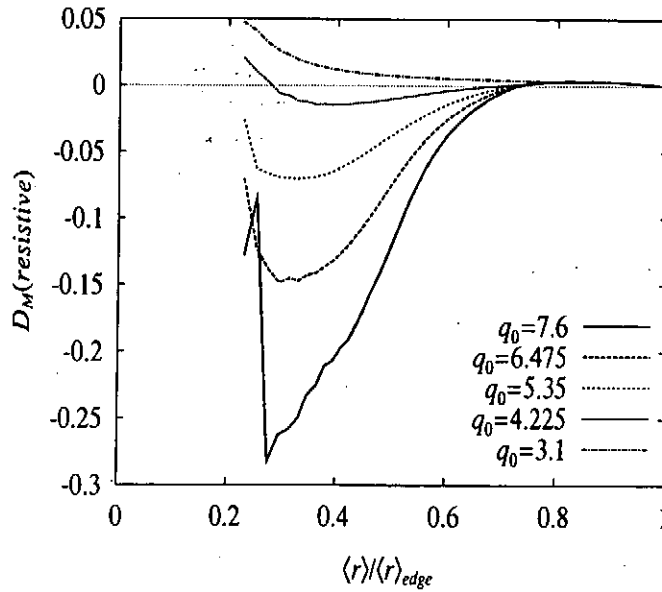
Fig. 3: $D_M(resistive)$ is plotted as a function of normalized minor radius $\langle r \rangle / \langle r \rangle_{edge}$. It is seen that the resistive interchange modes become more unstable as q_0 is increased. For $\langle r \rangle / \langle r \rangle_{edge} \lesssim 0.2$, the numerical accuracy is not sufficient in the VMEC code, thus $D_M(resistive)$ is not plotted here.
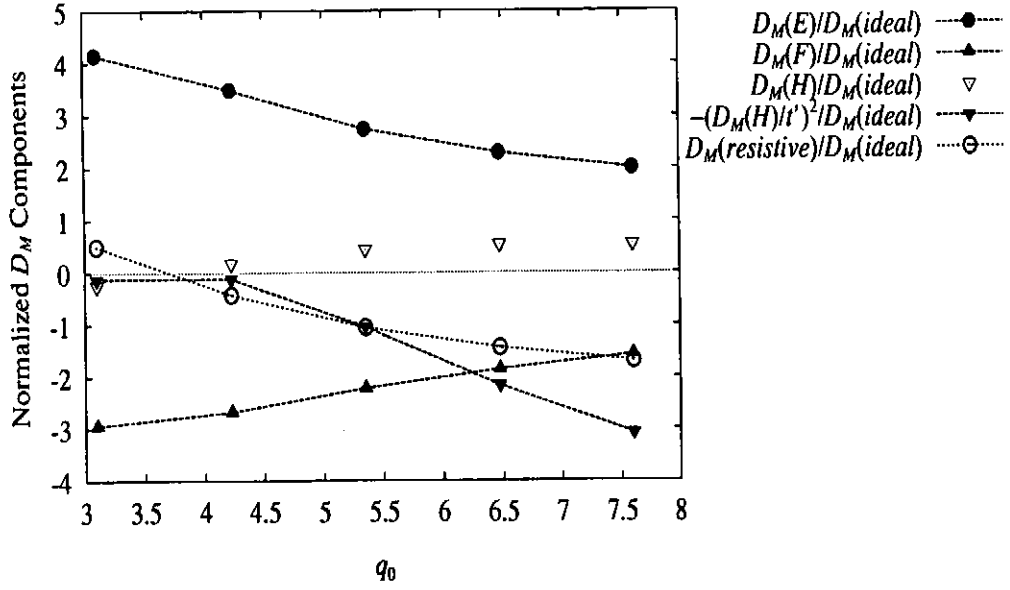
Fig. 4: Components of D_M are plotted separately as a function of q_0 at $\langle r \rangle / \langle r \rangle_{edge} = 0.5$. It is seen that the $D_M(H)$ term has a significant contribution for large q_0.
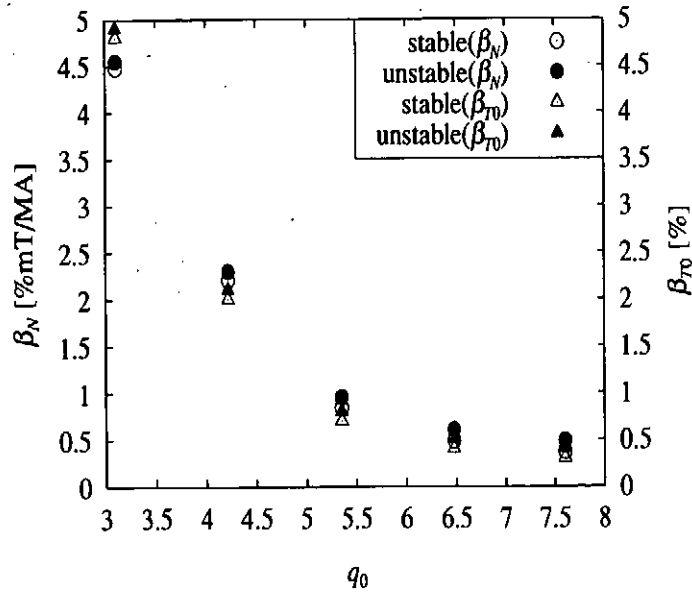
Fig. 5: Normalized beta β_N near the stability limit is shown as a function of q_0. Equilibria have the aspect ratio $A = 3$, and circular cross-section. It is noted that the $q_0 = 3.1$ case corresponds to a normal shear equilibrium. In this case, $D_M(resistive) < 0$ appears around $\langle r \rangle / \langle r \rangle_{edge} \simeq 0.3$.
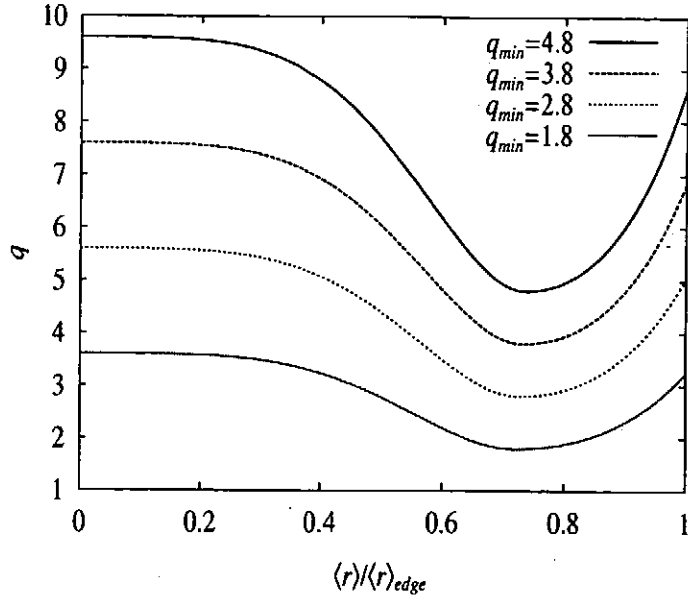
Fig. 6: q profiles for studying q_{min} dependence of resistive interchange mode are plotted. The ratios $q_0/q_{min} = 2.0$ and $q_{edge}/q_{min} = 1.8$ are fixed.
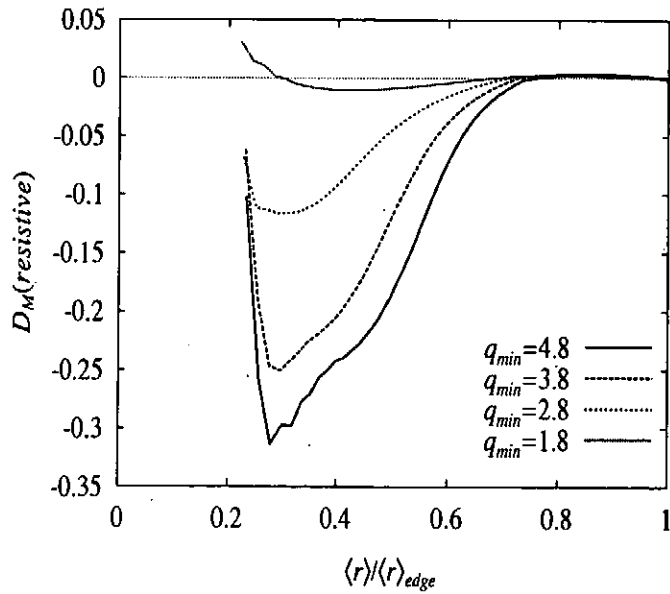
Fig. 7: $D_M(resistive)$ profiles calculated from the equilibria with q profiles shown in Fig. 6, $A = 3$, circular cross-section, and $\beta_{T0} = 3\%$ are assumed.
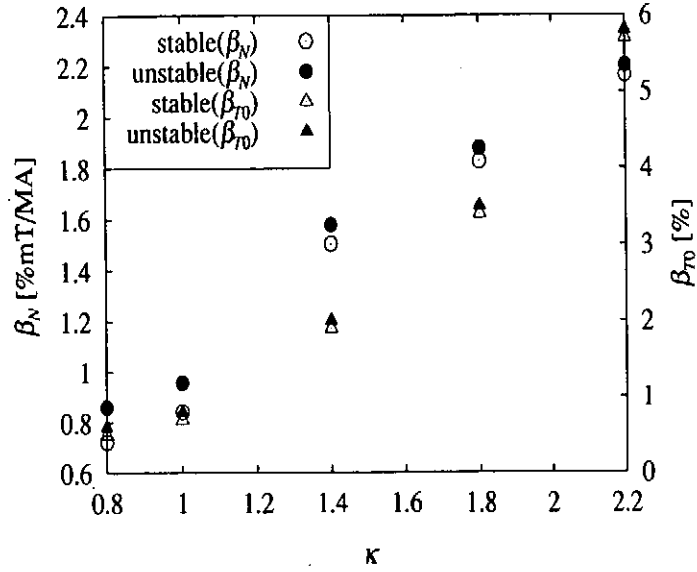
Fig. 8: Normalized beta near the stability limit is plotted versus κ. The larger κ gives the higher beta limit. The equilibria have $A = 3$, $\delta = 0$, and the q profile with $q_0 = 5.35$ in Fig. 2.
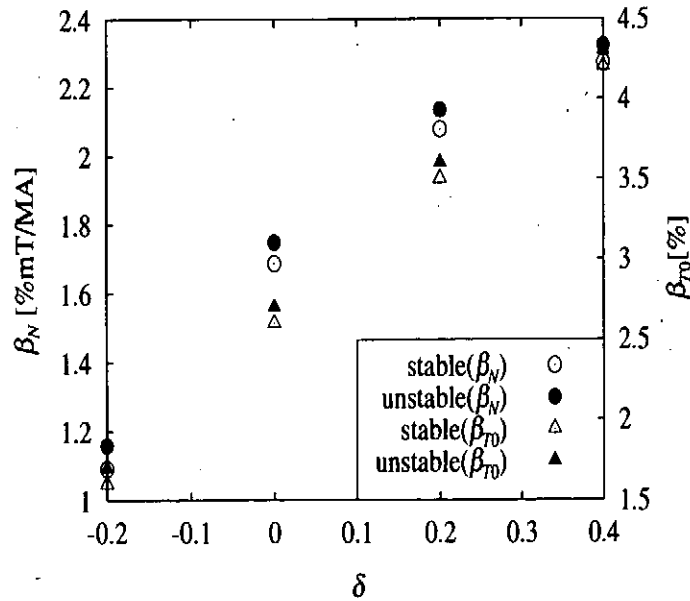
Fig. 9: Dependence of the normalized beta near the stability limit on δ is shown for the equilibria with $A = 3$, $\kappa = 1.6$, and the q profile with $q_0 = 5.35$ in Fig. 2. The higher beta can be obtained by increasing δ.
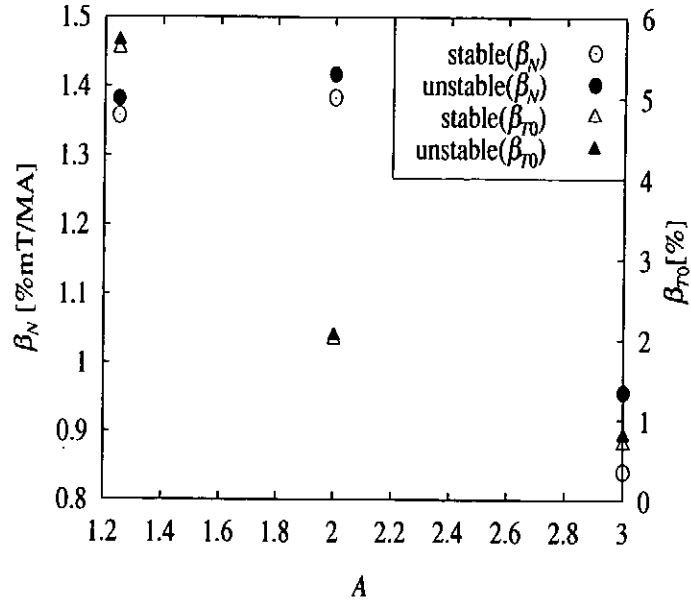
Fig. 10: Normalized beta near the stability limit is plotted versus A. In this sequence, the equilibria have circular cross-section and q profile with $q_0 = 5.35$ in Fig. 2. β_N has a maximum around $A \simeq 2$, although β_{T0} is larger for lower A.
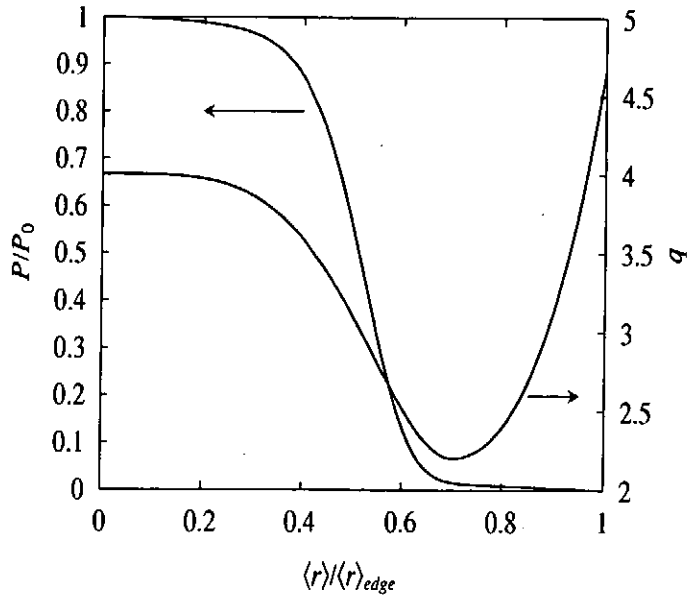

Fig. 11: Pressure and q profiles assumed for the MHD equilibrium corresponding to the JT-60U reversed shear discharge with ITB.

A Toroidally Symmetric Plasma Simulation Code for Design of Position and Shape Control on Tokamak Plasmas

Haruhiko Takase and Ikuo Senda[*]

Naka Fusion Research Establishment, Japan Atomic Energy Research Institute

801-1 Mukouyama, Naka-machi, Naka-gun, Ibaraki-ken, 311-0193, Japan

*Toshiba Corporation, Tsurumi-ku, Yokohama, 230-0045, Japan

Abstract

A Toroidally Symmetric Plasma Simulation (TSPS) code has been developed for investigating the position and shape control on tokamak plasmas. The analyses of three-dimensional eddy currents on the conducting components around the plasma and the two-dimensional magneto-hydrodynamic (MHD) equilibrium are taken into account in this code. The code can analyze the plasma position and shape control during the minor disruption in which the deformation of plasma is not negligible. Using the ITER (International Thermonuclear Experimental Reactor) parameters, some examples of calculations are shown in this paper.

Keywords: tokamak, plasma, position, shape, feedback control, eddy current, equilibrium, numerical simulation

1. Introduction

A plasma with non-circular cross section has several advantages for achieving high performance plasmas in tokamak devices. However, the plasma with non-circular cross section basically becomes unstable for vertical plasma motion. In general, this instability is stabilized using the passive effects by the conducting components (the conducting shell effect) in the case of the instability with short growth time and the active feedback control by the magnetic field coils in the case of the instability with long growth time. In the case of present machines, the vertical stability is not critical since the conducting components and the coils for the feedback control can be located near the plasma.

On the other hand, in the case of the ITER (International Thermonuclear Experimental Reactor), some in-vessel components without passive effects are located between the plasma and the conducting components for protecting the conducting components from the neutron damage. As a result, the conducting components and the coils for the feedback control must keep away from the plasma and there is a possibility that the electric power of feedback control exceeds the permitted limit. Therefore, the vertical stability is one of the critical issues and it is necessary for the engineering design to analyze the characteristics sufficiently.

In general, the modeling for analyzing the vertical stability consists of three parts: a) the conducting components, b) the core plasma and c) the poloidal coils for the active feedback control. One of the essential parts for the analysis is the modeling of the conducting components. The characteristics of the passive effects significantly depend on the shape of the conducting components since the path of the eddy current in the conducting components changes by the holes and the ports on the conducting components. That is, it is important to consider the three-

dimensional structure of the conducting components. Furthermore, in the case of the minor disruption, it is also important to treat the change of the plasma shape. Therefore, it is necessary for the modeling of plasma to treat the deformation of plasma shape. At least, it is important for the plasma to consider the two-dimensional model.

In previous studies, there are some codes for the analysis of the vertical stability in the tokamak machine. For example, some simulation codes are described by the linear model[1-3]. Although these codes include the three-dimensional model for the conducting components, only the motion of plasma current center is considered and the plasma shape is not essentially deformable by assuming the rigid model. Other simulation codes are described by the non-linear model[4,5]. In these codes, although all parts of numerical model are assumed the axisymmetric model, the three-dimensional conducting components are not taken into account.

The numerical model used in this study is similar to the linear model. This model adopts the three-dimensional model for the conducting components. Regarding the model of plasma, the motion of the plasma is essentially based on the rigid model. However, the non-linearity of plasma is considered by calculating the MHD equilibrium at each 20~30 time-steps typically and then by renewing the plasma parameters used in this code. Therefore, this model corresponds to the intermediate model between the linear model and the non-linear model. Furthermore, for extending from the rigid model to the non-rigid (deformable) model, the relation between the plasma surface position (gaps) and the plasma parameters is taken into consideration. In addition, this model is suitable for the design that we must calculate many cases since the reduction of the calculation time is expected comparing the non-linear model.

The development of the numerical simulation code for the analysis of vertical stability on the ITER is described in this paper as follows: The numerical model and method are described in Section 2. Section 3 presents some examples of numerical results. Summaries are given in the last section.

2. Numerical model

The simulation code consists of three modules: (1) a free-boundary MHD equilibrium calculation [6], (2) a three-dimensional finite element analysis [7] and (3) calculation for the time evolution of the motion of plasma, the eddy currents in the conducting components and the currents of the active feedback coils. The MHD equilibrium code solves the Grad-Shafranov equation by the Green function method and estimates the deformation of the plasma shape. The three-dimensional finite element analysis code solves the interaction between the plasma and the conducting components by using the thin shell approximation and estimates the passive effects by the conducting components.

The calculation for the time evolution of the motion of plasma, the plasma current, the eddy currents and the currents of the active feedback coils is described as below. Regarding the motion of plasma, it is assumed the rigid model, which the shape of the plasma does not change. Furthermore, the toroidal symmetry is assumed, and the equations of the motion in the vertical (Z) and the horizontal (R) directions are given as follows:

$$M_P \frac{d^2 Z_P}{dt^2} = -2\pi \int R dR dZ J_P B_R, \tag{1}$$

$$M_P \frac{d^2 R_P}{dt^2} = \frac{1}{2} \mu_0 I_P^2 \left\{ \ln\left(\frac{8R_P}{a_P}\right) + \beta_P + \frac{1}{2}(\ell_i - 3) \right\} + 2\pi \int R dR dZ J_P B_Z, \tag{2}$$

where M_P, t, J_P, μ_0, I_P, a_P, β_P and ℓ_i are the mass of plasma, the time, the plasma current density, the vacuum dielectric constant, the plasma current, the plasma minor radius, the poloidal beta, and the internal inductance of the plasma, respectively. B_R and B_Z are the magnetic fields with respect to the horizontal and the vertical directions, respectively. J_P, B_R and B_Z are obtained from the two-dimensional MHD equilibrium analysis. The integration is carried out over the whole area of the plasma. Here, by assuming the adiabatic compression and the conservation of the toroidal flux in the plasma and by expanding the Eqs.(6) with respect to the small displacements of the plasma position, δZ_P and δR_P, the following equations are obtained.

$$\frac{M_P}{I_P}\frac{d^2\delta Z_P}{dt^2} = 2\pi B_{V0} n \delta Z_P - 2\pi B_{V0} k \delta R_P + I_P \sum_i \frac{\partial M_{Pi}}{\partial Z_P}\frac{I_i}{I_P} + I_P \sum_k \frac{\partial M_{Pk}}{\partial Z_P}\frac{I_k}{I_P} - 2\pi R_P B_{Rd} \, , \quad (3)$$

$$\frac{M_P}{I_P}\frac{d^2\delta R_P}{dt^2} = \left\{ 2\pi B_{V0}\left(1 - \frac{1}{\Lambda_0} - n\right) - \frac{\mu_0 I_P}{4R_P} - \frac{7}{6}\mu_0 I_P \frac{\beta_P}{R_P} \right\}\delta R_P - 2\pi B_{V0} k \delta Z_P$$

$$-\left(2\pi R_P B_{V0} + \mu_0 I_P \beta_P\right)\frac{\delta I_P}{I_P} \qquad\qquad , \qquad (4)$$

$$+I_P \sum_i \frac{\partial M_{Pi}}{\partial R_P}\frac{I_i}{I_P} + I_P \sum_k \frac{\partial M_{Pk}}{\partial R_P}\frac{I_k}{I_P} + \frac{\mu_0 I_P}{2}\left(\delta\beta_P + \frac{1}{2}\delta\ell_i\right) + 2\pi R_P B_{Zd}$$

where M_{Pi}, M_{Pk}, I_i, I_k, B_{Rd} and B_{Zd} are the mutual inductance between the plasma and the i-th feedback control coil, the mutual inductance between the plasma and the k-th eddy current mode, the current of the i-th feedback control coil, the current of the k-th eddy current mode, the radial and the vertical disturbance fields, respectively. B_{V0}, n, k and Λ_0 are defined as follows:

$$B_{V0} = \frac{1}{I_P}\int dRdZ B_Z J_P \, , \qquad (5)$$

$$n = -\frac{1}{I_P B_{V0}}\int dRdZ R \frac{\partial B_Z}{\partial R} J_P \, , \qquad (6)$$

$$k = -\frac{1}{I_P B_{V0}}\int dRdZ R \frac{\partial B_Z}{\partial Z} J_P \, , \qquad (7)$$

$$\Lambda_0 = \ln\left(\frac{8R_P}{a_P}\right) + \beta_P + \frac{1}{2}(\ell_i - 3) \, . \qquad (8)$$

Furthermore, for extending from the rigid model to the non-rigid (deformable) model, several gaps between the plasma surface and the wall are defined as Figure 1 and the relation between the gaps and the parameters (the plasma,

the coils...) is previously estimated by calculating some MHD equilibrium states.

$$\mathbf{y} = \mathbf{Cx} \ , \tag{9}$$

where

$$\mathbf{y} = \begin{pmatrix} g_1 \\ g_2 \\ g_3 \\ g_4 \\ g_5 \\ g_6 \end{pmatrix}, \qquad \mathbf{x} = \begin{pmatrix} \delta Z_P \\ \delta R_P \\ \delta I_P / I_P \\ \vdots \\ I_i / I_P \\ \vdots \\ I_k / I_P \\ \vdots \end{pmatrix}, \tag{10}$$

and $\mathbf{C}$ is obtained from some results of the MHD equilibrium analysis with respect to the small changes of the poloidal beta and the internal inductance, numerically. That is, $\mathbf{C} \equiv \Delta \mathbf{y} / \Delta \mathbf{x}$, and six gaps in Eq. (10) are defined as shown in Fig.1.

The time evolution of the plasma current, the eddy currents of the conducting components and the currents of the active feedback coils is described by the circuit equations as follows:

$$\frac{d}{dt}\left(L_P I_P\right) + \sum_i \frac{d}{dt}\left(M_{Pi} I_i\right) + \sum_k \frac{d}{dt}\left(M_{Pk} I_k\right) + \eta_P I_P = 0 \tag{11}$$

$$L_i \frac{dI_i}{dt} + \frac{d}{dt}\left(M_{Pi} I_P\right) + \sum_j M_{ij} \frac{dI_j}{dt} + \sum_k M_{ik} \frac{dI_k}{dt} + \eta_i I_i = V_i \tag{12}$$

$$\tau_k \frac{dI_k}{dt} + \frac{d}{dt}\left(M_{Pk} I_k\right) + \sum_i M_{ik} \frac{dI_i}{dt} + I_k = 0, \tag{13}$$

where L_P, η_P, L_i, M_{ij}, η_i, I_j and τ_k are the plasma self-inductance, the plasma one-turn resistance, the self-inductance of the i-th coil, the mutual inductance between the i-th coil and the j-th coil, the resistance of the i-th coil, the j-th coil current and the time constant of the k-th eddy current mode, respectively. τ_k, M_{Pk} and M_{ik} are obtained from the three-dimensional finite element analysis. V_i is the voltage of the control coil and is applied by the PD decoupled controller in this paper.

By assuming the toroidal flux conservation, Eq.(11) is expanded as follows:

$$-\left(2\pi R_P B_{V0} + \mu_0 I_P \beta_P\right)\frac{d\delta R_P}{dt} + I_P L_P \frac{d\delta I_P}{dt} + \sum_i I_P M_{Pi} \frac{dI_i}{dt} + \sum_k \frac{d}{dt}\left(M_{Pk} I_k\right) + \eta_P \delta I_P = 0. \tag{14}$$

Furthermore, in Eqs.(12) and (13), the following approximation is applied:

$$\frac{dM_{Pi}}{dt} \approx \frac{\partial M_{Pi}}{\partial Z_P} \frac{d\delta Z_P}{dt} + \frac{\partial M_{Pi}}{\partial R_P} \frac{d\delta R_P}{dt} \tag{15}$$

By neglecting the mass of the plasma, Eqs.(3), (4), (12), (13) and (14) are summarized as follows:

$$\mathbf{A}\dot{\mathbf{x}} + \mathbf{R}\mathbf{x} = \mathbf{b}. \tag{16}$$

where $\mathbf{A}$, $\mathbf{R}$ and $\mathbf{b}$ are

$$
\mathbf{A} = \begin{bmatrix}
2\pi B_{V0}n, & -2\pi B_{V0}k, & 0, & \cdots, & I_P\frac{\partial M_{Pi}}{\partial Z_P}, & \cdots, & I_P\frac{\partial M_{Pk}}{\partial Z_P}, & \cdots \\
-2\pi B_{V0}k, & a_{22}, & -(2\pi R_P B_{V0} + \mu_0 I_P \beta_P), & \cdots, & I_P\frac{\partial M_{Pi}}{\partial R_P}, & \cdots, & I_P\frac{\partial M_{Pk}}{\partial R_P}, & \cdots \\
0, & -(2\pi R_P B_{V0} + \mu_0 I_P \beta_P) & L_P I_P, & \cdots, & I_P M_{Pi}, & \cdots, & I_P M_{Pk}, & \cdots \\
\vdots & \vdots & \vdots & \ddots & \vdots & & \vdots & \\
I_P\frac{\partial M_{Pi}}{\partial Z_P}, & I_P\frac{\partial M_{Pi}}{\partial R_P}, & I_P M_{Pi}, & \cdots, & I_P L_i & & 0 & \\
\vdots & \vdots & \vdots & \cdots, & & \ddots & & \\
I_P\frac{\partial M_{Pk}}{\partial Z_P}, & I_P\frac{\partial M_{Pk}}{\partial R_P}, & I_P M_{Pk}, & & 0 & & I_P \tau_k & \\
\vdots & \vdots & \vdots & \cdots, & & & & \ddots
\end{bmatrix} \tag{17}
$$

$$
\mathbf{R} = \begin{bmatrix}
0 & & & & \\
& 0 & & & \\
& & I_P \eta_P & & 0 \\
& & & \ddots & \\
& & & & I_P \eta_i \\
& 0 & & & \ddots \\
& & & & & I_P & \ddots
\end{bmatrix}
\qquad
\mathbf{b} = \begin{bmatrix}
2\pi R_P B_{Rd} \\
-\frac{\mu_0 I_P}{2}\left(\delta\beta_P + \frac{\ell_i}{2}\right) - 2\pi R_P B_{Zd} \\
0 \\
V_i \\
\vdots \\
V_i \\
\vdots \\
0 \\
\vdots
\end{bmatrix}, \tag{18}
$$

where a_{22} is

$$a_{22} = 2\pi B_{V0}\left(1 - \frac{1}{\Lambda_0} - n\right) - \frac{\mu_0 I_P}{4R_P} - \frac{7}{6}\frac{\mu_0 I_P \beta_P}{R_P}. \tag{19}$$

The calculation sequence is carried out as in Figure 2. After giving the results of the initial equilibrium analysis and the eddy current analysis, Eq.(16) combined with Eq.(9) can be solved by the Fehlberg formula and the Adams-Moulton method with the 8-th order, numerically. If the displacement of the plasma current center or the number of iteration exceeds a certain value, then the MHD equilibrium calculation is carried out and the coefficients required for Eq.(16) are renewed, and the Eq.(16) is solved again.

3. Application results

To show some examples of the plasma position and shape control analyses by this simulation (TSPS) code, the ITER design parameters in the Final Design Report (ITER-FDR) were used[8] in this paper. The main parameters used are the plasma major radius 8.14m, the plasma minor radius 2.8m, the elongation 1.6, the triangularity 0.24, the plasma current 21MA,, the toroidal magnetic field at the plasma center 5.68 T, respectively.

Figure 3 shows an example of the three-dimensional finite element mesh models used in the eddy current analysis. This mesh model includes the blanket modules, the backplate and the vacuum vessel with the double layers. The backplate and the vacuum vessel are electrically connected in the toroidal direction. The material used for all conducting components is the stainless steel and the value of the electric resistivity is 0.9 $\mu\Omega$m.

Figure 4 shows the frequency response of the stabilization index n_S obtained by the three-dimensional finite element analysis (the eddy current analysis). In Fig.4, n is the n-index, which is the strength of the vertical instability. The criterion with respect to the vertical stability is represented by $n+n_S=0$, and in the case of the ITER, Start Of Burning (SOB) plasma, the growth rate is 0.98 s^{-1}. The feedback control by the poloidal coils is applied to the instability that has slower time constant comparing the growth rate.

Figure 5 shows the time evolution of (a) the poloidal beta β_p, the internal inductance ℓ_i, the ratio of the volume averaged thermal energy, (b) the plasma current, (c) the total active power of the poloidal coils and (d) the six gaps between the plasma surface and the wall in the case of minor disruption of the SOB plasma ($\beta_p=0.9$ and $\ell_i=0.9$) by the PD decoupled feedback control, respectively. In this case, the poloidal coils are used for the equilibrium and the control. The minor disruption at SOB is defined as instantaneous step-like reduction of the poloidal beta by 0.2 simultaneous with instantaneous step-like reduction of the internal inductance by 0.1. As shown in Fig.5, the maximum total active power is about 180MW and the maximum gap is about 0.12m, and these results satisfy the request of the ITER design sufficiently.

4. Summaries

The Toroidally Symmetric Plasma Simulation (TSPS) code has been developed for investigating the position and shape control on tokamak plasmas. The analyses of three-dimensional eddy currents on the conducting components around the plasma and the two-dimensional magneto-hydrodynamic (MHD) equilibrium are considered in this code. Regarding the model of plasma, the motion of the plasma is essentially based on the rigid model. However, the deformation of plasma shape is considered by calculating the MHD equilibrium at each 20~30 time-steps typically, and then the plasma parameters used in this code are renewed. Furthermore, for extending from the rigid model to the non-rigid (deformable) model, the relation between the gaps and the parameters (the plasma, the coils...) is previously estimated by calculating some MHD equilibrium states. Therefore, this code can analyse the plasma

position and shape control during the minor disruption in which the deformation of plasma is not negligible. In addition, this model is suitable for the design that must calculate many cases since the reduction of the calculation time is expected comparing the non-linear model.

TSPS code is useful for designing fusion reactors and, actually, using the ITER (International Thermonuclear Experimental Reactor) parameters, some examples of calculations were shown in this paper.

References

[1] KASAI, M., KAMEARI, A., MATSUOKA, F., SHINYA, K., IIDA, H., FUJISAWA, N., Fusion Eng. Des., **5** (1988) 343.

[2] NISHIO, S., SUGIHARA, M., SHIMOMURA, Y., Fusion Eng. Des., **23** (1993) 17.

[3] ALBANESE, R., COCCORESE, E., RUBINACCI, G., Nucl. Fusion, **29** (1989) 1913.

[4] JARDIN, S.C., POMPHERY, N., DELUCIA, J., J. Comput. Phys. **66** (1986) 481.

[5] SAYER, R.O., PENG, Y.K.M., JARDIN, S.C., KELLMAN, A.G., WESLEY, J.C., Nucl. Fusion, **33** (1993) 969.

[6] NINOMIYA, H., KAMEARI, A., SHINYA, K., JAERI-M 9127 (1980).

[7] KAMEARI, A., J. Comput. Phys. **42** (1981) 124.

[8] Technical Basis for the Final Design Report, Cost Review and Safety Analysis, ITER EDA Documentation Series, IAEA, Vienna (1998).

Figure Captions

Fig.1 Six reference gaps between plasma surface and wall

Fig.2 Sequence of calculation

Fig.3 example of three-dimensional finite element mesh model

Fig.4 Frequency response of vertical stabilization index

Fig.5 Time evolution of (a) poloidal beta, internal inductance, ratio of volume averaged thermal energy, (b) plasma current, (c) total active power of poloidal coils and (d) gaps between plasma surface and wall.
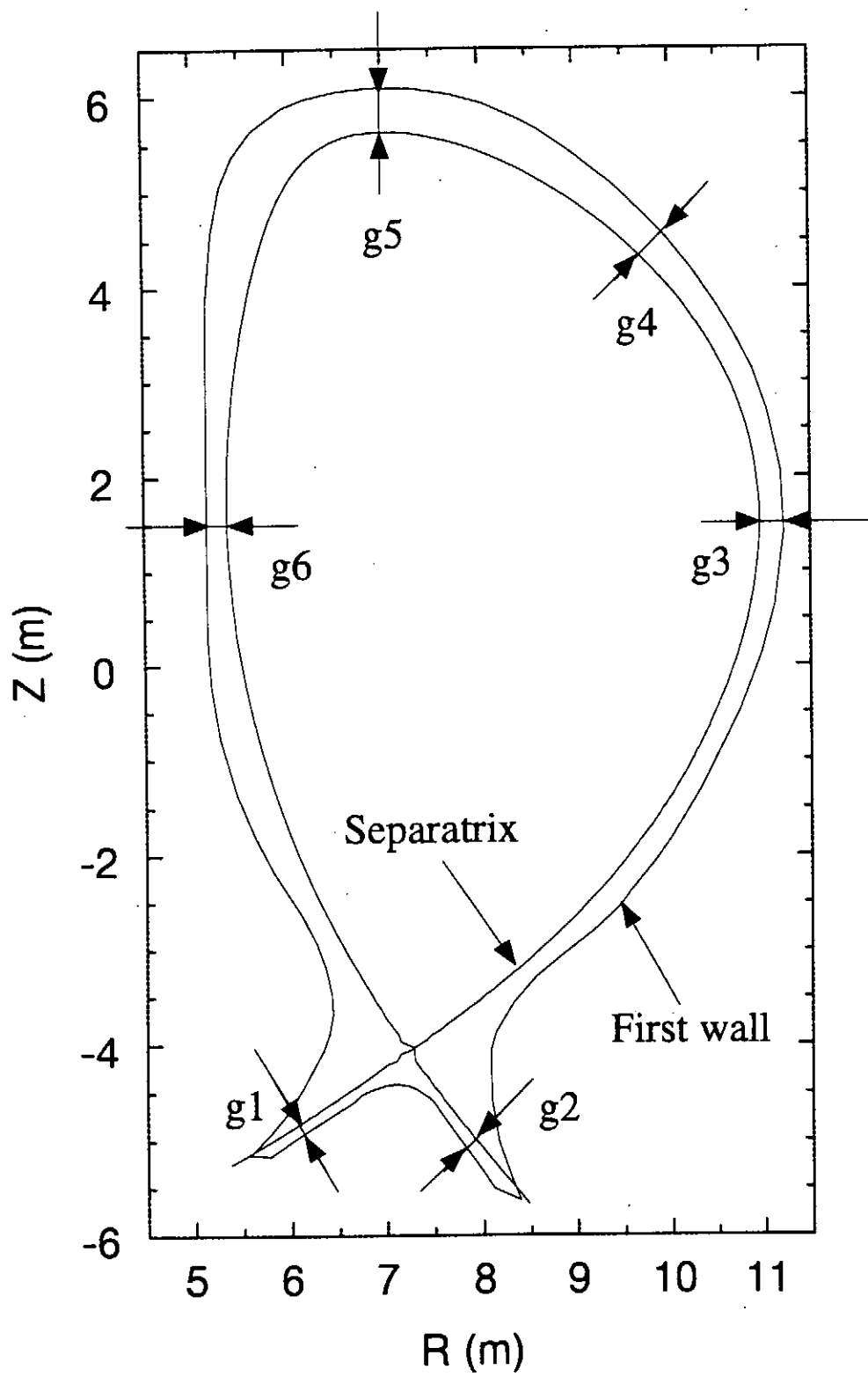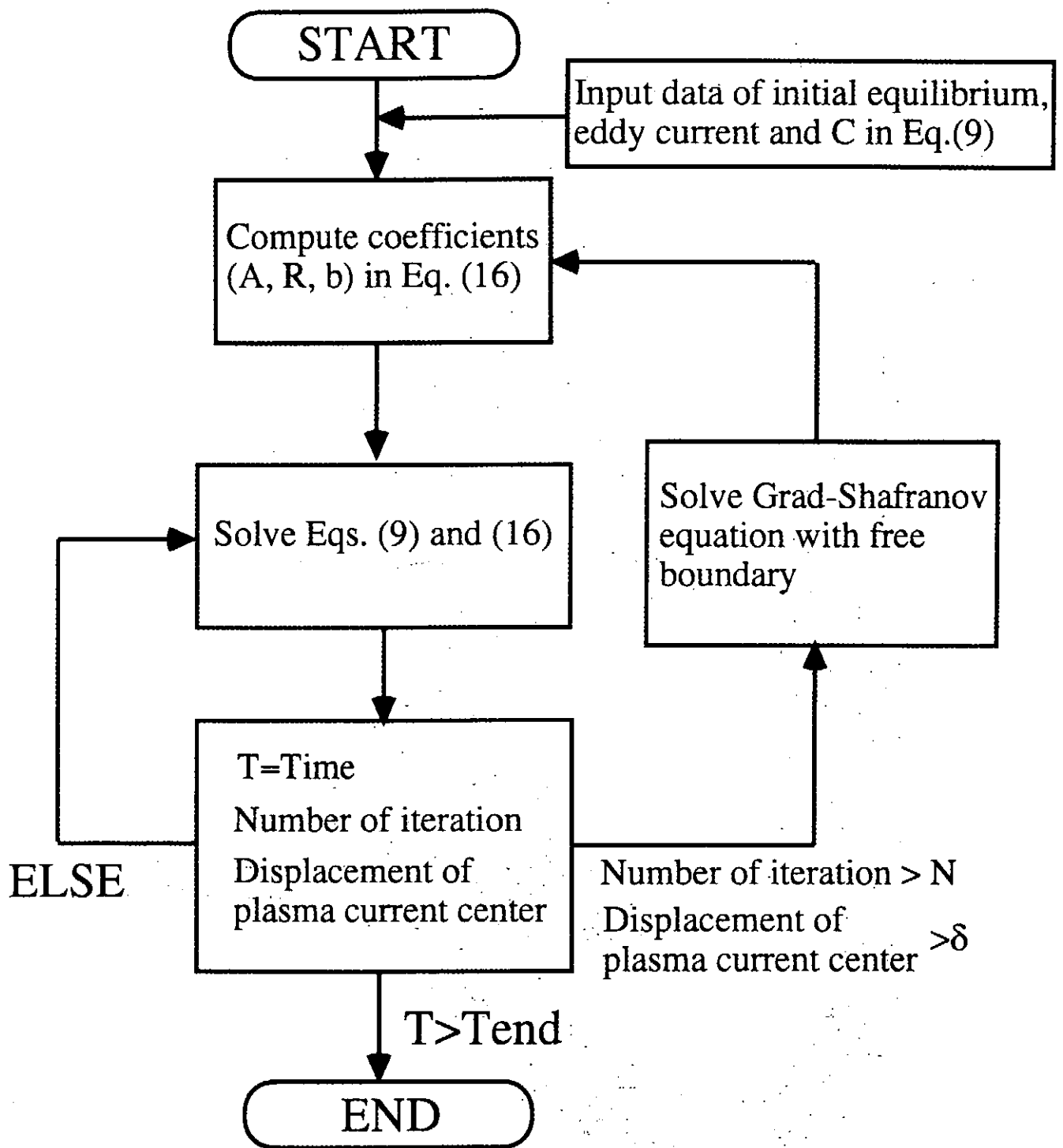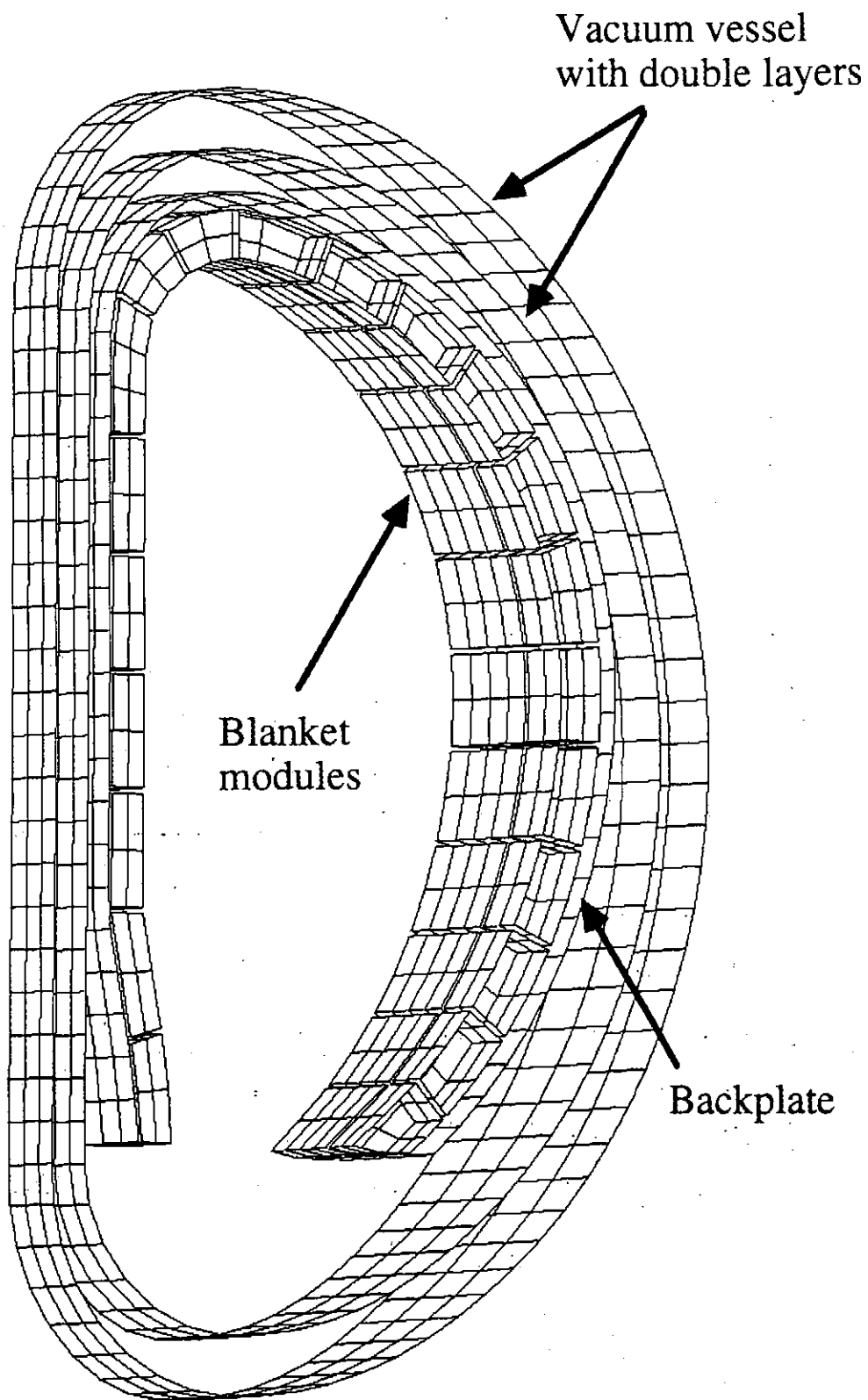
Fig.1

Fig. 2

Vacuum vessel
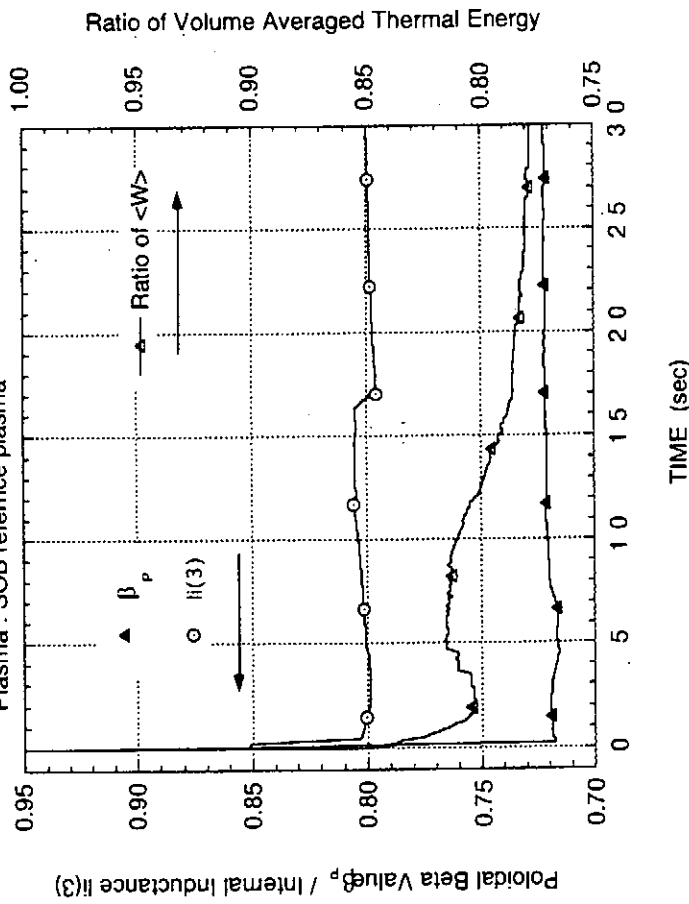with double layers

Blanket
modules

Backplate

Fig. 3

Fig. 4

(b)

Evolution of the plasma current

Disturbance : $\delta\beta_p = -0.2$ & $\delta li(3) = -0.1$ in 10 msec
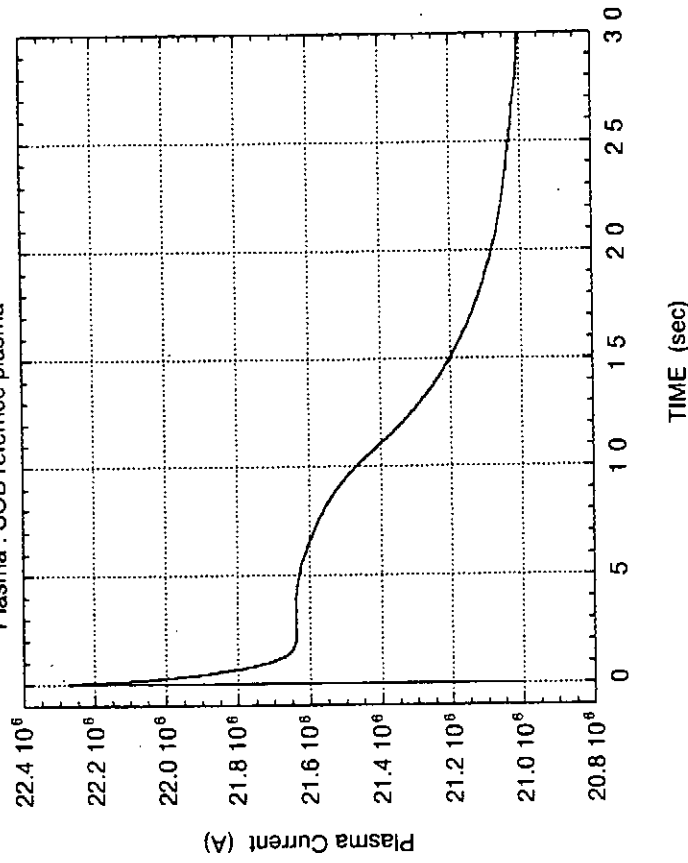Plasma : SOB refernce plasma

Plasma Current (A)

TIME (sec)

Fig.5(b)
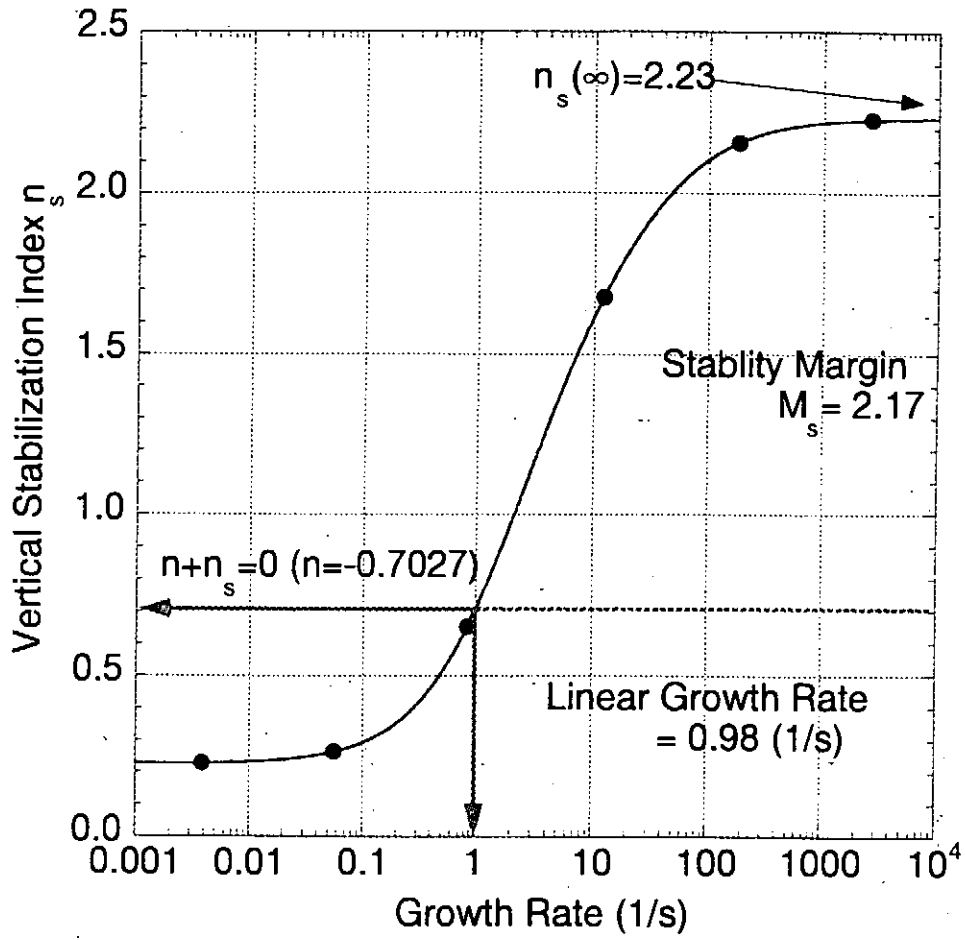
(a)

Evolution of the poloidal beta value, internal inductance Ii(3) and the ratio of the volume averaged thermal energy

Disturbance : $\delta\beta_p = -0.2$ & $\delta li(3) = -0.1$ in 10 msec
Plasma : SOB refernce plasma

Ratio of Volume Averaged Thermal Energy

Ratio of <W>

β_p

Ii(3)

Poloidal Beta Valueβ_p / Internal Inductance Ii(3)

TIME (sec)

Fig. 5(a)

(d)

Evolution of separatrix displacements at the gaps

Disturbance : $\delta\beta_p = -0.2$ & $\delta l_i(3) = -0.1$ in 10 msec

Plasma : SOB refernce plasma

Fig.5(d)

(c)

Total active power of PF coils

Disturbance : $\delta\beta_p = -0.2$ & $\delta l_i(3) = -0.1$ in 10 msec

Plasma : SOB refernce plasma
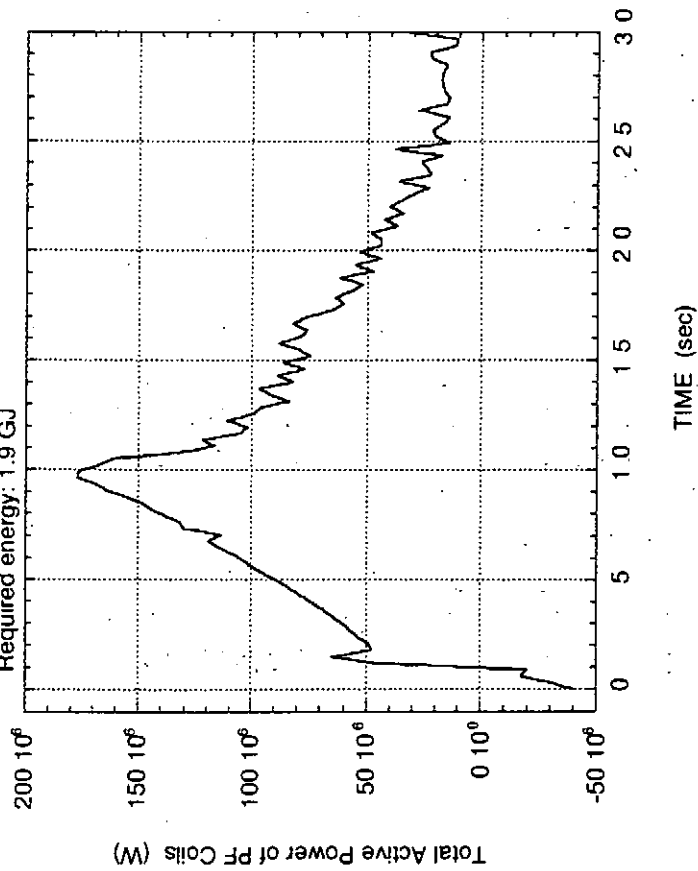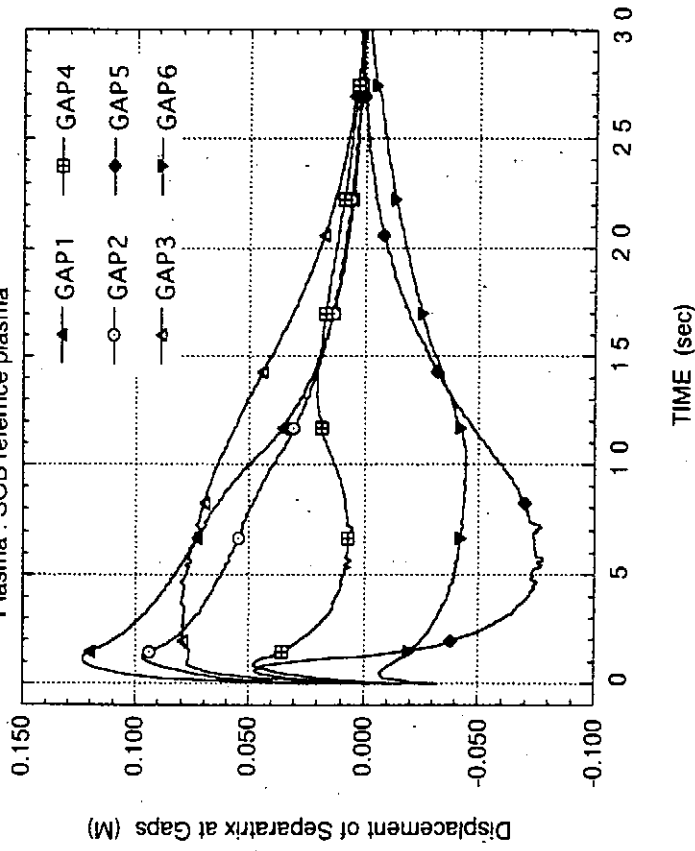
Required energy: 1.9 GJ

Fig. 5(c)

数理物理に現れる非線形問題と
その数学解析
(Nonlinear Problems in Mathematical Physics
and their Mathematical Analysis)

鈴木貴・大阪大学大学院理学研究科
(Takashi SUZUKI・Osaka University)

平成 10 年 12 月 27 日

abstract: Recent study on the nonlinear partial differential equations has revealed a peculiar behavior of (approximate) solutions; the bubble. This lecture describes the phenomenon for the system of chemotaxis. Relations to other phenomena and to other systems of mathematical physics such as compensated compactness and gauge theory e.g. are also presented.

Key Words: weak solution, bubble, statistical mechanics, gauge theory, chemotaxis

1 弱解と近似解

1.1 弱解概念の導入

「線形 v.s. 非線形」、「古典解 v.s. 弱解]、「正則性 v.s. 特異性」、「連続 v.s. 離散]、「決定論 v.s. 統計論」など、一見鋭く対立する概念は少し離れて双方を同時にみることによりどういう対象のどういう側面を問題としているかを明確に認識することができる。最初の軸でいうと線形偏微分方程式は作用する operator に、従ってより関数解析の方向に傾いているのに対し非線形偏微分方程式は作用を受ける function に、従ってより関数論を志向していることが了解できる。

偏微分方程式の取り扱いについては変分法、調和解析学、積分作用素論などの種々の方法が考えられて来ている。これらは同じ対象を扱っていながら激しく競合する側面を持ち、その歴史的な展開には興味深いものがある。Poisson

方程式

$$-\Delta u = f \quad \text{in} \quad \Omega, \qquad u = 0 \quad \text{on} \quad \partial\Omega \tag{1}$$

と Laplace 方程式

$$-\Delta u = 0 \quad \text{in} \quad \Omega, \qquad u = g \quad \text{on} \quad \partial\Omega \tag{2}$$

は共に変分構造を持ち、前者は Sobolev 空間 $X = H_0^1(\Omega)$ 上の汎関数

$$J(v) = \frac{1}{2}\int_\Omega |\nabla v|^2 - \int_\Omega vf$$

の停留点として、後者は affine 空間 $X = \{v \in H^1(\Omega) \mid v = g \ \text{on} \ \partial\Omega\}$ 上の汎関数

$$J(v) = \int_\Omega |\nabla v|^2$$

の停留点として特徴付けることができる。このアイデアは最も先行したにもかかわらずすぐに捨て去られてしまった。例えば Poisson 方程式について言うと Perron の方法や、Fredholm の方法に取って代わられるが長い年月を経て正当な方法として復権し今日に至る。論理的問題の発見により一度は捨てたものが復活しえたのは数学自身の成熟に外ならないとすることもできようが、それでは Perron の方法や Fredholm の方法というのはどういうものであったのか。

まず Perron からいくと (2) を二つの微分不等式

$$-\Delta u \left\{\begin{array}{c} \geq \\ \leq \end{array}\right\} 0 \quad \text{in} \quad \Omega, \qquad u \left\{\begin{array}{c} \geq \\ \leq \end{array}\right\} g \quad \text{on} \quad \partial\Omega \tag{3}$$

に分解して優解、劣解を定める。積分作用素を用いてこれらの概念を連続関数に拡張しておいてから例えば

$$u(x) = \sup\{v(x) \mid v : (2) \ \text{の劣解}\}$$

をとる。次に Fredholm では主要部 $-\Delta$ の parametrix であるポテンシャル、例えば3次元では

$$\Gamma(x) = \frac{1}{4\pi|x|}$$

を用いて積分方程式

$$f(\xi) = \mu(\xi) + 2\int_{\partial\Omega} \mu(\eta)\frac{\partial}{\partial\nu}\Gamma(\xi - \eta)d\sigma(\eta) \qquad (\xi \in \partial\Omega)$$

と関係式

$$u(x) = 2\int_{\partial\Omega} \mu(\eta)\frac{\partial}{\partial\nu}\Gamma(x - \eta)d\sigma(\eta) \qquad (x \in \Omega)$$

を導出する。こうした定式化の後に、最大原理や積分方程式論（交代定理）が駆使されて解の存在・一意性・正則性が議論されることになる。

因みに変分法ではこの場合 J の X における最小化列 $\{v_k\}$ をとる。これが

$$J(v_k) \to j = \inf_X J, \qquad \|J'(v_k)\|_* = o(1)$$

をみたして Palais-Smale 列となるのである。

1.2 弱解概念の展開

これらの定式化のもたらした影響は計り知れない。それぞれの理論や方法に応じてその存在や一意性が吟味されることになるこうした解を（習慣と反する場合もあるが）弱解ということにする。

存在と一意性が確立されたとして、次に大切なことはこれらの弱解の相互の関係やそれが古典解となっているかどうかを検討することである。これが正則性の問題でありその研究方法は変分学、積分作用素論、ポテンシャル論のそれぞれにおいて相当に整備され確立されている。hard analysis という言葉はこれらを表すことも多い。しかし非線形問題においてより根本的なことは弱解が古典解となりえないことの認識であると思われる。

例えば $1 < p < \infty$ に対して

$$-\nabla \cdot \left(|\nabla u|^{p-2} \nabla u\right) = 0 \quad \text{in} \quad \Omega, \qquad u = g \quad \text{on} \quad \partial\Omega \tag{4}$$

を考える。変分法による弱解 $u \in W^{1,p}(\Omega)$ が定義され一意存在が示される。$p = 2$ のときは (2) と全く同じものであるが、そうでないときは $u(x)$ は $C^{1,\alpha}$ の正則性しか持ち得ない。これは領域 Ω に $\nabla u = 0$ となる点（特異点）が出現するからであるが、このことが実は (4) の現象論的に興味深い所であり、これらの特異点の control が解析的にも重要な問題と考えられるのである。

言ってみれば、非線形の場合解に特異点や退化がおこるところで方程式の理解があいまいになる。このことを乗り越えるためには存在、一意性といった基本定理が成り立つように弱解を定義し直さなければならない。すなわち弱解とは単に古典解の要請を弱めたものではない。局所的にはそのようにする一方大域的には逆に制約を課してこうした目的を達成せんとするものなのである。

では弱解にはどのようなものがあるだろうか。(1) で言えばひとつの定式化は $u \in L^1_{loc}(\Omega)$ かつ

$$\int_\Omega u \cdot (-\Delta\phi) = \int_\Omega u \cdot \phi \qquad \text{for all} \qquad \phi \in \mathcal{D}(\Omega)$$

もうひとつは $u \in H^1_0(\Omega)$ かつ

$$\int_\Omega \nabla u \cdot \nabla\phi = \int_\Omega f\phi \qquad \text{for all} \qquad \phi \in H^1_0(\Omega)$$

であろう。いずれも試験関数 φ をとるところに特徴があり、前者を Schwartz 流、後者を Lax-Kato 流と言ってもよい。前者はより局所的、後者はより大域的である。どちらも線形理論から生まれてきたものだが非線形に移っても十分に役に立つ。

作用素に対する関心を取り戻すとき関数解析的な取り扱いとなるのは冒頭述べた通りである。非線形問題に広く適用できる重要な性質が単調性であって極大単調作用素論、非線形半群論を育んできた。また幾何的な問題では varifold、Aleksandroff といった非常に特徴的な弱解概念が生まれている。

最近に現れた重要な弱解のひとつは Boltzmann 方程式に対する端を発するもので試験関数の取り方を解と関連させて非線形にとるというものであり、もうひとつは Hamilton-Jacobi 方程式の研究に端を発するもので微分不等式 (3) を試験関数を用いて定式化し直すというものである。前者を renormalized solution、後者を viscosity solution と呼んでいる。

これらの方法により単調な問題からコンパクトな摂動が加えられたものを統一的に解析する手だては十分に整備されてきているといえよう。

1.3 近似解の解析

微分方程式の研究においておよそ理論と呼ばれるものは弱解をどのように定めるかという定式化であり、成功する例ではこうして解をとらえて正則性を議論してきたことが了解されるであろう。それではそれがうまくいかないときにはどのようなことがおこっているのだろうか。

思い起こしてみるとこれらの理論はまた同時に近似解の構成方法の提示でもあった。可算な近似列として作ることができることもあれば、超越的なときには背理法によって証明することもある。いずれにしろ弱解がつかまえられないときの近似解のふるまいはいくつかのパターンに分けられるのである。

ここでは関数列のふるまいとして次の３つを指摘しておく。すなわち

1. 遠方に逃げる
2. 振動する
3. 集中する

最初のは領域がコンパクトでないときに起こる。第２はベクトル値関数で１階の微分が働くときよく起こる。非線形項にキャンセルする効果があると事前に防ぐことができ compensated compactness と呼ばれている。第３は楕円型や放物型で非線形項が拡散と対立する働きをするときによく起こる。変数変換により集中していく点（爆発点）の周囲の様子を詳しく control することができ、concentrated compactness と呼ばれている。このように弱解に収束しない近似解の挙動が control できれば従来の粗い議論ではつかまえられなかった解の存在の証明や性質の解明に役立つ。すなわち逆にこうしたこ

とが起こらないことをひとつひとつ確認していけばよい。

次節との関わりから第3の挙動についてもう少し言及しておく。

1. このような現象は、例えば散逸的である線形部分と集中化を促進する非線形部分との競合からおこる。微少なレベルでは線形部分が支配的であるのでこうしたことがおこるためには、近似解列がある程度以上のポテンシャルを持っていなければならない。通常このような量は関数のノルムではかることができる。すなわち concentration がおこるとき系の支配的なノルムはある定数以上である。こうした事実は幾何学において早くから認識されておりその用語を転用して rigidness と呼ぶことにする。

2. こうしたことはいろいろの場所で同規模におこる。言って見ればひとつ、ふたつ、と数えることができ本来連続的であった現象が量子化される。逆にこうした量子化されたスペクトルからはずれる部分では真の解への収束が起こりうる。concentration をこのように global な立場から見ることは topology において盛んになされてきた。そこでこうしたことをその分野にゆかりの深い言葉である bubble によって表すことにする。

3. こうした現象をひきおこす方程式は、大抵変数変換 (rescale) に関するある種の不変性を持っておりこれを利用してひとつひとつの bubble の生成の様子をより詳しく control することができる。rescale された関数はもとの方程式と類似の形状をもつのであるからもとの方程式に対して開発されてきた方法が適用できる。例えば double well を見てもよいし、線形化をしてもよい。さらにもう一度 rescale をすることもできる。このような rescale を繰り返す解析は代数幾何においてよく用いられてきておりその用語に従って blow-up analysis と呼ぶことにする。

4. 最後に blow-up analysis の変形ないし強化である matched asymptotic expansion についてふれておく。通常 blow-up analysis では爆発点の極小近傍の事しかわからない。一方 bubble の遠方では解は急速に decay していく。前項の方法が成功する問題では極小近傍が遠方をコントロールしていることになる。そうでない場合にはこの二つの領域の境目、変曲点のあたりに本質的な現象が隠されていることになる。ひとつの考え方は両者がうまくつながるようにパラメータを定めることであって常微分方程式などの特異摂動問題で開発されてきた方法である。その用語を転用して matched asymptotic expansion と呼ばれ最近注目されている。

2 粘菌方程式の数理

2.1 Modelling

　粘菌は通常はアメーバー状の微生物で何らかの状況によりいくつかの固まりに分かれ始めやがて胞子を作って次の世代に移行する。動物態と植物態とを経過して世代交代する奇妙な生物であるがこの生物の動物態から植物態への移行を説明するものとして 1970 年に Keller と Segel により提出されたのが放物型方程式系

$$
\begin{aligned}
u_t &= \nabla \cdot (\nabla u - u \nabla \phi(v)) &\quad \text{in} &\quad \Omega \times (0, T) \\
\tau v_t &= \Delta v - av + u &\quad \text{in} &\quad \Omega \times (0, T) \\
\frac{\partial u}{\partial \nu} &= \frac{\partial v}{\partial \nu} = 0 &\quad \text{on} &\quad \partial\Omega \times (0, T) \\
u|_{t=0} &= u_0(x), \quad v|_{t=0} = v_0(x) &\quad \text{in} &\quad \Omega
\end{aligned}
\tag{5}
$$

である。ただしいくつかの定数を 1 とした。ここで $\Omega \subset \mathcal{R}^2$ は境界 $\partial\Omega$ が滑らかな有界領域、ν は外向き単位法ベクトル、$u = u(x, t)$ が場所 $x \in \Omega$、時刻 $t \in (0, T)$ の粘菌の密度をあらわしている。$v = v(x, t)$ が粘菌の放出する化学物質の濃度でありこの作用を考慮すれば上記の現象が説明できるとされたのである。

　(5) では最初の方程式が特徴的である。ここで $v \mapsto \phi(v)$ は単調増加で知覚関数とよばれる。$\phi(v) = v$、$\phi(v) = v^p$、$\phi(v) = \log v$ などが用いられる。さて この方程式は $\omega \subset \Omega$、$F = \nabla u - u \nabla \phi(v)$ に対して

$$
\frac{d}{dt} \int_\omega u = \int_{\partial\omega} F \cdot \nu
$$

であることを示す。すなわち $-F$ が $u(x, t)$ の流量をあらわしている。このベクトル場は $-\nabla u$ と $u \nabla \phi(v)$ の和であるが前者は粘菌がその密度勾配にしたがって外側に移動すること、すなわち拡散を示し後者は $\phi(v)$ の密度勾配に比例してその高い方向にむかうこと、すなわち走化性をあらわしている。$\phi(v)$ を知覚関数と呼ぶこともこのことから了解できるのである。

　これに対し2番目の方程式は線形であり、化学物質 $v(x, t)$ が拡散し一定の割合で消滅し一定の割合で粘菌により生成されることをあらわす。境界条件は粘菌や化学物質が考えている領域の外へ流れ出さないことをあらわし、初期条件が課せられている。$\tau > 0$ は十分小さな定数で、この条件は化学物質にとっての時間が粘菌にとっての時間よりも早いスケールで流れていることを示しているのである。

　方程式論としての出発点が基本定理にあることは言うまでもない。この場合方程式は準線形で多少複雑ではあるが解析半群の smoothing effect はまだ有効に働く。十分に滑らかな初期値に対しては時間局所的な古典解の一意存在を示すことはできる。初期値が非負であれば解も同様であり、$u_0 \neq 0$ なら

ば時刻正で $u(x,t) > 0$、$v(x,t) > 0$ となることは最大原理の簡単な応用である。そこで解はどこまで延長できるかということが問題となる。延長し得る最大の時間を $T_{\max}$ と書き $T_{\max} < +\infty$ のとき解は有限時間で爆発するという。$T_{\max} = +\infty$ のときは時間大域解となる。

　方程式がある関数空間のなかの不動点方程式に変換され反復法によって解けたとすると、初期値のその空間でノルムは解のノルムを上から、存在時間を下から評価することになる。このようなとき $T_{\max} < +\infty$ であれば解のノルムは時刻が $T_{\max}$ に近づくにしたがって $+\infty$ に発散することになる。古典解のままで考えると通常このノルムは非線形性が強まるほど強くとらなければならない。しかし多分この方程式系については L^∞ ノルムでよい。したがって解の爆発が起こるときはその L^∞ ノルムが $+\infty$ に発散することになる。解の爆発は現象的には粘菌が植物態に移行することと考えられるのである。

　実際 1973 年 Nanjundiah [13] は $T_{\max} < +\infty$ のときにはその時刻において $u(x,t)$ は δ 関数的な形状になるだろうと予想したが、その正当性はその後の数学的な研究により確立していくことになる。

2.2　爆発条件と定常解

　(5) において L^1 保存則

$$\|u(t)\|_1 = \|u_0\|_1 \qquad (0 < t < T_{\max}) \tag{6}$$

が成り立つのは見やすい。簡単のため $\phi(v) = v$ とし最初の式を

$$u_t = \nabla \cdot (u\nabla(\log u - v))$$

と書くと

$$\int_\Omega u_t (\log u - v) = -\int_\Omega u |\nabla(\log u - v)|^2$$

が得られるが (6) から

$$\frac{d}{dt}\int_\Omega u\log u = \int_\Omega u_t \log u$$

であり

$$\int_\Omega u_t v = \frac{d}{dt}\int_\Omega uv - \int_\Omega uv_t$$

において (5) 第2式より

$$\begin{aligned}\int_\Omega uv_t &= \int_\Omega (\tau v_t - \Delta v + av)v_t \\ &= \tau \int_\Omega v_t^2 + \frac{1}{2}\frac{d}{dt}\int_\Omega \left(|\nabla v|^2 + av^2\right)\end{aligned}$$

であるから

$$W = \int_\Omega u \log u - \int_\Omega uv + \frac{1}{2}\left(\|\nabla v\|_2^2 + a\|v\|_2^2\right)$$

は Lyapunov 関数、

$$\frac{d}{dt}W + \tau \int_\Omega v_t^2 + \int_\Omega u \left|\nabla\left(\log u - v\right)\right|^2 = 0 \qquad (7)$$

が成り立つ。このことは (5) の解の時間大域挙動において定常解が一定の役割を果たすことを示す。さらに (7) から自明でない定常解において定数 $\sigma > 0$ により $\log u - v = \log \sigma$ となり、したがって (5) 第2式より

$$-\Delta v + av = \sigma e^v \qquad \text{in} \qquad \Omega$$

が得られる。

ここで (6) に注意して $\lambda = \|u\|_1$ とおく。$u = \sigma e^v$ から $\sigma = \lambda/\int_\Omega e^v$ となり λ をパラメータとして楕円型境界値問題

$$-\Delta v + av = \lambda e^v / \int_\Omega e^v \quad \text{in} \quad \Omega, \qquad \frac{\partial v}{\partial \nu} = 0 \quad \text{on} \quad \partial\Omega \qquad (8)$$

が出現する。(8) は常に定数解 $v = \lambda/a|\Omega|$ を持っている。

1981 年 Childress と Percus はこれを Ω：円板 v：回転対称で考え数値計算を試みて次のように考えた。

1. $0 < \lambda < 8\pi$ ではこの場合定数以外に解はない
2. 爆発が起こるとすれば解の形状は回転対称に近づくはずである
3. 従って任意の領域において $\|u_0\|_1 < 8\pi$ ならば (5) において解の爆発は起こらず、逆に $\|u_0\|_1 > 8\pi$ のときは解の爆発が起こり得る

この予想は Jäger-Luckhaus [7]、Nagai [10]、Herrero-Velázquez [4] [5] [6] により研究されてきた。特に Nagai-Senba-Yoshida [12] は次のことを示している。

1. Ω：円板、$u_0 = u_0\left(|x|\right)$、$v_0 = v_0\left(|x|\right)$ の場合確かに $\|u_0\|_1 < 8\pi$ のときは $T_{\max} = +\infty$ となる
2. それ以外の場合は $\|u_0\|_1 < 4\pi$ のとき $T_{\max} = +\infty$ となる

解の爆発については上記の論文により詳しく議論されてきた。それにより上の定理の第1項は sharp であることがわかる。第2項と Childress-Percus の予想とのくいちがいが生ずる理由は Nagai-Senba-Suzuki [11] によりある程度理解できる。この論文では次のことが示されている。

1. $4\pi \leq \|u_0\|_1 < 8\pi$ で $T_{\max} < +\infty$ のときは解は境界上の1点に集中してくる
2. 一般に孤立爆発点においては $u(x,t)dx$ は $t \uparrow T_{\max}$ において 8π 以上の mass をもつ δ 関数に集積する

2.3 bubble としての植物態移行

上の第2項と関連することであるが、実は孤立しない爆発点や 8π より大きい mass の存在は知られていない。このことからこうしたことはありえないのではないかという予想がたち、そうであるとすると粘菌の植物態移行は bubble なのではないかと考えられる。実際上記の Jäger-Luckhauss 以来の仕事は rigidness に関するものであり Herrero と Velázquez による2つの論文では matched asymptotic expansion が用いられているのである！また第1項と関連して Childress-Percus の「誤り」は回転対称な解のみを考えているところにあり実は回転対称な解は時間局所的にも不安定ではないかとも考えられる。こうしたことを理解する上で (5) の定常解の構造の解明が役立つことを述べてみたい。

まず (8) には変分構造が存在する。すなわちその解は $H^1(\Omega)$ 上の汎関数

$$J_\lambda(v) = \frac{1}{2}\|\nabla v\|_2^2 + \frac{a}{2}\|v\|_2^2 - \lambda \log\left(\fint_\Omega e^v\right)$$

の停留点である。このことから解 $v(x)$ のまわりの線形化作用素は $L^2(\Omega)$ 内の自己共役作用素 $A_\lambda(v)$ であり $H^1(\Omega) \times H^1(\Omega)$ 上の双線形形式

$$\mathcal{L}_\lambda(\phi,\phi) = \int_\Omega \left(|\nabla\phi|^2 - p\phi^2\right) + \frac{1}{\lambda}\left(\fint_\Omega p\phi\right)^2 + a\int_\Omega \phi^2$$

に付随することになる。ただし $\fint_\Omega = \frac{1}{|\Omega|}\int_\Omega$、$p = \lambda e^v / \int_\Omega e^v$ である。特に定数解についてはその線形化固有値や固有関数を $-\Delta_N$ のそれらにより定めることができる。こうした線形化固有値と安定性との関係には次のような関係がある。

定理 1 $V(x)$ が $\lambda > 0$ に対する *(8)* の解で $A_\lambda(V)$ の固有値がすべて正であるようなものとすると *(5)* の定常解 (U, V) ただし $U = \lambda e^V / \int_\Omega e^V$ は安定である。すなわち初期値 (u_0, v_0) が

$$\|u_0\|_1 = \lambda, \qquad \|u_0 - U\|_{L\log L} \ll 1, \qquad \|v_0 - V\|_{H^1(\Omega)} \ll 1$$

をみたすとき $T_{\max} = +\infty$ であり

$$\lim_{t\to+\infty}\|u(t) - U\|_\infty = \lim_{t\to+\infty}\|v(t) - V\|_\infty = 0$$

となる。ここで $\|\cdot\|_{L\log L}$ は *Zygmund* ノルムである。

そこで (8) の解集合の構造であるが次の定理が基本的である。

定理 2 固定された $a > 0$ に対し $\{v_\lambda\}$ を *(8)* の解の族で

$$\lambda \longrightarrow \lambda_0 \in [0, +\infty), \qquad \|v_\lambda\|_\infty \longrightarrow +\infty$$

なるものとすると部分族に対して整数 $\ell = 1, 2, \cdots$ が存在して $\lambda_0 = 4\pi\ell$ となる。ℓ は境界上の爆発点の個数と内部爆発点の個数の2倍を足したものであり、爆発点の位置や極限関数は線形部分 $(-\Delta + a)_N$ の *Green* 関数で *control* できる。

これを用いると次の事が証明できる。

1. $0 < \lambda \ll 1$ では非定数解は存在しない
2. Ω : 有限連結で $\lambda_1 = |\Omega|(a + \mu_2^*) < 4\pi$ のとき $\lambda \in (\lambda_1, 4\pi)$ において $J_\lambda(v)$ の非定数 global minimizer が存在する
3. Ω : 有限連結で $\lambda_1 > 4\pi$ のときは $\lambda \in (4\pi, \lambda_1) \setminus 4\pi\mathcal{N}$ において $J_\lambda(v)$ の mountain pass 臨界点が存在する

ただし μ_2^* は $-\Delta_N$ の第2固有値をあらわす。Polyá-Szegö の等周不等式から $|\Omega|\mu_2^* \le \ell^2\pi$、$\ell = 1.841...$ であり $0 < a \ll 1$ では $\lambda_1 < 4\pi$ となることに注意。

最後は解の安定性に関する示唆に富む定理である。

定理 3 Ω : 単連結とすると $\delta > 0$ が存在して各 $\lambda \in (4\pi, 4\pi + \delta)$ に対し $a > 0$ が十分小さければ *(8)* のすべての解 $v(x)$ の線形化作用素 $A_\lambda(v)$ は負の固有値をもつ

これらの定理から (8) の解の構造に関する [3] の数値計算に基づく予想の精密化、特に隠された解の存在が得られ、またそれにより (5) の解の挙動に関する新しい示唆が得られた ([14])。

3　ゲージ理論の物理と数理:エピローグ

(8) には2次元 Euler 流の vortex points に関する統計力学 (propagation of chaos) および常温超伝導に関する Chern-Simons-Higgs のゲージ理論 (multivortices の発生) が関連する ([1], [9], [16])。実際最終的に前者は有界領域 $\Omega \subset \mathcal{R}^2$ 上の

$$-\Delta v = \lambda e^v / \int_\Omega e^v \quad \text{in} \quad \Omega, \qquad v = 0 \quad \text{on} \quad \partial\Omega \qquad (9)$$

に、後者は flat torus $\Omega = \mathcal{R}/a\mathcal{Z} \times b\mathcal{Z}$ 上の

$$-\Delta v = \lambda \left(\frac{e^v}{\int_\Omega e^v} - \frac{1}{|\Omega|} \right) \quad \text{in} \quad \Omega, \qquad \int_\Omega v = 0 \qquad (10)$$

に帰着される。ここでは後者について簡単に描写しておきたい。

この理論は anyon model とよばれ、その condensate (multi-vortex) 解が常温超伝導等、いろいろな分野で関心を集めているものである。数学的に

は (2 + 1)-Minkowski 空間での古典場の理論であって、Lagrangean はスカラー (Higgs) 場、Yang-Mills (Maxwell) 場、および Chern-Simons ゲージ場の coupling である。最後の Chern-Simons 項が電磁 charge の multi-vortices (anyon) を発生させていると考えられる。

このままでは Euler-Lagrange 方程式が複雑であるから Yang-Mills 項を取り除いたもの (reduced Abelian Chern-Simons-Higgs 系) の condensate 解を考えるがこれは large distances と low energies で正当とされている。さらに Taubes らの古典的な vortex 理論と同様の方法により、複素変数を用いると定常 vortex 解のみたすべき方程式系が Bogomoln'y 型の self-dual なものとなるように Higgs ポテンシャルを選ぶことができる。このようにして得られたものは全平面 $\mathcal{R}^2$ における 2 階の非線形楕円型方程式で ground state な解として確かに symmetric vacuume が現れている。

この方程式において electric charge や magnetic charge が量子化された解が topological solution であり、non-topological solution ではこれらが fractal である。どちらも Spruck, Yang, Wang, Jackiw, Lee, Weinberg 達によってその存在が証明された。

'tHooft の周期条件下でも同様な議論ができる。Higgs 項の零点を指定し Chern-Simons の coupling 定数 $k > 0$ を十分小さくしたとき multi-vortex 解が存在することが Caffarelli と Yang により証明されている。[16] は変分法により mountain pass type の第 2 の解の存在を証明しそれが $k \downarrow 0$ に収束した極限で (10) をみたしていることをつきとめた。したがってこの方程式 (10) の解の構造がすべて明らかになれば、第 2 の multi-vortex 解の性質やその（多重）存在の問題は明確になる。[16] は (9) に関する [15] に対応する結果（一意性）を想定したが、その後の研究でこの点に関しては両者は著しく相違していることがわかってきている。

本講演後夜半に至り著者は原因不明の腹痛及び下痢に襲われ、翌朝緊急に入院して研究会の参加者や主催者に大変ご心配をおかけしました。ここにお詫びとともに地域の方々に謝意を表するものです。

参考文献

[1] Caglioti, E., Lions, P.L., Machioro, C., Pulvirenti, M., *A special class of stationary flows for two-dimensional Euler equations: a statistical mechanics description*, Comm. Math. Phys. **143** (1992) 401-425; **174** (1995) 229-260

[2] Childress, S., *Chemotactic collapse in two dimensions*, in; Lecture Notes in Biomath. **55**, Springer, 1984, pp.65-66

[3] Childress, S., Percus, J.K., *Nonlinear aspects of chemotaxis*, Math. Bios. **56** (1981) 217-237

[4] Herrero, M.A., Velázquez, J.J.L., *Singularity patterns ina chemotaxis model*, Math. Ann. **306** (1996) 583-623

[5] Herrero, M.A., Velázquez, J.J.L., *Chemotaxis collaplse for the Keller-Segel model*, J. Math. Biol. **35** (1996) 177-194

[6] Herrero, M.A., Velázquez, J.J.L., *A blow-up mechanism for a chemotaxis model*, Ann. Scoul. Norm. Sup. Pisa IV **35** (1997) 633-683.

[7] Jäger, W., Luckhauss, S., *On explosions of solutions to a system of partial differential equations modelling chemotaxis*, Trans. Amer. Math. Soc. **329** (1992) 819-824

[8] Keller, E.F., Segel, L.A., *Initiation of slime mold aggregation viewed as an instability*, J. Theor. Biol. **26** (1970) 399-415

[9] Kiessling, M.K.-H., *Statistical mechanics of classical particles with logarithmic interactions*, Comm. Pure Appl. Math. **46** (1993) 27-56

[10] Nagai, T., *Blow-up of radially symmetric solutions to a chemotaxis system*, Adv. Math. Sci. Appl. **5** (1995) 581-601

[11] Nagai, T., Senba, T., Suzuki, T., *Concentration behavior of bolow-up solutions for a simplified system of chemotaxis*, preprint

[12] Nagai, T., Senba T., Yoshida, K., *Application of the Trudinger-Moser inequality to a parabolic system of chemotaxis*, Funckcjal. Ekvc. **40** (1997) 411-433

[13] Nanjundiah, V., *Chemotaxis, signal relaying, and aggregation morphology*, J. Theor. Biol. **42** (1973) 63-105.

[14] Senba, T., Suzuki, T., *Some structures of the solution set for a stationary system of chemotaxis*, preprint

[15] Suzuki, T., *Global analysis for a two-dimensional elliptic eigenvalue problem with the exponential nonlinearity*, Ann. Inst. Henri Poincaré, Analyse no linéaire **9** (1992) 367-398.

[16] Tarantello, G., *Multiple condensate solutions for the Chern-Simons-Higgs theory*, J. Math. Phys. **37** (1996) 3769-3796

A Numerical Analysis of Time-Dependent Schödinger Equation and Quantum Chaos

H. Igarashi, T. Yoshikawa and T. Honma

Graduate School of Engineering, Hokkaido University

Kita 13, Nishi 8, Kita-ku, Sapporo, 060, Japan

Abstract

This paper describes a numerical analysis of the time-dependent Schrödinger equation (TSE) governing the dynamics of an electron which ballistically moves in single electron devices. The numerical methods considered here are the finite difference method (FDM) with the explicit central difference scheme, and Trotter-Suzuki method (TSM). In the TSM the exponential function of space differential operator, which is the formal solution of the TSE, is approximately evaluated by eigenvalue analysis. The FDM is shown to be conditionally stable when applied to the TSE. On the other hand, the TSM, which computes the time evolution of the wave function by multiplication of unitary matrices, is unconditionally stable. The convergence of the TSM of the lowest order is shown to be slower than that of FDM when their spatial approximation is identical. The numerical results show that the wave function of an electron in a stadium-shaped domain forms complex spatial patterns, which suggest the quantum chaos.

1   Introduction

Solids have two characteristic length: the inelastic scattering length l_{in} and elastic one l_e. The former is the characteristic length for which electrons are scattered by lattice vibration. If the scale of a solid is smaller than l_{in}, which strongly depends on temperature, electrons can move through the solid without losing its phase information. In this situation electrons interfere with each other so that the quantum effects due to this electron coherency can experimentally be observed. On the other hand, l_e, usually shorter than l_{in}, concerns the elastic scattering of electrons by impurities and lattice defect. Nowadays

devices smaller than l_e can be produced by the micro electronics. In such micro-devices electrons can ballistically move as if they were in vacuum. Under these situations electrons behaves as individual particles rather than collective whose property is described by the band theory. Since the engineering applications of this new state are expected to open a door to novel semiconductor devices, considerable attention has been paid on this research topic.

The motion of an electron in the ballistic regime is expected to well be described by the Schrödinger equation for single electron. For this reason the devices which operate in the ballistic regime are called single electron devices or nanoscale devices. The electric properties such as conductivity of the single electron devices immersed in magnetic fields have extensively been investigated, e.g., [1, 2] since they provide useful data for the study of the quantum chaos.

The behavior of a ballistic electron in magnetic fields has been analyzed by the boundary and finite element methods [3, 4] provided that the system under consideration is in steady states. In these analyses electrons are treated as waves so that the uncertainty of the position of the electron is infinity.

In this paper motions of a wave packet, which stands for an electron having dual properties of wave and particle, are numerically analyzed taking effects of magnetic fields into account. Transient behavior of the electron wave packet is computed by numerically solving the time-dependent Schrödinger equation.

Since electron wave packets are usually modulated by waves whose wavelength is much shorter than the wave-packet width, the distance between space grids must be much shorter than the wave-packet width. The resultant matrix, therefore, is expected to become too large for implicit schemes. For this reason the Schrödinger equation is here solved by two explicit methods : the finite difference method (FDM) with the central difference scheme, and the Trotter-Suzuki method (TSM) [5, 6] based on matrix expansion. The performance of the two methods is compared by computing motions of a wave packet in a rectangular and stadium-shaped domain connected with electron waveguides. Finally chaotic behavior of an electron wave packet in the stadium is graphically displayed.

2　Formulation

Let us consider an electron in a uniform magnetic field, confined in a two-dimensional region spanned by coordinates system (x, y). The dynamics of the electron is governed by the time-dependent, two-dimensional Schrödinger equation

$$i\hbar \frac{\partial \psi}{\partial t} = -\frac{(-i\hbar \nabla + e\boldsymbol{A})^2}{2m}\psi, \tag{1}$$

where ψ is the wave function, A is magnetic vector potential, and m is the effective mass of the electron. Equation (1) is written in a non-dimensional form as

$$\frac{\partial \psi}{\partial t} = i\alpha(\nabla + i\beta A)^2 \psi, \tag{2}$$

where ∇, t and A are normalized by length d, period T corresponding to the electron energy, and $B_0 d$, B_0 is applied magnetic field, and $\alpha = \hbar T/(2md^2)$, $\beta = eB_0 d^2/\hbar$. The constant α, which determines the electron's energy, can further be rewritten using the relationships $2\pi\hbar/T = \hbar^2 k^2/(2m)$ as

$$\alpha = \frac{2\pi}{(kd)^2}, \tag{3}$$

where k denotes the wavenumber of the electron.

2.1 Finite Difference Method

By employing the central difference approximation at a time step n, we have an explicit scheme

$$\begin{aligned}
\psi_0^{n+1} &= \psi_0^{n-1} + 2i\alpha\frac{\delta}{\Delta^2}(\psi_1^n + \psi_2^n + \psi_3^n + \psi_4^n - 4\psi_0^n) \\
&\quad -\alpha\beta\frac{\delta}{\Delta}[(A_x\psi)_1^n - (A_x\psi)_3^n + (A_y\psi)_2^n - (A_y\psi)_4^n \\
&\quad + A_{x0}(\psi_1^n - \psi_3^n) + A_{y0}(\psi_2^n - \psi_4^n)] \\
&\quad -i\delta\alpha\beta^2 A_0^2\psi_0^n,
\end{aligned} \tag{4}$$

where δ and Δ denote the time-step and grid sizes, and indices 0, 1, 2, 3, 4 represent the grid points (i,j), $(i+1,j)$, $(i-1,j)$, $(i,j+1)$, $(i,j-1)$, respectively.

2.2 Trotter-Suzuki method

In this method we begin with the formal solution of (2) which can be regarded as a first order differential equation with respect to time,

$$\psi(t) = e^{it\alpha(\nabla + i\beta A)^2}. \tag{5}$$

Note that the exponent in (5) is an operator. From (5) it follows that

$$\psi(t + \delta) = e^{i\delta\alpha(\nabla + i\beta A)^2}\psi(t), \tag{6}$$

for which we introduce approximation in the following. The operator in the exponent in (6) is now decomposed into two components as

$$(\nabla + i\beta A)^2 = Q_1 + Q_2, \tag{7}$$

where

$$Q_i = \frac{\partial^2}{\partial x_i^2} + i\beta \left[\frac{\partial}{\partial x_i} A_i + A_i \frac{\partial}{\partial x_i} \right] - \frac{1}{2}\beta^2 A_i^2, \tag{8}$$

$i = 1, 2$ correspond to x and y, respectively. Introduction of the central difference approximation in space for Q_1 yields

$$Q_1 = \begin{bmatrix} -\frac{2}{\Delta^2} - \frac{\beta^2 A_{x,1}^2}{2} & \frac{1}{\Delta^2} + i\beta a_1 & 0 & \cdots \\ \frac{1}{\Delta^2} - i\beta a_1 & -\frac{2}{\Delta^2} - \frac{\beta^2 A_{x,2}^2}{2} & \frac{1}{\Delta^2} + i\beta a_2 & \cdots \\ 0 & \frac{1}{\Delta^2} - i\beta a_2 & -\frac{2}{\Delta^2} - \frac{\beta^2 A_{x,3}^2}{2} & \cdots \\ \vdots & \vdots & \vdots & \ddots \end{bmatrix}, \tag{9}$$

where $a_i = (A_{x,i} + A_{x,i+1})/(2\Delta)$, and Q_2 is expressed in matrix form in a similar manner. We can see that the matrix Q_i is Hermitian so that $e^{i\delta\alpha(Q_1+Q_2)}$ is unitary. We further decompose Q_i into two components in the form

$$Q_1 = \begin{bmatrix} M_1 & 0 & \cdots \\ 0 & M_3 & \cdots \\ \vdots & \vdots & \ddots \end{bmatrix} + \begin{bmatrix} \xi_1 & 0 & \cdots \\ 0 & M_2 & \cdots \\ \vdots & \vdots & \ddots \end{bmatrix}, \tag{10}$$

where the Hermitian matrix M_i is defined by

$$M_i = \begin{bmatrix} \xi_i & \eta + i\zeta_i \\ \eta - i\zeta_i & \xi_{i+1} \end{bmatrix}, \tag{11}$$

$\xi_i = -1/\Delta^2 - \beta^2 A_{x,i}^2/4$, $\eta = 1/\Delta^2$ and $\zeta_i = \beta a_i$. The first and second matrices in (10) will be denoted by Q_{11} and Q_{12}, respectively, and matrices Q_{21} and Q_{22} are defined from Q_2 likewise.

Now we have a product formula for the amplitude factor in (6), i.e.,

$$e^{i\delta\alpha(\nabla+i\beta\boldsymbol{A})^2} \simeq e^{i\delta\alpha\sum_{i,j} Q_{i,j}}$$
$$\simeq \prod_{i,j} e^{i\delta\alpha Q_{ij}}, \tag{12}$$

where i and j run from 1 to 2. The matrix $e^{i\delta\alpha Q_{11}}$ in (12) can be evaluated by performing eigenvalue analysis as follows:

$$e^{i\delta\alpha Q_{11}} = \begin{bmatrix} e^{i\delta\alpha M_1} & 0 & \cdots \\ 0 & e^{i\delta\alpha M_3} & \cdots \\ \vdots & \vdots & \ddots \end{bmatrix}, \tag{13}$$

where

$$e^{i\delta\alpha M_i} = \frac{e^{i\delta\alpha u_i}}{\lambda} \begin{bmatrix} \lambda\cos\gamma - iv_i\sin\gamma & (\zeta_i - i\eta)\sin\gamma \\ -(\zeta_i + i\eta)\sin\gamma & \lambda\cos\gamma + iv_i\sin\gamma \end{bmatrix}, \tag{14}$$

$u_i = (\zeta_i + \zeta_{i+1})/2$, $v_i = (\zeta_i - \zeta_{i+1})/2$, $\gamma = \lambda\delta\alpha$ and $\lambda = \sqrt{\eta^2 + \zeta_i^2 + v_i^2}$. Similarly $e^{i\delta\alpha Q_{ij}}$ for $\{1,2\}, \{2,1\}, \{2,2\}$, can easily be evaluated. In conclusion the time evolution of ψ is computed from (6) and (12)-(14). Note that since $e^{i\delta\alpha M_i}$ is unitary, the resultant amplitude factor (12) for this method is always unitary.

2.3 Numerical stability

Theoretical analysis of numerical stability of the finite different scheme (4) is not easy because it contains the vector potential which is a function of position, and because the boundary condition would affect on the stability. When both effects are neglected, we can apply von Neumann's analysis to (4). That is, assuming the form $\psi^n(x,y) = \varphi^n e^{i(k_x x + k_y y)}$ in (4), we obtain

$$\varphi^{n+1} + 2i\Lambda\varphi^n - \varphi^{n-1} = 0, \tag{15}$$

where Λ is defined by

$$|\Lambda| = 4\alpha\frac{\delta}{\Delta^2}\left[\sin^2\left(\frac{k_x\Delta}{2}\right) + \sin^2\left(\frac{k_y\Delta}{2}\right)\right]. \tag{16}$$

From (15) it follows that $\varphi^{n+1} = c\varphi^n$, where $c = (-\Lambda i \pm \sqrt{-\Lambda^2 + 1})$. It can be seen that $|c| = 1$ if $\Lambda \leq 1$ while $|c| > 1$ if $\Lambda > 1$. Hence (4) is concluded to be conditionally stable. The stability condition for Λ can then be evaluated to have

$$8\alpha\frac{\delta}{\Delta^2} \leq 1. \tag{17}$$

(In contrast the diffusion equation in which $i\alpha$ in (4) is replaced by α is proved to be unconditionally instable for the scheme (4).) As mentioned above, this result is valid provided that the effects of magnetic field and boundary conditions are negligible. In the next section the stability of (4) will numerically be evaluated.

On the other hand, the Torotter-Suzuki method, in which the amplitude factor (12) is unitary, guarantees unconditional stability being independent from the effects of magnetic field and boundary conditions.

3 Numerical Results

3.1 Numerical model

Figure 1 depicts the numerical model under consideration. A wave packet goes into a domain Ω after passing through an electron waveguide. The uniform magnetic field is assumed to be applied only on Ω. On the walls of the domain and waveguide the boundary condition $\psi = 0$ is imposed. In the analysis the wavenumber k of the electron, which determines the electron's energy, is always taken to be $10/d$. The wave packet in the waveguide is assumed to be expressed by

$$\psi = e^{(-y^2/2d^2 + iky)}\sin[\pi(x + d/2)]. \tag{18}$$

The Fourier transform of (18) gives

$$\psi = \frac{d}{\sqrt{2\pi}}\int_{-\infty}^{\infty} e^{-d^2(k'-k)^2/2}e^{ik'y}dk'\sin[\pi(x + d/2)], \tag{19}$$
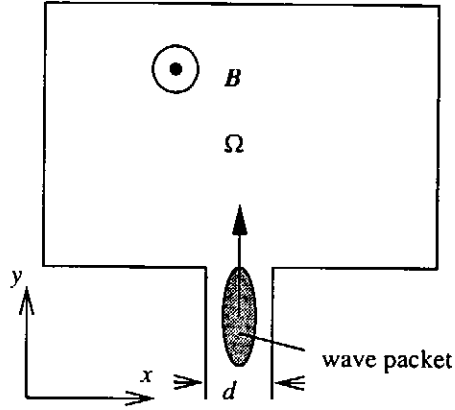
Figure 1: A wave packet moving into domain Ω

from which we can see that the Fourier spectrum has also the Gaussian form with a peak at k in wavenumber space. It can be shown that the wavenumber k must be well larger than π/d for propagation [1]. Moreover the grid space Δ is required to be well smaller than the wavelength $2\pi/k$ for numerical analysis. These requirement leads to extremely dense finite difference grids so that implicit schemes are thought to be ineffective for the numerical solutions.

3.2 Rectangular domain

The motion of a wave packet which is ejected from a waveguide and moves in the rectangular domain shown in Fig. 1 is analyzed by FDM and TSM. This model has been analyzed by the boundary element method [7]. In this analysis, the steady electron probability density is computed by solving the time-independent Schrödinger equation on the basis of the wave picture of electrons. According to this result, the electron behaves like a classical particle moving in magnetic field, that is, its motion resembles the Larmor gyration.

Figure 2 illustrates the time evolution of the probability density $\psi\psi^*$ computed by FDM. It can be seen that the locus of the wave packet, which has the duality of particle and wave, is strongly bent by the magnetic field to form the semi-circles, which suggest the Larmor gyration as seen in the steady state computation mentioned above. Moreover, when the wave packet bounds on the domain wall, there appear interference fringes due to the wave character of the electron. The further computation of the time evolution of this wave packet shows that it gradually diffuses in space. The numerical stability of FDM for this model is shown in Fig. 3. One observes that the increase in either δ or β makes the computations instable. Moreover, under this computational condition the marginal value
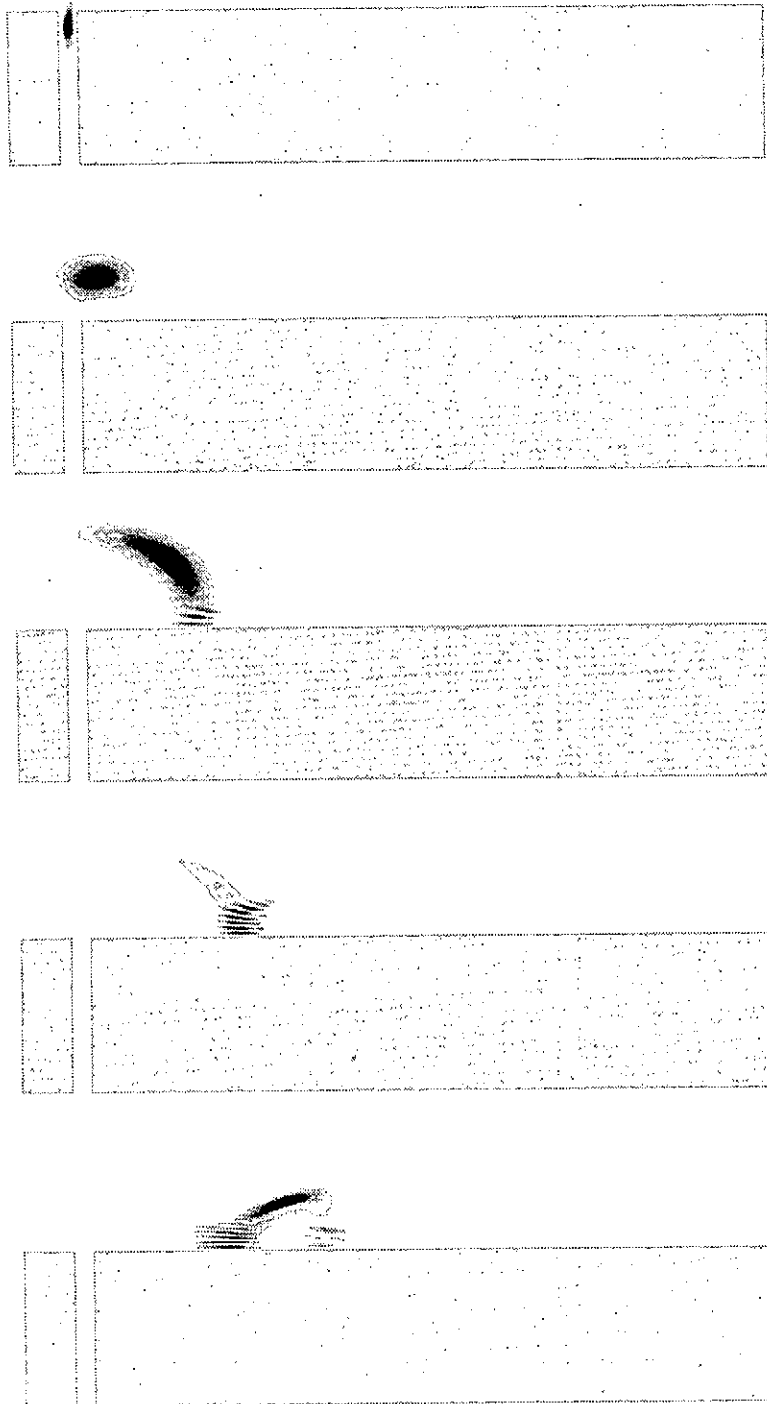
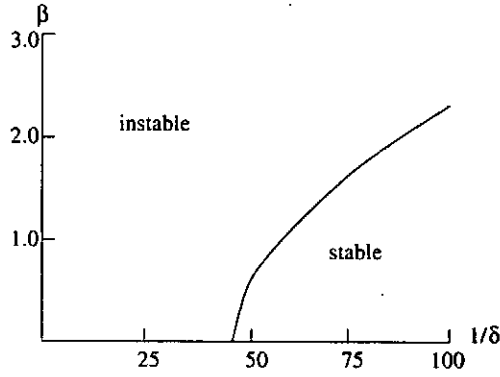Figure 2: Time evolution of probability density computed by FDM, $\beta = 2.0, \Delta = 1/19, \delta = 1/300$

Figure 3: Numerical stability diagram for FDM ($\Delta = 1/9$)

for $1/\delta$ is evaluated from (17), that is

$$
\begin{aligned}
1/\delta &= \Delta^2/8\alpha \\
&= (kd\Delta)^2/16\pi \\
&\simeq 40.7,
\end{aligned}
\tag{20}
$$

for $\beta = 0$, which agrees with the result shown in Fig. 3. On the other hand the unconditional stability of TSM was confirmed by numerical experiments.

Table I displays convergence of the numerical solutions, measured by the normalized error defined by

$$
\varepsilon(\psi,\psi_0) = \frac{\sum_j (\psi_j - \psi_{0j})(\psi_j - \psi_{0j})^*}{\sum_j \psi_{0j}\psi_{0j}^*}.
\tag{21}
$$

The error ε is evaluated for $\beta = 2.0$, $\Delta = 1/19$ at $t = 29/3$. In table I, $\varepsilon(\text{FDM} - \text{FDM})$ means $\varepsilon(\psi,\psi_0)$, where ψ and ψ_0 are computed by FDM, and ψ_0 is computed for the minimum δ, i.e., $1/1200$. We use the same rule for $\varepsilon(\text{TSM} - \text{TSM})$ and $\varepsilon(\text{TSM} - \text{FDM})$. That is, the first two errors measure the convergence of each numerical scheme, and the last error measures the distance between the solutions computed by the two methods. We can see from Table I that the convergence of FDM is significantly better than that

Table I: Convergence for rectangular domain model

$1/\delta$	$\varepsilon(\text{FDM} - \text{FDM})$	$\varepsilon(\text{TSM} - \text{TSM})$	$\varepsilon(\text{TSM} - \text{FDM})$
300	6.2×10^{-4}	9.1×10^{-1}	9.7×10^{-1}
600	1.2×10^{-4}	4.3×10^{-1}	8.1×10^{-1}
900	1.0×10^{-5}	9.2×10^{-2}	6.2×10^{-1}
1200	-	-	4.8×10^{-1}

of TSM. Lax's theorem guarantees that if FDM solution converges then the converged solution is the exact solution. Thus $\varepsilon(\text{TSM} - \text{FDM})$ would be regarded as a measure of the errors in TSM.

The computing time for FDM was more than two times shorter than that of TSM. This can be understood by comparing (4) with (6) and (12). That is, the latter requires four steps of computations at each time step while the former requires just one step.

3.3 Stadium-shaped domain

The motion of a wave packet in a stadium-shaped domain is analyzed. The time evolution of the probability density of an electron, computed by FDM, is shown in Fig.4. The wave packet is ejected from the left hand side of the stadium where no magnetic field is imposed. We clearly observe the interference fringe patterns due to reflection of the waves from the wall. The distribution gradually becomes very complicated. The further computation shows the more complicated patterns which consist of a number of small islands whose distribution seems to be random. These results are thought to suggest the quantum chaos.

Figure 5 shows the time evolution of the probability density in the stadium where magnetic field is imposed. The locus of the wave packet is bent to collide with the wall. The complexity of the pattern in Fig. 5 seems to be lower than that in Fig. 4. This suggests that the magnetic field has a tendency to suppress the appearance of the quantum chaos.

Table II displays the convergence of the numerical methods for the stadium-shaped domain when $\beta = 0.6$, $t = 50/3$. Although FDM solution converges rapidly also in this case, TSM seems to require more fine time-step size for convergence.

4 Conclusions

In this paper ballistic electron motions under magnetic fields have been analyzed by numerically solving the time-dependent Schrödinger equation. The two explicit numerical methods, FDM and TSM, have been chosen for the analysis. Although FDM is shown

Table II: Convergence for stadium-shaped domain model

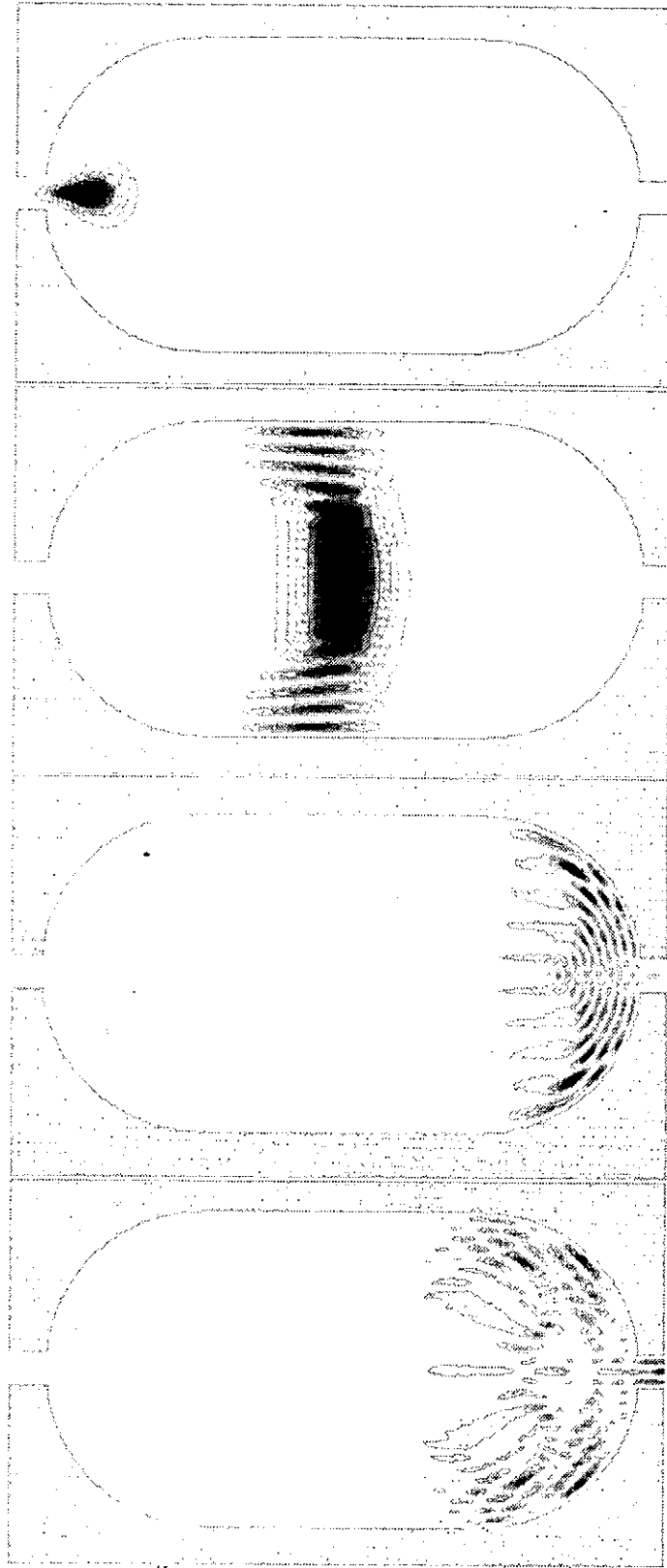| $1/\delta$	$\varepsilon(\text{FDM} - \text{FDM})$	$\varepsilon(\text{TSM} - \text{TSM})$	$\varepsilon(\text{TSM} - \text{FDM})$
300	1.4×10^{-4}	9.9×10^{-1}	9.9×10^{-1}
600	4.5×10^{-5}	7.9×10^{-1}	9.8×10^{-1}
900	9.2×10^{-6}	2.8×10^{-1}	9.3×10^{-1}
1200	-	-	8.5×10^{-1}

Figure 4: Time evolution of electron probability density in a stadium without magnetic field, $\beta = 0.0, \Delta = 1/19, \delta = 1/300$
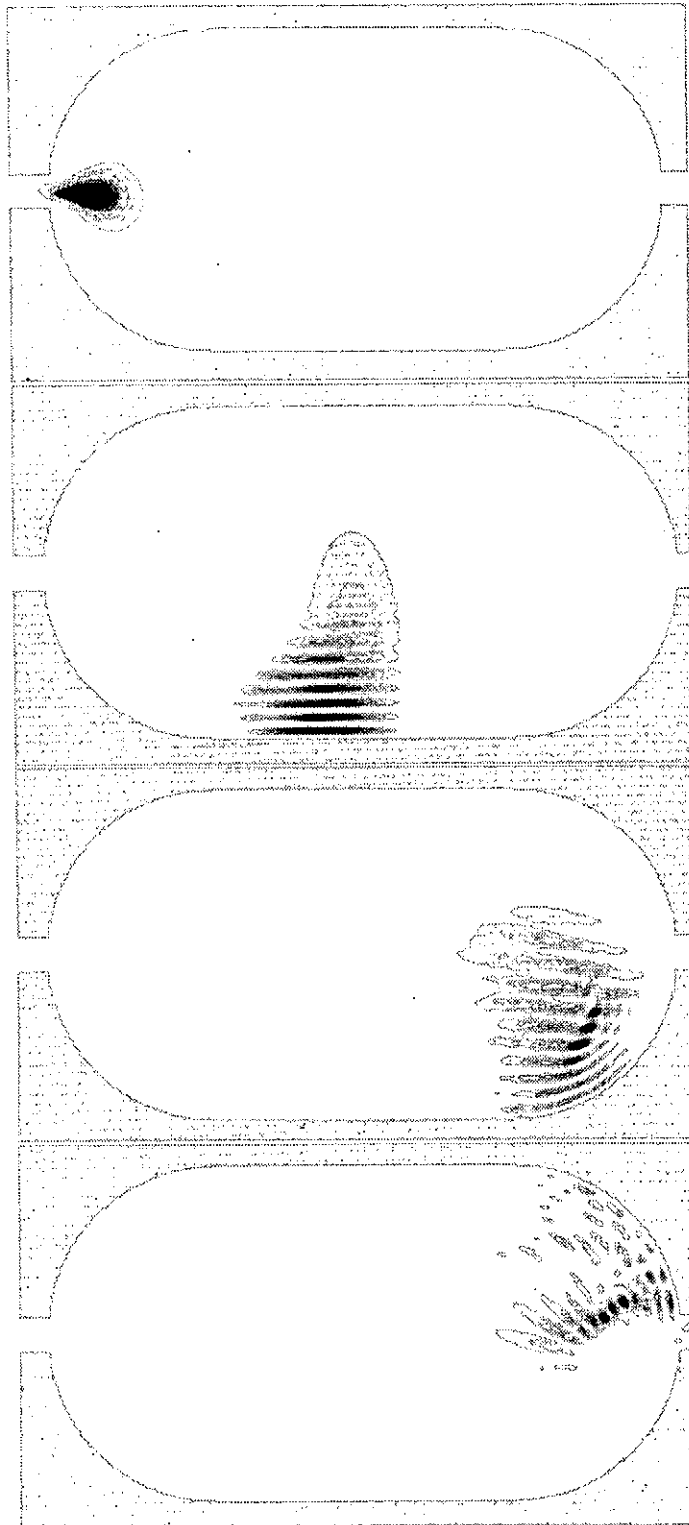
Figure 5: Time evolution of electron probability density in a stadium with magnetic field, $\beta = 0.6, \Delta = 1/19, \delta = 1/300$

to be conditionally stable by theory and numerical experiment, TSM is confirmed to be unconditionally stable, as expected from theory. FDM is superior to TSM of the lowest order used here from view points of convergence and computing efficiency. The accuracy of TSM could be improved by using a symmetric formula in the approximation (12) [5, 8]. This technique, however, increases computational cost.

The pattern of the distribution function of an electron in the stadium-shaped domain suggests the quantum chaos. The magnetic field has a tendency to suppress the chaotic motion of the electron.

References

[1] R.L. Schult, H.W. Wyld and D.G. Ravenhall, "Quantum Hall effects and general narrow-wire circuits" *Phys. Rev. B*, **41**, (1990), 12760-12780.

[2] C.M. Marcus, R.M. Westervelt, P.F.Hopkins and A.C.Gossard, " Phase breaking in ballistic quantum dots: Experiment and analysis based on chaotic scattering", *Phys. Rev. B*, **48**, (1993), 2460-2464.

[3] K.Nakamura, K.Ito and Y.Takane, "Magnetoconductance in open stadium billiard", *J. Phys. Soc. Japan*, **63**, (1994), 1320-1323.

[4] Y.Wang, J.Wang and H.Guo *Phys. Rev. B*, **49**, (1994), 1928-1933.

[5] H.D. Raedt, "Product formula algorithm for solving the time dependent Schrödinger equation", *Computer Phys. Report*, **7**, (1987), 1-72.

[6] H. Natori and T. Munehisa, "Time dependent Schrödinger equations with vector potentials -Numerical calculations and visualizations", *J. Phys. Soc. Japan*, **66**, (1997), 351-359.

[7] T. Ueta, "Boundary element method for electron waves in uniform magnetic fields", *Engineering Analysis with Boundary Elements*, **17**, (1996), 69-74.

[8] H. De Raedt, "Quantum dynamics in nanoscale devices", in *Computational Physics*, eds. K. H. Hoffmann and M. Schreiber, Springer, Berlin, (1996), 209-224.

Multivalent Property of Charged Particle Trajectory Estimation by Using Lienard-Wiechert Superpotentials

Hideki KAWAGUCHI

Div. Systems & Information Eng., Graduate School of Eng., Hokkaido University
Kita 13, Nishi 8, Kita-ku, Sapporo 060, Japan

Abstract

The Lienard-Wiechert potentials can be derived from its superpotentials. Then a special kind of the superpotentials have a clear physical meaning as the source particle coordinates. It was shown that, to use the concept of the Lienard-Wiechert superpotentials, the charged particle trajectory can be estimated from the electromagnetic fields produced by the moving particle. In that work, the main interest was to show the possibility of the source particle trajectory estimation, so some ideal situations were assumed there, for example exact field value measurement, single point source particle, etc. For these assumptions, this paper discusses influence of measurement error and source particle bunching in the estimation procedure. The consideration is done by a numerical method because the time domain measurements of the electromagnetic radiation fields are still very difficult technology. It is found that the estimation method is tough for the measurement error but seriously affected from particle bunching.

Keywords : Lienard-Wiechert potentials, superpotentials, trajectory estimation

INTRODUCTION

One of the authors introduced a concept of the Lienard-Wiechert superpotentials which was derived from consideration on the particle retarded time and positions [1]. Then, the superpotentials had a clear physical meaning as the source particle coordinates. After that it was also shown that, to use the concept of the Lienard-Wiechert superpotentials, the charged particle trajectory can be estimated from the electromagnetic fields produced by the moving particle [2][3]. In that work, the main interest was to show the possibility of the source particle trajectory estimation, so some ideal situations were assumed there, for example exact field value measurement, single point source particle, etc. To reconsider these assumptions, this paper discusses influence of measurement error and source particle bunching in the estimation procedure. The consideration is done by a numerical method because the time domain measurements of the electromagnetic radiation fields are still very difficult technology.

CONCEPT OF LIENARD-WIECHERT SUPERPOTENTIALS AND ELECTRON TRAJECTORY ESTIMATION

Electromagnetic fields produced by moving charged particles are described by the Lienard-Wiechert potentials.

$$\phi(t,x) = \frac{e}{4\pi\varepsilon_0} \frac{1}{R(t_r) - \frac{R(t_r)\bullet v(t_r)}{c}} \tag{1}$$

$$A(t,x) = \frac{e}{4\pi\varepsilon_0 c^2} \frac{v(t_r)}{R(t_r) - \frac{R(t_r)\bullet v(t_r)}{c}} \tag{2}$$

c is the velocity of the light, ε_0 is the dielectric constant, $v(t)$ is the particle velocity and $R(t) = x - y(t)$ is the displacement vector from a source particle position $y(t)$ to an observation point x. All the value of the right hand side are evaluated at the retarded time t_r, which is defined by,

$$t_r = t - \frac{|x - y(t_r)|}{c} \tag{3}$$

Accordingly, the retarded time t_r is a function of the observation coordinates t and x.

$$t_r = t_r(t, x) \tag{4}$$

and the retarded position $y(t_r)$ as well (Fig.1). This causality relation contains essential characteristics of the Lienard-Wiechert potentials, for example, complex spatial and frequency structures of the synchrotron radiation are understood by appearance of the properties of this relation. Concerning on the causality relation, a concept of the Lienard-Wiechert superpotentials is introduced as follows [1],

$$\Box t_r(t,x) = \frac{8\pi\varepsilon_0}{ec} \phi(t,x) \tag{5}$$

$$\Box y(t_r(t,x)) = \frac{8\pi\varepsilon_0 c}{e} A(t,x) \tag{6}$$

$\Box$ denotes the D'Alembert operator. The retarded time and position are "potentials of the Lienard-Wiechert potentials". Here one find analogy with the inhomogeneous wave equation for the scalar and vector potentials in Eqs.(5) and (6),
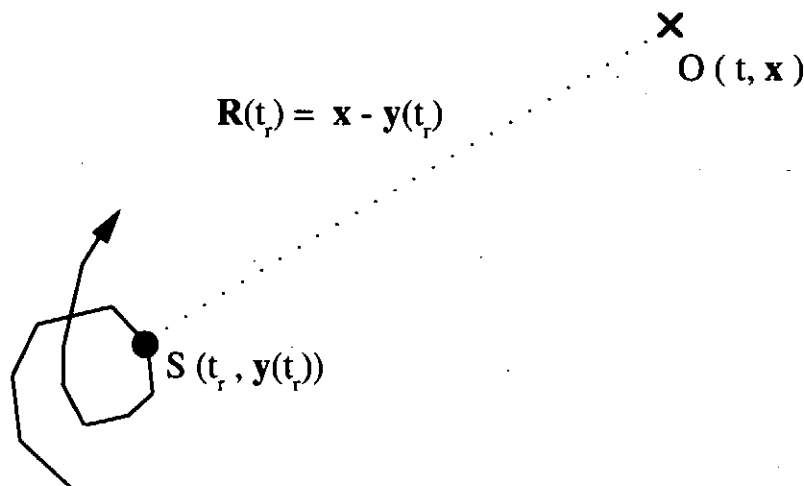

Fig.1 Moving particle and retarded time

$$\Box \, t_r \, (t,x) \; = \; \frac{8\pi\varepsilon_0}{ec} \, \phi \, (t,x) \tag{7}$$

$$\Box \, A(t,x) \; = \; \frac{1}{\varepsilon_0 c^2} \, J \, (t,x) \tag{8}$$

This analogy shows us a possibility of a charged particle trajectory estimation method from electromagnetic fields. To solve Eqs.(7) and (8) means to obtain the functions t_r and $y(t_r)$ from $\phi(t)$ and $A(t)$ and it is just estimation of the particle trajectory from the electromagnetic fields. This kind of estimation is indeed possible but achieved in a slightly different way [2][3]. Firstly, we shall explicitly express the function $y(t_r)$ by the observation coordinates t and x as follows,

$$y \, (t,x) \; = \; y_0 \, (t,x) + \frac{1}{\pi} \sum_{n=1}^{\infty} \frac{1}{n} \int_0^{2\pi} \sin\left[n\left(\omega t - \sigma - \omega\frac{|x - y\,(\sigma)|}{c}\right)\right] dy\,(\sigma) \tag{9}$$

On the other hand, the Fourier expansion of for the electric field corresponding to this motion is

$$E \, (t,x) \; = \; \frac{-e\omega^2}{4\pi^2\varepsilon_0 c^2}\frac{1}{|x|} \sum_{n=1}^{\infty} n \left[\frac{\omega}{c} \frac{x}{|x|} \int_0^{2\pi} \sin\left[n\left(\omega t - \sigma - \omega\frac{|x - y\,(\sigma)|}{c}\right)\right] d\sigma \right.$$
$$\left. - \int_0^{2\pi} \sin\left[n\left(\omega t - \sigma - \omega\frac{|x - y\,(\sigma)|}{c}\right)\right] \frac{dy\,(\sigma)}{d\sigma} d\sigma \right] \tag{10}$$

These two functions are also expressed in the following forms,

$$y \, (t,x) \; = \; y_0 \, (t,x) + \frac{1}{\pi} \sum_{n=1}^{\infty} \frac{1}{n} \, g_n(t,x) \tag{11}$$

$$E \, (t,x) \; = \; \frac{-e\omega^2}{4\pi^2\varepsilon_0 c^2}\frac{1}{|x|} \sum_{n=1}^{\infty} n \left[\frac{x}{|x|}\left(g_n(t,x)\bullet\frac{x}{|x|}\right) - g_n(t,x) \right] \tag{12}$$

where the vector function $g_n(t,x)$ are defined as follows,

$$g_n \, (t,x) \; \equiv \; \int_0^{2\pi} \sin\left[n\left(\omega t - \sigma - \omega\frac{|x - y\,(\sigma)|}{c}\right)\right] \frac{dy\,(\sigma)}{d\sigma} d\sigma \tag{13}$$

If we ignore the first term of Eq.(11),

$$y_\perp \, (t,x) \; = \; y_0 \, (t,x) + \frac{4\pi\varepsilon_0 c^2}{e\,\omega^2} \, |x| \sum_{n=1}^{\infty} \frac{1}{n^2} \, E_n(t,x) \tag{14}$$

where $y_\perp$ is the perpendicular component of y to the normal vector $x / |x|$ and E_n denote the n-th harmonic component of the function E,

$$E \, (t,x) \; = \; \sum_{n=1}^{\infty} E_n(t,x) \tag{15}$$

The relation (14) are obtained by comparison of each Fourier component of Eqs.(11) and (12) (See Fig.2). Then, $y_\perp$ is regarded as a projected trajectory of true 3D trajectory to a perpendicular plane to

x / |**x**| . Accordingly, if we observe the electric field on three axes at a distance, the Fourier components of each observation data give us the Fourier component of projections of the 3D particle trajectory to each coordinate planes (Fig.3). Therefore, the projected trajectories to the coordinate planes are calculated summarizing up all the Fourier components and 3D true trajectory can be reconstructed from the projected trajectories. Consequently, we get the particle trajectory estimation method based on the concept of the Lienard-Wiechert superpotentials. (To do the concrete trajectory estimation, some more data processing are required, cf. the treatment of the first term of Eq.(11) (see Ref.[2][3] for the details).)

DISCUSSION ON PRACTICAL SITUATION AND NUMERICAL SIMULATION

In the above trajectory estimation procedure, some ideal situations are assumed, especially
 - exact electric far field measurement
 - single charged particle motion

To make the estimation scheme approach to practical one, the following modifications are required for the measurement data

$$\mathbf{E}(t,\mathbf{x}) \;\rightarrow\; \mathbf{E}(t,\mathbf{x}) + \mathbf{e}(t,\mathbf{x}) \tag{16}$$

$$\mathbf{E}(t,\mathbf{x}) \;\rightarrow\; \sum_i \mathbf{E}^i(t,\mathbf{x}) \tag{17}$$

where $\mathbf{e}(t,\mathbf{x})$ is random measurement error which is much smaller than $\mathbf{E}(t,\mathbf{x})$ and $\mathbf{E}^i(t,\mathbf{x})$ is the electric field produced by i-th particle. For the modification (16), Eq.(15) becomes

$$\mathbf{E}(t,\mathbf{x}) = \sum_{n=1}^{\infty} \mathbf{E}_n(t,\mathbf{x}) + \sum_{n=1}^{\infty} \mathbf{e}_n(t,\mathbf{x}) \tag{18}$$

Then it can be predicted that most of components of $\mathbf{e}_n(t,\mathbf{x})$ are concentrated to comparably higher n because of the random function. Accordingly, we can expect that the measurement error will not seriously affect to the estimated trajectory. On the other hand, if the charged particles have the Gaussian bunch distribution, the superposed electric field (17) loses the higher harmonics components comparing with the wave length equal to the bunch length.

$$\mathbf{E}(t,\mathbf{x}) = \sum_{i=1}^{\infty} \mathbf{E}^i(t,\mathbf{x}) \approx \sum_{n=1}^{n_c} \mathbf{E}_n(t,\mathbf{x}) \tag{19}$$
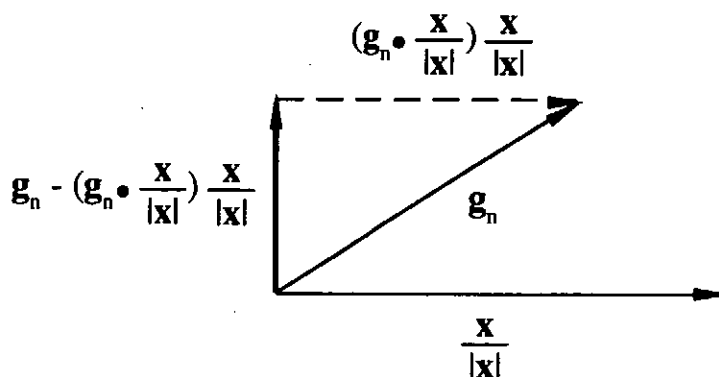

Fig.2 Vector function $\mathbf{g}_n(t,\mathbf{x})$ and projection

where n_c is roughly defined as $n_c \omega = 1 / \sigma$ (ω is fundamental frequency of the particle motion, σ is bunch length). This means that a large amount of information may be lost from the superposed field. The above considerations are also confirmed by numerical simulations. The figures 4(a) and (b) are estimated and original trajectory for circular motion with the ideal situation and Figs.5(a) and (b) are for helically circulating motion. The velocity of the particle for all the cases is taken to be 95% of the light velocity. On the other hand, Figs.6(a) and (b) are for circular motion with 3% and 1% Gaussian random measurement error respectively and Figs.7(a) and (b) are for the helically circulating motion. And for the case of Gaussian bunch particles, the estimation is was impossible even for the bunch length = 0.1% of the total trajectory path. The projected trajectories are in Figs.8. One find inconsistency between the projected trajectories.

SUMMARY

This paper has discussed influence of measurement error and source particle bunching in an particle trajectory estimation procedure based on the Lienard-Wiechert superpotentials. It is found that the estimation method is tough for the measurement error but seriously affected from particle bunching.

REFERENCES

[1] H.Kawaguchi and S.Murata, J. Phys. Soc. Japan **58[3]**, (1989) 848-855.
[2] H.Kawaguchi and T.Honma, J. Phys. A: Math. Gen. **25**, (1992) 4437-4442.
[3] H.Kawaguchi and T.Honma, J. Phys. A: Math. Gen. **26**, (1993) 4431-4439.
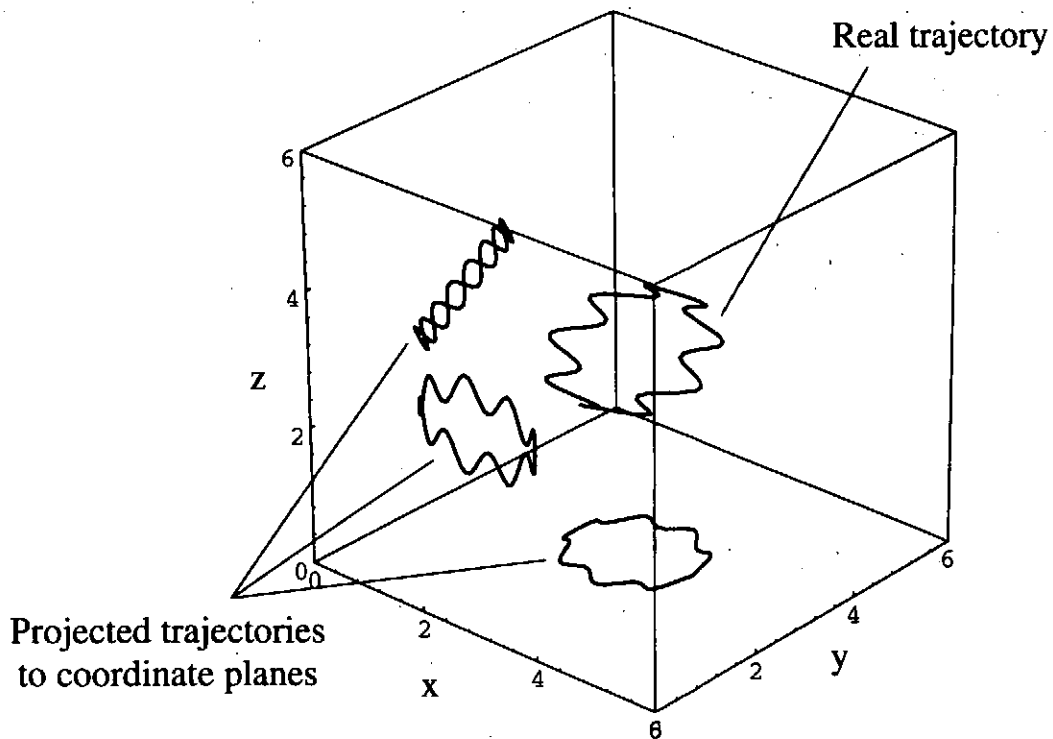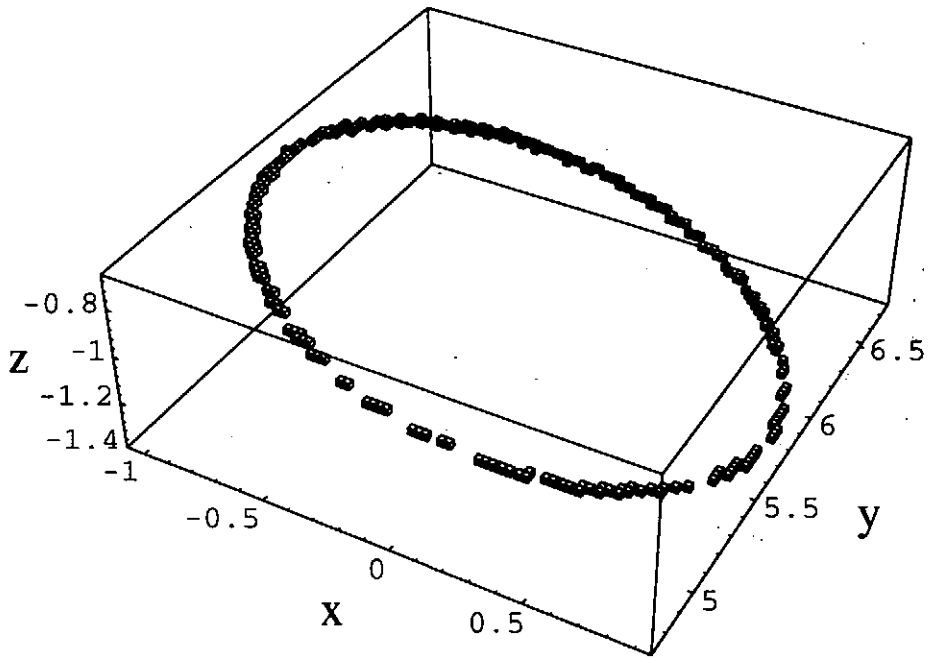
Fig.3 Real 3D trajectory and projected one

Fig.4(a) Estimated trajectory for circular motion with ideal situation
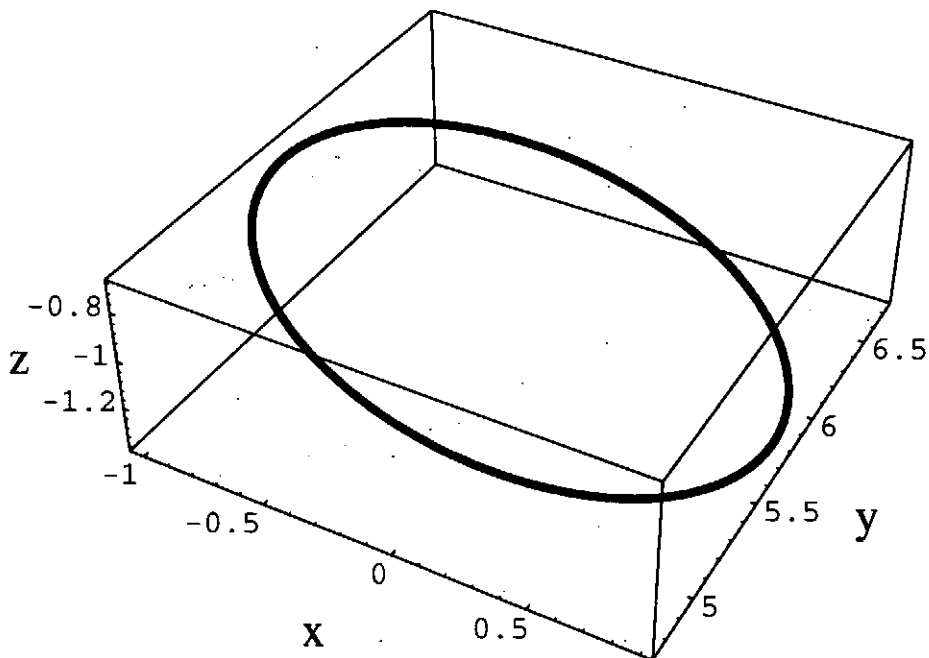

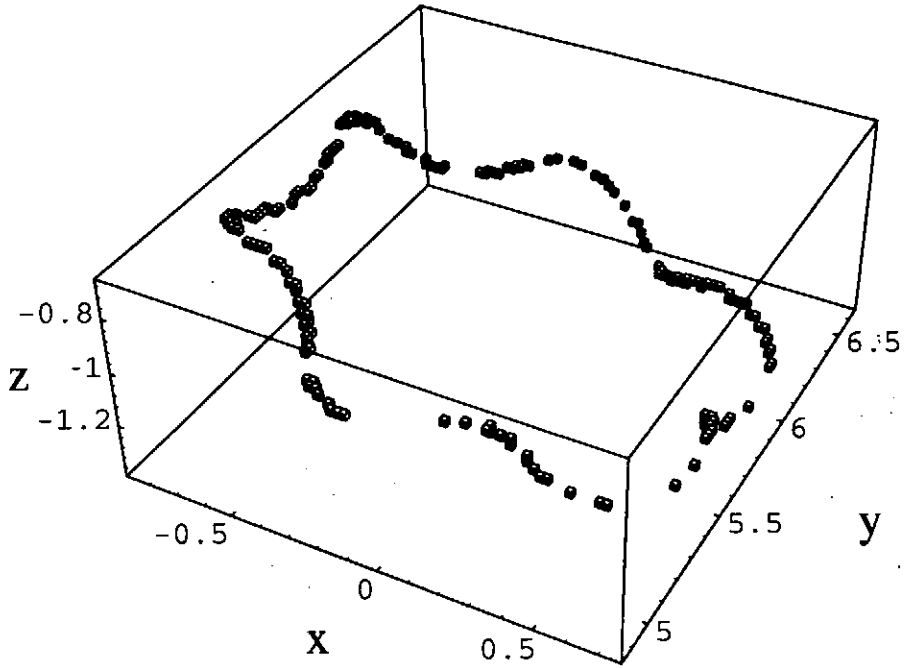Fig.4(b) Original trajectory for circular motion with ideal situation

Fig.5(a) Estimated trajectory for helically circulating motion with ideal situation
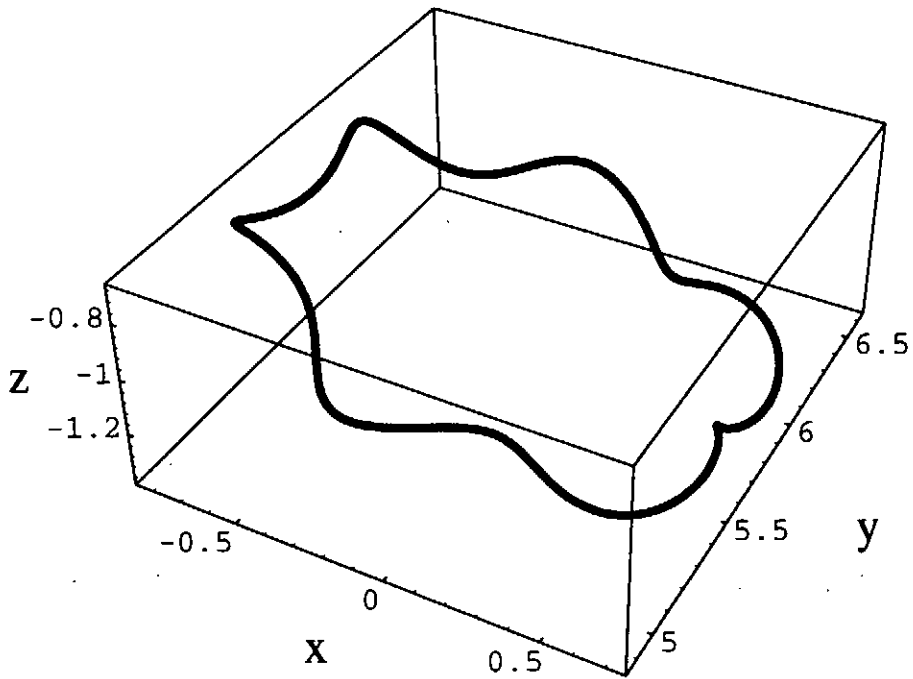

Fig.5(b) Original trajectory for helically circulating motion with ideal situation
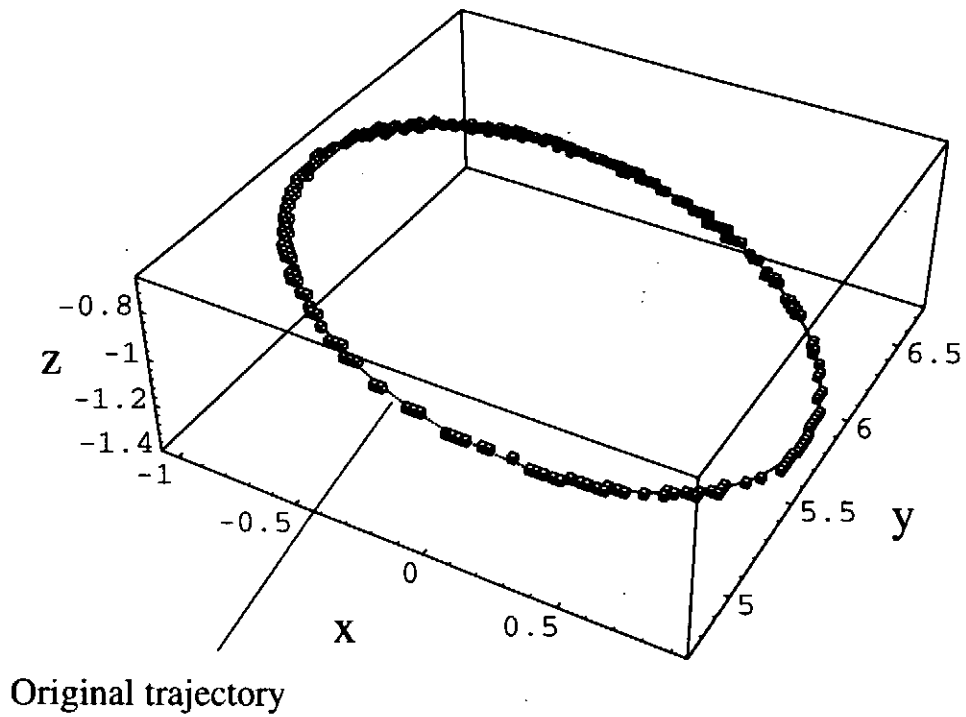
Original trajectory

Fig.6(a) Estimated trajectory for circular motion with 3% Gaussian random measurement error

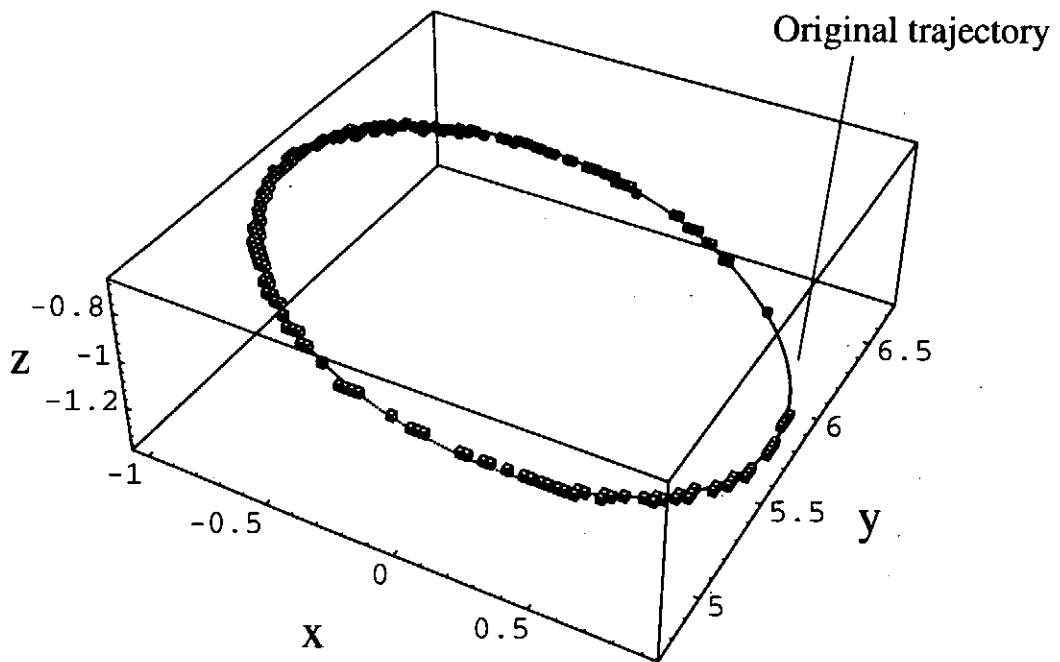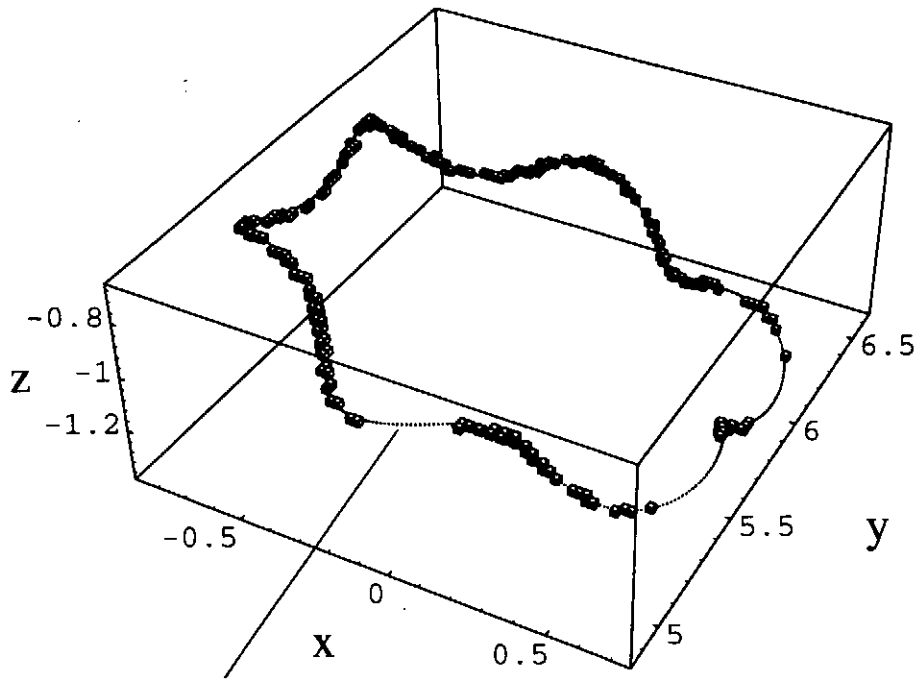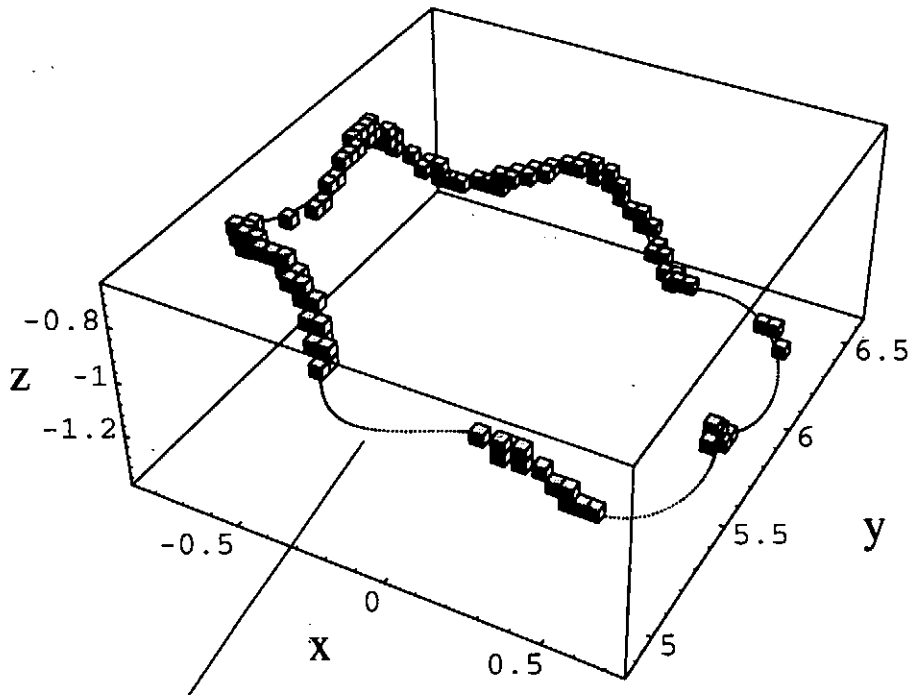Fig.6(b) Estimated trajectory for circular motion with 1% Gaussian random measurement error

Original trajectory

Fig.7(a) Estimated trajectory for helically circulating motion with 3% Gaussian random measurement error

Original trajectory

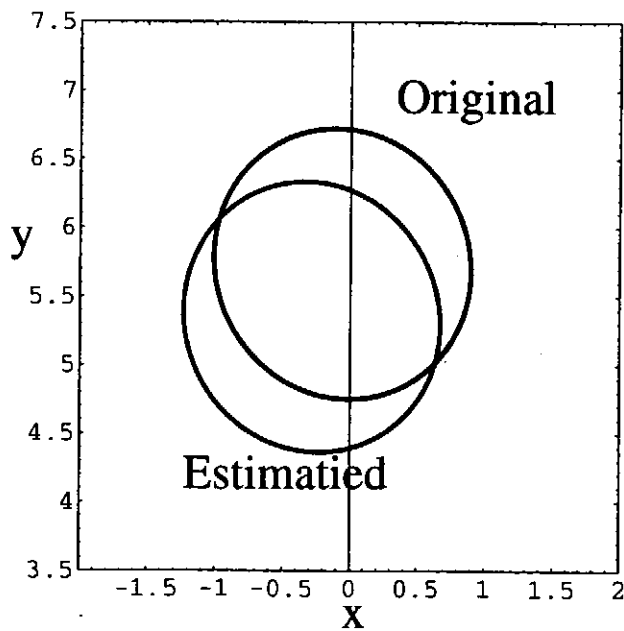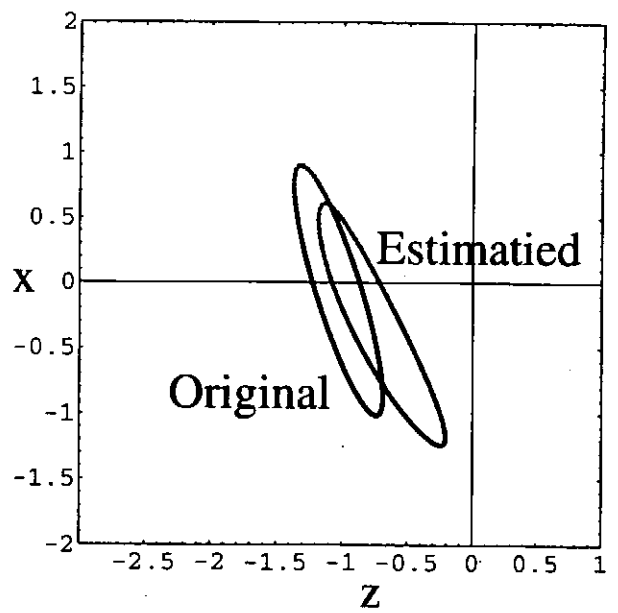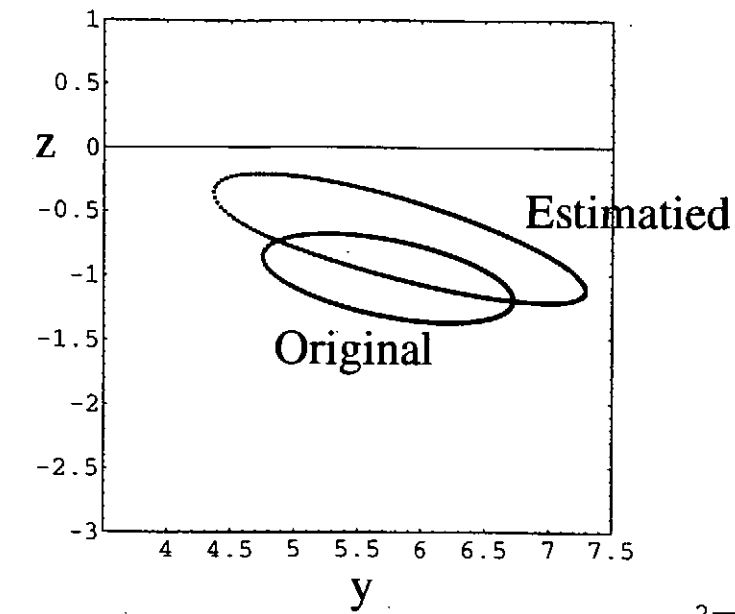Fig.7(b) Estimated trajectory for helically circulating motion with 1% Gaussian random measurement error

Fig.8   Projected trajectory for the case of Gaussian bunch particles

On the Treatment of Boundary in Incompressible Flow Simulation

Itaru Hataue

Department of Computer Science, Kumamoto University

Kurokami 2-39-1, Kumamoto, Kumamoto 860, Japan

Abstract

In the present study, we analyze the nonlinear qualitative structure of asymptotic numerical solutions calculated by solving the Navier-Stokes equations directly. Some kinds of finite difference schemes are applied to the incompressible Navier-Stokes equations. Explicit method and the well-known marker-and-cell(MAC) method are used. The model adopted in the present study is the flow around two-dimensional circular cylinder. The dependence of the temporal discretization parameter, Δt, and the dependence of 4th order artificial viscosity terms on structure of asymptotic numerical solutions are discussed. Nonlinear dynamics approaches are utilized in order to analyze the structure in detail. For the nonlinear dynamics approaches, time series of the drag coefficents are used. The attractors are reconstructed and classified into several types and the stability of each attractors are compared on the basis of several computational conditions.

Key Words: Numerical simulation, Unsteady incompressible flow, Nonlinear dynamics

1 Introduction

In this paper we want to analyze the characteristic behavior of quasi-steady state numerical solutions of the Navier-Stokes equations by utilizing the nonlinear dynamics approaches such as bifurcation diagram and so on. In the recent physical literature, there are numerous references about the computed chaotic behavior. However, chaotic solutions, even when true solutions of the original differential equation approach limit cycles or fixed points, are often obtained as a consequence of the omission of the local discretization errors in the transfer from the continuous differential equations to their discretized counterparts. They are often called spurious solutions or ghost solutions.[1-9] We investigated typical features of stable and unstable spurious asymptotes (periodic points, limit cycles, tori and chaotic motions) which are given by the discretizing some type of fundamental nonlinear differential equations, one- and two-dimensional Burgers' equations and the Lorenz equations.[8-9] In those reports, we studied the characteristic behavior of the asymptotic

numerical solutions of those nonlinear differential equations. In particular, we discussed the dependence of initial data and boundary conditions on the nonlinear instability. Though the structure of solutions becomes simple as the dimension of discrete dynamical system which corresponds to the number of spatial grid points increases, the spurious solutions appear in all of those cases. Even if we adopt the more accurate scheme, e.g. high-order Runge-Kutta scheme, the appearance of ghost solutions may be inevitable. As described above, the structure of the numerical solution is often complicated in the cases of scalar equations by the nonlinear instabilities even below the linear stability limit. By the way, how about the structure of the asymptotic numerical solution in the case of the system of fluid equations? Recent development of supercomputer has made it possible to calculate the complicated unsteady flow fields. Though direct numerical simulation results concerning the complicated unsteady flow structure, "numerical turbulence", are reported in many references, it has not been left unknown whethere this "numerical turbulence" corresponds to the true solutions of the original fluid equations or not. The correctness of the computed results are evaluated from the view point of comparison with experimental studies or physical intuition of researchers. In many cases, computed results are discussed by using the flow visualization technique, comparing the averaged $C_p(C_d$(drag coefficient), C_l(lift coefficient)) values with experimental data, calculating some statistical quantities and so on. Though these methods are usuful to discuss the simultaneous and global structure of the computed flow fields, most of those methods are not so effective that we can not elucidate their clear unsteady characteristics in detail. It is no doubt that most of the fruitful results by large computations are left untouched without adequate analyses in many cases. In this paper, we apply the nonlinear dynamics approaches which were used in the case of simple cases to analyses of the unsteady structure of numerical results of direct simulations of the practical fluid motions. Generally speaking, these analyses of the nonlinear structure are equivalent to studies of instability of dynamical system. In the present study, we adopted the flow around the circular cylinder as the simple model and discussed the difference of the structure in some cases of the low and high 4th order artificial viscosity terms. Furthermore, we try to analyze the dependence of the grid points on the calculation results of practical systems.

On the other hand, researchers in the field of computational fluid dynamics select the suitable scheme in order to get the physically reasonable results from many kinds of numerical schemes, e.g. incompressible and compressible ones, explicit and implicit ones and so on. The most popular schemes are some kinds of upwind schemes which stabilize the system. In our previous reports, we also discuss the dependence of some upwind schemes on the nonlinear structure of the asymptotic numerical solutions.[9] In the case of the upwind

spatial discretization, no spurious numerical solution appeared in some cases. However, we got many types of complicated spurious solutions in some other cases even when we used the high-order accurate upwind schemes. As for the practical computation of fluid motion, high order accurate upwind schemes usually applied and the reasonable solutions have been given. In some studies, the bifurcation scenario and the chaotic behaviour have been reported. In particular, Pullium et al. studied the nonlinear dynamical structure of the physical variable such as the velocity component in the subsonic flow around the airfoil by using the compressible scheme.[10] In that paper, they not only showed the bifurcation sequence but also evaluated the effect of the grid refinement and some numerical schemes. The main purposes of our paper are the comparison of influences of the schemes on the qualitative structure and to clarify dependence of the amplitude of 4th order artificial viscosity term on the asymptotic numerical solutions in the practical computation of fluid motion.

The numerical schemes used in the present paper, the incompressible one, are expressed briefly in Section 2. Other conditions of computations such as the grid systems, boundary conditions and so on are also discribed. In Section 3, the dependence of the amplitude of 4th order artificial viscosity term and grid points on the asymptotic numerical solutions are discussed. Furthermore, we evaluated the dimension of the attractors which are reconstructed from the time series of the C_d data and make the quatitative differences of the attractors clear.

2 Basic Equation and Numerical Algorithm

2.1 The incompressible Navier-Stokes equation

The non-dimensional governing the incompressible Navier-Stokes equations and the continuity equation are given as follows:

$$\text{div}\mathbf{V} = 0 \quad , \qquad \qquad ....(1)$$

$$\frac{\partial \mathbf{V}}{\partial t} + (\mathbf{V}\cdot \text{grad})\mathbf{V} = -\text{grad}p + \frac{1}{Re}\Delta\mathbf{V} \quad , \qquad \qquad ....(2)$$

where $\mathbf{V} = (u,v)$, p and Re denote velocity vector, pressure and the Reynolds number, respectively.

2.2 Numerical algorithm

The Poisson equation for pressure can be derived on the basis of marker-and-cell(MAC) method.[11]

$$\Delta p = -\text{div}(\mathbf{V}\cdot \text{grad})\mathbf{V} + R \quad , \qquad \qquad ....(3)$$

where

$$R = -\frac{\partial D}{\partial t} + \frac{1}{Re}\Delta D \quad , \quad D \equiv \mathrm{div}\mathbf{V} \quad .$$

In the present study, we employed the generalized transformation of coordinates, $(x, y) \rightarrow (\xi, \eta)$, then we get the transformed Poisson equation as follows:

$$\widetilde{\Delta}p = -\frac{(y_\eta u_\xi - y_\xi u_\eta)^2 + 2(x_\xi u_\eta - x_\eta u_\xi)(y_\eta v_\xi - y_\xi v_\eta) + (x_\xi v_\eta - x_\eta v_\xi)^2}{J^2}$$

$$-\frac{y_\eta u_\xi - y_\xi u_\eta + x_\xi v_\eta - x_\eta v_\xi}{J\Delta t} \quad , \qquad \dots (4)$$

where J is the Jacobian of transformation. The Poisson equation is solved using SOR scheme. For the time marching of the Navier-Stokes equations, simple Euler forward scheme and second order improved Euler scheme are considered. All spatial derivatives except for those of the nonlinear convection terms are discretized by using the central finite difference. For those of the convection terms, we considered parameter ε in order to discuss the effects of 4th-order artificial viscosity term,

$$f\frac{\partial u}{\partial \xi} = \frac{f_i(-u_{i+2} + 8u_{i-1} - 8u_{i+1} + u_{i-2})}{12\Delta\xi}$$

$$+\varepsilon\frac{\mid f_i \mid (u_{i+2} - 4u_{i-1} + 6u_i - 4u_{i+1} + u_{i-2})}{4\Delta\xi^4} \quad . \qquad \dots (5)$$

Eq. (5) is based on the third-order upwind schemes[12]. In the present paper in which the two-dimensional generalized coordinates are used, ε_ξ shows the parameter for ξ-direction and ε_η for η-direction, respectively.

2.3 Grid systems

The O-type grid systems are used in all cases. The body surface corresponds to $K = 1$, the circle of which radius is equal to 1. Outer flow region corrsponds to $K = KMAX$, the circle of which radius is set to from 30 to 35. The mesh points are strongly concentrated in the boundary-layer and the minimum spacing normal to the surface of the body is set to be less than $\frac{0.1}{\sqrt{Re}}$ or $\frac{0.05}{\sqrt{Re}}$ (fine grid case).

2.4 Boundary conditions

The boundary conditions on the body surface are as follows: The no-slip condition is used for the velocity components. At the far boundaries, the free-stream values are specified.

3 Results and Discussion

The sampling period of the time series of C_d is from T(non-dimensional time)=400 to 500. In this period, we can regard the flow fields as the quasi-steady state. As it is well-known from a lot of historical studies, the larger the Reynolds number becomes, the more complicated the flow field becomes. At Re=2000, the flow field is still periodic. We compared several characteristics of structure of quasi-steady flow field on the basis of nonliniear dynamics approaches such as the three-dimensional profiles of attractor which are reconstructed from the time series of C_d data. We got some asymptotic solutions such as limit cycles and so on for different parameter ε. Figure 1 is the comparison of the typical characteristics of structure of attractors given from the time series of C_d. We can classify these asymptotic solutions on the casis of the qualitative features of reconstructed attractors by using the nonlinear dynamics approaches. Figure 2 is the dynamic regimes which shows the basin of asymptotic numerical solutions. In the cases of quite low ε value, the profile of time series of C_d becomes non-periodic and the structure of solutions looks like the one which is often given in the calculations for the higher Reynolds number case. Therefore, if we used the upwind scheme, there is possibility that we may get the ghost solutions. From this figure, the region of each attractor looks to be separated. However, it is shown these solutions depends on the initial condition sensitively. Figure 3 shows the dynamic regimes of attractors which are given from the calculations from the different initial data which have been given in other calculations. In this figure, attractors from the different initial data are shown by different symbols. It can be seen that the types of attractors sensitively change by using the different initial data. This result shows that the stability of these numerical solutions are almost same and they coexist even in the same ε value case. When we performed the calculation under the hard condition of convergency for the Poisson equation for pressure, we got other different types of attractors, Therefore, we suppose that this fact of coexistence of the asymptotic solutions sensitively depends on the degree of convergency of the Poisson equation for pressure. On the other hand, we studied the influences of grid points. In the fine grid cases shown in figure 4, it becomes a little hard to see these ghost structure. This shows that these characteristics sensitively depend on the treatment of the bounday conditions. Characteristics of the flow fields can be easily given by the contour plots of physical variables such as the pressure, velocity components, vorticity and so on. However, clear differences between the some periodic motions can not be found from these approaches. What we want to emphasize is that we can not realize the unsteady spurious structure only from the instantaneous global structure of the flow field. Therefore, in addition to the conventional approaches, we must use the nonlinear
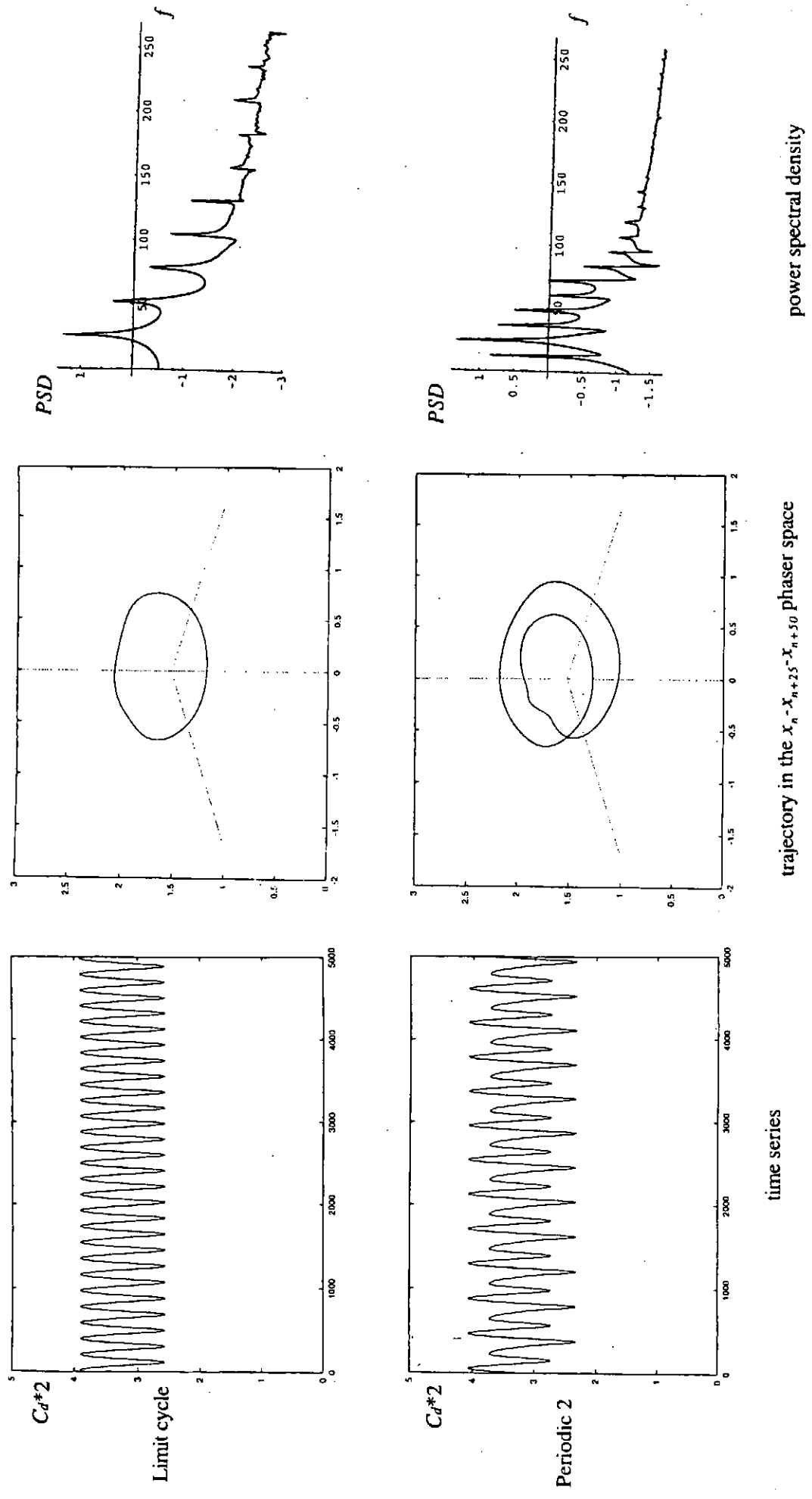
Fig.1 Typical characteristics of structure of attractors given from the time series of C_d. (Re=2000)

power spectral density

trajectory in the x_n-x_{n+25}-x_{n+50} phaser space

time series
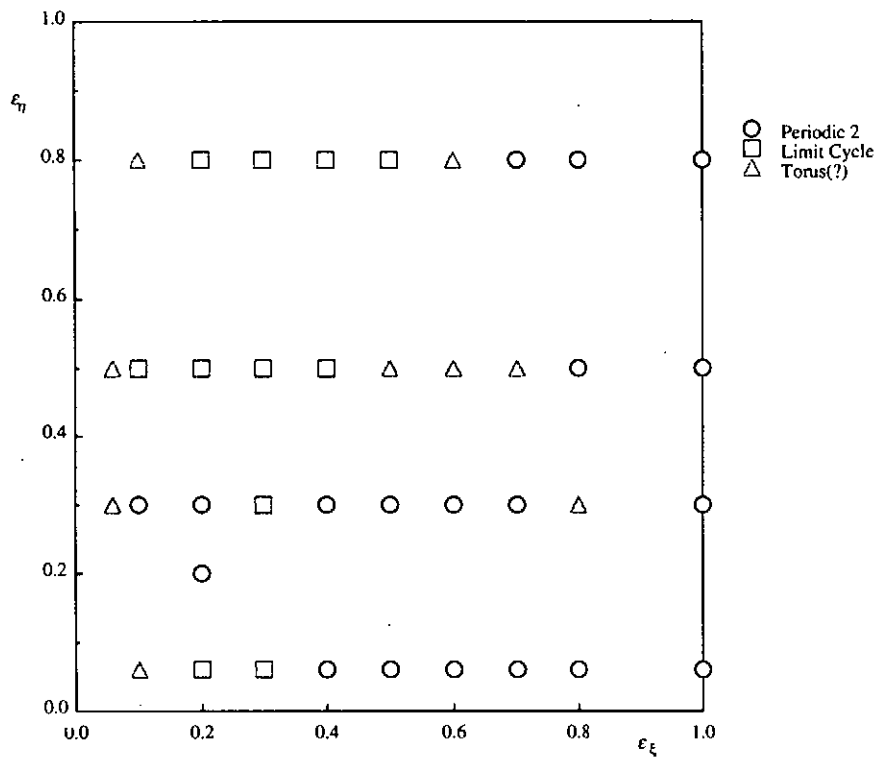
Fig.2 Plotted points shows the dynamic regimes in the case of standard grid points case.

Fig.3 Sensitive dependence of initial data on the types of attractor.

Fig.4 Plotted Points shows the dynamic regimes in the case od fine grid case.

dynamics approaches in order to discuss the unsteady structure of asymptotic numerical solutions.

4 Conclusions

The supercomputer and the development of visualization technique have made it possible to simulate the complicated phenomenon such as flow motions as if they were open before our eyes actually. However, on the other hand, the strong nonlinearlity of the computational discrete dynamical system still makes it difficult to make the com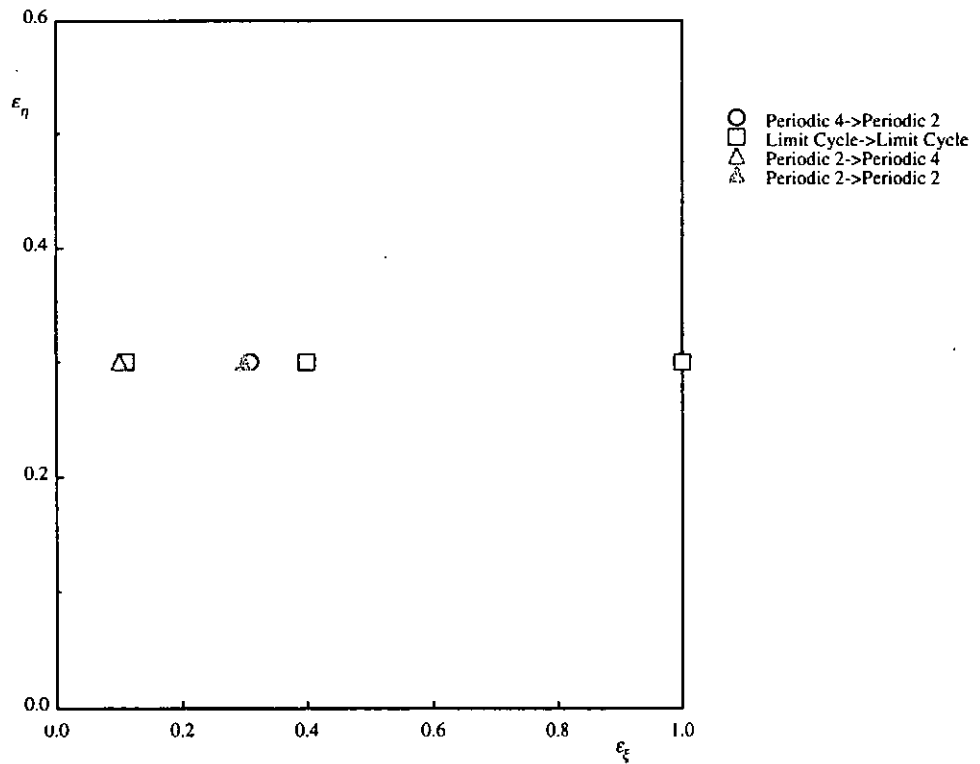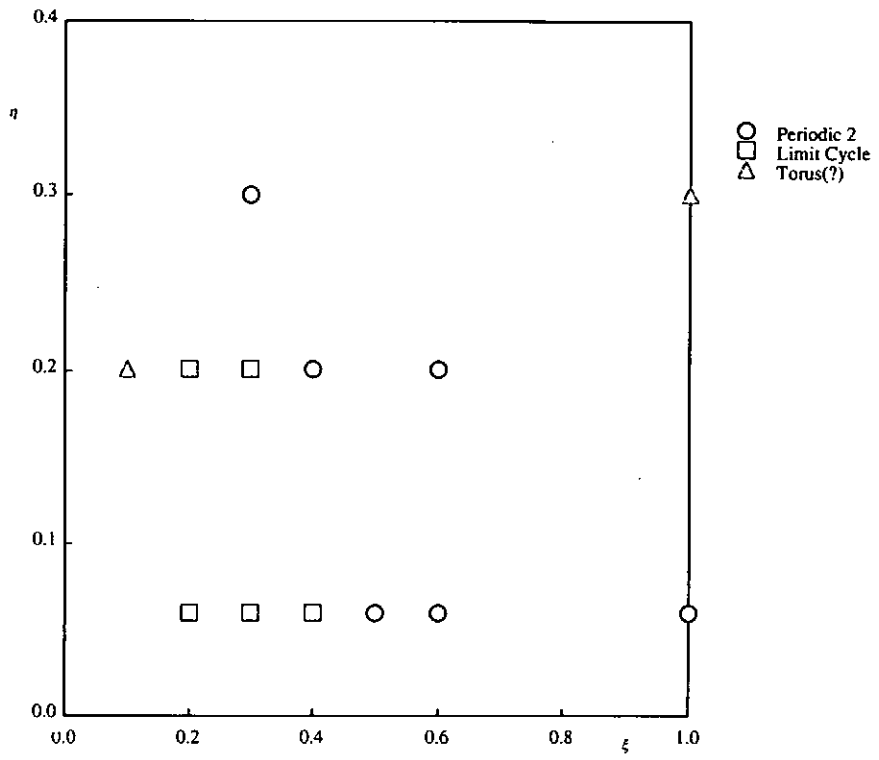puted results reliable as shown in the appearance of the spurious numerical solutions. In the present study, we showed the spurious numerical solutions appear not only in the cases of low-dimensional simple nonlinear differential equations such as the Burgers' equation and so on, but also appear in the multi-dimensional and system equations such as the flow equations. In order to discuss the reliability of their numerical solutions, since only the usual methods used in the common analyses in the field of computational fluid dynamics is not adequate, we need more effective methods to analyze the complicated unsteady structure of the numerical solutions in detail. We proposed some nonlinear dynamics approaches which are used in the fields of mathematics, theoretical and experimental physics and so on. To study the characteristics of attractors which were constructed by the computed time series of C_d at the quasi-steady state can not only make the differences of the unsteady structure clear but also give us the important information about the convergence speed to the steady state. We discussed the dependence of the 4th order artificial viscosity terms on the structure of the numerical asymptotic solution. It is shown that some strange phenomenon occur when we use the small ε values. If the adequate convergence condition of the Poisson equation of the pressure was not attained in each time step, we may get the non-diverging numerical solutions which never appear actually. As described above, we must pay much attention to the selection of suitable schemes and the descretized parameters in order to the physically reasonable results.

References

1) Stuart, A.: Nonlinear instability dissipative finite difference schemes, *SIAM Review*, **31**(1989), pp.191-220.

2) Lorenz, E. N.: Computational chaos-A prelude to computational instability, *Physica D*, **35-3**(1989), pp.299-317.

3) Yee, H. C. , Sweby, P. K. and Griffiths, D. F.:Dynamical approach study of spurious

steady-state numerical solutions of nonlinear differential equations. I. The dynamics of time discretization and its implications for algorithm development in computational fluid dynamics, *J. Comput. Phys.*, **97**(1991), pp.249-310.

4) Griffiths, D. F., Sweby, P. K. and Yee, H. C.:On spurious asymptotic numerical solutions of explicit Runge-Kutta methods, *IMA J. Num. Anal.*, **12**(1992), pp.319-338.

5) Lafon, A. and Yee, H. C.:On the numerical treatment of nonlinear source terms in reaction-convection equations, *AIAA Paper*,92-0419(1992).

6) Humphries, A. R. :Spurious solutions of numerical methods for initial value problems, *IMA J. Num. Anal.*, **13**(1993), pp.263-290.

7) Griffiths, D. F., Stuart, A. and Yee, H. C.:Numerical wave propagation in hyperbolic problems with nonlinear source terms, *SIAM J. Num. Anal.*, **29**(1992), pp.1244-1260.

8) Hataue, I.:Spurious numerical solutions in higher dimensional discrete systems, *AIAA J.*,**33**(1995), pp.163-164.

9) Hataue, I.:Ghost numerical solutions in upwind difference scheme and effects of linearization, *AIAA-Paper*,97-0870(1997).

10) Pullium, T. H. and Vastano, J. A.:Transition to chaos in an open unforced 2D flow, *J. Comput. Phys.*, **105**(1993), pp.133-149.

11) Harlow, F. H. and Welch, J. E.:Numerical calculation of time-dependent viscous incompressible flow of fluid with free surface, *Phys. Fluids*, **8**(1965), pp.2182-2189.

12) Kawamura, T. and Kuwahara, K. :Computation of high Reynolds number flow around a circular cylinder with surface roughness, *AIAA Paper*,84-0340(1984).

FEM-CSM Combined Method
for 2D Exterior Laplace Problem

USHIJIMA, Teruo
Department of Computer Science
and Information Mathematics
Faculty of Electro-Communications
The University of Electro-Communications

ABSTRACT

Consider the Poisson equation $-\Delta u = f$ in a planar exterior domain of a bounded domain $\mathcal{O}$. Assume that $f = 0$ in the outside of a disk with sufficiently large diameter. The solution u is assumed to be bounded at infinity. Discretizing the problem, we employ the finite element method (FEM, in short) inside the disc, and the charge simulation method (CSM, in short) outside the disc. Results of mathematical analysis for this FEM-CSM combined method are reported in this paper. The combined method is applicable to planar exterior reduced wave equations. Our discretization procedure for the reduced wave equation is also described

Keywords: two dimensional exteior Laplace problem, finite element method, charge simulation method, FEM-CSM combined method, reduced wave equation, Helmholtz equation, fundamental solution method, FEM-FSM combined method.

二次元外部ラプラス問題の FEM-CSM 結合解法

牛島　照夫　（電気通信大学　電気通信学部　情報工学科）

0. はじめに

二次元有界領域 $\mathcal{O}$ の外部で、例えば、ポアッソン方程式 $-\Delta u = f$ を考える。$\mathcal{O}$ を含む十分大きな円の外部では、$f = 0$ とし、u は遠方では有界調和なものとする。円の内部は、有限要素法 (FEM) で、円の外部は、代用電荷法 (CSM) で離散化する。この手法に関する数学解析の結果を報告する。

代用電荷法は、基本解近似法 (FSM) の一つである。この観点から、二次元外部ヘルムホルツ問題、すなわち、帰着波動問題の数値解法を構成出来る。その場合の離散化の手順を FEM-FSM 結合解法として、標題の報告に続いて報告する。

1. 円外有界調和関数にかかわるスチェクロフ型境界双一次形式

本結合解法の出発点となるのが本節標題事項である。ここで、円外有界調和関数にかかわる当該円周上での

スチェクロフ作用素とは、着目している有界調和関数の円周上での境界値を、そこでの法線方向微分係数に対応させる作用素である。法線の方向は、円板内部に向かうものである。スチェクロフ作用素は、円周上の L^2 空間における非負値自己共役作用素として実現される。対応する非負値エルミート形式 $b(u, v)$ を考えるのが自然である。

円周 Γ_a 上の実数値連続関数 $f(\mathbf{a}(\theta))$ が与えられているとする。$\mathbf{a}(\theta)$ は、複素数 $ae^{i\theta}$ に対応する。$f(\mathbf{a}(\theta))$ は、周期 2π の θ の関数である。円周 Γ_a の外部を Ω_e とする。**円周 Γ_a 上で f と一致し Ω_e で有界かつ調和な u を求める問題を $(\mathrm{E_f})$ で表す**：

$$(\mathrm{E_f}) \quad \begin{cases} -\Delta u = 0 & \text{in } \Omega, \\ u = f & \text{on } \Gamma_a, \\ \sup_{\Omega_e} |u| < \infty. \end{cases}$$

関数 f のフーリエ係数を a_n, b_n とする。すなわち、

$$a_n = \frac{1}{\pi} \int_{-\pi}^{\pi} f(\mathbf{a}(\theta)) \cos n\theta \, d\theta,$$

$$b_n = \frac{1}{\pi} \int_{-\pi}^{\pi} f(\mathbf{a}(\theta)) \sin n\theta \, d\theta,$$

$$(n = 0, 1, 2, \cdots)$$

とおく。問題 $(\mathrm{E_f})$ の解は唯一つ存在して、

$$u = u(\mathbf{r})$$

$$= \frac{1}{2}a_0 + \sum_{n=1}^{\infty} \{a_n \cos n\theta + b_n \sin n\theta\} \left(\frac{a}{r}\right)^n,$$

$$r > a$$

と表示される。この表示を用いて、前述のスチェクロフ作用素 Λ を、

$$\Lambda f = \sum_{n=1}^{\infty} \frac{n}{a} \{a_n \cos n\theta + b_n \sin n\theta\}$$

と無限級数表示することが出来る。級数の和に意味を持たせるためには、$f \in H^1(\Gamma_a)$ のような制限を設けることになる。ここで、一般に非負実数 s に対して

$$H^s(\Gamma_a) = \{f : \sum_{n=0}^{\infty} (1 + n^{2s})(a_n^2 + b_n^2) < \infty\}$$

とおいている。

一般に Γ_a 上の実数値可積分関数 v に対するフーリエ係数を $a_n(v), b_n(v), n = 0, 1, \cdots$、と書く。スチェクロフ作用素 Λ に対応する Γ_a 上の関数に対する双一次形式として

$$b(u, v) = \pi \sum_{n=1}^{\infty} n \{a_n(u)a_n(v) + b_n(u)b_n(v)\}$$

を考えるのが自然である。実際、双一次形式 $b(u, v)$ の定義域を $H^{1/2}(\Gamma_a)$ とし、適切に複素化して議論すれば、複素ヒルベルト空間 $L^2(\Gamma_a)$ における作用素 Λ は、$b(u, v)$ に対応する自己共役作用素であることが解る。すなわち、

$$D(\Lambda) = H^1(\Gamma_a), \quad D(b) = H^{1/2}(\Gamma_a)$$

として、

$$(\Lambda u, v)_{L^2(\Gamma_a)} = b(u, v),$$

$$u \in D(\Lambda), \quad v \in D(b),$$

および

$$(\Lambda^{1/2} u, \Lambda^{1/2} v)_{L^2(\Gamma_a)} = b(u, v),$$

$$u, v \in D(\Lambda^{1/2}) = D(b)$$

が成立している。ここで、$\Lambda^{1/2}$ は、

$$\Lambda^{1/2} f = \sum_{n=1}^{\infty} \sqrt{\frac{n}{a}} \{a_n \cos n\theta + b_n \sin n\theta\}$$

と表現される。

2. 境界双一次形式の CSM 近似

本節では、第1節で導入した境界双一次形式 $b(u, v)$ を代用電荷法にもとづいて近似する。二つの双一次形式 $b^{(N)}(u, v)$ と $\overline{b}^{(N)}(u, v)$ を提案する。

一般に平面 $\mathbf{R}^2$ の点を $\mathbf{r}$ と表わす。原点を中心とする極座標 $\{r, \theta\}$ によって $\mathbf{r}$ の直交座標表示 $\mathbf{r} = (x, y)$ が

$$\mathbf{r} = (r \cos \theta, r \sin \theta)$$

と表せるとして $\mathbf{r}$ を複素数

$$z = re^{i\theta}$$

と対応させる。

先ず原点を中心とする半径 a の開円板 D_a を固定する。D_a の円周を Γ_a で表す。実数 ρ を

$$0 < \rho < a$$

の範囲に固定し原点を中心とする半径 ρ の円 Γ_ρ を考える。

正整数 N を固定する。

$$\theta_1 = \frac{2\pi}{N}, \qquad \theta_j = j\theta_1, \quad j = 0, \pm 1, \pm 2, \cdots$$

とおく。円 Γ_ρ の上に点 $\vec{\rho}_j, 0 \leq j \leq N-1$、を配置し、円 Γ_a の上に点 $\mathbf{a}_j, 0 \leq j \leq N-1$、を配置する。このとき、複素数 $\rho e^{i\theta_j}, 0 \leq j \leq N-1$、と $ae^{i\theta_j}, 0 \leq j \leq N-1$、が、それぞれ $\vec{\rho}_j, 0 \leq j \leq N-1$、と $\mathbf{a}_j, 0 \leq j \leq N-1$、に対応しているものとする。代用電荷法の言葉では、$\vec{\rho}_j$ は電荷点、$\mathbf{a}_j$ は拘束点と言われている。今述べた電荷点と拘束点の配置を、この報告では、**電荷点ー拘束点円周上等間隔同相配置**と呼ぶことにする。

電荷点-拘束点円周上等間隔同相配置の場合の問題 $(\mathrm{E_f})$ **の代用電荷法による近似問題** $(\mathrm{E_f^{(N)}})$ を次のように定める：

$$(\mathrm{E_f^{(N)}}) \quad \begin{cases} u^{(N)}(\mathbf{r}) = \sum_{j=0}^{N-1} q_j G_j(\mathbf{r}) + q_N, \\[2mm] u^{(N)}(\mathbf{a}_j) = f(\mathbf{a}_j), \ 0 \leq j \leq N-1, \\[2mm] \sum_{j=0}^{N-1} q_j = 0. \end{cases}$$

この問題における、基底関数 $G_j(\mathbf{r})$ は、ラプラス作用素の基本解 $E(\mathbf{r})$:

$$E(\mathbf{r}) = -\frac{1}{2\pi}\log r$$

を用いて、

$$G_j(\mathbf{r}) = E(\mathbf{r} - \vec{\rho}_j) - E(\mathbf{r}), \quad 0 \le j \le N-1$$

と定められるものを用いる。

問題 $(\mathrm{E}_\mathrm{f}^{(N)})$ は、「問題中にある条件をみたすように $N+1$ 個のパラメタ $q_j, 0 \le j \le N$, を決めよ。」という問題である。

円周 Γ_a 上の N 個の拘束点を用いて得られる関数 $f(\mathbf{a}(\theta))$ の複素型の離散フーリエ係数を $f_n^{(N)}, n = 0, \pm1, \pm2, \cdots$, とおく。すなわち、

$$f_n^{(N)} = \frac{1}{N}\sum_{k=0}^{N-1} f(\mathbf{a}_k)\omega^{-nk}, \quad \omega = e^{i\theta_1}, \quad \theta_1 = \frac{2\pi}{N}$$

である。

定理1. 問題 $(\mathrm{E}_\mathrm{f}^{(N)})$ の解 $u^{(N)}(\mathbf{r})$ は存在して、一意である。離散フーリエ級数を用いると

$$u^{(N)}(\mathbf{r}) = f_0^{(N)} + \sum_{j=1}^{N-1} f_j^{(N)}\frac{\varphi_j^{(N)}(\mathbf{r})}{\varphi_j^{(N)}(\mathbf{a}_0)}$$

と表される。ここで

$$\varphi_j^{(N)}(\mathbf{r}) = \frac{N}{4\pi}\sum_{m \in j+N\mathbf{Z}}\frac{1}{|m|}\left(\frac{\rho}{r}\right)^{|m|}e^{im\theta},$$

$$1 \le j \le N-1$$

である。特に、

$$q_N = f_0^{(N)}$$

である。

上述の**定理1**は、桂田－岡本の論文 [1] から、その自然な拡張として得られる。

この結果を踏まえて、**境界双一次形式** $b(u,v)$ **の代用電荷近似の第一型**として、

$$b^{(N)}(u,v) = \int_{\Gamma_a}\left(-\frac{\partial}{\partial r}u^{(N)}(\mathbf{r})\right)v^{(N)}(\mathbf{r})d\Gamma$$

を考えるものとする。ここで、境界 Γ_a 上の関数 $u(\mathbf{a}(\theta))$ と $v(\mathbf{a}(\theta))$ を、それぞれ f として問題 $(\mathrm{E}_\mathrm{f}^{(N)})$ を定め、その解として得られるものが、定義式の右辺にある $u^{(N)}(\mathbf{r})$ と $v^{(N)}(\mathbf{r})$ である。

次いで、境界双一次形式の代用電荷近似の第二型を定めるために、電荷伝達ベクトル $\mathbf{g}$ と、電荷伝達行列 G、電界表示ベクトル $\mathbf{h}$ と、電界表示行列 H をそれぞれ定める。

始めに、$l \in \mathbf{Z}$ に対して

$$g_l = -\frac{1}{2\pi}\log|a - \rho\omega^l| + \frac{1}{2\pi}\log a$$

とおく。両側無限列 $\{g_l : l = 0, \pm1, \pm2, \cdots\}$ は周期 N を持っている。更に $N/2$ に関して対称である。**電荷伝達ベクトル** $\mathbf{g} \in \mathbf{R}^N$ は、

$$\mathbf{g} = (g_l)_{0 \le l \le N-1}$$

によって定める。**電荷伝達行列** G は、

$$G = (g_{jk})_{0 \le j,k \le N-1},$$

$$g_{jk} = g_{k-j}, \quad 0 \le j,k \le N-1$$

によって定める。行列 G は、N 次の実対称巡回行列である。問題 $(\mathrm{E}_\mathrm{f}^{(N)})$ は、

$$\text{(E)} \qquad \begin{pmatrix} G & \mathbf{1} \\ \mathbf{1}^\mathsf{T} & 0 \end{pmatrix}\begin{pmatrix} \mathbf{q} \\ q_N \end{pmatrix} = \begin{pmatrix} \mathbf{f} \\ 0 \end{pmatrix}$$

と表される。ここで、

$$\mathbf{1} = \begin{pmatrix} 1 \\ 1 \\ \cdot \\ \cdot \\ \cdot \\ 1 \end{pmatrix}, \quad \mathbf{q} = \begin{pmatrix} q_0 \\ q_1 \\ \cdot \\ \cdot \\ \cdot \\ q_{N-1} \end{pmatrix}, \quad \mathbf{f} = \begin{pmatrix} f(\mathbf{a}_0) \\ f(\mathbf{a}_1) \\ \cdot \\ \cdot \\ \cdot \\ f(\mathbf{a}_{N-1}) \end{pmatrix}$$

である。

行列 G の固有値を、$\lambda_j, 0 \le j \le N-1$, とすると、それ等は、

$$\lambda_0 = \frac{1}{2\pi}\log\frac{a^N}{a^N - \rho^N},$$

$$\lambda_j = \frac{N}{4\pi}\sum_{m \in j+N\mathbf{Z}}\frac{1}{|m|}\left(\frac{\rho}{a}\right)^{|m|}, \quad 1 \le j \le N-1$$

と表される。各 λ_j に対応する長さ 1 の G の固有ベクトル $\vec{\varphi}_j$ は、

$$\vec{\varphi}_j = \frac{1}{\sqrt{N}}\left(\omega^{jk}\right)_{0 \le k \le N-1}$$

と表される。N 個のベクトルの組 $\vec{\varphi}_j, 0 \le j \le N-1$, は、$\mathbf{C}^N$ の正規直交基底である。G の固有値は、全て零と異なるから G は正則である。このことに基づいて**定理1**を証明することが出来る。

変数 $\mathbf{r}$ の関数 $E_j(\mathbf{r}) = E(\mathbf{r} - \vec{\rho}_j)$ の原点に向かう半径方向偏導関数を H_j とする。すなわち、

$$H_j(\mathbf{r}) = -\frac{\partial}{\partial r}E_j(\mathbf{r}), \quad 0 \le j \le N-1$$

である。そこで、$l \in \mathbf{Z}$ に対して

$$h_l = H_0(\mathbf{a}_l)$$

とおく。両側無限列 $\{h_l : l = 0, \pm1, \pm2, \cdots\}$ は周期 N を持っている。更に $N/2$ に関して対称である。**電界表示ベクトル h** $\in R^N$ は、

$$\mathbf{h} = (h_l)_{0 \leq l \leq N-1}$$

によって定める。**電界表示行列** H は、

$$H = (h_{jk})_{0 \leq j, k \leq N-1},$$

$$h_{jk} = h_{k-j}, \quad 0 \leq j, k \leq N - 1$$

によって定める。行列 H は、N 次の実対称巡回行列である。

問題 $(\mathbf{E}_f^{(N)})$ の解 $u^{(N)}(\mathbf{r})$ の Γ_a 上における Ω_e から見た外向き法線微分係数の $\mathbf{r} = \mathbf{a}_j$ における値は、ベクトル $H\mathbf{q}$ の第 j 成分である。すなわち、(E) における $\mathbf{q}$ によって

$$\left(\frac{\partial u^{(N)}}{\partial n_e}(\mathbf{a}_j) \right)_{0 \leq j \leq N-1} = H\mathbf{q}$$

と表される。

さて $\mathbf{C}^N$ の元

$$\mathbf{u} = (u_j)_{0 \leq j \leq N-1}$$

と

$$\mathbf{v} = (v_j)_{0 \leq j \leq N-1}$$

に対して、その複素内積 $(\mathbf{u}, \mathbf{v})$ を

$$(\mathbf{u}, \mathbf{v}) = \sum_{j=0}^{N-1} u_j \overline{v_j}$$

とする。右辺の $\overline{v_j}$ は、v_j の共役複素数である。直交射影作用素 P と Q を、$\mathbf{C}^N$ の元 $\mathbf{v}$ に対して、

$$P\mathbf{v} = \frac{1}{N}(\mathbf{v}, \mathbf{1})\mathbf{1}, \qquad Q\mathbf{v} = \mathbf{v} - P\mathbf{v}$$

と定める。

以上の準備の下に、**境界双一次形式** $b(u, v)$ **の代用電荷近似の第二型**として

$$\overline{b}^{(N)}(u, v) = \frac{2\pi a}{N} \left(G^{-1} H Q \mathbf{u}, \mathbf{v} \right)$$

を考える。ここで

$$\mathbf{u} = (u(\mathbf{a}_j))_{0 \leq j \leq N-1}, \quad \mathbf{v} = (v(\mathbf{a}_j))_{0 \leq j \leq N-1}$$

である。

次の定理2において、実際の数値計算に際して使用する第二型の行列表現を与える。

定理2. 関数 $h(\theta)$ を次のように定める。

$$h(\theta) = \frac{1}{2\pi} \cdot \frac{a - \rho \cos\theta}{a^2 - 2a\rho\cos\theta + \rho^2}$$

そこで $j = 0, 1, \cdots, N-1$ に対して

$$h_j = h(\theta_j), \quad h_j^{(N)} = \frac{1}{N} \sum_{k=0}^{N-1} h_k \omega^{-jk},$$

として

$$\mathbf{h} = (h_j)_{0 \leq j \leq N-1}, \quad \mathbf{c} = G^{-1}\mathbf{h} = (c_j)_{0 \leq j \leq N-1}$$

と置く。境界双一次形式 $b(u, v)$ の代用電荷近似の第二型 $\overline{b}^{(N)}(u, v)$ に対して、

$$\overline{b}^{(N)}(u, v) = \left(B\mathbf{u}, \mathbf{v} \right), \quad B = \left(b_{jk} \right)_{0 \leq j, k \leq N-1}$$

と置く。つぎの表示が成立する。

(1)
$$c_j = \sum_{l=0}^{N-1} \frac{1}{\lambda_l} h_l^{(N)} \omega^{jl}, \quad 0 \leq j \leq N-1.$$

(2)
$$b_{jk} = \frac{2\pi a}{N} \left\{ c_{k-j} - \frac{1}{\lambda_0} h_0^{(N)} \right\}, \quad 0 \leq j, k \leq N-1.$$

(3)
$$b_{jk} = \frac{2\pi a}{N} \sum_{l=1}^{N-1} \frac{1}{\lambda_l} h_l^{(N)} \omega^{(k-j)l}, \quad 0 \leq j, k \leq N-1.$$

((2) の右辺の c_{k-j} の値は、(1) 式を任意の整数 j に対して拡張して定める。)

3. モデル問題の設定とその誤差評価

平面内の有界単連結領域 $\mathcal{O}$ を固定する。$\mathcal{O}$ の境界 $\mathcal{C}$ は十分に滑らかなものとする。$\mathcal{C}$ の外部領域を Ω と書く。

関数 $f \in L^2(\Omega)$ は、その台 $\mathrm{supp}(f)$ が有界なものとする。

正数 a を十分大きくとって、開円板 D_a が $\mathcal{O} \cup \mathrm{supp}(f)$ をその完全内部に含むようにする。

モデル問題として、次のポアッソン方程式 (E) を採用する。

(E)
$$\begin{cases} -\Delta u = f & \text{in} \quad \Omega, \\ u = 0 & \text{on} \quad \mathcal{C}, \\ \sup_{|\mathbf{r}| > a} |u| < \infty. \end{cases}$$

領域 Ω と円板 D_a の共通部分を内部領域と呼び、Ω_i で表す:

$$\Omega_i = \Omega \cap D_a.$$

さて $u, v \in H^1(\Omega_i)$ に対して、ディリクレ内積 $a(u, v)$ を考える:

$$a(u, v) = \int_{\Omega_i} \mathrm{grad}\, u \, \mathrm{grad}\, v \, d\Omega.$$

$v \in H^1(\Omega_i)$ なら、その Γ_a 上へのトレース $\gamma_a v$ は $H^{1/2}(\Gamma_a)$ の元である。したがって、$u, v \in H^1(\Omega_i)$ に対して境界双一次形式 $b(u,v)$ は適切に定義されている。そこで対称双一次形式：

$$t(u,v) = a(u,v) + b(u,v)$$

を $u, v \in H^1(\Omega_i)$ に対して定めることが出来る。

$H^1(\Omega_i)$ 上の連続線形汎関数 $F(v)$ は、

$$F(v) = \int_{\Omega_i} fv \, d\Omega$$

で定められるものである。

関数空間 V を以下のように定める：

$$V = \{v \in H^1(\Omega_i) : v = 0 \quad \text{on} \quad \mathcal{C}\}.$$

これらの記法を用いて、次の弱形式問題 (II) を定める。

$$(\text{II}) \quad \begin{cases} t(u,v) = F(v), & v \in V, \\ u \in V. \end{cases}$$

我々は、方程式 (E) と問題 (II) の同値性を認めて、今後は、(II) とその近似問題を考察する。

正数 ρ を、$0 < \rho < a$ をみたすように選んで固定する。正整数 N に対して、1 節で定めたように**電荷点ー拘束点円周上等間隔同相配置**となるように $\bar{\rho}_j, \mathbf{a}_j, 0 \leq j \leq N-1$、を設定する。

空間 V の有限次元部分空間の族

$$\{V_N : N = N_0, N_0 + 1, \cdots\}$$

は次の性質をみたすものとする。

$(V_N - 1)$ $\qquad V_N \subset C(\overline{\Omega_i}).$

$(V_N - 2)$
$$\begin{cases} V_N \text{の元 } v \text{ は、} \Gamma_a \text{上では、拘束点 } \mathbf{a}_j \text{を節点とし、} \\ \text{弧長に関して区分一次連続関数である。} \end{cases}$$

$(V_N - 3)$
$$\min_{v \in V_N} a(v - v_N) \leq \frac{C}{N}\|v\|_{H^2(\Omega_i)}, \quad v \in V \cap H^2(\Omega_i).$$

上の性質 $(V_N - 3)$ においては、C は、N と v に依存しない定数であり、

$$a(v) = a(v,v)^{1/2}, \quad v \in V$$

である。

上のような空間の族 $\{V_N : N = N_0, N_0 + 1, \cdots\}$ は、内部領域 Ω_i の境界を適切に折れ線近似して、多角形領域 $\Omega_i^{(N)}$ とし、$\Omega_i^{(N)}$ を三角形分割して標準的な

区分一次連続要素の空間 $\widehat{V}_N$ を作る。次いで $\Omega_i^{(N)}$ の境界上に辺を持つ三角形に対しては、Zlamal[3] の曲要素の考え方を用いて、$\widehat{V}_N$ を $C(\overline{\Omega_i})$ に含まれるように修正する。このような手順によって、条件 $(V_N - 1), (V_N - 2), (V_N - 3)$ をみたす族

$$\{V_N : N = N_0, N_0 + 1, \cdots\}$$

を作ることが出来る。

近似空間 V_N の元 v は、Γ_a 上では、

$$v(\mathbf{a}(\theta)) = \frac{\theta_{j+1} - \theta}{\theta_1}v(\mathbf{a}(\theta_j)) + \frac{\theta - \theta_j}{\theta_1}v(\mathbf{a}(\theta_{j+1})),$$

$$\theta_j \leq \theta \leq \theta_{j+1}, \quad 0 \leq j \leq N-1$$

と表現されていることに注意する。

さて、$u, v \in H^1(\Omega_i) \cap C(\overline{\Omega_i})$ に対して、

$$t^{(N)}(u,v) = a(u,v) + b^{(N)}(u,v),$$

$$\bar{t}^{(N)}(u,v) = a(u,v) + \bar{b}^{(N)}(u,v)$$

と定める。

次の二つの近似問題 $(\text{II}^{(N)})$ と $(\overline{\text{II}}^{(N)})$ を設定する。

$$(\text{II}^{(N)}) \quad \begin{cases} t^{(N)}(u_N, v) = F(v), & v \in V_N \\ u_N \in V_N. \end{cases}$$

$$(\overline{\text{II}}^{(N)}) \quad \begin{cases} \bar{t}^{(N)}(\bar{u}_N, v) = F(v), & v \in V_N \\ \bar{u}_N \in V_N. \end{cases}$$

我々の結果は次のようにまとめられる。

定理3.　ある定数 C が存在して、次の評価が成立する。

$$\left.\begin{array}{c} \|u - u_N\|_{H^1(\Omega_i)} \\ \|u - \bar{u}_N\|_{H^1(\Omega_i)} \end{array}\right\} \leq \frac{C}{N}\|u\|_{H^2(\Omega_i)}.$$

ここに、C は、(II) の解 u と N に依存しない。

4．二次元帰着波動問題における結合解法

ここまで考察してきた、二次元外部ラプラス問題の FEM-CSM 結合解法の手順は、自然に二次元外部ヘルムホルツ問題、すなわち帰着波動問題 (reduced wave problem) に適用できる。本節においては、この場合の手順をまとめる。

4．1．開円板外帰着波動問題

波数ベクトルの長さを表す正数を k とする。原点を中心とする半径 a の円 Γ_a の外部領域 Ω_e における帰着波動問題 (E_f) を考える。

$$(E_f) \quad \begin{cases} -\Delta u - k^2 u = 0 & \text{in } \Omega_e, \\ \qquad\qquad u = f & \text{on } \Gamma_a, \\ \lim_{r\to\infty}\left\{\dfrac{\partial u}{\partial r} - iku\right\} = 0. \end{cases}$$

ここで f は境界 Γ_a 上の複素数値連続関数である。

問題 (E_f) の解 $u = u(\mathbf{r})$ は、

$$u = \sum_{n=-\infty}^{\infty} f_n \frac{H_n^{(1)}(kr)}{H_n^{(1)}(ka)} e^{in\theta}$$

と表せる。ここで、f_n は、$f(\mathbf{a}(\theta))$ のフーリエ係数:

$$f_n = \frac{1}{2\pi}\int_{-\pi}^{\pi} f(\mathbf{a}(\theta)) e^{-in\theta} d\theta,$$

であり、$H_n^{(1)}(z)$ は、n 次の第一種ハンケル関数である。

問題 (E_f) に対応する**スチェクロフ境界双一次形式** $b(u,v)$ は

$$b(u,v) = \sum_{n=-\infty}^{\infty} \mu_{|n|}(u,e_n)_{L^2(\Gamma_a)}(v,e_n)_{L^2(\Gamma_a)}$$

として与えられる。ここで、$n = 0,1,2,\cdots$ に対して

$$\mu_n = k\frac{\dot{H}_n^{(1)}(ka)}{H_n^{(1)}(ka)}, \quad \dot{H}_n^{(1)}(z) = \frac{d}{dz}H_n^{(1)}(z)$$

であり、$n = 0, \pm 1, \pm 2, \cdots$ に対して

$$e_n = \frac{e^{in\theta}}{\sqrt{2\pi a}}$$

である。

4．2．開円板外帰着波動問題の FSM 離散化問題

原点を中心とする半径 a の開円板 D_a を固定する。D_a の円周を Γ_a で表す。実数 ρ を

$$0 < \rho < a$$

の範囲に固定し原点を中心とする半径 ρ の円 Γ_ρ を考える。

正整数 N を固定する。このとき 2 節で記述した**電荷点－拘束点円周上等間隔同相配置**が得られる。本節では、$\bar{\rho}_j$ は波源点、$\mathbf{a}_j$ は拘束点と言う。今述べた波源点と拘束点の配置を、**波源点－拘束点円周上等間隔同相配置**と呼ぶことにする。

波源点-拘束点円周上等間隔同相配置の場合の問題 (E_f) の基本解（FSM）法による近似問題 $(E_f^{(N)})$ を次

のように定める:

$$(E_f^{(N)}) \quad \begin{cases} u^{(N)}(\mathbf{r}) = \sum_{j=0}^{N-1} q_j G_j(\mathbf{r}), \\ u^{(N)}(\mathbf{a}_j) = f(\mathbf{a}_j),\ 0 \le j \le N-1. \end{cases}$$

この問題における、基底関数 $G_j(\mathbf{r})$ は、外向き放射条件をみたすヘルムホルツ方程式の基本解の定数倍である $H_0^{(1)}(kr)$ を用いて、

$$G_j(\mathbf{r}) = H_0^{(1)}(k|r - \rho e^{-i\theta_j}|), \quad 0 \le j \le N-1$$

と表されるものを用いる。

4．3．スチェクロフ境界双一次形式の FSM 離散化

始めに、

$$g(\theta) = H_0^{(1)}(k|ae^{i\theta} - \rho|)$$

と置き、$l \in \mathbf{Z}$ に対して

$$g_l = g(\theta_l)$$

とおく。両側無限列 $\{g_l : l = 0, \pm 1, \pm 2, \cdots\}$ は周期 N を持っている。更に $N/2$ に関して対称である。**波動伝達ベクトル** $\mathbf{g} \in \mathbf{R}^N$ は、

$$\mathbf{g} = (g_l)_{0 \le l \le N-1}$$

によって定める。**波動伝達行列** G は、

$$G = (g_{jk})_{0 \le j,k \le N-1},$$

$$g_{jk} = g_{k-j}, \quad 0 \le j,k \le N-1$$

によって定める。行列 G は、N 次の複素対称巡回行列である。すなわち

$$g_{jk} = g_{kj}, \quad 0 \le j,k \le N-1$$

が成立する。（エルミート対称ではないことに注意する。）

問題 $(E_f^{(N)})$ は、

$$(E) \qquad\qquad G\mathbf{q} = \mathbf{f}$$

と表示される。ここで、$\mathbf{q}$ と $\mathbf{f}$ は 2 節と同様に定めるものである。

行列 G の固有値を、$\lambda_j, 0 \le j \le N-1$、とすると、それ等は、

$$\lambda_j = \sum_{l=0}^{N-1} g_l \omega^{jl}, \quad 0 \le j \le N-1$$

と表示される。各 λ_j に対応する長さ 1 の G の固有ベクトルは、2 節で与えた $\vec{\varphi}_j$ である。N 個のベクトルの組 $\vec{\varphi}_j, 0 \le j \le N-1$, は、$C^N$ の正規直交基底である。G の固有値が、全て零と異なることと行列 G が正則であることは同値である。したがって、問題 $(\mathrm{E}_f^{(N)})$ の一意可解条件は、

$$\lambda_j \ne 0, \quad 0 \le j \le N-1$$

である。

変数 $\mathbf{r}$ の関数 $G_j(\mathbf{r})$ の原点に向かう半径方向偏導関数を H_j とする。すなわち、

$$H_j(\mathbf{r}) = -\frac{\partial}{\partial r} G_j(\mathbf{r}), \quad 0 \le j \le N-1$$

である。そこで、$l \in Z$ に対して

$$h_l = H_0(\mathbf{a}_l)$$

とおく。両側無限列 $\{h_l : l = 0, \pm 1, \pm 2, \cdots\}$ は周期 N を持っている。更に $N/2$ に関して対称である。波動微分ベクトル $\mathbf{h} \in R^N$ は、

$$\mathbf{h} = (h_l)_{0 \le l \le N-1}$$

によって定める。波動微分行列 H は、

$$H = (h_{jk})_{0 \le j,k \le N-1},$$

$$h_{jk} = h_{k-j}, \quad 0 \le j, k \le N-1$$

によって定める。行列 H は、N 次の複素対称巡回行列である。

問題 $(\mathrm{E}_f^{(N)})$ の解 $u^{(N)}(\mathbf{r})$ の Γ_a 上における Ω_e から見た外向き法線微分係数の $\mathbf{r} = \mathbf{a}_j$ における値は、ベクトル $H\mathbf{q}$ の第 j 成分である。すなわち、本節の (E) における $\mathbf{q}$ によって

$$\left(\frac{\partial u^{(N)}}{\partial n_e}(\mathbf{a}_j)\right)_{0 \le j \le N-1} = H\mathbf{q}$$

と表される。

定義 1. （FSM 離散化境界双一次形式の行列表現） 関数 $h(\theta)$ を次のように定める。

$$h(\theta) = -k \cdot \frac{a - \rho\cos\theta}{|ae^{i\theta} - \rho|} \cdot H_1^{(1)}(k|ae^{-i\theta} - \rho|) .$$

そこで $j = 0, 1, \cdots, N-1$ に対して

$$h_j = h(\theta_j), \quad h_j^{(N)} = \frac{1}{N}\sum_{k=0}^{N-1} h_k \omega^{-jk}$$

として

$$\mathbf{h} = (h_j)_{0 \le j \le N-1}$$

と置く。可解条件:

$$\lambda_j \ne 0, \quad 0 \le j \le N-1$$

が成立するものとして、

$$\mathbf{c} = G^{-1}\mathbf{h} = (c_j)_{0 \le j \le N-1}$$

と置く。つぎの表示が成立する。

(1) $\quad c_j = \sum_{l=0}^{N-1} \frac{1}{\lambda_l} h_l^{(N)} \omega^{jl}, \quad 0 \le j \le N-1.$

ここで任意の整数 j に対し (1) 式の右辺で c_j の値を定義して

(2) $\quad b_{jk} = \frac{2\pi a}{N} c_{k-j}, \quad 0 \le j, k \le N-1.$

と定義する。b_{jk} は次のように表されることに注意する。
(3)

$$b_{jk} = \frac{2\pi a}{N}\sum_{l=0}^{N-1} \frac{1}{\lambda_l} h_l^{(N)} \omega^{(k-j)l}, \quad 0 \le j, k \le N-1.$$

境界双一次形式 $b(u,v)$ の FSM 近似型 $\bar{b}^{(N)}(u,v)$ を、

$$\bar{b}^{(N)}(u,v) = (B\mathbf{u}, \mathbf{v}), \quad B = (b_{jk})_{0 \le j,k \le N-1}$$

によって定める。

Γ_a 上の連続関数 $v(\mathbf{a}(\theta))$ の集中質量近似関数を、

$$[v](\theta) = \sum_{j=0}^{N-1} v(\mathbf{a}_j)[w_j](\theta)$$

によって定義する。ここで、$[w_j](\theta)$ は、区間 $(\theta_j - (1/2)\theta_1, \theta_j + (1/2)\theta_1)$ の定義関数である。行列 B の固有値は、$0 \le l \le N-1$ なる l に対して

$$\mu_l^{(N)} = \frac{1}{N}\sum_{j=0}^{N-1}\omega^{jl}\left\{\sum_{m=0}^{N-1}\frac{\omega^{jm}}{\lambda_m}\left(\sum_{n=0}^{N-1} h_n \omega^{-nl}\right)\right\}$$

であり、対応する固有ベクトルは、$\vec{\varphi}_l$ である。$\mu_l^{(N)}$ の右辺は、整数 l に関して N を法として同じ値を定めている。そのようにすべての整数 l に対して $\mu_l^{(N)}$ を定めると、FSM 離散化境界双一次形式のスペクトル表現として以下の表示が成立する。

$$\bar{b}(u,v) = \sum_{n=-\frac{N}{2}}^{\frac{N}{2}} \mu_{|n|}^{(N)}([u],[e_n])_{L^2(\Gamma_a)}([v],[e_n])_{L^2(\Gamma_a)}.$$

4．4．一般散乱体に対する帰着波動問題の FEM-FSM 結合解法

平面内の有界単連結領域 $\mathcal{O}$ を固定する。$\mathcal{O}$ の境界 C は十分に滑らかなものとする。C の外部領域を Ω と書く。波数ベクトル (l, m) を持つ平面波を表わす関数を g と置く。すなわち、

$$g(x, y) = e^{i(lx + my)}, \qquad l^2 + m^2 = k^2$$

である。

次の帰着波動方程式 (E) を考える。

$$(E) \quad \begin{cases} -\Delta u - k^2 u = 0 & \text{in} \quad \Omega, \\ u + g = 0 & \text{on} \quad C, \\ \lim_{r \to \infty} \left\{ \frac{\partial u}{\partial r} - iku \right\} = 0. \end{cases}$$

正数 a を十分大きくとって、開円板 D_a が $\mathcal{O}$ をその完全内部に含むようにする。領域 Ω と円板 D_a の共通部分を内部領域と呼び、Ω_i で表す：$\Omega_i = \Omega \cap D_a$.

複素数値関数 $u, v \in H^1(\Omega_i)$ に対して、ディリクレ内積 $a(u, v)$ を考える：

$$a(u, v) = \int_{\Omega_i} \mathrm{grad}\, u \, \mathrm{grad}\, \bar{v} \, d\Omega.$$

ここで $\bar{v}$ は、v の共役複素数を表している。さらに $u, v \in L^2(\Omega_i)$ の L^2 内積を $m(u, v)$ とする：

$$m(u, v) = \int_{\Omega_i} u\bar{v} \, d\Omega.$$

$v \in H^1(\Omega_i)$ なら、その Γ_a 上へのトレース $\gamma_a v$ は $H^{1/2}(\Gamma_a)$ の元である。したがって、$u, v \in H^1(\Omega_i)$ に対して境界双一次形式 $b(u, v)$ は適切に定義されている（Zebic[2] など参照）。そこで対称双一次形式：

$$t(u, v) = a(u, v) - k^2 m(u, v) + b(u, v)$$

を $u, v \in H^1(\Omega_i)$ に対して定めることが出来る。以下では、関数空間 $H^1(\Omega_i)$ を W と書き、

$$V = \{ v \in W : v = 0 \quad \text{on} \quad C \}$$

とする。

これらの記法を用いて、次の弱形式問題 (II) を定める。

$$(II) \quad \begin{cases} t(u, v) = 0, & v \in V, \\ u + g = 0 & \text{on} \quad C, \\ u \in W. \end{cases}$$

我々は、方程式 (E) と問題 (II) の同値性を認めて、今後は、(II) とその近似問題を考察する。

正数 ρ を、$0 < \rho < a$ をみたすように選んで固定する。正整数 N に対して、本節第 2 小節で定めたように**波源点－拘束点円周上等間隔同相配置**となるように $\vec{\rho}_j, \mathbf{a}_j, 0 \le j \le N-1$, を設定する。

空間 W の有限次元部分空間の族

$$\{ W_N : N = N_0, N_0 + 1, \cdots \}$$

は次の性質をみたすものとする。

$(W_N - 1) \qquad W_N \subset C(\overline{\Omega_i}).$

$(W_N - 2)$
$$\begin{cases} W_N \text{の元 } v \text{ は、} \Gamma_a \text{上では、拘束点 } \mathbf{a}_j \text{を節点とし、} \\ \text{弧長に関して区分一次連続関数である。} \end{cases}$$

そこで V の近似空間 V_N を

$$V_N = W_N \cap V$$

とおき、$u, v \in H^1(\Omega_i) \cap C(\overline{\Omega_i})$ に対して、

$$\bar{t}^{(N)}(u, v) = a(u, v) - k^2 m(u, v) + \bar{b}^{(N)}(u, v)$$

と定める。内部境界 C 上の節点において g と一致する W_N の元を一つ固定して g_N とする。

次の近似問題 $(\overline{II}^{(N)})$ を設定する。

$$(\overline{II}^{(N)}) \quad \begin{cases} \bar{t}^{(N)}(\bar{u}_N, v) = 0, & v \in V_N, \\ \bar{u}_N + g_N = 0 & \text{on} \quad C, \\ \bar{u}_N \in W_N. \end{cases}$$

具体的な計算問題においては、内部境界 C もしかるべく折れ線近似された C_N に置き換わることが多いと思われる。かくして、**一般散乱体 $\mathcal{O}$ に関する帰着波動問題の FEM-FSM 結合解法**が定式化された。

問題 $(\overline{II}^{(N)})$ の解 $\bar{u}_N$ の真の解 u への収束性と誤差評価に関しては、筆者には、現在のところ不明である。さらに、数値的経験も今後の課題である。

参考文献

[1] Katsurada, M. and Okamoto, H., A mathematical study of the charge simulation method I, J. Fac. Sci. Univ. Tokyo, Sect. IA, Math, Vol. 35, pp. 507-518 (1988).

[2] Zebic, A., Equation de Helmholtz: Étude numérique de quelques précondeitionnements pour la methode GMRES, Raport de Recherche de INRIA, Numéro 1802, Décembre 1992.

[3] Zlámal, M., Curved elements in the finite element method. I, SIAM J. Numer. Anal. Vol. 10, pp. 229-240 (1973).

Publication List of NIFS-PROC Series

NIFS-PROC-1   " *U.S.-Japan on Comparison of Theoretical and Experimental Transport in Toroidal Systems Oct. 23-27, 1989* ", Mar. 1990

NIFS-PROC-2   " *Structures in Confined Plasmas —Proceedings of Workshop of US-Japan Joint Institute for Fusion Theory Program— *"; Mar. 1990

NIFS-PROC-3   " *Proceedings of the First International Toki Conference on Plasma Physics and Controlled Nuclear Fusion —Next Generation Experiments in Helical Systems— Dec. 4-7, 1989* " Mar. 1990

NIFS-PROC-4   " *Plasma Spectroscopy and Atomic Processes —Proceedings of the Workshop at Data & Planning Center in NIFS—* "; Sep. 1990

NIFS-PROC-5   " *Symposium on Development of Intensed Pulsed Particle Beams and Its Applications February 20 1990* "; Oct. 1990

NIFS-PROC-6   " *Proceedings of the Second International TOKI Conference on Plasma Physics and Controlled Nuclear Fusion , Nonlinear   Phenomena in Fusion Plasmas -Theory and Computer Simulation-* "; Apr. 1991

NIFS-PROC-7   " *Proceedings of Workshop on Emissions from Heavy Current Carrying High Density Plasma and Diagnostics* "; May 1991

NIFS-PROC-8   " *Symposium on Development and Applications of Intense Pulsed Particle Beams, December 6 - 7, 1990* "; June 1991

NIFS-PROC-9   " *X-ray Radiation from Hot Dense Plasmas and Atomic Processes* "; Oct. 1991

NIFS-PROC-10   " *U.S.-Japan Workshop on "RF Heating and Current Drive in Confinement Systems Tokamaks" Nov. 18-21, 1991* , Jan. 1992

NIFS-PROC-11   " *Plasma-Based and Novel Accelerators (Proceedings of Workshop on Plasma-Based and Novel Accelerators) Nagoya, Japan, Dec. 1991* "; May 1992

NIFS-PROC-12   " *Proceedings of Japan-U.S. Workshop P-196 on High Heat Flux Components and Plasma Surface Interactions for Next Devices* "; Mar. 1993

NIFS-PROC-13   「NIFS シンポジウム
「核燃焼プラズマの研究を考える－現状と今後の取り組み方」
1992 年 7 月 15 日、核融合科学研究所」 1993 年 7 月
NIFS Symposium "Toward the Research of Fusion Burning Plasmas -Present Status and Future strategy-", 1992 July 15, National Institute for Fusion Science"; July 1993 (in Japanese)

NIFS-PROC-14   " *Physics and Application of High Density Z-pinches* ", July 1993

NIFS-PROC-15   岡本正雄、講義「プラズマ物理の基礎」
平成 5 年度　総合大学院大学1994 年 2 月
M. Okamoto,
"Lecture Note on the Bases of Plasma Pysics" Graduate University for Advanced Studies Feb. 1994
(in Japanese)

NIFS-PROC-16   代表者　河合良信
平成 5 年度　核融合科学研究所共同研究
研究会報告書「プラズマ中のカオス現象」
"Interdisciplinary Graduate School of Engineering Sciences" Report of the meeting on Chaotic Phenomena in Plasma Apr. 1994 (in Japanese)

NIFS-PROC-17   平成 5 年度 NIFS シンオジウム報告書
「核融合炉開発研究のアセスメント」平成 5 年 11 月 29 日-30 日　於　核融合科学研究所
"Assessment of Fusion Reactor Development" Proceedings of NIFS Symposium held on November 29-30, 1993 at National Insitute for Fusion Science" Apr. 1994(in Japanese)

NIFS-PROC-18   *"Physics of High Energy Density Plasmas Produced by Pulsed Power"* June 1994

NIFS-PROC-19   K. Morita, N. Noda (Ed.),

Proceedings of 2nd International Workshop on Tritium Effects in Plasma Facing Components at Nagoya University, Symposon Hall, May 19-20, 1994", Aug. 1994

NIFS-PROC-20　研究代表者　阿部　勝憲　（東北大学・工学部）
所内世話人　野田信明
平成 6 年度　核融合科学研究所共同研究［研究会］「金属系高熱流束材料の開発と評価」成果報告書

K. Abe and N. Noda (Eds.),
"Research and Development of Metallic Materials for Plasma Facing and High Heat Flux Components"
Nov. 1994(in Japanese)

NIFS-PROC-21　世話人：森田　健治（名大工学部）、金子　敏明（岡山理科大学理学部）
「境界プラズマと炉壁との相互作用に関する基礎過程の研究」研究会報告
K. Morita (Nagoya Univ.), T. Kaneko (Okayama Univ. Science)(Eds.)
NIFS Joint Meeting "Plasma-Divertor Interactions" and "Fundamentals of Boundary Plasma-Wall Interactions" January 6-7, 1995 National Institute for Fusion Science" Mar. 1995 (in Japanese)

NIFS-PROC-22　代表者　河合　良信
プラズマ中のカオス現象
Y. Kawai,
"Report of the Meeting on Chaotic Phenomena in Plasma, 1994" Apr. 1995 (in Japanese)

NIFS-PROC-23　K. Yatsui (Ed.),
New Applications of Pulsed, High-Energy Density Plasmas"; June 1995

NIFS-PROC-24　T. Kuroda and M. Sasao (Eds.),
Proceedings of the Symposium on Negative Ion Sources and Their Applications, NIFS, Dec. 26-27, 1994",
Aug. 1995

NIFS-PROC-25　岡本　正雄
新古典輸送概論（講義録）
M. Okamoto,
"An Introduction to the Neoclassical Transport Theory" (Lecture note), Nov. 1995 (in Japanese)

NIFS-PROC-26　Shozo Ishii (Ed.),
"Physics, Diagnostics, and Application of Pulsed High Energy Density Plasma as an Extreme State";
May 1996

NIFS-PROC-27　代表者　河合　良信
プラズマ中のカオスとその周辺非線形現象
Y. Kawai ,
"Report of the Meeting on Chaotic Phenomena in Plasmas and Beyond, 1995", Sep. 1996 (in Japanese)

NIFS-PROC-28　T. Mito (Ed.),
Proceedings of the Symposium on Cryogenic Systems for Large Scale Superconducting Applications", Sep.
1996

NIFS-PROC-29　岡本　正雄
講義「核融合プラズマ物理の基礎 - I」
平成 8 年度　総合研究大学院大学　数物科学研究科　核融合科学専攻 1996年 10月
M. Okamoto
Lecture Note on the Fundamentals of Fusion Plasma Physics - I" Graduate University for Advanced Studies; Oct. 1996 (in Japanese)

NIFS-PROC-30　研究代表者　栗下　裕明（東北大学金属材料研究所）
所内世話人　加藤　雄大
平成 8 年度核融合科学研究所共同研究「被損傷材料の微小体積強度評価法の高度化」研究会　1996年 10月　9日　於：核融合科学研究所

H. Kurishita and Y. Katoh (Eds.)
NIFS Workshop on Application of Micro-Indentation Technique to Evaluation of Mechanical Properties of Fusion Materials, Oct. 9, 1996, NIFS ; Nov. 1996 (in Japanese)

NIFS-PROC-31　岡本　正雄
講義「核融合プラズマ物理の基礎 - II 」
平成 8 年度　総合研究大学院大学　数物科学研究科　核融合科学専攻　1997年 4月
M. Okamoto
"Lecture Note on the Fundamentals of Fusion Plasma Physics - II" Graduate University for Advanced

Studies; Apr. 1997 (in Japanese)

NIFS-PROC-32   代表者　河合　良信
平成8年度　核融合科学研究所共同研究　研究会報告「プラズマ中のカオスとその周辺非線形現象」

Y. Kawai (Ed)
Report of the Meeting on Chaotic Phenomena in Plasmas and Beyond, 1996; Apr. 1997 (mainly in Japanese)

NIFS-PROC-33   H. Sanuki,
Studies on Wave Analysis and Electric Field in Plasmas; July 1997

NIFS-PROC-34   プラズマ対向機器・PSI・熱・粒子制御合同研究会報告
平成9年6月27日（金）9:00～16:20　核融合科学研究所・管理棟4F第1会議室
1997年　10月
T. Yamashina (Hokkaido University)
Plasma Facing Components, PSI and Heat/Particle Control June 27, 1997, National Institute for Fusion Science T. Yamashina (Hokkaido University) ; Oct. 1997 (in Japanese)

NIFS-PROC-35   T. Watari,
Plasma Heating and Current Drive; Oct. 1997

NIFS-PROC-36   T. Miyamoto and K. Takasugi (Eds.)
Production and Physics of High Energy Density Plasma; Production and Physics of High Energy Density Plasma; Oct. 1997

NIFS-PROC-37   (Eds.)T. Fujimoto, P. Beiersdorfer,
Proceedings of the Japan-US Workshop on Plasma Polarization Spectroscopy and The International Seminar on Plasma Polarization Spectroscopy January 26-28, 1998, Kyoto; June 1998

NIFS-PROC-38   (Eds.) Y. Tomita, Y. Nakamura and T. Hayashi,
Proceedings of the Second Asian Pacific Plasma Theory Conference APPTC '97, January 26-28, 1998, Kyoto; Aug. 1998

NIFS-PROC-39   (Ed.) K. Hirano,
Production, Diagnostics and Application of High Energy Density Plasmas; Dec. 1998

NIFS-PROC-40   研究代表者　加古　孝（電気通信大学）
所内世話人　渡辺　二太
平成10年度核融合科学研究所共同研究 研究会「プラズマ閉じ込めに関連する数値計算手法の研究」
Ed. by T. Kako and T. Watanabe

Proceeding of 1998-Workshop on MHD Computations "Study on Numerical Methods Related to Plasma Confinement Apr. 1999